UNIVERSITÀ DI SIENA 1240

DEPARTMENT OF PHYSICAL SCIENCES, EARTH AND ENVIRONMENT

PhD in Experimental Physics

XXXVI Cycle

Coordinator: Prof. Riccardo Paoletti

MAGIC Observations of the Blazar TON 116 in a Multi-wavelength Context

Disciplinary Scientific Sector: FIS/01

A thesis submitted in partial fulfillment of the requirements for the degree of Doctor of Philosophy

PhD Student
Andrea Lorini
University of Siena
Via Roma 56

Signature

Supervisor
Dr. Sofia Ventura
INFN - Section of Pisa

Signature

Co-Supervisor
Dr. Giacomo Bonnoli
INAF-OA Brera

Signature

A. Y. 2022/2023

Abstract

This thesis focuses on the long-standing discussion on the blazar sequence intriguing the astrophysical community since the end of the '90s. Blazars constitute a subclass of Active Galactic Nuclei (AGNs) with a powerful radio jet pointing towards the Earth. They are characterized by a double-peaked Spectral Energy Distribution (SED), whose low-energy bump is thought to be due to synchrotron emission of electrons streaming in the jet, while the high-energy hump is likely due to inverse-Compton (IC) up-scattering of synchrotron photons by the same parent electrons. This emission mechanism is known as Synchrotron Self Compton (SSC). Blazars are further subdivided in Flat Spectrum Radio Quasars (FSRQs) and BL Lac objects, and their overall spectral trend follows a sequence which allows to discriminate the source type. The nature of the blazar sequence is still debated as actual feature of the blazar class or due to observing bias.

Here we investigate TON 116, a High-frequency-peaked BL Lac (HBL) object supposed to be a candidate outlier of the dubbed blazar sequence. As a matter of fact, if the largest proposed values for its uncertain redshift are assumed, it happens to constitute one of the overluminous HBL that are hardly accommodated in the picture of the blazar sequence. This motivated us to start an observing campaign in the Very High Energy (VHE, $E > 100$ GeV) domain, which has never been explored before for this source, with the Major Atmospheric Gamma Imaging Cherenkov telescopes (MAGIC), one of the currently operating atmospheric Cherenkov detectors.

A detection at VHE has a crucial role in assessing the nature of the targeted source, as it allows to put a solid constraint on the redshift, which is uncertain for TON 116 ($z > 0.483$). Unfortunately, MAGIC has not detected the source, but the observations unveiled its VHE emission for the first time, effectively constraining the blue tail of the IC bump, and confirming the *Fermi*-LAT insight about an IC peak at $\lesssim 100$ GeV and a highly suppressed spectrum well before 1 TeV. Moreover, we studied the source in a multi-wavelength context, exploiting observations carried out by further instruments in different spectral bands, namely *Fermi*-LAT (HE γ-ray), Swift-XRT (X-ray), and Sierra Nevada Observatory (OSN, optical). All the analyzed datasets allow us to obtain an overall picture of the spectral behaviour of TON 116, which is further processed by very recently developed fitting tools (python-based `agnpy-sherpa` packages and convolutional-neural-network-based MMDC platform). The broadband SED of the source is fitted with three SSC one-zone models, considering a power-law (PL) and a broken power-law (BPL) for the electron distribution, and a normalization to the total density. Including the upper limits improves the SSC PL model at VHE, but predicts an extreme HBL nature for TON 116. For this reason, the SSC BPL model turns out to be the best, as it also accounts for the upper limits without including them in the fitting procedure. This model is very similar to the one indicated by MMDC platform, involving a simple PL and a normalization to the electron luminosity. The best-fit parameters are then compared with the ones reported in the literature, validating our results about the most plausible broadband emission of TON 116 and confirming its HBL nature.

Contents

Introduction

The study and characterization of the blazar emission is among the most vibrant and exciting research fields in the scientific community of high-energy astrophysics. Blazars are intriguing objects among the wide Active Galactic Nuclei (AGNs) family. They are characterized by extended relativistic jets whose axis is basically coincident with the observer's line of sight (LoS). Blazars are known to be among the most powerful persistent objects in the Universe, emitting across the whole electromagnetic spectrum, and also visible from cosmic distances. Further extreme properties include e.g. strong variability at all wavelengths and high polarization degree. As blazars are jet-dominated active galaxies, they can either show broad emission lines in their optical spectra, or not, and they are called Flat Spectrum Radio Quasars (FSRQs) or BL Lac objects (BL Lacs) respectively (Subsec. 1.3.6). The Spectral Energy Distribution (SED) of blazars is typically characterized by two major bumps (Sub-subsec. 1.3.6.1): the low-energy part being commonly associated with synchrotron radiation from accelerated electrons streaming in the jet. While the high-energy component can be due either to inverse-Compton (IC) scattering of the synchrotron photons by the same parent electrons, to interactions between accelerated protons, nuclei, and photons, or to more exotic models involving a mixture between leptonic and hadronic scenarios (Subsec. 1.4.1 and 1.4.2).

At the end of the '90s, a new classification was proposed for blazars, based on their spectral trend: the so-called *blazar sequence*, defined for the first time in Fossati et al. (1998). According to this interpretation, the peak of the two broad humps is expected to be shifted to smaller frequencies, if the overall luminosity of the object is larger. Moreover, BL Lacs are on average found to be fainter than FSRQs. More recently, the blazar sequence was updated by Ghisellini, Righi, et al. (2017) thanks to the advent of next-generation instruments, such as the *Fermi*-LAT satellite (Subsec. 2.3.1). In the latter work, FSRQs show a more prominent Compton hump, since they show larger luminosity, and a hardened X-ray spectral slope, while BL Lacs are actually redder, i.e., both their hump peaks are shifted towards smaller frequencies (Sub-subsec. 1.3.6.1). However, the regular trend associated with the blazar sequence turned out to be quite controversial. Indeed, a significant part of the scientific community attributed the claimed trend to a mere bias caused by selection effects (e.g. Padovani 2007, Giommi et al.

2012, Sub-subsec. 1.3.6.2). The long-standing discussion on the nature of the blazar sequence culminated in the claim of the end of the blazar sequence by Keenan et al. (2021). The authors stressed that no significant synchrotron peak frequency-luminosity anti-correlation was found in a sample of more than 2 000 jetted AGNs.

In this uncertain sequence-related panorama, the present PhD work aims at searching for *outliers* of the blazar sequence in order to clarify the existence of the claimed trend as an intrinsic property of blazars rather than an observing bias. For this purpose, we focus on a High-frequency-peaked BL Lac object (HBL, Sec. 1.3.6) known as TON 116, which apparently seems not to follow the regular trend traced by the blazar sequence. Indeed, it shows an unexpectedly high γ-ray flux between a few tens of MeV and a few hundreds of GeV as measured by *Fermi*-LAT satellite (Sec. 4.1). Moreover, in the 4LAC catalogue (Ajello et al. 2020), an enhanced luminosity is associated to the source assuming a redshift $z \approx 1$. Under this hypothesis, TON 116 could belong to the overluminous HBL associated with the outliers of the blazar sequence. However, the distance (redshift) of the source is uncertain, and this evidence contributes to the puzzle. The latest distance estimation associates a lower limit $z > 0.483$ (Paiano et al. 2017, Sec. 4.1). In this framework, given the high state at HE (*Fermi*), measured until 2020, and the redshift largely undetermined, we have considered TON 116 as an ideal candidate for a deeper inspection into potential outliers of the blazar sequence.

In this context, observations in the VHE γ-ray band have a key role in clarifying the real nature of the source. For the exploration of the VHE band, we exploited the MAGIC telescopes (Ch. 3), one of the current operating Imaging Atmospheric Cherenkov Telescopes (IACTs; Subsec. 2.3.3) located at La Palma (Canary Islands, Spain). These instruments indirectly detect the primary γ-rays which hit the top of the Earth's atmosphere exploiting the Cherenkov radiation emitted by secondary particles of the electromagnetic showers triggered in the primary photons' travel to the ground (Subsec. 2.3.3). For the very first time ever, VHE data have been analyzed and the results are reported in this work (Sec. 4.2).

Additionally, the inclusion of VHE data in a multi-wavelength (MWL) context, spanning from optical to gamma rays (Sec. 4.3), allowed to derive a global picture of the source emission behaviour (Subsec. 4.3.4). Indeed, the combination of MWL observations allowed us to reach a complete characterization of the TON 116 emission.

Finally, we performed the modeling of TON 116 broadband SED exploiting two different, recently-developed, methods: the python-based `agnpy` package (with a `sherpa` wrapper, Sec. 5.1), and an online convolutional-neural-network-based tool (MMDC, Sec. 5.2). The two software allowed us to estimate the most plausible emission mechanisms featuring the TON 116 broadband SED.

The thesis is organized as follows. The first chapter contains a detailed overview about AGNs in the astroparticle context, concentrating in particular on blazars and their emission

mechanisms. The second chapter shows the instruments, and related detection techniques, which were exploited for the observation of TON 116, with a special focus on ground-based detectors. The third chapter describes the MAGIC telescopes with an insight into both the detector system and the standard analysis chain. The fourth chapter contains a detailed state-of-the-art description of our targeted source TON 116, highlighting the reasons that motivated us to study this source, and the analysis results, spanning from optical to the VHE regime (explored here for the first time). Finally, the fifth chapter deals with the interpretation and modeling of the broadband SED of TON 116 in a MWL context, in order to reach the conclusions of this work, summarized at the end of this thesis.

Chapter 1

VHE Astrophysics framework of blazars

This initial chapter contains a detailed description about the extragalactic sources known as AGNs, whose assumed structure and main classifications will be presented. This is done in the context of the main particles that we can detect from them, including *Cosmic Rays* (CRs) and photons[1]. Then we will focus on *blazars*, an extreme type of AGNs which our source TON 116 belongs to. However, TON 116 is a potential outlier of a claimed trend for blazars, the so-called *blazar sequence*, which will be described in detail as well. The final part of this chapter deals with the main radiative processes believed to be ongoing within blazars, able to explain their broadband emission.

1.1 Cosmic Rays

The Earth is continuously bombarded by energetic particles coming from any direction throughout the Universe. Their starting point are extreme cosmic accelerators, able to give them enough energy by which they can travel along very large distances, until eventually reaching us. The exact sources and processes that give rise to them are still uncertain though. The first studies about this mysterious extraterrestrial matter date back to the beginning of XX century. At the time, radioactivity had been freshly discovered by Henri Becquerel (1896), and its effects on the leaves of any electroscope, getting discharged by charged particles emitted by an intense enough radioactive source, were well known. Later on, improvements were possible by which electroscopes could get discharged even in the absence of any ionizing material. As a consequence, the question arose whether the source of radioactivity shall be of terrestrial origin, or instead come from outside our planet. To try to give an answer, soon scientists realized that the most effective way was to perform specific measurements far from the ground level. After some significant attempts, by e.g. Theodor Wulf and Karl Bergwitz, in 1912 Victor Hess was able to

[1]We remind that in the current multi-messenger (MM) framework, neutrinos and gravitational waves (GWs) do also constitute effective probes.

reach an altitude of about 5 200 m with a balloon flight, thanks to which the general increase of ionization level with height was undoubtedly shown. It was clear that this sort of environmental radioactivity comes from space, and in 1936 Hess was awarded the Nobel Prize in physics for unveiling *cosmic rays* (CRs) for the first time. Due to his pionieristic searches, he was de facto the initiator of *astroparticle* physics.

The composition of CRs was hard to clarify as well. Given their penetrating property, they were firstly believed to be *gamma* (γ) rays. These are classically defined as radiation quanta carrying an energy of at least 100 keV. However, after the confirmation of intensity variation with position due to the Earth geomagnetic field, since 1930's the idea got spread according to which CRs basically consist of positively charged particles. Nowadays, we know that all stable (and some unstable) atomic nuclei of the periodic table of elements contribute to CRs, but mostly protons ($\approx 90\%$) and α particles (helium nuclei, $\approx 9\%$). Also electrons and positrons are present, but in a tiny component, because they are easily prone to energy losses during their journey given their small mass.

If one wishes to concisely represent the CR flux, above an energy value of a few GeV to let the contribution from the Sun be negligible, the standard picture is Fig. 1.1. The plot, in logarithmic scale, represents the differential energy spectrum of CRs, i.e., the number of CRs per unit time, surface, energy, and solid angle as a function of the energy of the incoming particle. The trend spans many orders of magnitude for both of the axes, and is steadily decreasing with increasing energy. In terms of CR flux above a certain energy threshold (integral spectrum, see Subsec. 3.5.4), the left part corresponds to about 1 000 particles per second per square centimeter, while the right part, reaching an energy of the order of 10^{20} eV, to a particle per square kilometer per century only. The behaviour can be analytically expressed as

$$\Phi(E) = K \left(\frac{E}{E_0} \right)^{-\alpha} , \tag{1.1}$$

which is just a power-law with reference energy value $E_0 = 1$ GeV, numerical value of normalization constant $K \approx 3.0$ (e.g. Wiebel-Sooth, Biermann, and Meyer 1998), and slope α. The latter is about 2.7 until $E \approx 3 \cdot 10^{15}$ eV, above which the spectrum steepens with a new slope of 3.1. For this reason, the break position is known as *knee*. The standard interpretation of this feature is a change of the particle acceleration mechanism, and sources of cosmic particles. After the steepening, there is another position above which the slope changes again, called the *ankle*, approximately at 10^{18} eV where the index decreases back to $\alpha \approx 2.6$. Above this threshold, cosmic particles are called *Ultra High Energy Cosmic Rays* (UHECRs), and are thought to have an extragalactic origin. This is because at such high energies they are no longer significantly affected by the presence of interstellar and intergalactic magnetic fields, which randomize the direction of less energetic charged particles due to the Lorentz force. For this reason, they can be considered as relevant probes directly tracing back to the position of extreme astrophysical environments, basically at the same level of neutral particles such as photons and neutrinos. Beyond an energy $E \approx 5 \cdot 10^{19}$ eV, the spectrum is severely suppressed by the so-called *Greisen-*

Zatsepin-Kuzmin (GZK) cut-off, due to the interaction of CRs with the CMB[2] (Greisen 1966, Zatsepin and Kuzmin 1966). If the characteristic length associated to the energy loss due to CMB photons is taken into account, it is possible to show that UHECR protons can travel through a maximum distance of about 30 Mpc without being absorbed[3]. This value represents the *GZK horizon*. For major details see Chapter 2 in Spurio (2015).

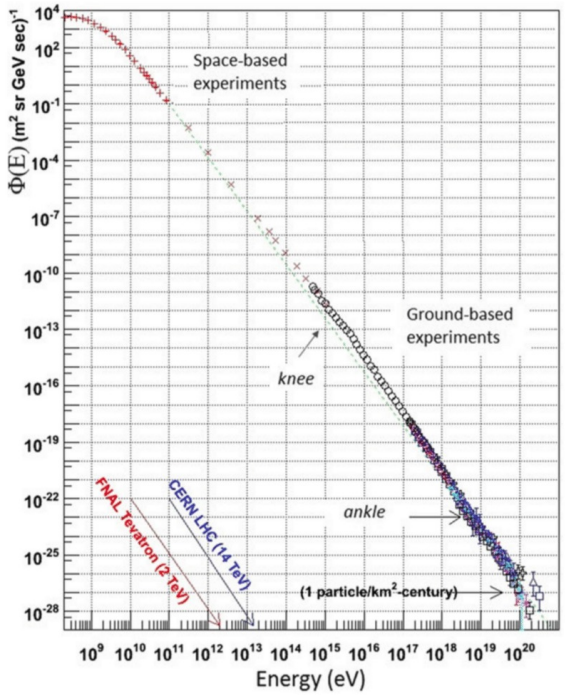

Figure 1.1: Differential energy spectrum of CRs, in which the positions corresponding to the slope changes, the "knee" and the "ankle", are respectively labelled. The dashed line stands for a spectral index equal to 3. The center of mass energy that can be reached at the TeVatron (Fermilab) and at the LHC (CERN) colliders are also indicated for comparison. Plot taken from Spurio (2015).

The study of particle messengers coming from space is the main means of investigation of astrophysical objects available to us. Cosmic rays can be divided into primary, the very particles accelerated in far, specific environments and spreading all over the space, and secondary, originated from collisions of the primary with intervening matter, either along their path through space, or in the Earth atmosphere. Up to an energy corresponding to that of the knee ($E \approx 3$ PeV), primary CRs can be directly detected out of the atmosphere by satellites or balloons, while above that feature, indirect measurements with ground-based instruments are required in order to get information about primary particles. In the latter case, this is possible because the interaction between primary and atmosphere's nuclei gives rise to *Extensive Air Showers* (EAS), basically vast cascades including a wealth of generated particles (Subsec. 2.3.2). In case of a highly

[2]The *Cosmic Microwave Background* is a radiation field uniformly permeating the Universe, which is commonly considered as an echo of the Big Bang. It corresponds to a thermal emission (the most perfect in nature) at about 2.73 K.

[3]Mpc := 10^6 pc. One *parsec* (1 pc $\approx 3.086 \cdot 10^{16}$ m) is the distance at which a length equal to the semi-major axis of the Earth orbit is seen at an angle of $1''$ (one arcsecond). It corresponds to about 3.26 l.y., where 1 l.y. (*light-year*) is the distance covered by light in one year ($\approx$ 9500 billion kilometers).

energetic proton p (or a heavier nucleus), the typical collision can be represented by

$$p + N \longrightarrow \pi^{\pm} + \pi^0 + K^{\pm} + K^0 + p + n + \dots \quad , \tag{1.2}$$

where N is an atmospheric nucleus, π are pions, K are kaons, p and n further nucleons (protons, neutron, or nuclei), etc. Many of the subproducts have a very short lifetime, and decay into further particles. In particular, the vast majority are charged pions (π^+, π^-) which fastly decay in muons and neutrinos, while neutral pions (π^0) are turned into two γ-rays. The latter start an *electromagnetic* (EM) component through conversion into electron-positron pairs and bremssthrahlung emission, until the energy losses due to excitation and ionization become dominant (details in Subsec. 2.3.2). The nucleon component can trigger further secondary cascades, while muons and neutrinos constitute the penetrating component reaching the ground. Among all the particle content of CRs, a small percentage consists of photons, which are massless particles making up light, and travelling at a speed $c = 299\,972\,458$ m/s in vacuum[4]. They do not have any electric charge, so, if not absorbed, they basically point back to the original source that emitted them, just like the elusive neutrinos[5]. Photons are the messengers which we are actually interested in for this work. More precisely, with regard to all the EM spectrum (see Sec. 2.1), our main focus is on γ-ray photons with very high energy. They represent an extreme emission range that only very peculiar astrophysical sources, like blazars, can significantly reach. In the following part of this chapter, this intriguing aspect will be clarified.

1.2 Very High Energy domain

In astrophysics, energy values above 100 GeV define the *Very High Energy* (VHE) domain. The exploration of such extreme band requires the usage of ground-based atmospheric detectors (Subsec. 2.3.3) in order to overcome the limitation due to much lower flux values, and thus, to increase the statistics of events collected in a reasonable amount of time. Furthermore, at those energies the γ-ray flux reaching the Earth can be heavily affected by interaction with ambient photons or intervening matter. The most common photon-photon interaction is represented by

$$\gamma + \gamma \longrightarrow e^- + e^+ \quad , \tag{1.3}$$

occurring if the total energy of the photons is larger than the rest mass of the electron and the positron produced, that is, 1.022 MeV in the center of mass. In general, this process can be

[4]Relativity sets this value as an upper limit for the speed of any object or information propagating throughout the Universe.

[5]Neutrinos are very light, neutral particles which interact extremely weakly with matter, as their cross section is much smaller than that of photons or other particles. They come in three flavours (electron, muon, tau) which oscillate between each other during propagation.

caused by dense radiation fields along the γ-ray path. At the largest scales, also *Extragalactic Background Light* (EBL) can act as a barrier for γ-rays, as described e.g. by Stecker, De Jager, and Salamon (1992). This is basically a radiation field made up of photons coming from stellar activity, eventually re-processed by interaction with dust or matter throughout the whole cosmological evolution. The presence of this diffuse light actually causes a suppression of γ photons via the pair production 1.3. The process gets enhanced with increasing both the photon energy and the distance. Therefore, VHE observations are distance-limited: if the emitter is relatively close, say, at $z < 0.05$, only energies above few TeV are affected, while if it is located at cosmological distances, all the VHE band may in principle get suppressed. For instance, if $z > 0.5$ then energies of the order of 100 GeV are already significantly absorbed. Thus, it is important to take into account the EBL, in order to trace back the γ-ray flux as intrinsically emitted by a certain source. However, it is not easy to measure the exact EBL spectrum, the main problem being the presence of the so-called *zodiacal* light[6]. The most plausible shape, following Hauser and Dwek (2001), consists of a double-peak trend in the near- and far-infrared bands, but given the difficulty of a direct derivation, many models have been developed since then (like Stecker, Malkan, and Scully 2006 and Franceschini, Rodighiero, and Vaccari 2008, updated in 2016 and 2018 respectively, or Gilmore et al. 2012, Kneiske and Dole 2010, Domínguez et al. 2011, Inoue et al. 2013).

The "matter" version of the interaction 1.3 results in a pair production as well, but it occurs through the electric Coulomb field of a nucleus:

$$\gamma + N \longrightarrow N + e^- + e^+ \quad . \tag{1.4}$$

The energy threshold is the same as the photon-photon one (≈ 1.022 MeV), but high energy of photons and high atomic number of matter are required for the process to be effective. In interstellar or intergalactic space this process can usually be neglected, therefore VHE γ-ray photons can reach our planet with no significant suppression if the emitting objects are not located too far from us.

The official catalogue of extragalactic sources detected at VHE is called TeVCat[7], and currently includes about 80 entries. They are mostly blazar (Subsec. 1.3.6), the class of objects we are interested in for this thesis, in particular belonging to the High-energy-peaked BL Lac object class (HBLs) with Compton hump peaking at 100 GeV or above. The most extreme case is represented by Extreme HBLs (EHBLs), which are 14 out of all the TeVCat sources so far. These sub-divisions of the blazar class are clarified in the following part of the chapter, once an overview about AGNs is provided.

[6]This is a softly bright cone of whitish light extending in the direction of the Sun and all along the ecliptic (the yearly apparent path of the Sun onto the sky). It is caused by scattering of solar photons by dust particles located within the solar system.

[7]See reference paper Wakely and Horan 2008, and official website http://tevcat.uchicago.edu/.

1.3 AGN overview and classification

1.3.1 Historical context

In the mid 1920's the astronomer Edwin Hubble discovered some Cepheid stars inside the great Andromeda nebula, hence, thanks to a period-luminosity relation specific to that kind of variable stars (found by Henrietta Leavitt shortly before), he was able to estimate their distance. His result undoubtedly showed that Andromeda is so distant from us that cannot belong to our galaxy. This finally solved the so-called "Great Debate" about the purely galactic or eventually extragalactic nature of the visible nebulae in the sky. Hubble's conclusion also made it evident that the Universe is much bigger than ever thought until that time. Likely, it can be considered as another revolution in astronomy, after the one represented by Galileo Galilei's telescope at the beginning of XVII century.

Few years later, Hubble measured the redshift z (Sub-subsec. 1.3.6.3) of a set of nearby galaxies, obtaining a very famous law simply linking their radial recessing speed to their distance d. The proportionality constant is the so-called Hubble constant, $H_0 \approx 70\,\mathrm{km\,s^{-1}\,Mpc^{-1}}$, but at that time overestimated by almost an order of magnitude due to a significant underestimation of distances. H_0 is the inverse of a time quantity, in particular, of the typical expansion time of the Universe, i.e. its age as a first approximation ("Hubble time"). Nearly all galaxies, apart from a few, very close ones (among which the above-mentioned Andromeda), were actually discovered to be moving away from us, the faster, the more distant they are. The law represented the first real proof against the dominant idea regarding a static Universe, hence the starting point of modern cosmology. According to the accepted scenario, the Universe was born about 13.8 billion years ago from a singularity with basically infinite both temperature and density known as "Big Bang", and since then, it is overall expanding and cooling. This is also in agreement with the Friedmann-Le Maître cosmological solutions of Einstein's master result, the General Relativity's field equation, one of the cornerstones of modern astrophysics. It is thought that the current expansion of the Universe is driven by *Dark Energy* (DE), considered as a sort of "vacuum energy" and representing about 70% of the total content (*contrast density* value $\Omega_\Lambda \approx 0.7$). Despite many candidates, either inside or outside the Standard Model (SM) of particles and interactions, also *Dark Matter* (DM) is still unknown, which accounts for up to about 25% of the Universe content ($\Omega_{DM} \approx 0.25$). Its presence can be revealed by a much larger amount of mass with respect to the visible one, especially from galactic scales on. According to current evidences, the common atomic matter which we are familiar with, constitutes only about 5% ($\Omega_m \approx 0.05$) of our Universe[8].

Since the first research programs about galaxy morphology in the '30s by means of optical photometry, it is known that galaxies can be divided into two main types. Namely, *elliptical* (or *early-type*) galaxies have a somewhat spheroidal shape more or less flattened, apparently with

[8]The ΛCDM (Λ *Cold Dark Matter*) model states that the dark component (Λ) is dominant. *Cold* DM means that it was no more relativistic when matter and radiation got decoupled in the hot early phases after the Big Bang.

no clear sub-structure, while *spiral* (or *late-type*) galaxies show a differentially-rotating disk composed by a central bulge, and external arms with a variable degree of curliness. Spirals also have variable bulge/disk brightness ratio. Morphologically, *lentil-shaped S*0 galaxies are a middle way between elliptical and spiral ones, but are considered as early-type galaxies. There also exist *irregular* galaxies, showing no particular shape and usually relatively small. They can come as a consequence of galactic collisions. This general Hubble classification is just a visual-based separation with no evolution aim, obviously prone to projection effects too. Interestingly, the different galaxy types just listed are characterized by major spectral differences. In general, elliptical galaxies tend to show an emission dominated by redder wavelengths, due to an old stellar population combined with both high dust and low gas content, while spiral galaxies show also a bluer spectral component due to the presence of young hot stars. These stars keep forming thanks to a relevant fraction of interstellar gas available (especially along the arms). In the case of irregular galaxies, usually the blue emission is even more significant, because of a highly enhanced star formation rate. In any case, the standard emission of galaxies is mainly attributable to stars, with a small contribution by gas and dust. Hence, a typical galaxy spectrum can be seen as a superposition of Planck curves, mostly ranging from ultraviolet (UV) bands to infrared (IR) ones[9].

However, a rare class of galaxies exists whose emission cannot be described as a simple addition of stellar spectra. These "abnormal" objects are most commonly known as Active Galaxies; in particular, in AGNs the source of the vast majority of their radiation is restricted to a very small region located at their very center, as we will see later. Yet, these intriguing objects turn out to be the most powerful persistent sources in the Universe, detectable up to very remote distances, as far as several billion light-years away from us ($z > 3$). Indeed, AGNs host very violent physical processes, including strong acceleration mechanisms by which, combined with relativistic effects, they are made incredibly bright virtually all across the electromagnetic spectrum, from radio to γ-rays. For the same reason, they are also thought to be the main source of the most energetic particles that we can detect (*Ultra High Energy Cosmic Rays*, Sec. 1.1). These facts became clearer and clearer since the last century, as soon as technological improvements and new instruments allowed scientists to reveal particles in a very broad energy range, and investigate still unexplored EM portions different from just the naturally-available optical. It was also possible to find out another crucial property of AGN emission, that is, variability. This kind of objects can show very rapid changes in flux values, possibly going down to minute time-scales in the most extreme cases. In general, the larger is the radiation frequency, the shorter is the time variability. Among the wide AGN family (Sec. 1.3), there is an even rarer class of radio-emitters with a pair of narrow symmetrical jets developing from the host galaxy center up to kpc-Mpc scales. In case the jets are nearly displaced in the Earth direction, they are called *blazars* (Subsec. 1.3.6). Many systematic studies have been performed over them, with

[9] Stars can be described with a set of optically-thick layers in thermodynamical equilibrium at a given temperature and density decreasing outwards. Thus, the emission from their surface (range $\sim 2\,000$ - $50\,000$ K) follows well the one of a black-body.

important achievements for the comprehension of the blazar phenomenon, but a lot of questions are still open. The most debated concern e.g. a SED (Spectral Energy Distribution)-driven unified view, the central acceleration mechanisms, and the leptonic or hadronic origin of the emission. This is especially true for the most recently-developed γ-ray astronomy.

1.3.2 Emission mechanism

Among all the known galaxies, about 1% do have emission characteristics not compatible with expected thermal processes. This kind of objects, instead, show a core which can overcome in luminosity the whole host galaxy itself by several orders of magnitude, making them up to a factor of a thousand more luminous ($L \approx 10^{44}$-10^{48} erg/s) with respect to standard galaxies. They are actually called AGNs. These objects constitute special laboratories for uncommon physics, and their brightness makes them crucial probes of the large-scale Universe (Urry and Padovani 1995). The outstanding quantity of persistent radiation from AGNs is not restricted to some particular bands, but rather, it typically comprises all of the spectral wavelengths from radio up to γ-rays. Also, the emission changes over time, of some orders of magnitude down to minute time scales in the most extreme cases.

These basic properties are commonly explained by accretion phenomena onto a central supermassive black hole (SMBH) with a size of the order of 1 A.U. and a mass of the order of 10^6-10^{10} $M_\odot$ approximately[10]. As far as we know, all galaxies do likely host a SMBH at their center (also the Milky Way), but only those characterized by a considerable quantity of matter that falls towards it actually become active. This is ultimately attributable to the release of potential gravitational energy, firstly converted into kinetic energy of the infalling material. The latter is organized as a hot accretion disk reaching distances of sub-pc scale from the SMBH, and emitting thermal radiation as a black-body (BB). The disk rotates differentially, and undergoes viscous and turbulent phenomena which cause losses of angular momentum. This also gives rise to emission in the optical, ultraviolet, and X-ray bands. Matter reaching a typical distance of less than three times a *Schwarzschild radius* is not on a stable orbit anymore, and will get swallowed by the SMBH. It is useful to quantify the rapidity at which this occurs by means of the mass accretion rate $\dot{M}_{BH} := dM_{BH}/dt$ (the SMBH mass is denoted as M_{BH} for brevity), linked to the accretion luminosity L_{acc}. Part of the matter, however, falls into the SMBH without radiating, so it is convenient to introduce a parameter η representing the radiative efficiency of the accretion. The latter can be used to write the accretion luminosity as

$$L_{disk} = \eta \, \dot{M}_{BH} \, c^2 \quad , \tag{1.5}$$

with c speed of light in vacuum (Frank, King, and Raine 2002). A first-order estimate of the

[10]The Astronomical Unit (A.U.) is the average distance between the Earth and the Sun, equal to around 149.6 million kilometers. The mass of the Sun is $M_\odot \approx 1.99 \cdot 10^{30}$ kg.

SMBH mass can be inferred through the *Eddington luminosity*, which is defined as

$$L_{edd} := \frac{4\pi G c m_p}{\sigma_T} M_{BH} \approx 1.3 \cdot 10^{38} \frac{M_{BH}}{M_\odot} \text{ erg s}^{-1} \quad , \tag{1.6}$$

where $G \approx 6.67 \cdot 10^{-11}\,\text{m}^3\,\text{kg}^{-1}\,\text{s}^{-2}$ is the gravitational constant, $m_p \approx 1.673 \cdot 10^{-27}$ kg is the proton mass[11], and $\sigma_T \approx 6.65 \cdot 10^{-25}\,\text{cm}^2$ is the Thomson cross-section. This corresponds to the maximum luminosity for an emitting object in order not to get broken apart by its own radiation pressure. Clearly, if matter is infalling, the SMBH gravitational force (assumed as largely dominant) must be greater than the radiation one, thus the SMBH mass in the above definition 1.6 can be considered as a lower limit (Schneider 2006). The accretion rate is usually expressed in terms of the correspondent rate at the Eddington luminosity through

$$\dot{m} = \frac{\dot{M}_{BH}}{\dot{M}_{edd}} \quad . \tag{1.7}$$

In most cases, it is also useful to consider the link between the Eddington luminosity and the related accretion rate. The formula for such a link includes the squared speed of light:

$$L_{edd} = \dot{M}_{edd}\, c^2 \quad . \tag{1.8}$$

If we combine eq. 1.5 and eq. 1.8 into the definition 1.7, another relevant expression can be obtained for the accretion rate, that is

$$\dot{m} = \frac{1}{\eta} \frac{L_{disk}}{L_{edd}} \quad . \tag{1.9}$$

This formula is particularly useful to provide a measure of the accretion mode in the case of blazars, as will be pointed out in Subsec. 1.3.6. In general, models related to high $\dot{m}$ values ($\dot{m} \gtrsim 0.01$, Ghisellini, Tavecchio, et al. 2011) predict the formation of a geometrically thin and optically thick accretion disk called *Shakura-Sunyaev Disk* (SSD, Shakura and Sunyaev 1973). Its radiation activity is efficient and can be approximated as thermal, with a temperature gradient increasing inward. Specifically, the inner part mostly emits in the X-ray band, while the outer part in the ultraviolet (UV)-optical. Low accretion rates, on the contrary, are responsible for geometrically thick and optically thin disks, not radiatively efficient due to the fact that much of the radiation remains confined inside them. They are known as *Advection-Dominated Accretion Flows* (ADAF) and their particle density is much lower than the Shakura-Sunyaev case, implying an energy exchange time between protons and electrons larger than the accretion time (Narayan and Yi 1994). Therefore, a non-thermal radiation arises in the plasma of the disk, in the form of

[11] The electron mass is neglected because about 2 000 times smaller ($m_e \approx 9.109 \cdot 10^{-31}$ kg).

synchrotron, inverse-Compton, and bremsstrahlung. It is mostly due to electrons and typically ranges form radio to soft X-rays (energy up to about 10 keV).

1.3.3 AGN structure

The large-scale structure of a typical AGN is thought to be like the one shown in Fig. 1.2. Nearby the accretion disk, discrete clumps of totally or partially ionized plasma are in rapid motion around the SMBH, as fast as 10^3-10^4 km/s. The related Doppler shift widens their strong emission lines at visible and UV wavelengths, caused by de-excitation of atoms and ions previously excited by thermal radiation coming from the accretion disk. Due to this spectral feature, they are considered as the components of the Broad Line Region (BLR), extending between 0.1 and 1 pc approximately.

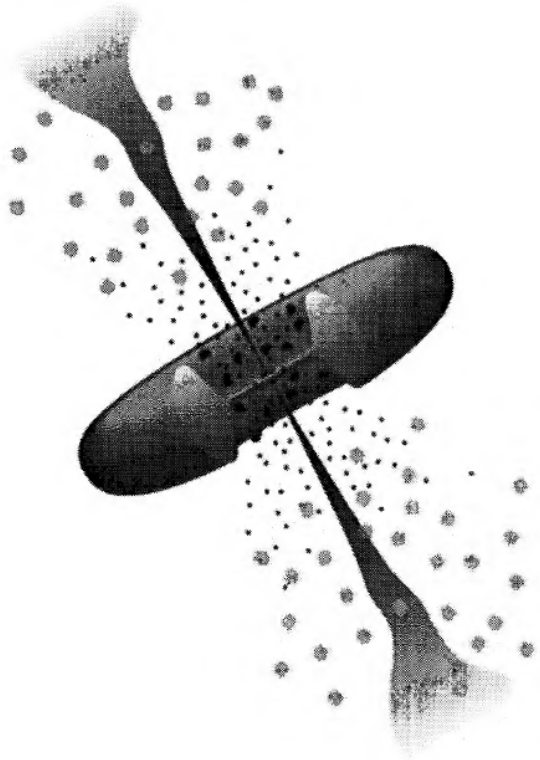

Figure 1.2: Not-to-scale image representing the structure commonly assumed for AGNs (see text for details). Sketch taken from Urry and Padovani 1995.

At farther distances from the accretion disk, typically from 1-10 pc up to 100 pc, an optically thick system made of gas and dust with a thoroidal shape acts as a barrier for optical and UV radiation coming from the inner parts. This basically prevents light of those bands to be detected along any external direction crossing the torus. The occurrence of such an obscuration can be proved through spectro-polarimetry observations, by which polarization likely due to electron scattering is revealed. Nevertheless, the obscuring torus re-emits the absorbed radiation of the disk and BLR at infrared (IR) bands (Netzer 2013). Indeed, it becomes essentially transparent in

the far-IR ($\lambda \sim 100\ \mu$m), where thermal emission by dust grains occurs (Pier and Krolik 1993). According to some models, the dusty torus is composed by isolated, dense clouds rather than by a uniform distribution of matter (e.g. Stalevski et al. 2012).

More outside, up to a distance of the order of 100 pc from the SMBH, the space is referred to as Narrow Line Region (NLR), as it is filled with more sparse clouds of ionized gas which are moving more slowly (300-500 km/s). Thus, with respect to the BLR, their emission lines are narrower, and characterized by both permitted and forbidden lines[12]. The latter evidence allows to derive a number density of 10^3-10^4 cm^{-3} for the NLR, which is typically a factor 10^6 smaller than the one estimated for the BLR. As the NLR is not surrounded by the torus, it is in principle always visible in the AGN spectra.

Eventually, energetic matter from the plasma orbiting within the disk gets somehow accelerated along the rotation axis of those systems. This results in a collimated outflow of high-speed particles giving rise to radio-emitting jets, whose extension may be much larger than the host galaxy itself, reaching up to 1 Mpc-length scale. The ending point of the radio-jets are usually *lobes*, which are extended structures where the accelerated plasma likely stops because it interacts with the local medium. The radiation from the jets is non-thermal, extremely beamed, and boosted due to relativistic effects. The latter can also make the jets appear asymmetric, as the radiation originated from particles streaming away from us undergoes a de-boosting phenomenon. In such cases, evidence of the presence of the counter-jet can arise from polarized optical emission, or from modest *superluminal* motions. However, the exact origin and composition of the jets are still debated (e.g. Blandford, Meier, and Readhead 2019). For instance, they may originate by extraction of energy or angular momentum from the accretion disk, or by extraction of rotational energy from the SMBH spinning at the AGN center (Blandford and Payne 1982, Blandford and Znajek 1977 respectively). In addition, the jets seem not to consist of uniform streams of particles, but rather of *knots*, i.e., zones with larger densities maybe caused by shocks propagating downward (e.g. Müller et al. 2011). In any case, the jets host accelerated particles moving at relativistic speeds, and emitting radiation from radio to γ-ray band through a variety of different phenomena. For such an extreme behaviour, both leptons and hadrons can be involved, and the presence of an ambient magnetic field plays a fundamental role. The main emission models are discussed in Sec. 1.4.

1.3.4 AGN classes

Many AGN classes have been defined over time, forming a wide zoology based on different empirical criteria. One of the first classifications was made by the astronomer Carl Seyfert (1911-1960), who introduced the separation between *Seyfert I* and *Seyfert II* active galaxies according to their optical spectra. The former class shows a bright continuum and both broad

[12] Spectral lines are permitted or forbidden depending on whether they are likely or unlikely to occur, according to selection rules of quantum mechanics. The medium density has a key role for spontaneous or collisional transitions within atomic energy levels.

and narrow emission lines, while the latter shows a weak continuum and narrow emission lines. Another fundamental classification concerns the intensity of radio emission with respect to the optical one. In particular, AGNs can be divided into radio-loud or radio-quiet, depending on a *radio loudness* parameter larger or smaller than a reference value of 10. This parameter is defined as the ratio between the radio flux and the blue one, conventionally taken at 5 GHz and 2 500 Å in the source frame respectively (Stocke, Morris, Weymann, et al. 1992):

$$\mathsf{R}_\ell = \frac{F_{5\,\mathrm{GHz}}}{F_{2\,500\,\text{Å}}} \quad . \tag{1.10}$$

About 10% of the AGNs are radio-loud. The empirical quantity R_ℓ has been one of the first used to classify AGNs, as radio was actually the first observational window to be opened other than optical[13]. However, one of the main issues is that the optical emission can be heavily obscured (Subsec. 1.3.3), such that it may be not representative of intrinsic radiation properties (e.g. jet/disk ratio). Padovani (2017) recently suggested a new classification based on the "jetted"/"non-jetted" dichotomy to discern underlying physical differences among AGN objects.

Focusing instead on the optical and UV properties, another historical AGN classification is into Type 1 or Type 2. Type 1 AGNs are characterized by high continuum level and broad emission lines believed to be directly related to hot and fast matter nearby the SMBH. This class includes both radio-quiet sources, e.g. low-luminosity Seyfert I galaxies and high-luminosity quasars[14] and radio-loud sources. The latter can be Broad-Line Radio Galaxies (BLRG) if having low luminosity, or if the luminosity is high, they can be Steep Spectrum Radio Quasars (SSRQs) or Flat Spectrum Radio Quasars (FSRQs). The latter couple of objects, in turn, depends on the continuum slope found at GHz radio band (separation index 0.5). Type 2 AGNs show instead a low continuum level and narrow emission lines, thus they are known as Narrow Line Radio Galaxies (NLRGs). This is likely because their inner radiation gets absorbed by an optically thick layer. Mainly, Seyfert II galaxies constitute the radio-quiet members with low luminosity, while high luminosity members are thought to be AGNs showing large IR emission. Typical radio-loud Type 2 sources are the Fanaroff-Riley (FR) radio galaxies, which come in two morphological flavours: FRI have low luminosity with a brighter nucleus and two fading off jets, whereas FRII have high luminosity with a weaker nucleus and more collimated jets showing two bright lobes (Fanaroff and Riley 1974). The brightness value discriminating between the two FR classes is considered to be 10^{32} erg s^{-1} Hz^{-1} sr^{-1}, taken at a frequency $\nu = 175$ MHz. FRI and FRII appearance is also believed to reflect different accretion rates.

Beside the AGN types presented above, a special class of more bizarre objects was found, concerning in particular time variability and polarization degree. The set includes e.g. radio-quiet Broad Absorption Lines (BAL) quasars, Optically Violently Variable (OVV) quasars, Highly

[13] It developed since 1930's, after the revelation of some extraterrestrial "disturbances" in the telecommunications (Jansky 1933).

[14] A quasar, i.e. *Quasi-Stellar Object* (QSO), is a powerful radio source with point-like appearance in the optical. Since their discovery (Schmidt 1963), quasars represent atypical targets due to strong lines indicating high redshifts.

Polarized Quasars (HPQ), Core-Dominated Quasars (CDQ). Two relevant radio-loud categories are in as well, i.e., BL Lac objects and FSRQs, which fall under the class of blazars. The latter will be better explained in the following, after a brief recap about the model unifying all AGNs (see Fig. 1.3 for an all-encompassing classification).

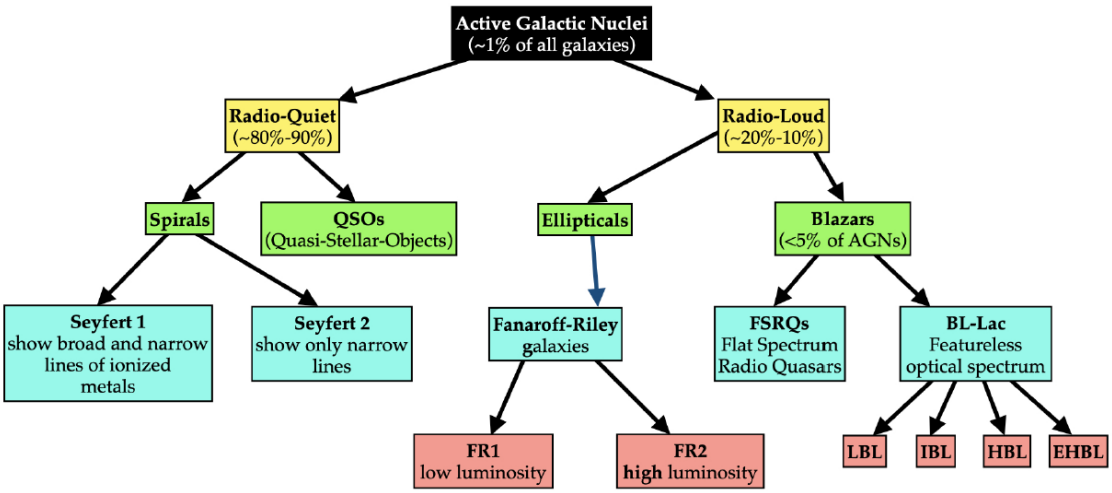

Figure 1.3: Flow chart representing the standard classification of AGNs. At the bottom right, LBL (Low-frequency peaked BL Lac), IBL (Intermediate-frequency peaked BL Lac), HBL (High-frequency peaked BL Lac), and EHBL (Extremely high-frequency peaked BL Lac) are further acronyms referring to the position of the synchrotron peak in BL Lac objects (see Subsec. 1.3.6). Plot taken from Ventura (2023).

1.3.5 Unified Model

From what has been outlined above, one can expect that random spatial orientations of AGNs make them appear as very different objects, but often the underlying physics was believed to be similar. For this reason, many attempts to unify them by means of more general, comprehensive schemes were proposed in the past. For instance, Scheuer and Readhead (1979) suggested that radio-loud quasars are radio-quiet ones aligned to the LoS. Similarly, Orr and Browne (1982) considered FSRQs as aligned SSRQs. Also, the weakness of BL Lac emission lines made them to be believed as more aligned quasars (Blandford and Rees 1978). The currently-adopted unification is based on the review by Urry and Padovani (1995). The paper has been a milestone in that, beside a description of the assumed structure of any AGN (see previous section), it contributed to make us look at them as essentially the same objects. The differences revealed are basically due to different displacements with respect to our point of view, according to which inner AGN components can be more or less appreciable. This is very well suggested by fig. 1.4. If we take the jet axis as reference direction, for large angles we have that the disk and the BLR are obscured by the torus, and only a very little amount of scattered light can reach us. In case of

radio-loud AGNs, we have radio galaxies likely lobe-dominated. Decreasing the angle, more and more inner parts become visible, in particular we can expect the spectrum to show broad emission lines. For small angles, the emission will be completely jet-dominated, which is the case of blazars. Perhaps they are the objects with the most peculiar displacement, as we are directly looking at their jets. For this reason, they show the most extreme behaviour among the whole AGN population, ultimately caused by relativistic particles streaming towards us. As this work mainly deals with a blazar source, the properties of the latter class will be described in detail in the next section.

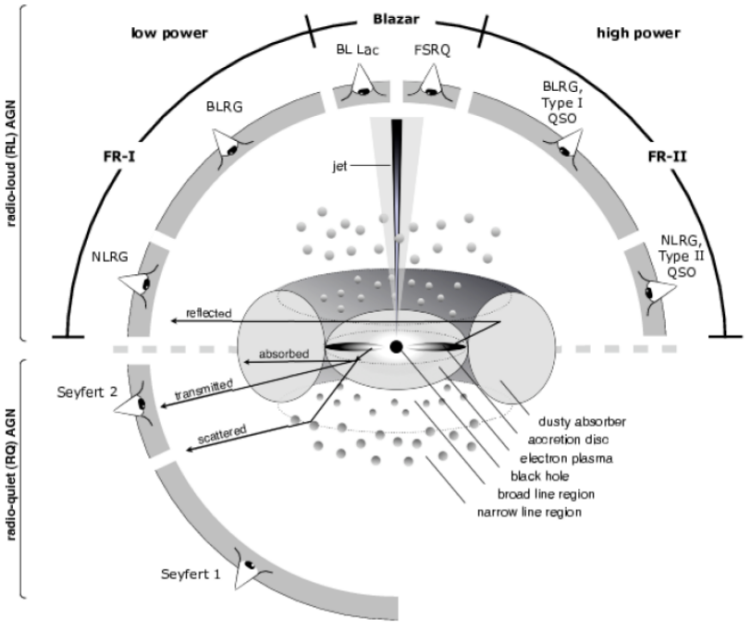

Figure 1.4: Unified scheme of AGNs, showing that they basically consist of the same kind of objects seen from different angles. Image credits Beckmann and Shrader 2012.

1.3.6 Blazars

Whenever a radio-loud AGN is such that the axis of its jets is nearly coincident to the line of sight of an observer on Earth ($\theta < 20^\circ$, Padovani 2017), it is called *blazar*. Curiously, this term was born as a combination of BL Lac[15] and quasar thanks to Edward Spiegel in a talk during a banquet of the first BL Lac conference in Pittsburgh, 1978. This was because this kind of objects were somehow showing hybrid characteristics related to both of those AGN subclasses. The new name got soon spread, until it was officially adopted among the scientific community (Angel and Stockman 1980).

About 1% of the radio-loud AGNs are blazars. They became well-known a few decades ago, when EGRET on board the CGRO satellite detected some tens of them at energies above

[15]Initially classified as a variable star, *BL Lacertae* is a blazar located at $z \approx 0.07$ (Oke and Gunn 1974). It is the prototype of blazars with basically no line in their spectra, as specified later in the text.

100 MeV. All the bands of the EM spectrum take part into the blazar emission, but γ-rays usually turn out to be dominant by a factor up to 10^3 (e.g. von Montigny et al. 1995). The fact that the jets of blazars are oriented towards us, confers them the most extreme characteristics of AGNs. They actually are the most powerful among the long-lived objects in the Universe, capable to reach a bolometric luminosity of 10^{48} erg/s (Beckmann and Shrader 2012). Furthermore, they show strong polarization and rapid, high-amplitude variability, sometimes with sub-hour scale. Indeed, it is known since a few decades that the flux can change by a factor of some tens with a time scale down to minutes (Gaidos et al. 1996). The peculiar displacement of the jet also enhances all the effects predicted by special relativity transformations. That is, light emitted from highly accelerated plasma is beamed in the path (i.e. sight) direction, so the observer perceives a much more intense radiation than the one it would sense if at rest. Another likely occurrence is superluminal motion, caused by variability time-scales seen as shorter than the real ones (e.g. Rees 1966, Ghisellini, Padovani, et al. 1993). The phenomenon consists of apparent speeds larger than that of light c, related to sub-structures getting farther from the source center. These sub-structures are relativistically (but still with $v < c$) moving at a small angle to the observing direction. Given their powerful engine, blazars are believed to be the main accelerators of UHECRs (Sec. 1.1), and are likely sources of cosmic neutrinos (Sub-subsec. 1.4.2.3).

Blazars are typically classified into two main flavours depending on the presence or absence of broad emission lines in their optical spectra. Following the classical definition given by Stocke, Morris, Gioia, et al. (1991), FSRQs show broad emission lines in the optical, with Equivalent Width (EW) larger than 5 Å in the frame comoving with the source. Conversely, BL Lac objects show very weak rest-frame emission lines in the optical, with EW less than 5 Å, if any[16]. Indeed, many BL Lacs do actually have a featureless spectrum. This empirical difference, among many shared similarities (e.g., the continuum behaviour), is commonly interpreted as a likely signature of differences in the underlying emission mechanisms. However, given the variability, the definition can be misleading. Indeed, a source might be classified as a BL Lac during a high-continuum state, or vice-versa as a FSRQ during a low-continuum state. Furthermore, there also exist so-called *masquerading* BL Lacs, i.e., intrinsic FSRQs whose very bright, boosted jet basically swamps their emission lines (e.g. TXS 0506+056, Padovani, Oikonomou, et al. 2019). Ghisellini, Tavecchio, et al. (2011) proposed a different separation based on the luminosity of the BLR normalized to the Eddington luminosity. In particular, if $L_{blr}/L_{edd} \geq 5 \cdot 10^{-4}$, the source is classified as a FSRQ, otherwise it is classified as a BL Lac. This method turns out to be more physically supported, because as pointed out in Subsec. 1.3.2, the BLR luminosity is directly linked to the radiation produced by the accretion disk. Therefore, relating L_{blr} with the Eddington luminosity provides information about the accretion rate. In particular, it tells us whether the accretion mode is efficient or not, according to the formula 1.9. To summarize, FSRQ and BL Lac blazar classes are likely distinct objects because of a different accretion efficiency. This implies intrinsic differences concerning matter distribution and radiation fields in their inner parts. In particular, strong emission lines in FSRQs spectra suggest that these

[16]A complementary or alternative characterization for BL Lacs is a blue break contrast such that $Br_{4000\,\text{Å}} \leq 25\%$.

objects are characterized by a radiatively efficient accretion rate. This means that they may be characterized by a SSD, plus a dense BLR. BL Lacs, instead, host a radiatively inefficient accretion mechanism, which likely is ADAF-driven (Subsec. 1.3.2). Also, the BLR of these sources is expected to be very scarce, so that the scattered light from the inner disk does not originate a significant line emission.

Given that the low-energy peak can be located inside quite a large portion of the electromagnetic spectrum, and in order to take into account some other spectral features (concerning e.g. X, radio detections), a further separation of BL Lac sources was introduced according to the kind of the most emitted synchrotron radiation. Namely, Padovani and Giommi (1995) called as Low-energy-peaked BL Lacs (LBLs) the ones mostly displaying the low-energy hump in the form of IR photons, and as High-energy-peaked BL Lacs (HBLs) the ones that instead mostly show a UV - soft X component for it. Intermediate cases are generally referred to as IBLs. On the other hand, there are also *extreme* BL Lac objects (EHBLs), also known as *Ultra High-frequency-peaked BL Lacs* (UHBLs) whose synchrotron bump peaks at extremely high frequencies, above the soft X-ray band (10^{17} Hz at least). According to the scenario envisaged by the blazar sequence (described in Sub-subsec. 1.3.6.1), this kind of sources should be very dim, but some relatively bright were already reported by Costamante et al. (2001). Moreover, some HBLs are found to behave as EHBLs, with harder TeV spectrum along with γ-ray flares (e.g. Ghisellini 1999, MAGIC Collaboration, Ahnen, et al. 2018). So far, there are basically 14 EHBL objects known, but the change of spectral properties just mentioned might indicate the existence of further subclasses among them (Foffano et al. 2019). In addition, the IC bump of these extreme BL Lacs can be largely due to hadronic interactions (Subsec. 1.4.2), as shown by Cerruti et al. (2015). The hadronic explanation represents a good solution against the leptonic SSC scenario (Sub-subsec. 1.4.1.1), the latter predicting very high values of either the minimum Lorentz factor of the energy distribution of electrons, or the bulk Doppler factor.

TON 116, the source under study in this thesis, is a blazar of the BL Lac class (more precisely an HBL, Sec. 4.1). Thus, here it is worth to provide some additional information related to this kind of objects. The "continuum-dominated" evidence for BL Lacs is interpreted as an exceptional alignment of the jet outflow to the LoS (see Subsec. 1.3.5), and makes the redshift estimation extremely difficult for these sources. It is thought that host galaxies of BL Lac objects are exclusively giant ellipticals, whose basic properties seem to be very similar to each other. In particular, we can generally assume them to have a De Vaucouleurs profile with a typical effective radius[17] $r_e = 10$ kpc, but most importantly, their total luminosities do basically lay within ± 1 mag (e.g. Urry, Scarpa, et al. 2000, Scarpa et al. 2000). In fact, the absolute magnitude of these host galaxies, following Sbarufatti, Treves, and Falomo (2005), shows a dispersion so narrow that they can be considered as standard candles. In particular, a value of $M_R = -22.9 \pm 0.5$ mag up to $z \approx 0.7$ turns out to hold[18], which allows for a direct derivation of redshift from images if the host galaxy can be spatially resolved from the AGN; if not, some

[17] Defined as the distance from the center containing half of the total galaxy surface brightness.

[18] True if assuming the cosmological values listed in Subsec. 1.3.1 for H_0, Ω_Λ, Ω_{DM}, and Ω_m.

guess about z might still be drawn by means of high quality spectroscopy.

Indeed, some spectral feature (usually at least two) suggesting a significant contribution of the host galaxy to the AGN emission may be present, which is the standard way to derive a pure spectroscopic redshift (see Sub-subsec. 1.3.6.3). With this regard, the *Lyman-α forest* is also considered as a reliable indicator[19]. If the spectrum is particularly noisy, or only weak features (just one sometimes) arise, then the redshift estimation is called tentative. A special case is represented by an absorption doublet consistent with lab frame wavelengths $(2796, 2804)$ Å related to MgII, whose presence can intervene at the very source level, or elsewhere in the space between the AGN and the observer. Therefore, a lower limit on the redshift can be set. Finally, if a spectrum is completely featureless or showing a too high noise level, no redshift value can be confidently inferred, which thus remains unknown. This kind of sources are still thought to have $z < 2.2$, due to the lack of the Lyman-α forest. However, if a good spectral decomposition for many out of a large sample of objects is possible, which shows a systematic flux density ratio between the AGNs and the host galaxies, one can assume the same value to hold for sources lacking any mixture indicator between those two components. In the latter case, an upper limit can be associated to the host galaxy emission, thus leading to a lower limit on the redshift. Such derivation is quite rough, as there could be nearby objects with basically no spectral feature at all (at least with current instrumental resolution), indicating strongly beamed jets. However, it seems that this kind of extremely featureless sources are mostly located far away; see e.g. Plotkin et al. (2010), which used the outlined techniques for the redshift determination restricted to the R-band.

1.3.6.1 Blazar Sequence

In the late '90s, a sort of coherent trend characterizing the SED of blazars, potentially able to unify them according to a single parameter, was claimed. In particular, after some preliminary indication (e.g. Sambruna, Maraschi, and Urry 1996, Maraschi et al. 1995), Fossati et al. (1998) studied the spectral behaviour of a set of 126 sources, either BL Lacs (from the X Einstein Slew and the radio 1-Jy surveys, Perlman et al. 1996 and Stickel, Meisenheimer, and Kuehr 1994 respectively) or FSRQs (from the radio 2-Jy survey, Padovani and Urry 1992). The selection was made in order to provide a large, complete sample of blazars well detected at 7 specific frequencies representative for the general spectral shape. The frequencies considered are: 5 GHz (radio), 230 GHz (millimeter), 60 and 25 μm (far IR), 2.2 μm (near IR), 5 500 Å (optical), 1 keV (soft X-rays). Nevertheless, the analysis also included the γ band, at which a significant fraction (about one fourth) of the considered targets had been detected. This was mostly thanks to EGRET on board the Compton Gamma-ray Observatory (CGRO), or by the ground-based Whipple (Subsec. 2.3.3). As the radio luminosity at 5 GHz seemed to correlate the most with other spectral parameters, the authors decided to bin the sources according to it (also because

[19]This feature consists of a dense set of absorption lines which were firstly detected in quasars. They are likely due to the Lyman-α transition of neutral hydrogen placed between the source and us.

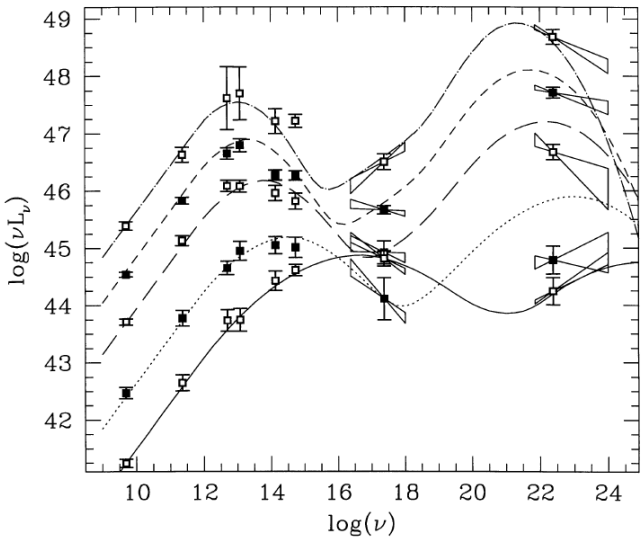

Figure 1.5: Average SEDs with analytic functions of the radio-binned blazar sample considered in Fossati et al. (1998). Actually, a blazar sequence appears: if bolometric luminosity increases, the two humps peak at lower frequencies and the Compton/synchrotron luminosity ratio gets larger. Plot taken from the same paper.

always available), and computed average SEDs. As a result, they found that the SED of blazars is characterized by two broad humps, one peaking at lower frequencies ($\nu_{p,s} \approx 10^{13}$-$10^{17}$ Hz between IR and X-ray band) most likely due to synchrotron emission from electrons in the relativistic jet, the other peaking in the MeV-TeV range ($\nu_{p,c} \approx 10^{21}$-$10^{25}$ Hz), which could arise either from synchrotron-self-Compton process of the same electron population emitting by synchrotron (Sub-subsec. 1.4.1.1), or from IC interaction with external photon seeds (Sub-subsec. 1.4.1.2), and is possibly associated to a hadronic component (Subsec. 1.4.2). Regarding the frequencies of the two peaks, they noticed a correlation between each other in the form of a constant ratio ($\nu_{p,c}/\nu_{p,s} \approx 5 \cdot 10^8$), but not only. Increasing the bolometric luminosity, the position of the peaks moves towards lower frequencies, see Fig. 1.5. From the same plot, also the Compton dominance, defined as the ratio between the Compton and the synchrotron luminosity, increases with bolometric luminosity. The relation between $\nu_{p,s}$ and $L_{5\,GHz}$ was found to be close to a power-law with index roughly equal to -1. From this systematic inspection it was possible to infer that, despite the higher luminosity bin is populated mostly by FSRQs, while BL Lacs tend to be fainter, the regular trends depending on radio luminosity only were still valid for the total sample. This was clearly pointing towards the existence of a unique blazar family, regardless of any deeper spectral difference. The conclusions drawn marked the birth of the *blazar sequence*, whose powerful simplicity also gave important perspectives about the detectability of that kind of objects at the most energetic spectral bands. In a separate paper, Ghisellini, Celotti, et al. (1998) attributed the anti-correlation between bolometric luminosity and position of the peaks to strong radiation fields at the BLR, causing γ_e to be lower at the break of the electron energy distribution, and thus, giving rise to a more efficient cooling, especially for FSRQs.

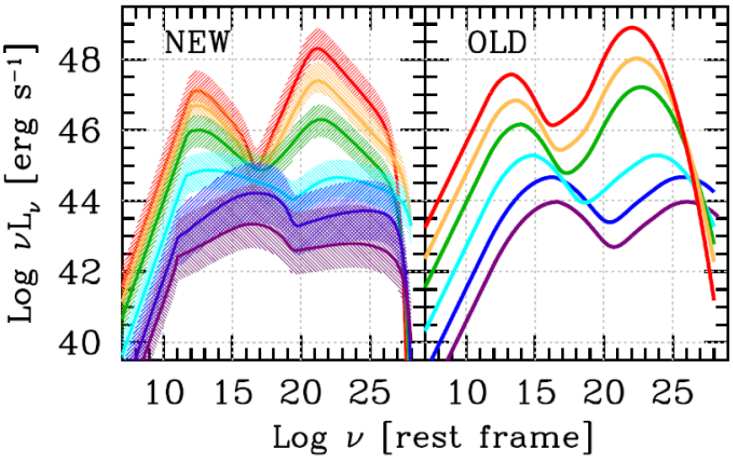

Figure 1.6: Comparison between the SED of FSRQs and BL Lacs in the context of the "new" (Ghisellini, Righi, et al. 2017, left) and the "old" (Fossati et al. 1998, right) blazar sequence trends. FSRQs, populating the upper part of the plots, show a larger Compton dominance and a harder X-ray slope with increasing γ-ray luminosity. BL Lacs, in the lower part of the plots, indeed follow a redder-when-brighter trend as the original version of the sequence. Image taken from Ghisellini, Righi, et al. (2017).

More recently, the blazar sequence underwent a revision by Ghisellini, Righi, et al. 2017. The work focused on a much larger sample of 747 γ-emitting objects selected from the third *Fermi*-LAT catalogue of AGNs (3LAC, Fermi-LAT Collaboration 2015). This time, the authors binned the sources according to γ-ray luminosity. Despite the use of the γ band instead of radio for binning the data, the previous trend of Fossati et al. (1998) was basically found, supporting the existence of the blazar sequence. However, some clarifications have been introduced concerning FSRQs and BL Lacs as separated objects (see Fig. 1.6). In particular, the former tend to share the same SED behaviour, with no peak shift with increasing luminosity. The main feature is a change in the Compton dominance, which increases with γ luminosity (range 0.5-15). As a consequence, the X-ray slope changes as well, getting harder with increasing γ luminosity. On the other hand, BL Lacs actually follow a remarkable trend according to which the peak frequencies are lower when the γ luminosity is larger. This behaviour has no significant effect on the Compton dominance.

1.3.6.2 Beyond the sequence

The blazar sequence is a very remarkable trend for the SED of blazars, but turned out to be controversial in the astrophysical community, and somehow is still under discussion. Padovani (2007), combining results from recent surveys, found that the frequencies of the peaks are not really anti-correlated with the radio luminosity. Moreover, some FSRQs were detected with a synchrotron peak located in UV or X-ray band, which is something unexpected in the blazar sequence framework. The most solid observational evidence was that the synchrotron peak

of FSRQs reaches frequencies systematically lower than those of the BL Lac case (a factor 10-100). Thus, the work led to the conclusion that the blazar sequence is not valid because biased by selection effects. Few years later, Giommi et al. (2012) confirmed the selection bias as responsible for the birth of nearly all existing blazar classifications and trends, blazar sequence included. In particular, by means of extensive Monte Carlo (MC) simulations and huge MWL datasets, the paper showed that the sequence can simply come from a comparison between shallow surveys both in radio and X-ray bands. On top of that, most of the BL Lac objects are likely associated with both high luminosity and high frequency of the synchrotron peak. This constitutes a serious issue for the blazar sequence scenario, because this kind of sources are basically not contemplated. The latter also represent the preferential targets of γ-ray selected samples, like the *Fermi*-LAT (Subsec. 2.3.1) ones. The lack of lines in the optical spectra contribute to make these sources mysterious, as for most of them the redshift can not be firmly determined. This is exactly the case of TON 116, the blazar that we want to analyze in this thesis. The reason why did we choose the source is strictly related to how can the source itself help in clarifying the existence of the blazar sequence being a likely "outlier" (see Sec. 4.1). This is also motivated by the conclusion recently drawn by Keenan et al. (2021) about the actual end of the sequence. This was claimed by considering more than 2000 accurate SED of jetted AGNs, a sample nearly 15 times larger than the original in Fossati et al. (1998). From a plot of the synchrotron peak frequencies and associated luminosities, no significant evidence for an anti-correlation, as expected in the blazar sequence context, was found. Thus, the authors agreed with a selection-based foundation of the sequence. Nevertheless, a strong dichotomy was found related to the accretion efficiency of the jets. Namely, type 1 i.e. weakly-accreting jets belong to low-excitation radio galaxies and blazars with $\nu_{p,s} > 10^{15}$ Hz (almost all BL Lacs), while type II i.e. efficiently-accreting jets belong to high-excitation radio galaxies, FSRQs, and most of LBLs. In this framework, our source is an HBL likely located in the upper right part of the $\nu_{p,s} - L_{p,s}$ plane, an area which should be forbidden according to blazar sequence expectations. The results of Keenan et al. (2021) suggest that the latter zone is populated by weak-jet (inefficiently accreting) BL Lac objects.

1.3.6.3 Distance estimation

The intrinsic luminosity L of a given astrophysical object can be found from the incoming energy flux F that we detect on Earth, once the distance from the object is known. In general, those quantities are linked through the formula

$$F = \frac{L}{4\pi D_l^2} \quad , \tag{1.11}$$

where D_l is called *luminosity distance*. This is the distance from which a given flux is perceived, which is associated to an object isotropically emitting in a euclidean space. This relation has to be

modified in case of very far distances, in order to take into account cosmological arguments. In addition, in the case of blazars or AGNs in general, relativistic effects actually causing luminosity boosting have to be accounted for. For this kind of sources (like all the extragalactic ones), the main information about the distance is delivered by the redshift, commonly defined as

$$z = \frac{\lambda_{obs} - \lambda_{em}}{\lambda_{em}} \quad , \tag{1.12}$$

with λ_{obs} and λ_{em} the wavelength at which a certain atomic energy transition is observed and the wavelength at which that transition occurs in the lab frame (at rest), respectively. The two are in general different because of source-observer relative motion, i.e., the Doppler effect. From the definition 1.12, the actual distance is estimated with laws like the Hubble's one (Subsec. 1.3.1), considering the application of cosmological corrections.

From the above, the standard way to determine the distance of blazars is by spotting at least one known emission or absorption line in their spectra, better if two or more for providing stronger reliability of the result. The procedure leads to obtain a spectroscopic redshift, which is the most solid estimation of distance. However, this is not an easy task to be performed, especially for BL Lac sources, whose spectrum by definition lacks any line, or if present, they are very weak. In such cases, as presented in Subsec. 1.3.6, it can be still possible to disentangle the AGN from the host galaxy, or put some lower limit on the redshift, thanks to absorption of intervening matter.

Alternatively, Prandini et al. (2010) recently described a method to measure blazar distances by looking at their GeV-TeV emission. The VHE regime is affected by EBL absorption which, as outlined in Sec. 1.2, increases with distance, consequently we do expect that the de-absorbed flux becomes harder with z. However, this spectral change cannot be applied indefinitely, also taking into consideration the behaviour found in lower-energy bands. In particular, a basic assumption is that the EBL-corrected VHE spectrum can not be harder than the HE one, which thus represents a firm upper limit to the redshift. Starting from this point, the authors calculated the intrinsic VHE emission related to all TeV-emitting *Fermi*-LAT sources with known distance, and found how it changes as a function of redshift. From a comparison between a power-law fit to the VHE trend and the *Fermi* slope, they found empirical laws between VHE values and true redshift. These relations can be used to attempt an estimation of z for sources whose distance is unknown. If z^* is the redshift corresponding to the maximally-hardened TeV spectrum corrected for the EBL absorption, the trend with the true redshift z_{true} was naturally assumed to be linear as the steepening of the observed TeV slope due to the EBL absorption itself. In particular, a simple $z^* = A + B z_{true}$ expression was assumed. We report in Fig. 1.7 the plot related to such an estimation, together with the linear fit values (table below the figure) for three different EBL models (low level by Kneiske and Dole 2010, medium level by Franceschini, Rodighiero, and Vaccari 2008, high level by Stecker, Malkan, and Scully 2006).

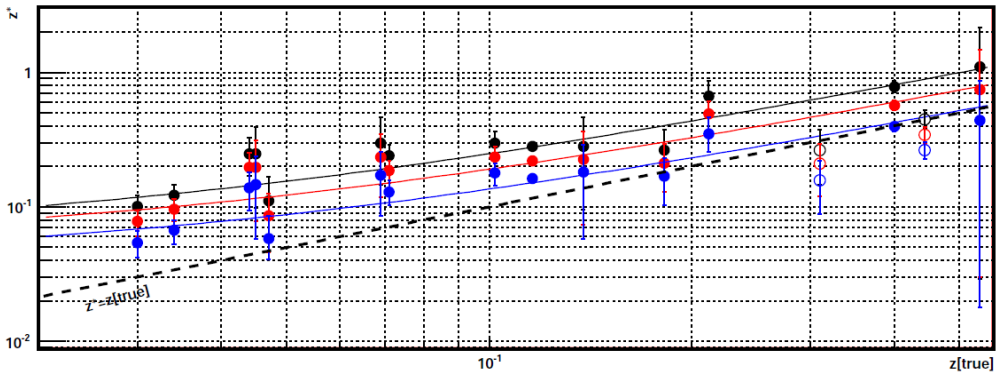

EBL Model	A	B
Low level	0.062±0.017	1.86±0.17
Mean level	0.054±0.012	1.36±0.14
High level	0.040±0.009	0.96±0.08

Figure 1.7: Redshift z^* corresponding to the maximum hardening of TeV spectrum (until matching the HE slope found by *Fermi*) versus true redshift (z_{true}) as found by a linear fit on the values of a blazar sample with known redshift (Prandini et al. 2010). Three different EBL models are assumed: low level (Kneiske and Dole 2010, black line), medium level (Franceschini, Rodighiero, and Vaccari 2008, red line), high level (Stecker, Malkan, and Scully 2006, blue line). The corresponding fit values are visible in the table below the figure. Plot and table taken from Prandini et al. (2010).

1.4 Modeling of blazar radiation

As discussed above, the SED of blazars is characterized by two broad humps, one due to synchrotron radiation and the other due to Inverse-Compton scattering, peaking at lower and higher frequencies respectively. The primary goal of deep MWL campaigns, carried out with a large variety of instruments relying on different detection techniques, is covering the entire frequency spectrum as much as possible with observational data, in order to get a full view of the spectral behaviour. Ideally, after this first step, a scientific work dealing with data interpretation follows in order to assess, from the observed radiation, the emission mechanism of the target sources. The interpretation must be coherent with the observation, meaning that the speculations have to correctly reproduce, within a tolerance threshold, the quantities related to the detected emission. Although it is practically impossible to reach a complete spectral coverage with real observations, there are seven *observables* that in principle can be directly derived by collected datasets: the frequency of both the synchrotron and IC peak ($\nu_{p,s}$, $\nu_{p,c}$), the corresponding flux values at the two respective peaks ($\nu_{p,s}F_{\nu_{p,s}}$, $\nu_{p,c}F_{\nu_{p,c}}$), the indices for the spectral slope below and above the peaks (α_1, α_2), and the minimum time variability t_{var} of the observed flux. However, it is not rare that some sources are so poorly sampled that the information regarding

the peaks can only be uncertainly inferred through fitting procedures consistent with analytical modelization, which is the topic of the following section.

Blazar spectra can show very different features one with respect to the other, in terms of bolometric and differential luminosity, eventual presence of absorption and emission lines, underlying continuum and so on. Also a given source can appear differently over time, because of flux variability affecting multiple spectral bands with different timescales. The unified model of AGNs and the general double-peaked trend certified by observations, however, pushed towards a search for common roots able to explain the blazar phenomenon. In particular, the focus is on known radiation mechanisms powerful enough to justify the extreme, persistent brightness associated to this kind of sources. While the low-energy bump is commonly associated to synchrotron radiation from jet particles, the origin of the high-energy one is still debated. The differences between emission models depend on the main particles that one assumes to be effectively radiating while streaming at very high speed along the jets, once a bulk structure for them and a configuration for the magnetic field are provided. Beside this, also plausible photon fields acting as further targets can play a significant role, and other relevant properties of the surrounding medium shall be taken into account.

1.4.1 Leptonic models

Scenarios that attribute the shape of the blazar SED to physical interactions involving electrons are called *leptonic*. The most important ones are recapped here below.

1.4.1.1 Synchrotron Self-Compton

The simplest model often able to represent a good description of the blazar broadband emission is the Synchrotron Self-Compton (SSC, Dermer and Menon 2009b, Finke, Dermer, and Böttcher 2008), according to which the low-energy peak is due to a population of ultra-relativistic electrons in the jet emitting synchrotron radiation because of a tangled magnetic field $\overline{B}$. These produced photons in turn constitute a target for Inverse-Compton interaction with the same parent electrons, by which they are up-scattered giving rise to the second peak in the γ-ray band (see Fig. 1.6). Therefore, this leptonic scenario is based on a single set of electrons which can explain both the observed peaks in the blazar SED at once. This is considered as the most suitable model for BL Lac objects, given the overall lack of external photon fields (Subsec. 1.3.6). SSC scenario implies the SED peaks to be strongly related to each other. In general, this model can justify well simultaneous flares occurring in different bands, such as X-ray and VHE γ-ray, which have been observed for several sources, like the well-known blazar 1ES 1959+650 (MAGIC Collaboration, Acciari, et al. 2020, but also single-band flares have been detected). In its one-zone, homogeneous version, the electrons are assumed to be in motion within a bulk relativistic region (e.g. Tavecchio, Maraschi, and Ghisellini 1998). The latter can be thought as a *blob* filled with accelerated plasma particles and relativistically moving at a speed v, with a given Lorentz factor Γ_b, at a small angle

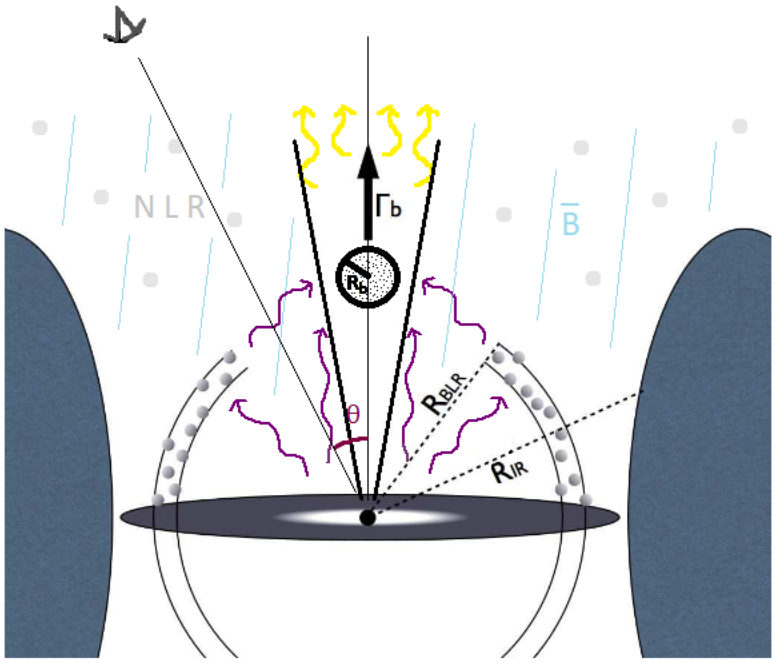

Figure 1.8: Sketch of the one-zone SSC model for the explanation of the blazar SED. It consists in a relativistic blob (assumed spherical with radius R_b) filled with particles, moving outward with a bulk Lorentz factor Γ_b in a tangled magnetic field $\overline{B}$. The angle θ between the main axis of the system and the LoS is exaggerated for visualization purposes. The EC model requires an additional radiation field of direct or BLR-reprocessed photons (violet arrows) coming from the accretion disk. Image adapted from Tavecchio, Becerra González, et al. (2011).

θ with respect to the line of sight. As shown in Fig. 1.8, this sub-structure is usually assumed to be spherical, with a comoving size that can be estimated, as an upper limit, through the causality relation suggested by the minimum time variability t_{var} of the observed flux:

$$R_b = \frac{c\, t_{var}\, \delta_D}{1+z}\,, \tag{1.13}$$

where z is the redshift of the source, and δ_D is the bulk Doppler factor associated to the blob, depending on the Lorentz factor and the advancing angle as

$$\delta_D = \frac{1}{\Gamma_b\,(1-\beta\cos\theta)}\,, \tag{1.14}$$

with $\beta = v/c$. The factor defined in the last formula is particularly useful to evaluate the relativistic amplification of the incoming signal. The magnetic field is usually assumed to be constant and uniform. Looking at the individual components of the jet, we can describe their energy distribution as the numerical density of electrons having, in a unit volume, a given Lorentz factor, i.e. $n(\gamma)$. In most cases, a simple power-law in a proper interval $[\gamma_{min}, \gamma_{max}]$ is considered:

$$n(\gamma) = k\gamma^{-p}\,, \tag{1.15}$$

where k is a constant, used for normalizing the function to a certain physical value related to the emitting region[20], and p is the index identifying the slope of the distribution. As required by the spectral shape, it is often more appropriate to consider a distribution steepening with increasing energy: this is possible considering a so-called "broken power-law", that is, a composite function which can be seen as made up of two power-laws in the form of eq. 1.15 having different indices, and connected at a given break value γ_{br}. This is represented by

$$n(\gamma) = \begin{cases} k\gamma^{-p_1} & \gamma < \gamma_{br} \\ k\gamma^{-p_2} & \gamma \geq \gamma_{br} \end{cases} \tag{1.16}$$

where $p_2 > p_1$. The break value, corresponding to an energy $\gamma_{br} m_e c^2$ which is the dominant one of synchrotron power, can be obtained recalling the fact that most of the IC radiation, in the Thompson regime, will result in a frequency $\nu_{p,c} = \frac{4}{3}\gamma_{br}^2 \nu_{p,s}$. Thus, we simply have:

$$\gamma_{br} = \sqrt{\frac{3\,\nu_{p,c}}{4\,\nu_{p,s}}}\,, \tag{1.17}$$

If the peak frequencies are not found, γ_{br} can be restricted in its parameter space from considerations regarding a balance between cooling and escape of the particles forming the jet. The former is linked to which of the two processes, synchrotron or inverse-Compton, is the fastest to occur, depending in turn on which of the respective energy densities dominates. In addition, from the fact that in the reference frame comoving with the jet, the ratio of the total synchrotron and IC luminosities is directly equal to the one of the synchrotron radiation and the magnetic field energy densities, and by using eq. 1.13, the magnetic field and the Doppler factor can be related to each other, in a fashion that has to be changed if the Klein-Nishina regime is reached[21] (Tavecchio, Maraschi, and Ghisellini 1998).

From all the above, the homogeneous SSC model turns out to be completely determined by seven independent quantities: B, R_b, δ_D, k, p_1, p_2, γ_{br}. The aforementioned link between the peak occurrences usually simplifies the number of model parameters. In particular, the Doppler factor and the magnetic field can be directly estimated via

$$\delta_D = \left(\frac{3}{4}\,\frac{e}{2\pi m c}\right)^{1/2} \left(\frac{\nu_{p,c}}{\nu_{p,s}^2}\right)^{1/2} \left(\frac{2L_{p,s}^2}{c^3 L_{p,c} t_{var}^2}\right)^{1/4} \tag{1.18}$$

[20] It may refer to specific particle values such as the total numerical density, the total energy density, the total energy content, or directly the density for $\gamma = 1$.

[21] This corresponds to an IC interaction involving high energy photons, so that $h\nu \gtrsim m_e c^2$. In this case the cross section of the process is different with respect to the basic approach concerning $h\nu \ll m_e c^2$.

$$B = (1+z)\left(\frac{4}{3}\frac{2\pi mc}{e}\right)^{3/2}\left(\frac{\nu_{p,s}^2}{\nu_{p,c}}\right)^{3/2}\left(\frac{c^3 L_{p,c} t_{var}^2}{2L_{p,s}^2}\right)^{1/4} \quad , \tag{1.19}$$

where $L_{p,s} := L(\nu_{p,s})$ and $L_{p,c} := L(\nu_{p,c})$ are the luminosity of the synchrotron and IC peaks respectively.

There are also further quantities which are not necessary to unequivocally close the system describing the SSC emission, but can help in restricting the parameter space. For instance, as the high- and low-energy photons can interact and produce electron-positron pairs (see reaction 1.3), an upper limit can be set for the energy density of the soft ones, if a significant amount of γ-rays is detected. Indeed, this means that the optical depth of the target photons is small enough to let much of the energetic radiation pass through and reach us. Some works like Dondi and Ghisellini (1995) showed that, in this case, a lower limit on the Doppler factor can also be put.

Another interesting characteristic that could be pointed out is time lags in light curves between more energetic photons and less energetic ones in the X-ray band during remarkable flares. The most intuitive explanation relies on the energy loss of new high-speed particles just injected in the jet, so quite a precise cooling time can be directly inferred. Then, as already said, a check about the latter quantity at the break can be performed to see whether γ_{br} is consistent with the escape time from the emission zone, provided the estimate of its size R_b, and of both the magnetic and radiative energy densities. In general, the explanation provided by the SSC model is quite good, but in the low-frequency domain it easily leads to self-absorption processes, so that external emission coming from outside the jet may be required. Moreover, the SSC model could imply a low magnetization, contradicting the equipartition condition which has a key role for sustaining the jet in the proximity of the SMBH. A viable solution could be a synchrotron-Compton decoupling beside an additional source of soft target photons, as it is offered by the "Spine-Layer Model" (Tavecchio and Ghisellini 2014). This scenario is particularly indicated for VHE-detected sources which can be more strongly constrained, but it results in a larger number of parameters, and less powerful jets. The SSC model can also involve more than one emission zone, in order to e.g. account for different time-scale variations of the flux possibly detected at HE and VHE (see Tavecchio, Becerra González, et al. 2011).

1.4.1.2 External Compton

An additional (not alternative) explanation for the γ radiation from blazars relies on photon seeds with different origin for inverse-Compton scattering. According to this *external Compton* (EC) view, direct or reprocessed photons produced by thermal processes like the ones occurring in the accretion disk, the BLR, the dusty torus, or even the CMB can be scattered via IC by the electrons in the jet, and contribute significantly to the HE/VHE emission (Dermer, Finke, et al. 2009, Finke 2016, see also Fig. 1.8). If this is the case, a unique black-body approximation, especially for the dusty torus, often leads to a satisfactory modelization. However, considering multi-temperature components for the inner part of a blazar can improve the overall description of the incoming

radiation. Provided that radiation fields independent from the jet are included, the analytical treatment of such a model is in general more complicated. The EC scenario is mostly suitable for FSRQs, as they are thought to "live" in an enriched environment with plenty of external radiation sources (Subsec. 1.3.6). Furthermore, their Compton dominance (Sub-subsec. 1.3.6.1) is considered to fit well in the framework of a boost of those external fields from the relativistic blob inside the jet.

1.4.1.3 γ-γ absorption

As already pointed out in Sec. 1.2, the flux of incoming γ-rays can get significantly suppressed by EBL photons during their travel to Earth. The interaction results in an electron-positron pair (see reaction 1.3). The same kind of process can also occur at the source itself, through low-energy photons like the ones coming from thermal or line sources (disk, BLR, torus). The entity of such an absorption is commonly quantified through the optical depth $\tau_{\gamma\gamma}$, which represents the opacity against γ-rays propagation. In general, this quantity depends on both the γ-ray (E_γ) and the ambient field (E_ξ) energies, and also on the distance travelled. If the size of the source is R, the formula of the optical depth is (Dermer and Menon 2009a)

$$\tau_{\gamma\gamma}(E_\gamma) = \int_0^{+\infty} \sigma_{\gamma\gamma}(E_\gamma, E_\xi)\ n_{ph}(E_\xi)\ dE_\xi \quad , \tag{1.20}$$

where the cross section of pair production $\sigma_{\gamma\gamma}$ is a complex function of $\beta_{cm} := \sqrt{1-s^{-1}}$, with s the squared value of the Lorentz factor of the produced $e^\pm$ pair in the center-of-momentum reference frame (Finke 2018). The final effect is an attenuation of the intrinsic γ-ray flux by a factor $e^{-\tau_{\gamma\gamma}}$.

1.4.2 Hadronic models

Other scenarios able to explain the blazar SED are called *hadronic*, as they assume that a significant part of the whole emission is due to atomic nuclei relativistically moving in the jet (e.g. Cerruti et al. 2015). For the sake of clarification, pure hadronic emission is usually not considered. This is because, from theoretical arguments, leptons are expected to emit most of the synchrotron radiation due to their low mass. In addition, protons are associated with a relatively long cooling time, which is incompatible with observed time variability. Thus, the low-energy peak is still attributed to accelerated electrons. On the other hand, sometimes hadrons are thought to dominate the Compton bump radiation via a variety of different processes. From these considerations, hadronic models do actually include a leptonic component, so that in reality they are *lepto-hadronic*. Proton emission can also be invoked for the *valley* only, i.e., the spectral region (often X-ray band) located between the two peaks. The main interactions involving protons (and nuclei) are summarized below.

1.4.2.1 Proton synchrotron

The basic hadronic model includes a population of ultrarelativistic protons in the jet co-emitting by synchrotron. In this case, a particle distribution as the one of eq. 1.15 is usually assumed. The high-energy peak mostly arises for IC scattering of synchrotron photons by protons. As this scenario deals with synchrotron-emitting protons, either a very strong magnetic field ($B \gtrsim 10$ G) or high density of hadrons are required.

1.4.2.2 Bethe-Heitler interaction

Given the abundance of particles and photons inside the jet of any blazar, another hadronic model takes into account interactions between accelerated protons and low-energy radiation fields. The dominant process between relativistic protons and soft photons is

$$p + \xi \longrightarrow p + e^- + e^+ \quad , \tag{1.21}$$

which is known as Bethe-Heitler pair production. If γ_p is the Lorentz factor of the proton, E_ξ is the energy of the photon, m_e is the electron mass, the condition for such a reaction to occur is $\gamma_p E_\xi > m_e c^2$. A detailed study on the kinematics of the process allows to derive analytic expressions for the energy impinged on the produced pair. In particular, if $\gamma_p \gg 1$ and $E_\xi \ll \gamma_p m_p c^2$ (m_p mass of the proton), Kelner and Aharonian 2008 showed that the maximum energy attainable by the electron/positron turns out to be

$$E_{e,max} = \begin{cases} 4\gamma_p^2 E_\xi & m_e c^2 \ll \gamma_p E_\xi \ll m_p c^2 \\ \gamma_p m_p c^2 & \gamma_p E_\xi \gg m_p c^2 \quad . \end{cases} \tag{1.22}$$

The second of these cases corresponds to the fact that the energy of the proton is transferred to one of the produced leptons in its entirety. It is also possible to study more realistic situations, e.g. the effects of a cloud of ultrarelativistic protons interacting with a cloud of soft photons. From such an analysis, the collective energy spectrum of the leptonic pair, dN/dE_e, can be derived. For details related to this advanced approach, we address the reader to the above-mentioned paper.

1.4.2.3 Photo-production

An alternative explanation for a hadron-originated γ-ray bump is based on secondary particles coming from interactions between protons and ambient photons. These photo-production processes involve either photons and pions, or photons and electron-positron pairs (e.g. Mücke and Protheroe 2001), so they are also known as *photo-meson* interactions. The main scheme is

$$p + \xi \longrightarrow \Delta^{+} \longrightarrow \begin{cases} p + \pi^{0} \\ n + \pi^{\pm} \end{cases} , \tag{1.23}$$

where Δ^{+} is the intermediate resonance, and ξ represents a low-energy photon inside the jet (Mannheim and Biermann 1992) or coming from outside, like the disk or the BLR, the latter eventually re-processing it (Bednarek and Protheroe 1999, Atoyan and Dermer 2003 respectively). The interaction occurs as long as the energy of the proton fulfills $E_p \geq (m_{\Delta}^2 - m_p^2)/4E_{\xi}$, with m_{Δ} and m_p the mass of the resonance and of the proton respectively, and E_{ξ} the energy of the intervening photon. Within about 15 min, isolated neutrons turn into a proton, an electron, and an electron anti-neutrino by weak interaction decay. Regarding pions, in a time interval smaller than 1 μs, they mostly decay into two γ-rays if neutral (with a branching ratio reaching about 98.8%), else they decay into the respective charged muons and neutrinos (branching ratio $\approx$ 99.9%), i.e.,

$$\begin{cases} \pi^{0} \longrightarrow \gamma + \gamma \\ \pi^{+} \longrightarrow \mu^{+} + \nu_{\mu} \\ \pi^{-} \longrightarrow \mu^{-} + \overline{\nu}_{\mu} \end{cases} . \tag{1.24}$$

Muons, in turn, do have a mean life-time of 2.2 μs, after which they decay into the respective leptonic particles according to

$$\begin{cases} \mu^{+} \longrightarrow e^{+} + \overline{\nu}_{\mu} + \nu_{e} \\ \mu^{-} \longrightarrow e^{-} + \nu_{\mu} + \overline{\nu}_{e} \end{cases} . \tag{1.25}$$

Photons and $e^{\pm}$ pairs can initiate further EM cascades composed by the same particle content, in case their energy is larger than the one required for pair production. Secondary pairs can also emit by synchrotron, and the produced photons can give rise to further pairs, self-enhancing such a development. Moreover, if the magnetic field is particularly strong, pions and muons can significantly contribute to the synchrotron emission despite their short duration. In the case of pions, also the observation of the so-called *pion bump* can be considered as a direct signature of hadronic processes ongoing at the source[22]. In general, photo-production is dominant if the density of the ambient radiation field is larger than the environmental density of the medium. This is due to the much smaller cross section of the photo-production with respect to the one of proton-proton interaction. Note that, however, photo-production processes also constitute an interesting benchmark for multi-messenger (MM) studies, due to the presence of energetic neutrinos among the predicted subproducts. Recently, an intriguing detection as such was claimed in the direction of the blazar TXS 0506+056 during a γ-ray flare (IceCube et al. 2018).

[22]The pion bump is a broad feature at the maximum of the energy spectrum of γ-rays ($E_{\gamma} = (m_{\pi^0} c^2)/2 \approx$ 67.5 MeV) produced through π^0 decay. It is independent of both the pion and the parent proton distributions.

As stated in Subsec. 1.3.6, this source likely is an intrinsic FSRQ appearing as a BL Lac due to a very bright jet. Therefore, its rich radiation environment (same Subsec. 1.3.6) might increase photo-productions leading to neutrino emission (Padovani, Boccardi, et al. 2022).

Chapter 2

MWL instruments and γ-ray observatories

In this chapter we give an overview about the main astrophysical messenger considered throughout this thesis, i.e., the photon. We start by describing the electromagnetic spectrum and how can photons belonging to different bands be detected by our instruments, with a focus on the spectral bands and instruments considered in this work. The second part of the chapter restricts to the γ-ray band, which has a key role in the study of our source. γ band is special also because can be probed either by space-based or ground-based instruments, which we mainly associate with *Fermi*-LAT satellite and IACTs respectively. Concerning the latter category, we will describe in detail the Cherenkov method exploited by those instruments to indirectly reveal the most energetic γ-ray photons. We end this chapter with the current (including MAGIC, see next Ch. 3) and future generation (e.g. CTAO) of IACTs.

2.1 The multi-wavelength paradigm

In the last decades, scientists understood that the most effective way to study the huge variety of phenomena in the Universe is combining the information from different celestial messengers coming from the same astrophysical environment. Traditionally, CRs and photons represent the most studied messengers from astrophysical objects. In particular, the detection of photons all over the EM spectrum, led to a deeper understanding of the observed phenomena and to the birth of the MWL astrophysics.

The Earth's atmosphere absorbs part of the EM radiation coming from the outside. In particular, only optical, some near-infrared (IR), and radio wavelengths can reach the ground without being significantly absorbed, and ground-based optical telescopes and antennas were the first instruments used to study the sky. In all the other energy bands, photons can be *directly* detected only with space-based instruments mounted on balloon payloads or satellites, see Fig. 2.1. A particular case is represented by the γ-ray band, at which both space-based and ground-based instruments are employed. The telescopes on the ground detect *indirectly* the

primary photons through the Cherenkov light emitted by atmospheric showers. In this chapter, we will give an overview of the instruments and detection techniques adopted in the optical, X-ray and γ-ray bands that were considered in the study of TON 116. Particular attention will be devoted to ground-based γ-ray instruments and the imaging Cherenkov technique.

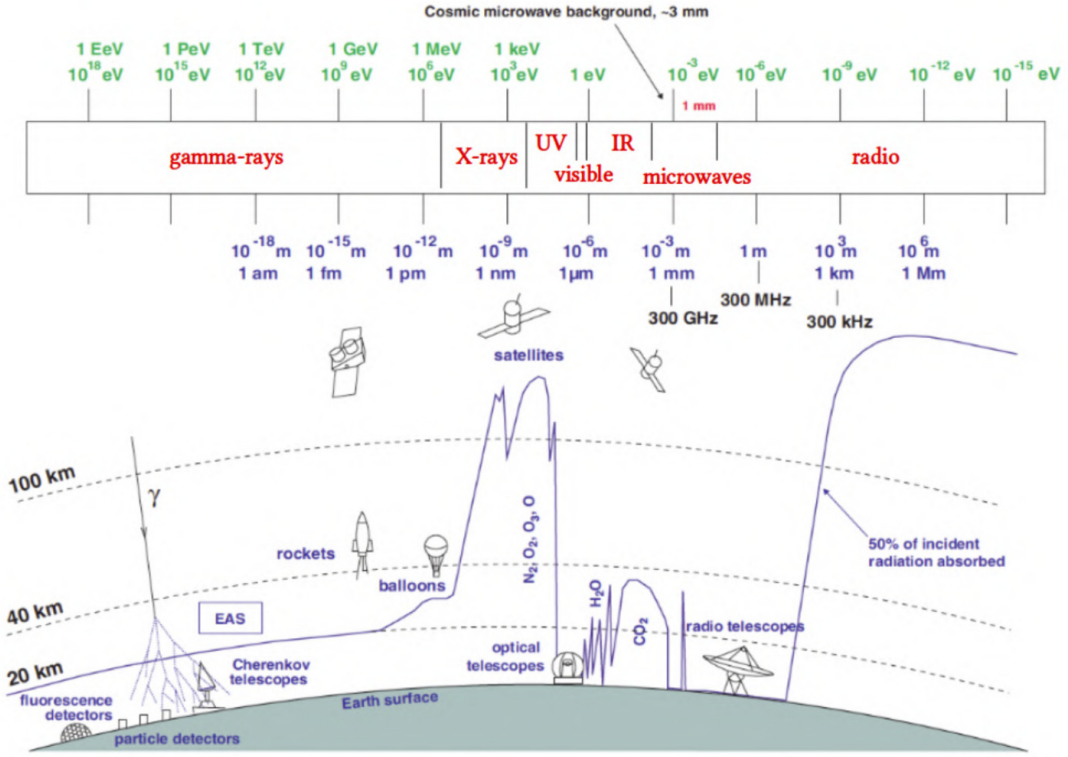

Figure 2.1: Different ground- and space-based photon detectors for observations over the whole EM spectrum. The top bar shows the EM spectrum classifying the radiation according to photon wavelength and energy, from radio up to γ-rays. The bottom illustration shows the level of atmospheric absorption depending on the altitude above the ground, and different satellites and ground-based detectors. Image adapted from López Coto (2017).

2.2 Optical and X-ray instruments

For many hundreds of years, the optical band ($\sim$ 400-800 nm wavelength) has been the only one exploited for observation of the sky, first with the naked eye and later using refractive or reflective telescopes. The visible light represents a significant part of the radiation emitted by objects either inside or outside our galaxy like stars, standard galaxies and also AGNs and blazars. For blazars the optical emission is associated to synchrotron processes and, in some cases, the synchrotron peak can occur within the visible range, see Sub-subsec. 1.3.6.1. In particular, the discrimination between FSRQs and BL Lacs is related to the blazar spectra restricted to the optical band (Subsec. 1.3.6). In the present work, the optical data from the Sierra Nevada Observatory have been employed. The observatory is briefly introduced in the next paragraph (Subsec. 2.2.1).

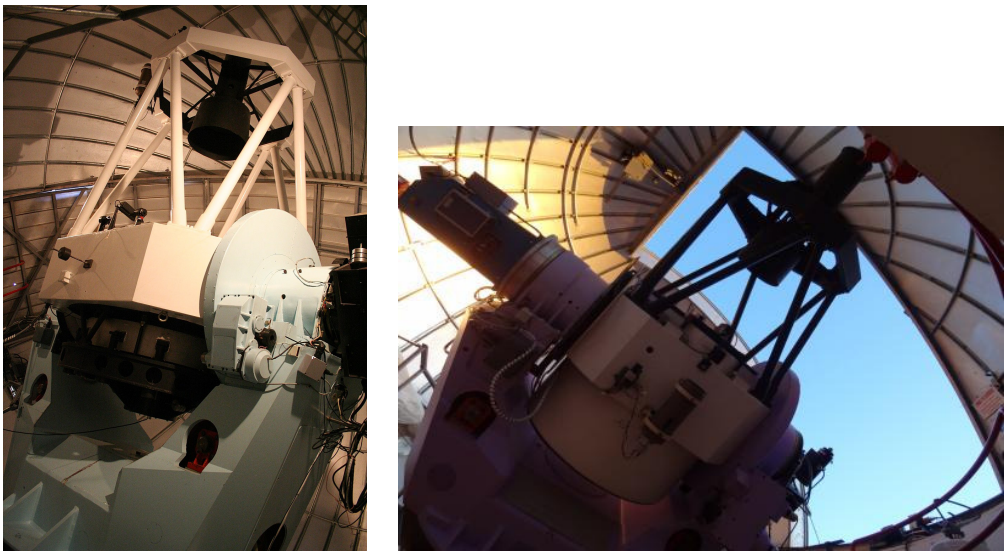

Figure 2.2: T150 (left) and T90 (right) optical telescopes at OSN. Credit: IAA-CSIC.

Throughout this thesis we also make use of observations in the X-ray band. These have to be carried out by means of space-based instruments, because the atmosphere is opaque to X-rays. Typical wavelengths of X spectral range are 10^{-8}-10^{-12} m, which roughly correspond to energies of 0.1-100 keV. In astrophysics, two sub-domains are commonly defined: *soft* X-rays have energy up to 10 keV, while *hard* X-rays have energy larger than that. In general, X-ray photons are probes of extreme astrophysical environments, which are associated with either thermal or non-thermal radiation. For AGNs, the inner part of an accretion disk reaches temperatures high enough to radiate X photons (Subsec. 1.3.2). An important non-thermal case is the synchrotron emission by charged particles streaming at relativistic velocities in jetted AGNs. This led to the use of the X band to derive X-selected samples for further categorization beside radio and optical. For blazars' SED, the X band is crucial, as it is the spectral range between the low-energy and the high-energy bump. Therefore, X-rays from blazars can be due to both synchrotron and IC processes (Sub-subsec. 1.3.6.1). In the present work, the X-ray data from the Swift satellite have been employed for TON 116. The instrument is briefly introduced in Subsec. 2.2.2.

2.2.1 Sierra Nevada Observatory

The *Sierra Nevada Observatory* (OSN) is an astronomical facility inaugurated in 1981 at Loma de Dílar (03° 23′ 05″ W, 37° 03′ 51″ N), in the Sierra Nevada (Granada, Spain), at an altitude of 2 896 m above the sea level (a.s.l.). Its major instruments are two optical telescopes with a Ritchey-Chrétien mirror displacement, and a Nasmyth focus configuration, which are under the management of the Andalusian Astrophysics Institute (IAA-CSIC)[1]. Their apertures are of 1.50 and 0.90 m respectively, see Fig. 2.2. They both employ a Johnson-Cousins R-band filter

[1] See the official OSN website (https://www.osn.iaa.csic.es/) for further details.

for photometric and polarimetric measurements. The data reduction of both photometric and polarimetric raw data relies on the python-based `iop4` pipeline, and is fully automatic (Escudero, Morcuende, and Otero-Santos 2024). These data are particularly useful for constraining blazars' magnetic field (e.g. Otero-Santos et al. 2024).

2.2.2 Swift

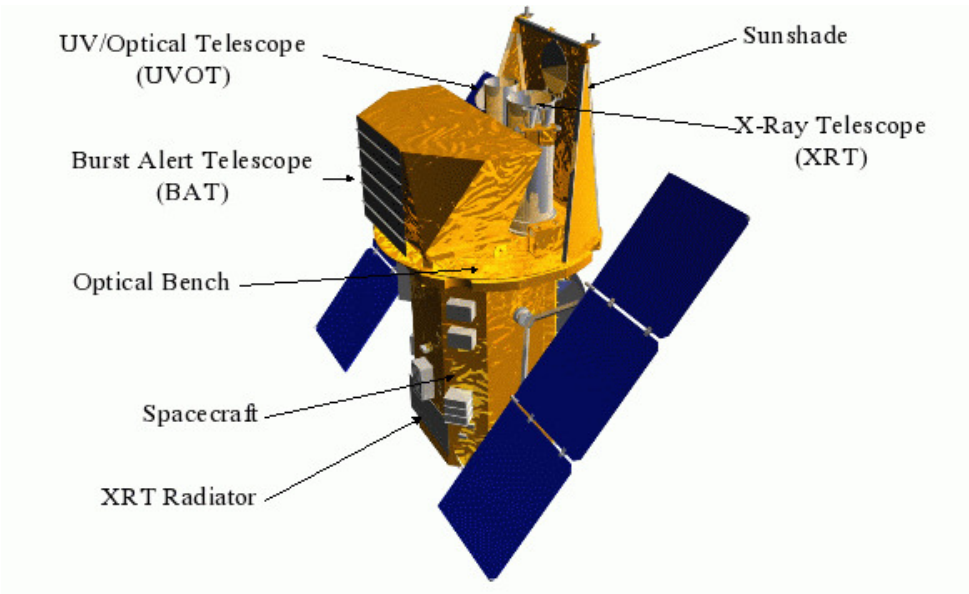

Figure 2.3: Overall structure of Swift satellite. Its main components are indicated with arrows. Image from the Swift website (https://www.swift.ac.uk/about/instruments.php).

The *Neil Gehrels Swift Observatory*, or simply *Swift* (Fig. 2.3) is an innovative, modular satellite that was launched in November 2004 to specifically study *Gamma-Ray Bursts* (GRBs)[2]. The satellite continuously surveys the sky, covering about 88% of it every day. Swift is equipped with three different, co-aligned instruments able to provide an accurate pointing in a short time interval. The *Burst Alert Telescope* (BAT, Barthelmy et al. 2005) observes in the 15-150 keV spectral range with a wide field of view (≈ 2 sr), and bins the data into an approximate time window of 300 s. Whenever a GRB is detected, its direction is calculated with an uncertainty of the order of 1 arcmin, and typically within 90 s an automatic repositioning procedure triggers both the X-ray (XRT, Burrows et al. 2005) and ultraviolet-optical (UVOT, Roming et al. 2005) telescopes for immediate follow-up. XRT is conceived for photons with energy between 0.3-10 keV, while UVOT is for those with wavelengths between 170-600 nm. Both XRT and UVOT can take images, spectra, and light curves to improve the GRB localization but also to analyze the evolution of the flaring activity of AGNs. Swift's measurements can help constrain the redshift of the transient and trigger fast follow-up observations from ground-based instruments.

[2]GRBs are the most powerful transient objects in the Universe. In a time of about 1-100 s they release more energy than the Sun in its whole life in form of γ-rays.

2.3 Gamma-ray instruments

The γ-ray band includes photons at the highest energies, above 100 keV. Being so wide in size, the γ-ray band is usually divided into several sub-domains, each of them characterized by specific detection techniques. At lower energies, γ-ray photons are detected from space with balloon payloads or satellites. At higher energies ground-based detectors with larger collection areas are required. A summary of the conventional γ-ray domains is given in table 2.1. The different detection methods rely on the same principle: while interacting with matter, γ-rays produce electrons and electron-positron pairs via photoelectric absorption, Compton scattering or pair production. From the products of this interaction, it is possible to reconstruct the energy and direction of the primary γ-ray photon. One of the most sensitive space-based γ-ray detectors currently in operation is *Fermi*-LAT, which is presented in the next subsection.

Table 2.1: Sub-domains commonly adopted within γ-ray astrophysics, with corresponding energy ranges and detection techniques.

Energy range	Class	Detection method
E < 10 MeV	Low Energy (LE)	balloons, satellites
10 MeV - 30 MeV	Medium Energy (ME)	satellites
30 MeV - 100 GeV	High Energy (HE)	satellites
100 GeV - 100 TeV	Very High Energy (VHE)	ground based
100 TeV - 30 PeV	Ultra High Energy (UHE)	ground based
E > 3 PeV	Extremely High Energy (EHE)	ground based

2.3.1 *Fermi*-LAT

The *Fermi* satellite (Atwood et al. 2009) is entitled to the Italian physicist Enrico Fermi (1901-1954) and was launched in June 2008. After a few months of calibration activities, it is fully operational since November of the same year. *Fermi* is continuously monitoring the γ-ray sky in the HE sub-domain, between 20 MeV and more than 300 GeV. Its major instrument is the Large Area Telescope (LAT), whose basic structure is shown in Fig. 2.4. It mainly consists of a *converter tracker* made of tungsten plates (atomic number $Z = 74$). The electron-positron pairs produced by the incoming γ-ray are tracked thanks to a grid of silicon detectors placed between the former plates. The tracks are used to reconstruct the direction of the primary γ-ray. The converter tracker is followed by a *calorimeter*, used to measure the energy losses of both the electron and positron. To reject background signals caused by CRs hitting the satellite, the detector is shielded by an anti-coincidence scintillator.

The launch of *Fermi*-LAT constituted a real breakthrough for studying the GeV sky. Thanks to its remarkably long duty cycle ($\gtrsim 90\%$) and a large field of view (FoV ≈ 3 sr), many extragalactic sources (mostly AGNs and in particular blazars) were finally confirmed to be HE-emitters. For

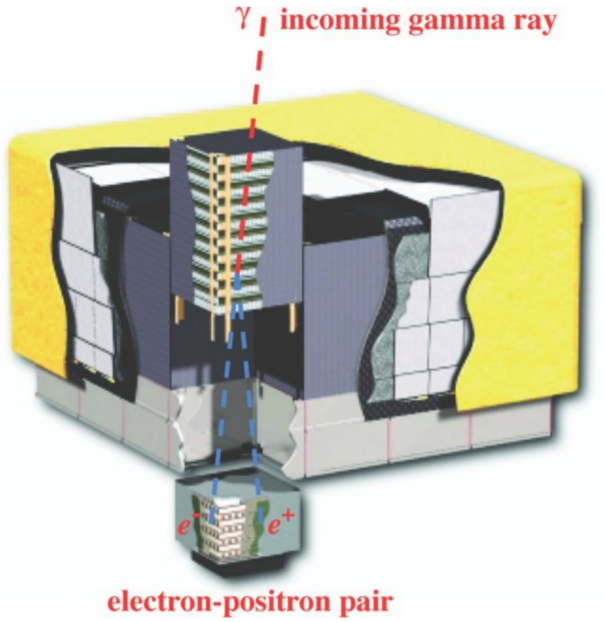

Figure 2.4: Sketch of the *Fermi*-LAT detector system, based on pair conversion and tracking from an incoming HE γ-ray. Taken from Atwood et al. (2009).

some sources, the results of *Fermi*-LAT regular monitoring supported the presence of even more energetic radiation, in the VHE range, pointing to TeV-emitter counterparts. Due to its small collection area (~ 1 m^2), *Fermi*-LAT becomes inefficient at VHE. VHE and UHE astrophysics require ground-based instruments with a large photon collection area ($\sim 10^4$ m^2). These detectors detect the primary γ-ray *indirectly* through Extensive Air Showers (EAS) and the associated Cherenkov light.

2.3.2 Atmospheric showers and Cherenkov radiation

When a γ-ray or a charged CR is absorbed in the Earth's atmosphere, a cascade of secondary particles called *Extensive Air Shower* (EAS) is generated. EAS were discovered by Pierre Auger in 1938 and can be sampled using ground-based detectors spread over a large area. Such instruments aim at reconstructing the properties of the primary γ-rays exploiting the Earth's atmosphere as a calorimeter.

In the atmosphere, the γ-ray interacts with the electric Coulomb field of air nuclei, giving rise to an electron-positron pair at a typical altitude of 20 km. These secondary particles move with relativistic speed towards the ground, losing energy via bremsstrahlung radiation and excitation/ionization processes. The emitted photons, in turn, produce further electron-positron pairs and a particle cascade, called an *electromagnetic shower*, is generated, see Fig. 2.5-left. A similar cascade can be initiated by electrons or positrons as well. The energy losses of the shower's particles can be parameterized with the following formula (Spurio 2015):

$$-\frac{dE}{dX} \approx \frac{E}{X_{0,e}} + \alpha(E) \quad , \tag{2.1}$$

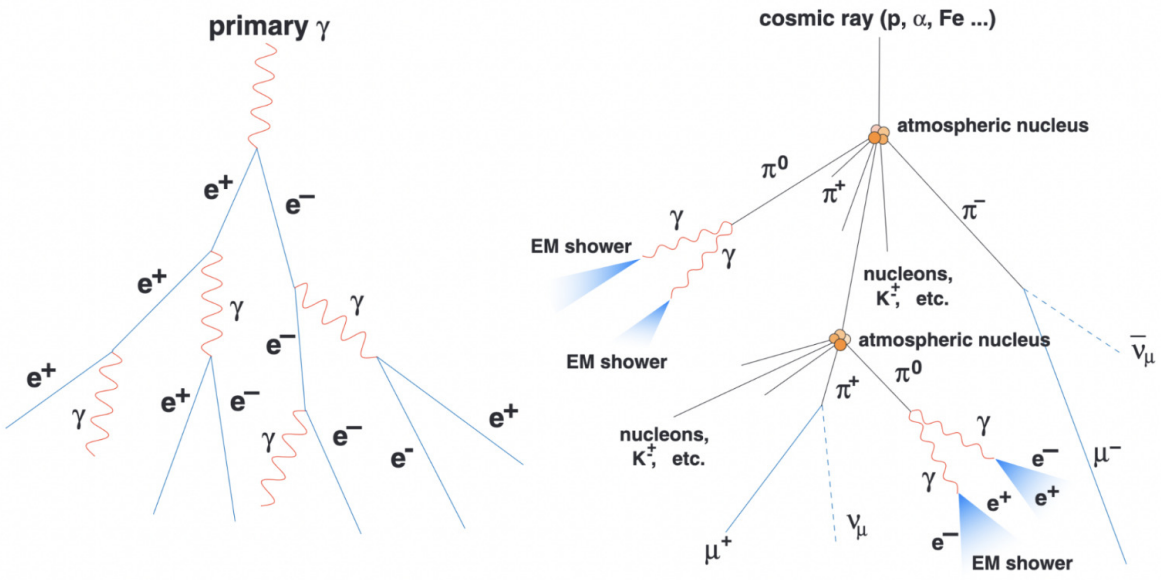

Figure 2.5: Sketch of an EM (left) and a hadronic (right) shower. Image from Wagner (2007).

where $X := \rho \cdot l$ is the *atmospheric depth*[3] from the first interaction point, $X_{0,e} \approx 37$ g cm^{-2} is the *radiation length* in air[4] and $\alpha(E)$ is the term accounting for excitation and ionization, weakly depending on energy.

A simple model able to describe the evolution of EM showers was developed by Walter Heitler in 1944. According to Heitler's model, an EM shower is governed by two main processes: bremsstrahlung and pair production, for which the same cross-section is assumed. Moreover, the radiation and conversion lengths are considered to be equal. Such a model consists of a cascade of sole electrons, positrons and γ-rays. After crossing a depth equal to $\ln 2 \cdot X_0$ in the atmosphere, each of the particles splits into two (an electron-positron pair for a parent γ-ray, or an electron/positron plus a γ-ray for a parent electron or positron) having half the energy of the parent particle. This means that at each i-th step the energy of each particle decreases by a factor 2, while the number of total particles increases by the same factor. The cascade goes on until the energy per particle $E_0/2^i$ drops to a critical energy E_c at which the energy losses by excitation and ionization are comparable to the ones due to bremsstrahlung. At this point, the number of particles reaches a maximum $N_{max} \sim E_0/E_c$, with E_0 the energy of the primary γ-ray, and the shower stops its development. The corresponding atmospheric depth is given by (Spurio 2015):

$$X_{max} = X_f + X_0 \ln\left(\frac{E_0}{E_c}\right) \quad , \tag{2.2}$$

with $X_f = X_0/2$ the atmospheric depth of the first γ-ray interaction. For pairs travelling through

[3] ρ is the air density and l is the travelled distance. The unit of X is g cm^{-2}.

[4] The radiation length is the depth after which an electron or positron decreases its energy by a factor $1/e$. For a γ-ray photon propagating in air, $X_{0,\gamma} = \frac{7}{9} X_{0,e}$.

air, the values of X_0 and E_c are around 37 g cm^{-2} and 86 MeV respectively. More detailed models including also Monte Carlo simulations are in overall agreement with Heitler's expectations (Matthews 2005). In particular, the total number of particles is proportional to the energy of the progenitor γ-ray (E_0), and the depth increases logarithmically with the same primary energy. From MC simulations it results that EM showers are roughly symmetric to their axis and their lateral distribution is relatively narrow, as can be seen in the left panel of Fig. 2.5.

Also charged particles and atomic nuclei can initiate a particle cascade and in this case, the cascade is referred to as *hadronic shower*. The typical development of such cascades can be seen in the right panel of Fig. 2.6. The inelastic scattering of incoming particles with air ones mostly produces charged and neutral pions up to a percentage of 90%, and kaons at about 10% (see e.g. Braibant, Giacomelli, and Spurio 2012). These are short-lived mesons that decay into other particles in a time interval smaller than 1 μs. Pions mainly follow these channels (see also Sub-subsec. 1.4.2.3):

$$\begin{cases} \pi^0 \longrightarrow \gamma + \gamma \\ \pi^+ \longrightarrow \mu^+ + \nu_\mu \\ \pi^- \longrightarrow \mu^- + \overline{\nu}_\mu \quad . \end{cases} \tag{2.3}$$

Notice that the neutral pions decay into two γ-rays, which then can initiate further EM showers. The charged pions decay into muons and neutrinos (or anti-neutrinos). Muons have a mean lifetime of 2.2 μs, after which they further decay according to (Spurio 2015):

$$\begin{cases} \mu^+ \longrightarrow e^+ + \overline{\nu}_\mu + \nu_e \\ \mu^- \longrightarrow e^- + \nu_\mu + \overline{\nu}_e \quad , \end{cases} \tag{2.4}$$

and can initiate additional EM cascades within the hadronic shower. As long as muons do not decay, they undergo very little energy losses while propagating in the atmosphere. Thus, they originate a steady Cherenkov front which is easy to be revealed if muons reach the camera of IACT telescopes (Subsec. 2.3.3). The tiny amount of secondary charged baryons can initiate further sub-showers on their own. The multiple cascades stop when particles reach the minimum energy for the pion production (≈ 1 GeV). Nearly $1/3$ of the primary particle's energy is converted into muons and neutrinos, which can reach the ground[5]. Due to the presence of all these multiple particle cascades, hadronic showers show a much more complex structure. They can still be studied with an approach similar to EM ones assuming the hadronic interaction length.

Assuming the same energy for the parent particle and photon, hadronic showers penetrate deeper into the atmosphere than EM ones. For heavier nuclei, the shower produced by a nucleus

[5]Despite the short life-time, muons can cross so deep the atmosphere as a consequence of relativistic time dilation.

with mass number A and energy E_0 is nearly the same of that of A nucleons with energy E_0/A (*superposition* model). Due to the complexity of the hadronic cascades, a realistic model can only be attained through full MC simulations. A major difference between hadronic and EM showers is the smaller number of produced particles for the same primary energy, due to the larger amount of energy dissipated through inelastic collisions. Moreover, hadronic cascades show more shower-by-shower fluctuations because of the many types of particles and interactions involved. Another important property is that secondary particles from strong force and weak decays have a large transverse momentum, making the lateral development wider than in the EM cascades (see Fig. 2.6).

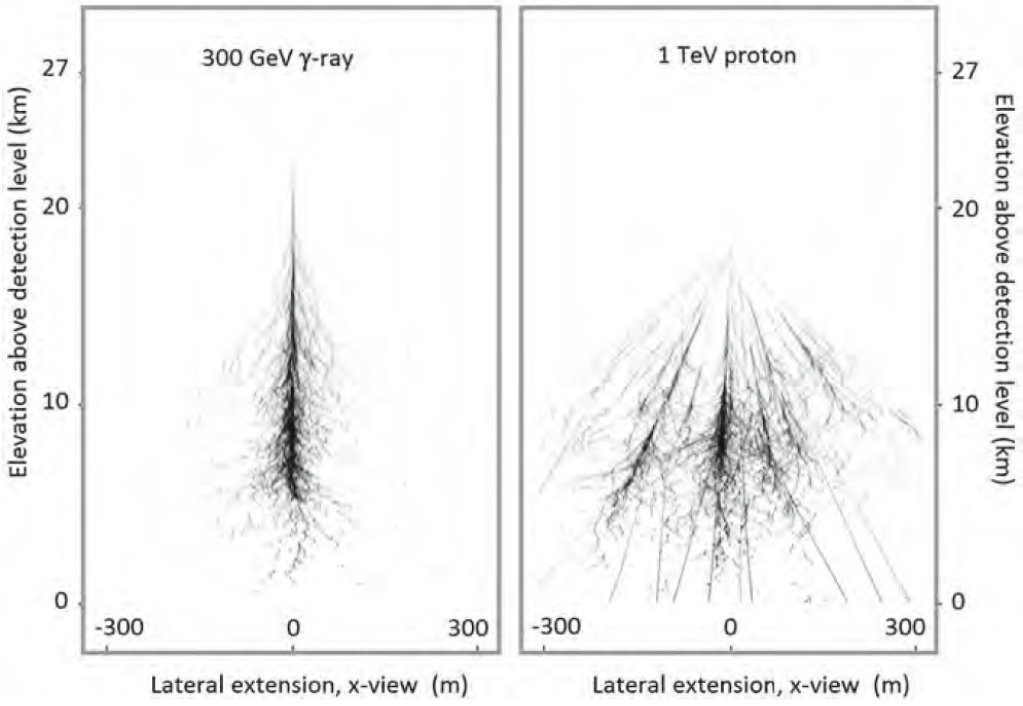

Figure 2.6: Simulated EAS initiated by a 300 GeV γ-ray (left panel) and a 1 TeV proton (right panel). Image taken from Spurio 2015 (original credits Dr. K. Bernloehr).

CRs are for the vast majority positively charged nuclei, therefore hadronic showers are much more abundant than EM ones. In the VHE regime, it is estimated that only one cascade out of 10^4 is due to a γ-ray. Thus, for VHE detectors, the ones initiated by hadrons represent an extremely challenging background over the signals coming from astrophysical sources. For this reason, effective rejection's methods must be put in play.

In particular, Cherenkov telescopes try to discriminate between hadronic and EM showers collecting the *Cherenkov radiation* emitted by EAS. This radiation is caused by the shower's particles propagating in the air at a speed v larger than the speed of light in the medium c/n, with c the speed of light in vacuum and n the refractive index of the air. The relativistic charged particle moving through the dielectric medium, causes a local re-orientation of the molecular dipoles and the collapse of this polarization state leads to the emission of Cherenkov light, see

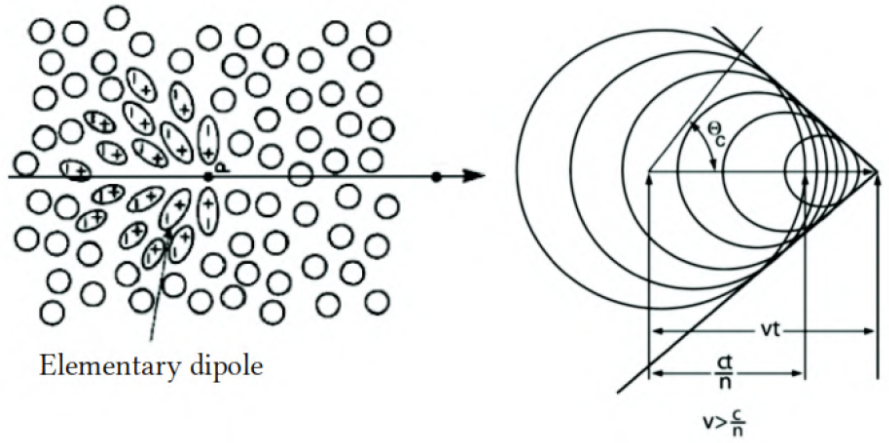

Figure 2.7: Illustration of the physical effect through which Cherenkov light is produced. Image adapted from De Naurois and Mazin (2015).

Fig. 2.7. Considering a charged particle with mass m, the energy threshold for the Cherenkov emission is:

$$E_{min} = \frac{m c^2}{\sqrt{1 - \frac{1}{n^2}}} \quad . \tag{2.5}$$

Cherenkov radiation propagates in a cone having an opening angle with respect to the particle direction given by

$$\cos \theta_{ch} = \frac{1}{\beta n} \quad , \tag{2.6}$$

where $\beta = v/c$. The number of emitted photons per unit depth and wavelength increases quadratically with the particle charge regardless of the sign and decreases as λ^{-2}. The Cherenkov radiation from EAS consists of extremely short, weak flashes peaking in the ultraviolet/blue band[6].

Due to the increase of the air density towards the ground, the angle encompassing the Cherenkov radiation also increases during the shower's propagation (see eq. 2.6). The Cherenkov pool on the ground of a γ-initiated shower, results from the superposition of the Cherenkov cones generated by all of the charged particles produced during the shower's development and will have a rather circular shape on the ground. If h is the height of the starting point of the cascade, and H is the observation altitude, the radius of the light pool can be approximated as Spurio (2015):

$$R_{ch} = \frac{h - H}{\tan \theta_{ch}} \quad . \tag{2.7}$$

[6]More precisely, in air and water the Cherenkov peak occurs at a wavelength of about 300-350 nm. This is also due to several attenuation and diffusive processes degrading it (e.g. Mie and Rayleigh scattering).

Considering the typical values $h = 10$ km and $H = 2$ km, the Cherenkov radius results $R_{ch} \approx 120$ m. The morphology of the Cherenkov pool produced by hadronic showers will be much more complex instead. Besides a wider lateral development, the light pool will include sub-pools originated by EM sub-components.

The typical duration of Cherenkov pulses is of a few ns. For this reason, prompt read-out electronics for the detection of these very faint signals is required. In the next subsection, we will describe in more detail the ground-based instruments focusing in particular on Cherenkov telescopes and the Imaging Atmospheric Cherenkov Telescope (IACT) technique.

2.3.3 IACTs: current and future generation

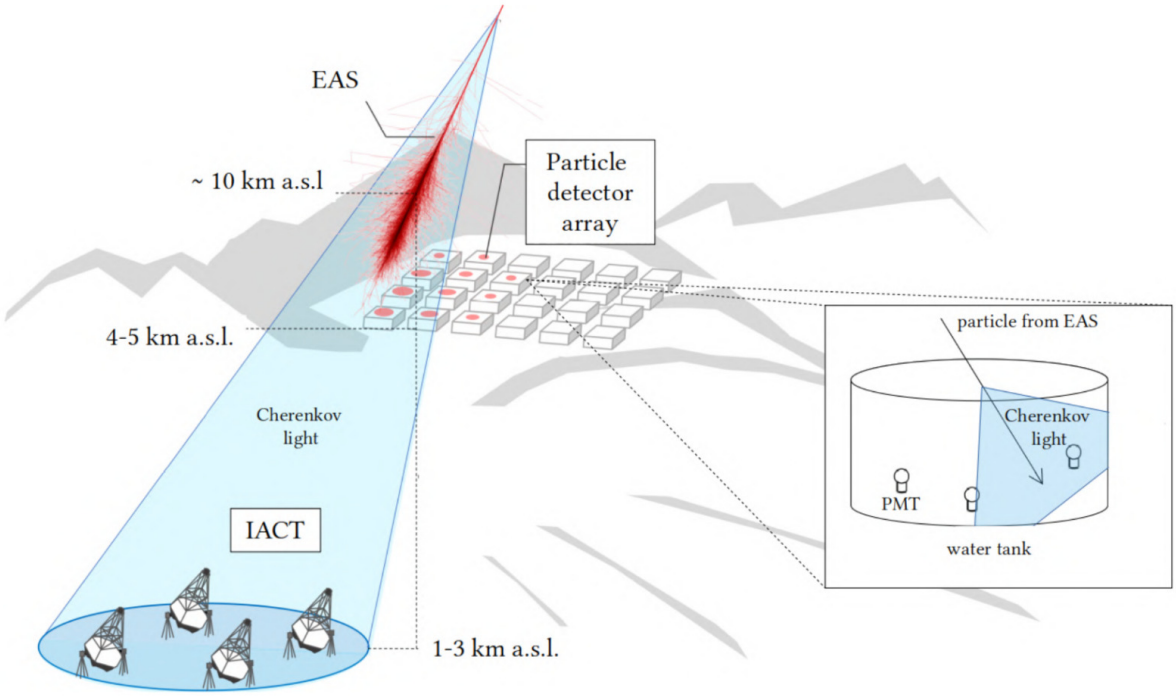

Figure 2.8: Sketch of the main types of ground-based γ-ray instruments. Image taken from Verna 2022 (original credits R. White, MPIK).

Two kinds of ground-based γ-ray observatories exist, particle detector arrays and Imaging Atmospheric Cherenkov Telescopes (IACTs), see Fig. 2.8. Particle detector arrays are located on average at higher altitudes (up to around 5 km a.s.l.), and they directly sample air-shower particles during their propagation through the atmosphere. This can be achieved using a large number of tanks filled with extremely pure water and equipped with *photo-multiplier tubes* (PMTs). The water acts as a target for incoming particles and flashes of Cherenkov light can be recorded by the PMTs. Particles belonging to the same shower can hit different tanks in coincidence. The collected signal is used to reconstruct the properties of the shower progenitor (CR or γ-ray), namely, its direction and energy. Two of the most representative observatories

exploiting such a technique are the *High Altitude Water Cherenkov* (HAWC, Abeysekara et al. 2017) at 4 100 m a.s.l. in Sierra Negra (Mexico) and *Large High Altitude Air Shower Observatory* (LHAASO, Cao et al. 2022)[7] at 4410 m a.s.l. in Mountain Haizi (China).

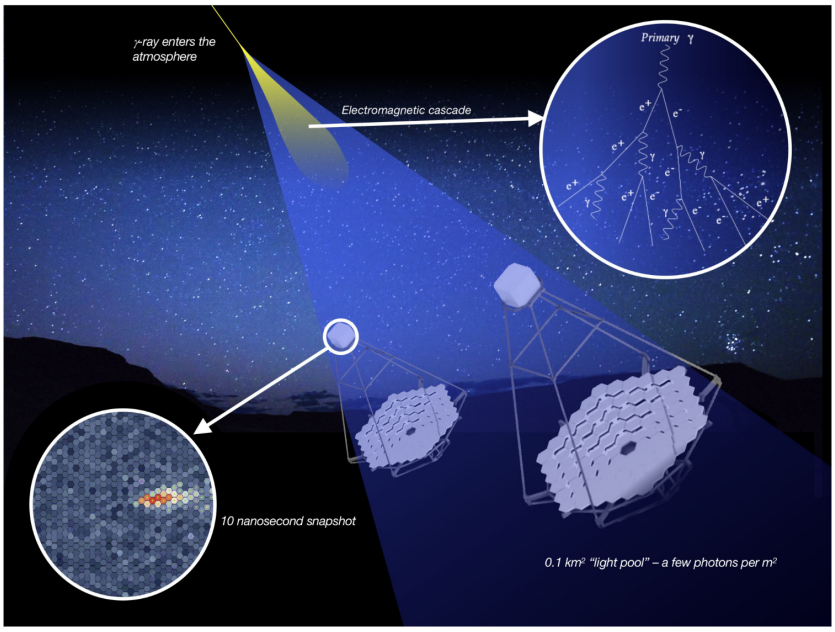

Figure 2.9: The basic technique exploited by any IACT. Cherenkov light from EAS initiated by VHE γ-rays is collected by huge reflectors and focused onto a pixeled camera equipped with high-speed PMTs. The final shower images are analyzed to reconstruct the direction and energy of the primary particle (see text). Credits: CTA Observatory (https://www.cta-observatory.org/).

The second class of ground-based observatories are IACTs, usually located at lower altitudes with respect to particle detector arrays. IACTs collect the Cherenkov light from EAS with large reflector dishes and fast cameras made of PMTs (Fig. 2.9). The telescope dish is usually spherical or parabolic, depending if it is smaller or larger than about 10 m. The mirror dish is segmented with single sub-mirrors of $\sim$ 1 m diameter. The sub-mirrors can be adjusted with adaptive control to focus the light onto the camera in the focal plane. The camera is composed of an array of pixels hosting sensitive, ultra-fast PMTs. The typical FoV of each single pixel is 0.1°, while the total FoV of the instrument can reach 5°. IACTs cannot operate during the day and must be installed in remote places with unpolluted nights. Still, due to the high sensitivity of the pixels, the telescopes have to face the *night sky background* (NSB), namely optical photons resulting in a diffuse brightness of the sky. This brightness always varies depending on different environmental conditions. Main NSB contributions are due to the Moon, stars, galactic sources, airglow and zodiacal light. Also artificial lights can eventually contribute to this unwanted background. The electronics of the camera pixels is designed to take into account different levels of NSB with high accuracy. This is crucial to better discriminate the Cherenkov light from EAS and background

[7]LHAASO can be considered as the initiator of the UHE astrophysics, being the most sensitive instrument above 100 TeV.

optical light[8].

Once the Cherenkov radiation is reflected and focused onto the camera pixels, an image of the shower is formed. This image is the charge distribution deposited in the camera pixels. IACTs arrays are arranged on the ground with a typical spacing of ~ 120 m which is comparable with the pool's size (see eq. 2.7). As each of the telescopes occupies a different position it will sample the Cherenkov light from the same cascade from a different perspective. In the so-called *stereo* mode, the images from different telescopes are combined to reconstruct the showers' parameters with more accuracy[9]. Combining the information from different images greatly helps the discrimination between electromagnetic and hadronic showers[10]. γ/hadron separation techniques rely on the differences in the overall shape of the Cherenkov images: roughly a regular ellipse for γ-rays, or an asymmetric and irregular distribution for hadrons. A major exception to the latter case is represented by muons, which are among the secondary particles initiating EM sub-showers or reaching the ground (Subsec. 2.3.2). Muons able to reach the pixeled-camera of IACTs give rise to a well-defined ring-like image, which is easily recognized and discarded from further analysis.

The first instrument exploiting the IACT technique has been the Whipple telescope, a 10-m diameter telescope inaugurated in 1968 at the Fred Lawrence Whipple Observatory (Arizona, USA). Despite being a single-dish detector and consisting of only 35 PMTs, it represented a milestone for VHE astrophysics, as it discovered the first object emitting in that energy range, the Crab Nebula (Weekes et al. 1989). This source is a fundamental standard candle for the γ-ray astronomy (Appendix B). The Whipple telescope has also discovered the first VHE extragalactic object, the blazar Mrk 421 (Punch et al. 1992). The first IACT observing in stereoscopic mode was *High Energy Gamma-Ray Astronomy* (HEGRA, Daum et al. 1997), an array of 5 telescopes arranged in a square, with one at its centre. It has operated from 1996 to 2002 at the Roque de Los Muchachos Observatory in La Palma (Canary Islands, Spain). Nowadays, there are three major IACTs, see also Fig. 2.10:

- *High Energy Stereoscopic System* (HESS, Aharonian et al. 2006), the only one in the Southern Hemisphere at about 1 800 m a.s.l. in Namibia, composed by four 12-m diameter dishes arranged in a 120-m side square, which was complemented by an additional 28-m dish at the centre in 2012;

- *Very Energetic Radiation Imaging Telescope Array System* (VERITAS, Weekes 2002), at about 1 275 m a.s.l. at the Fred Lawrence Whipple Observatory in Arizona (USA), composed of four 12-m dishes completed in 2007;

[8]Full Moon nights are usually excluded though, as the correspondent sky luminosity is too high for a safe IACT operation.

[9]Observations are still possible with only one instrument (*mono* mode), but require different reconstruction techniques.

[10]Stereoscopic observations also improve the selection efficiency against spurious signals triggering one IACT reflector only.

Figure 2.10: The three major IACTs currently in operation. HESS is on top (credits HESS collaboration, http://www.mpi-hd.mpg.de/hfm/HESS/), VERITAS is in the middle (credits VERITAS collaboration, http://veritas.sao.arizona.edu/), MAGIC is at the bottom (credits MAGIC collaboration, https://magic.mpp.mpg.de/).

- ***Major Atmospheric Gamma Imaging Cherenkov*** (**MAGIC**, Aleksić, Ansoldi, et al. 2016b), at about 2 200 m a.s.l. on La Palma (Canary Islands, Spain), composed by two 17-m dishes 85-m apart optimized for a relatively low VHE threshold and a fast repositioning response (≈ 30 s). It will be discussed in more detail in the next chapter.

All of them are multi-telescope instruments with around a factor 100 improved sensitivity with respect to the previous generation. They are optimised for the energy range between some tens of GeV up to around 100 TeV, and a FoV of around 4°. Their angular and energy resolution is around 0.1° and 15% respectively. The properties of such detectors make them able to reach an integral flux sensitivity of the order of 10^{-13} erg cm^{-2} s^{-1}.

The next generation of IACT detectors is already in construction and is the **Cherenkov Telescope Array Observatory** (**CTAO**, CTA Consortium et al. 2019). The project has been developed since 2006 and currently involves around 31 countries, 200 institutions and more

than 1 500 scientists. CTAO will be deployed in two sites, one at the Roque de Los Muchachos Observatory in La Palma (close to the MAGIC site), called CTAO Northern Array, and the other at the ESO site in Atacama (Chile), called CTAO Southern Array. The observatory will have 5-10 times better flux sensitivity than the current IACTs over a wider energy range, from 20 GeV to 300 TeV, see Fig. 2.11. Moreover, CTAO will reach unprecedented angular and energy resolutions. This will be possible thanks to three types of telescopes, Small Size Telescopes (SSTs), Medium Size Telescopes (MSTs), and Large Size Telescopes (LSTs) with 4 m, 12 m and 23 m dish's diameter, respectively. Each of them will maximize the sensitivity in a specific part of the energy range. In particular, LSTs will lower the energy threshold down to ~ 20 GeV, as their size will allow them to detect fainter Cherenkov signals. On the other hand, the SSTs, spread over a larger area, will improve the detection of the most energetic showers. Currently, the expected CTAO configuration is called *alpha* configuration, from the overall arrangement of the telescope arrays in the two sites. In particular, the Northern Array will consist of 4 LSTs and 9 MSTs, while the Southern Array will consist of 14 MSTs and 37 SSTs. For the time being, the *Instrument Response Function* (IRF) is the fundamental means for performance speculations about future observational activities[11].

The first LST prototype, LST-1, has been already built in the CTAO Northern array ~ 100 m away from the MAGIC telescopes. It is about to end its commissioning phase started in 2019. LST-1 has a FoV of around 4.5° and is mostly sensitive between 20 GeV and 3 TeV. The proximity of MAGIC allows for joint MAGIC + LST-1 observations and data analysis. In particular, it allows for the reconstruction of 20% more events and to lower the energy threshold of 15% with respect to MAGIC alone. Moreover, the minimum detectable flux is about 30-40% lower than the one reached by MAGIC and LST-1 alone (Abe et al. 2023).

[11]They are available at the *zenodo* repository https://zenodo.org/records/5499840 (from the official CTAO website).

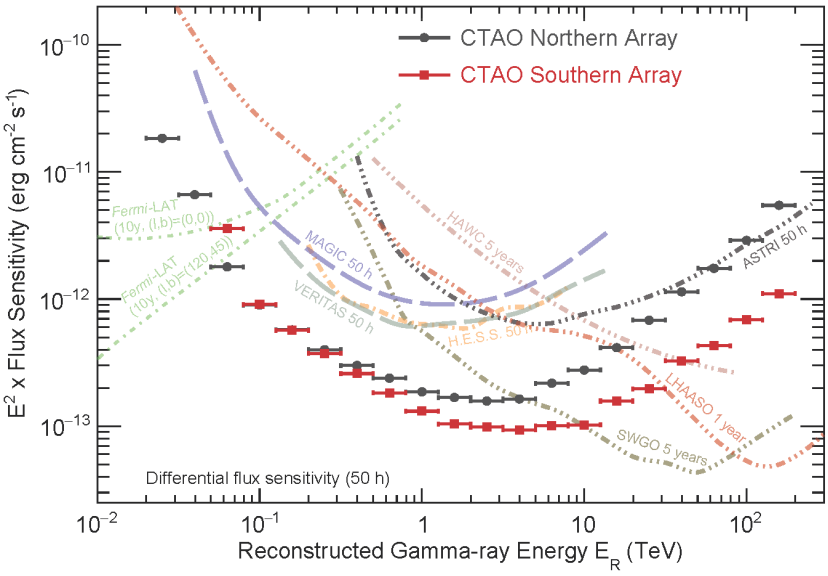

Figure 2.11: Expected sensitivity of the CTAO (assuming 50 h of observation time) compared with that of current instruments for γ-ray detection. Credits: CTA Observatory.

Chapter 3

The MAGIC telescopes and data analysis

In this chapter a description of the MAGIC telescopes is provided. First, we will report a general overview of the telescopes' structure and functioning. Then, we will describe all the steps of the MAGIC data analysis from raw data to high-level scientific results. This chapter is intended to be a reference for the first part of Ch. 4, focused on the MAGIC observations on TON 116.

3.1 The MAGIC telescopes

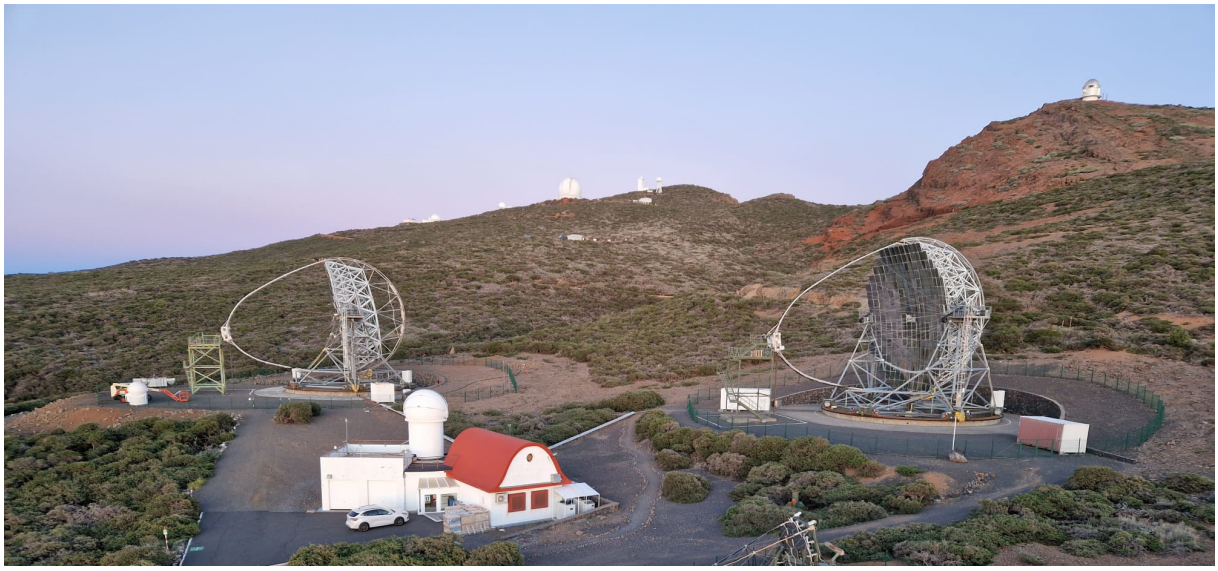

Figure 3.1: The MAGIC telescopes (M1 on the left, M2 on the right), the Counting House (red-roof building) and the LIDAR's dome (white dome). The picture was taken during my second shift in April 2023.

The MAGIC telescopes, also known as Florian Goebel Telescopes, is one of the major IACTs currently active (Fig. 3.1). It aims at indirectly observing VHE photons through the

Cherenkov light emitted by EAS, see Subsec. 2.3.2. MAGIC is located at an altitude of about 2 220 m at the Observatorio Roque de Los Muchachos (ORM, $28^\circ\,45.7'$ N, $17^\circ\,53.4'$ W) on La Palma, Canary Islands (Spain). The location has been chosen primarily due to the very good sky quality and very low NSB. MAGIC is composed of two telescopes, M1 and M2, with a diameter of 17 m and a focal length of 17 m, placed 85 m apart from each other. M1 was completed in 2003 and started operations in 2004, whereas M2 was inaugurated in 2008 and joined M1 observations the following year. Since then, M1 and M2 started observing in stereoscopic mode. The MAGIC telescopes are optimized for the detection of γ-rays in the range 50 GeV - 50 TeV, although the energy threshold can go down to ~ 30 GeV if a particular trigger system is used (*Sum-Trigger-II*, mentioned below). The integral flux sensitivity (Subsec. 3.5.4) that can be reached is $(0.66 \pm 0.03)\%$ of the Crab Nebula flux which is taken as a reference[1]. The structure of MAGIC reflectors consists of a carbon-fibre tube structure whose weight is of the order of 20 tons. The overall weight of the reflectors reaches around 60 tons. This relatively light structure allows for an altitude-azimuth (Alt-Az) mount and very fast re-pointing capabilities. The telescopes can turn of 360° in around 30 s, with an average speed of 4° per second, which can reach 7° per second in case of an alert[2]. These characteristics make MAGIC one of the most prompt instruments in reacting to transient phenomena like GRBs, neutrino or gravitational wave alerts.

Both M1 and M2 reflectors are made up of 247 mirrors of square shape with ~ 1 m side. The mirrors can be adjusted through specific actuators controlled by the Active Mirror Control (AMC), one of the MAGIC subsystems (see Sec. 3.2). The AMCs maintain the proper parabolic shape of the whole reflector during observations. Each of the MAGIC telescopes is equipped with a camera made of 1 039 ultra-fast photomultipliers that constitute the camera pixels. The PMTs collect the faint and fast flashes of Cherenkov light during a certain time window. The result is an image which is nearly a narrow ellipse for an incoming γ-ray. A specific reconstruction pipeline (see Sec. 3.5) allows to derive the fundamental parameters of the EAS: the energy, the incoming direction in the sky and the nature of the primary particle (γ or hadron). In particular, the discrimination between EM and hadronic showers relies on the different geometry and temporal development of the images, which are elliptical for EM showers, irregular and clustered for hadrons or ring-shaped for secondary muons.

MAGIC FoV is about 3.5°. The angular and energy resolution at around 1 TeV are $\sim 0.07^\circ$ ($\sim 6'$) and $\sim 15\%$ respectively (Aleksić, Ansoldi, et al. 2016a). The fraction of time used for data taking (i.e. the *duty cycle*) is mainly limited by the weather conditions and the presence of the Moon and is typically 40%. The 3-4 nights per month with nearly full Moon are usually exploited for maintenance activities and represent a break between the observation periods. In the next section, we will describe the main subsystems forming the MAGIC hardware in more detail.

[1]The *Crab Unit* is 1 C.U. $= (3.39 \pm 0.09) \cdot 10^{-11}$ cm^{-2} s^{-1} TeV^{-1}, taken at 1 TeV (see Appendix B).

[2]By construction, the range in azimuth and zenith is $[-90^\circ, 318^\circ]$ and $[-70^\circ, 105^\circ]$ respectively. Zenith angles less than around 3° are usually excluded due to mechanical issues in repositioning at such low angles.

3.2 Hardware overview

MAGIC operations are possible thanks to a complex hardware system, which is composed of a variety of *subsystems*, each having a specific task. The most important are:

- the *drive system*, which monitors the movement of the telescopes e.g. the pointing and tracking of the sources. The drive system software is `COSY` (Bretz et al. 2009);
- the *mirrors*, which can be adjusted through the AMC (Biland et al. 2007);
- the *MAGIC Integrated Readout* (MIR) and *Data AcQuisition* (DAQ), which consist of a memory chip, called Domino Ring Sampler 4 (DRS4), an Analog-to-Digital Converter (ADC) and a server which stores the events in `.raw` files;
- the *Camera Control* (CaCo), for the monitoring of the physical parameters inside the telescope's camera.

Each telescope has its subsystems which are supervised by a Central Control (CC) software called `SuperArehucas` (SA)[3]. SA sends commands and receives reports on the status of the subsystems every second through a dedicated Graphical User Interface (GUI). The GUI allows the operators on shift to interact with all the subsystems simultaneously.

Some ancillary devices support the telescopes' subsystems. Possible mispointings caused by gravitational deformation of the reflectors are corrected by two Charge Coupled Device (CCD) cameras located at the centre of the dishes: the *TPoint* camera, and the *Starguider* camera. Their purpose is to monitor if the direction in which the telescope is pointing is consistent with the expected coordinates and they allow to reach a pointing accuracy of the order of 0.01°. The TPoint camera takes pictures of the observed FoV to compare the observed stars' positions with the ones available in the catalogues. The Starguider camera compares the position of the telescope's camera (retrieved from a ring of 6 Light Emitting Diodes (LEDs) at its border) with the positions of the stars in the background FoV. Both devices provide information to the central system SA which can correct for possible mismatches. Also the AMC can correct the possible deformations due to gravity. Every single mirror is equipped with specific actuators which can be adjusted to reach the parabolic shape of the focused reflector. Moreover, the single-mirror actuators allow keeping the reflectors de-focused during the daytime to avoid possible fires caused by the Sunlight. The optical Point Spread Function (PSF)[4] can be lower than 10 mm. The optical PSF is evaluated every night before the data taking. The telescope is pointed toward a bright star and a picture is taken using a specific CCD camera (*SBIG* camera).

Other auxiliary subsystems, either on-site or remote are employed during standard observations. Two examples are the instruments for weather monitoring, described in Subsec. 3.3.2,

[3]The name is based on the aboriginal term *Arehucas*, from the ancient Guanche population of Canary Islands.

[4]The PSF is defined as the 39% containment radius of the light distribution from a point-like source (usually a bright star).

and the *Automatic Alert System* (AAS), able to receive transient alerts and command the fast re-pointing of the telescopes, see Subsec. 3.3.1.

The night's operations are managed by the on-site shifters from the control room in the *Counting House* (CH), see Fig. 3.1. The CH hosts also the PCs of all the single subsystems and the electronic structure of the acquired signals kept at low-temperature using a *Cooling-rittal* system.

3.3 PMT camera and standard trigger system

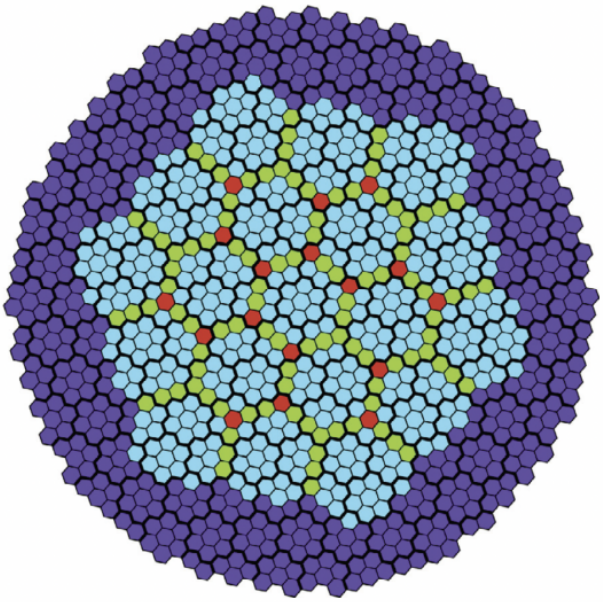

Figure 3.2: Sketch of the 1 039-pixel camera of the MAGIC telescopes. The purple pixels do not belong to the trigger region. The cyan hexagons in the inner part are the macrocells of the L1 trigger region. The shared pixels between two or three neighbour macrocells are coloured in dark yellow and red respectively. The black contours mark the 169 PMT clusters of 7 pixels each (see text). Credits: Aleksić, Ansoldi, et al. (2016a).

The PMT cameras are located in the focal plane of M1 and M2 and collect the Cherenkov photons reflected by the mirrors. The cameras are ~ 850 kg heavy and sustained by aluminium arcs. Each camera is made of 1 039 PMT pixels of 1 inch (2.54 cm) diameter. The PMTs are arranged in a circular shape and grouped into 169 clusters of 7 pixels (Fig. 3.2). Each PMT has a FoV of 0.1° and a Quantum Efficiency (QE) of $\sim 34\%$ for blue wavelengths of $\lambda_B \sim 350$ nm. The response time of the PMTs is of the order of 1 ns.

The charge accumulated in the PMT anode produces a current proportional to the input charge through the photoelectric effect. The gain of the PMTs can be tuned by setting different High Voltage (HV). The low-gain configuration is used to reduce the amount of charge hitting

the PMT i.e. *reduced* HV configuration. The reduced HV is used to increase the lifetime of PMTs and the telescope duty cycle by observing under moderate ($\sim$ 20 times the dark-time NSB) and strong (up to $\sim$ 100 times the dark-time NSB) moonlight conditions[5] (Ahnen et al. 2017). This is possible due to the UV band-pass filters mounted on the MAGIC cameras. In general, the PMTs' gain depends on the environmental conditions inside the camera, i.e. average temperature, humidity etc. and a calibration system is required (Gaug 2006). This system consists of a *calibration box* containing a laser located in the centre of the dish. The laser illuminates the PMTs with light pulses of 0.4 ns duration and at 355 nm wavelength. The laser's illumination is uniform across the camera plane (the so-called *flat fielding*) and the HV settings of each PMTs are adjusted to have the same gain in each pixel and to obtain the conversion factor between analog-to-digital counts and number of photoelectrons (p.e.). The p.e. collected by the PMTs constitute an electric signal which is converted into an optical one through vertical cavity surface emitting lasers (VCSELs) and sent to the DAQ in the CH, through $\sim$ 200 m-long optical fibres. The signal is converted back to electric and split toward the trigger system on one branch and to the readout system on the other.

The standard trigger system[6] includes three levels considering single pixels signals (L0), clusters of pixels in the same camera (L1), and coincidences between M1 and M2 (L3, Paoletti et al. 2007). Only the innermost part of the camera contributes to the camera trigger (see Fig. 3.2) and only if a signal passes all the trigger levels is recognized as a γ-ray event. The lowest level trigger L0 selects only the PMTs with a signal above a certain *Discriminator Threshold* (DT). The DT value can be tuned to account for different NSB levels:

- **Extragalactic DT**: lowest threshold DT ($\sim$ 4.24 p.e.) suitable for dark nights, with no Moon, and for extragalactic pointings. The L0 rate is $\sim$ 800 kHz;
- **Galactic DT**: medium threshold DT used for galactic sources observations for which more stars are expected in the FoV. The L0 rate is $\sim$ 15% higher than the Extragalactic DT one;
- **Moon DT**: highest threshold DT used when the presence of the Moon makes the sky very bright.

The DT is updated during the night according to the variations of the light conditions in order to keep stable rates in each PMT. The second trigger level L1 searches for spatial and temporal coincidences of adjacent pixels passing the L0 trigger level. In particular, it searches a minimum number n of adjacent pixels (Next Neighbour (NN) pixels) in a time interval of 8-9 ns. The number of adjacent pixels can be $n = 2, 3$ or 5 but usually $n = 3$ is considered in standard stereo observations (3NN configuration). The L1 trigger operates on 19 hexagonal *macrocells* occupying the innermost part of the camera (547 pixels in total), see Fig. 3.2. Each macrocell

[5]Maximum Moon's illumination phase 75%.

[6]Also a "not-standard" trigger system called *Sum-Trigger II* has been developed and can improve the MAGIC sensitivity below 80 GeV. This alternative trigger has not been considered in this work so the interested reader is referred to Dazzi 2016, Dazzi 2012.

includes 37 pixels, and the boundary pixels are shared with those of the neighbour macrocells. The typical rate of L1 trigger is 15 kHz. The output of each macrocell is sent to the last L3 trigger, i.e. the *stereo* trigger. L3 searches for time coincidences between M1 and M2 signals. Due to the 85 m distance between the two telescopes, a coincidence window of $\sim$ 180 ns is considered. The typical rate of L3 trigger is 250-350 Hz. If all the trigger levels are passed, the *event* is considered of astrophysical origin and the readout starts.

The readout system consists of the DRS4 memory chip where the signal is stored, waiting for the trigger decision. It is composed of an array of capacitors, which are charged by the electric signal. When the trigger conditions are fulfilled, their charge is converted into a digital signal through an ADC and the signal in each pixel is recorded into a waveform of ADC counts in a time window of 30 ns. The ADC signals are then sent to the DAQ which stores them in `.raw` data files and performs a preliminary analysis.

3.3.1 Additional subsystems

MAGIC operations require additional subsystems connected to SA and hosted in the CH. They perform preliminary data analysis and receive external information from other facilities. They include:

- the *On-Site Analysis* (OSA) which performs the first steps of the low-level analysis chain (see Sec. 3.5.1) after the data-taking[7]. In the morning, after the end of observations, both raw and processed data are sent to the external cluster Port d'Informació Cientifica (PIC, Barcelona), where they are available to analyzers (Oya et al. 2010);

- the *MAGIC Online Analysis* (MOLA) which performs a real-time analysis up to the high-level outputs (θ^2-plots, spectra and light curves, see Subsec. 3.5.3), for a first estimation of both significance and flux from the observed source. MOLA results are particularly important for possibly extending the observations of transient phenomena such as GRBs and flares (Tescaro et al. 2013);

- the *Automatic Alert System* (AAS) which processes real-time alerts from the General Coordinates Network (GCN)[8] for follow-up of transient events such as GRBs, neutrinos or GWs. If the transient can be observed by MAGIC, the telescopes are automatically re-pointed to the target position (Berti 2018);

- the *Data check* which is a program running at the end of each night of observations and providing different outputs for inspecting the quality of the data-taking. The information provided allows to monitor both the atmospheric conditions and the electronics performance during the full night.

[7] OSA works only for dark nights and if the standard trigger is used.
[8] https://gcn.nasa.gov/.

In the next section, we describe the other subsystems that constantly check the weather conditions of the MAGIC site.

3.3.2 Weather monitoring

The monitoring of the weather is of paramount importance for any IACT instrument, as the atmosphere is an active part of the detector (Subsec. 2.3.2). Atmospheric conditions directly affect the development of EAS, and consequently the amount and the quality of detected Cherenkov signals. For this reason, the weather conditions at the MAGIC site are continuously monitored by several auxiliary instruments such as:

- the *Weather station*, providing information about the ambient temperature, pressure, humidity, average wind speed, gust speed, and wind direction every 2 s;
- the *Rain sensor*, able to detect raindrops from the roof of the CH;
- the *All-sky camera*, taking pictures of the sky with a wide FoV (150°) every 2 min from the roof of the CH;
- the *LIght Detection And Ranging* (LIDAR) installed in a dome on the roof of the CH. The LIDAR measures the atmospheric transparency (between 0-1) as a function of the altitude (3, 6, 9, 12 km a.s.l.) by shooting laser pulses (532 nm wavelength) at around 4° from the MAGIC pointing. It measures the amount of back-scattering light from clouds and aerosols (Schmuckermaier et al. 2022);
- the *pyrometer*, installed on M1, monitors the presence of clouds. The pyrometer measures the sky temperature, which increases in the presence of clouds reflecting the thermal radiation from the ground.

All the outputs of these instruments should be available to the telescopes' operators in the CH. The weather station, the rain sensor and the all-sky camera are mainly used for a real-time monitoring during observations for security reasons. Indeed, observations can be carried out if there is no rain, the humidity is less than 90%, and wind average speed (gust speed) is less than 50 km/h (40 km/h). If one of these conditions is not fulfilled, an alert is issued and the lids of the cameras are automatically closed.

The transmission (cloudiness) parameter given by the LIDAR (pyrometer) complements the MAGIC observations and provides a useful indication of the data quality. Indeed, it is used by the analyzers to select the best quality data. In particular, the LIDAR transmission at 9 km is the most relevant parameter, as it corresponds to the altitude at which the EAS reach their maximum (Subsec. 2.3.2). LIDAR information can also be used to correct data for bad transmission. This is usually not required for transmission values larger than 0.8-0.9 (very good quality data) or $\lesssim 0.5$ (very bad quality data that should be discarded). In general,

transmission and cloudiness parameters are in agreement with each other because they provide correlated information. Cloudiness $\lesssim 30$ is considered as ideal, between 30-45 is moderately good quality, whereas $\gtrsim 45$ is very bad quality (i.e. highly cloudy). For quality selection, the LIDAR transmission is usually considered and the cloudiness is mainly used when the LIDAR is not available.

3.4 Data-taking

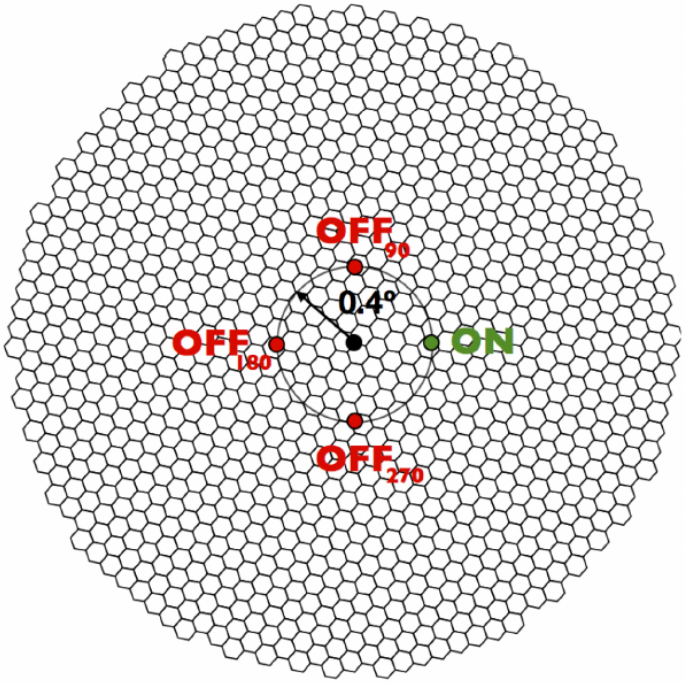

Figure 3.3: Schematic representation of the Wobble mode exploited by MAGIC. The black dot marks the camera centre, the green dot on the right marks the source position (ON) with an offset of 0.4° from the centre, while the red circles are the OFF positions (symmetric to the camera centre) where the background can be estimated. Credits: López Coto (2015).

Before every night of observations, the MAGIC telescopes perform some technical procedure and take different types of technical data. First, the start-up procedure is performed to power on the electronics which has to reach a nominal temperature for the operations. Then, a *pedestal subtraction run* is taken (only one for the whole night). It is a short observation of few minutes performed with closed camera's lids. It is done to calibrate the baseline of the DRS4 capacitors of the readout system (see Sec. 3.3). After the pedestal subtraction run, standard observations can start. For each observation, before pointing to the target source, other two technical runs are taken: the *pedestal run* and *calibration run*. The pedestal run is taken with the camera's lids open and it aims at estimating the number of background events due to both the readout noise and the NSB. Such random events are subtracted from the scientific data during data calibration (see Subsec. 3.5.1). The calibration run consists of a uniform illumination of the camera with a laser

pulse coming from the calibration box. This run allows to compute the conversion factor between the ADC counts and the number of p.e. After these two technical runs, the *data run* starts. It contains all the triggered events from the observed source and it has a duration of 15-20 min. Each data run is divided in *subruns* of $\sim$ 2 min ($\sim$ 1-2 GB of data). During the data acquisition, some interleaved pedestal and calibration runs are taken to monitor the possible changes in the telescope response and electronic noise.

Two main pointing modes are used in MAGIC observations: the *ON/OFF* and the *wobble* modes. In the ON/OFF mode, an ON and an OFF observations are performed separately. In the ON observation the telescopes point at the source coordinates (i.e. the source is at the centre of the camera FoVs), while in the OFF observation, the pointing is moved toward a position in the sky without VHE sources which is used for the background's estimation. The ON and OFF pointings should be taken with the same overall conditions i.e., Az, zenith distance (ZD) etc. In the ON/OFF mode, part of the observation time is lost due to the background runs so the wobble mode was developed and became the standard one (Fomin et al. 1994a). In the wobble mode, the telescopes' pointings are slightly offset from the source position to simultaneously collect the events from the source (ON) and the background (OFF), see green and red dots in Fig. 3.3. The standard offset angle for point-like sources is 0.4°, and the background is evaluated within one or more OFF positions symmetric to the camera centre. For bright sources like Crab (Appendix B), one OFF region only is usually sufficient for the background estimation. However, considering more than one OFF region can reduce the systematic effects due to the non-uniform PMT response across the camera. For the same reason, after each data run the wobble pointing is rotated of 90° or 180° around the source direction keeping the same offset of 0.4° from it. For extragalactic sources, four wobble pointings are usually considered but this number could vary depending on the presence of bright stars or other sources of background light in the FoV.

3.5 The standard analysis chain

The MAGIC data analysis allows to pass from the DAQ raw files to the production of high-level scientific results like spectra and light curves. For this, a proprietary software called *MAGIC Analysis and Reconstruction Software* (`MARS`) is employed (Zanin 2013). `MARS` includes `C++`-based scripts which are built on the `ROOT` environment[9]. The analysis chain is divided into three levels, see Fig. 3.4:

- the *Low-level* in which the `.raw` data of each telescope are converted to `.root` format through the program `merpp`; then, they undergo the calibration and the signal extraction through the program `sorcerer` and finally they are cleaned and parameterized through the program `star`;
- the *Intermediate-level* in which M1 and M2 individual data are combined. The estimation

[9] https://root.cern.ch/ (Brun and Rademakers 1997).

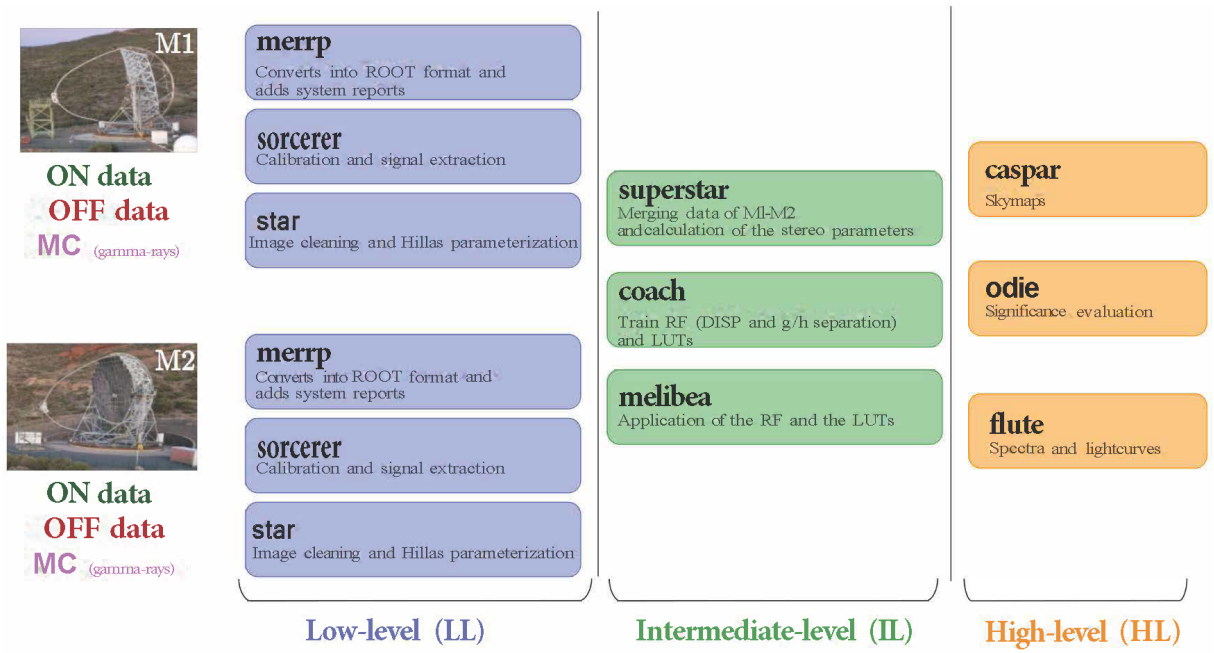

Figure 3.4: Flow chart of the steps of the MARS analysis starting from raw data (on the left) to the high-level scientific results (on the right).

of stereo parameters is performed through the program `superstar` and the *Random Forest* (RF) trained with MC simulations (using `coach`) is applied to the data through the program `melibea`;

- the *High-level* which consists in the calculation of the source's significance (using `odie`), the production of skymaps (using `caspar`) and the derivation of the spectra and the light curves (using `flute`).

At the beginning of the analysis, good-quality data are selected using the program *QUAlity TEster* (`quate`). The selection is mainly based on the transmission and/or cloudiness parameters (weather monitoring, see Subsec. 3.3.2), the trigger rate, the PMT current. Then, the analysis is applied to three types of data: the MC γ-ray data, the data coming from the observed source (ON data) and a sample of pure background data coming from other observations with no evidence of γ-ray signal (OFF data).

The MC data are simulated using the *MAGIC Monte Carlo Simulations* (`mmcs`) software (Majumdar 2005) which is a modified version of the *COsmic Ray SImulations for KAscade* (`CORSIKA`) software (Heck et al. 1998). MC simulations are obtained considering the technical and observational conditions of the telescopes during the specific data-taking. Different MC periods are available depending on the environmental conditions, technical problems or upgrades of the telescopes. The standard MC periods are referred to as ST.XX.YY, where ST stands for stereo, XX is the number associated with a major change in the hardware, and YY refers to the number of a minor hardware's change. Moreover, each MC period includes several simulations reproducing further observational conditions, such as different pointing modes (ON/Wobble), different source extensions (point-like/extended) and different ZD. Four zenith

ranges are available: 0°-35° (low ZD), 35°-50° (medium ZD), 50°-62° (high ZD) and $\geq 62°$ (very high ZD). Also the OFF data are chosen to match as much as possible the observational characteristics of the source (ON) and MC data in terms of zenith angle, extragalactic/galactic observations, dark/moon nights etc.

3.5.1 Low-level analysis

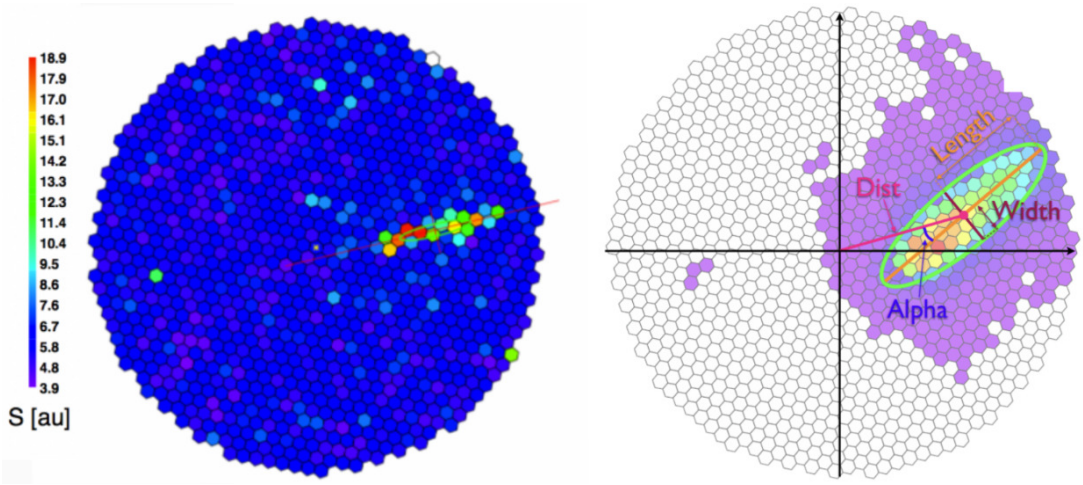

Figure 3.5: Example of a Cherenkov image and image parameterization of a γ-ray shower recorded in the MAGIC camera. Left: Cherenkov image before the image cleaning (Credits: López Coto 2017); Right: some Hillas parameters on top of the Cherenkov image (credits: Fernández Barral 2018).

The analysis starts with the raw data registered by the DAQ in the form of waveform. The raw data are converted into `ROOT` files using the *MERging and Preprocessing Pogram* (`merpp`). During this step, the data are merged with the reports from all the subsystems (e.g. pointing mode, transmission, cloudiness, etc.). Then, the stored intensity and the arrival time from individual pixels are extracted and calibrated by the *Simple Outright Raw Calibration Easy and Reliable Extraction Routines* (`sorcerer`). The baseline signal of the capacitors in the readout system is subtracted using the pedestal subtraction run (see Sec. 3.4). The calibration consists in converting the number of ADC counts into a number of p.e. using the so-called F-factor method (Mirzoyan 1997) on the calibration run (see Sec. 3.4). An example of the resulting charge-calibrated image is shown in Fig. 3.5-left. After the calibration, the *image cleaning* and *image parameterization* are performed using the *STandard Analysis and image Reconstruction* (`star`). The image cleaning allows for the selection of pixels that most likely contain the Cherenkov signal discarding noise-dominated ones. The cleaned Cherenkov image is further processed to better discriminate between the core and the boundary of the EAS signal. The cleaned image from a γ-ray originated shower has a characteristic elliptical shape whereas hadronic showers' images are usually rounded and characterized by multiple clusters of Cherenkov light.

The cleaned image is quantitatively described through the so-called *Hillas parameters* (Hillas 1985) which are crucial in reconstructing the properties of the parent particle in further steps of the

analysis. The Hillas parameters can be divided into different classes: the parameters describing the image shape without taking into account the source location (*Source-independent*), the ones related to the position of the source in the camera (*Source-dependent*), the ones discriminating the typical bright "head" and the faint "tail" of the shower image (*Directional*), the ones related to the arrival time of the Cherenkov photons in the camera (*Timing*) and finally, the parameters describing the general quality of the image e.g. its containment in the camera, the presence of sub-clusters etc. (*Quality*). The most important source-independent parameters are the following:

- *Size*: total charge (p.e.) in the cleaned image ($\longleftrightarrow$ primary energy of the shower);
- *Center of Gravity* (CoG): position of the weighted average of the cleaned charge distribution in the camera plane ($\longleftrightarrow$ shower's core);
- *Conc(N)*: fraction of the total charge inside the N brightest pixels;
- *Length*: semi-major axis of the image ($\longleftrightarrow$ longitudinal development of the shower);
- *Width*: semi-minor axis ($\longleftrightarrow$ lateral development of the shower).

The most important source-dependent parameters are:

- *Dist*: angular distance between the position of the image CoG and the expected position of the source in the camera;
- *Alpha*: angle between the line connecting the expected source position in the camera with the CoG and the ellipse major axis.

An example of some source-independent and source-dependent parameters is shown in Fig. 3.5-right in which the expected source position lies at the camera centre (ON-mode observation). The most important directional parameters are:

- *M3Long*: third momentum (i.e. *skewness*) of the shower image along its major axis (longitudinal);
- *Asymmetry*: sign of the difference between the position of the brightest pixel and the CoG.

The most important timing parameters are:

- *TimeRMS*: Root Mean Square (RMS) of the arrival times of the pixels in the Cherenkov image;
- *Time gradient*: slope of the linear fit of the arrival times distribution of the image's pixels in the coordinate system rotated along the image's major axis.

Finally, the most important quality parameters are:

- *LeakageN*: fraction of the image's size contained in the N outermost pixel rings of the camera;

- *Number of islands*: number of isolated clusters of pixels that survived image cleaning.

Most of the parameters mentioned above are fundamental for discriminating EM and hadronic showers. For instance, *Conc(N)* is usually larger for a primary γ-ray, as the image core tends to be compact. *Alpha*, instead, is usually smaller for γ-initiated showers, because the corresponding image roughly points at the position of the γ-ray source in the camera. On the other hand, hadronic showers tend to come isotropically from all positions in the sky. EM showers are also faster than hadronic ones (*TimeRMS* $\sim$ 3 ns versus $\sim$ 10 ns). And finally, the *Number of islands* is larger for hadronic showers since the related images are more sparse and multi-clustered.

In the low-level analysis, the data coming from each telescope are processed separately and this step is usually performed automatically by the OSA (Subsec. 3.3.1). The intermediate-level analysis consists of the stereoscopic reconstruction of the shower's parameters as explained in the next subsection.

3.5.2 Intermediate-level analysis

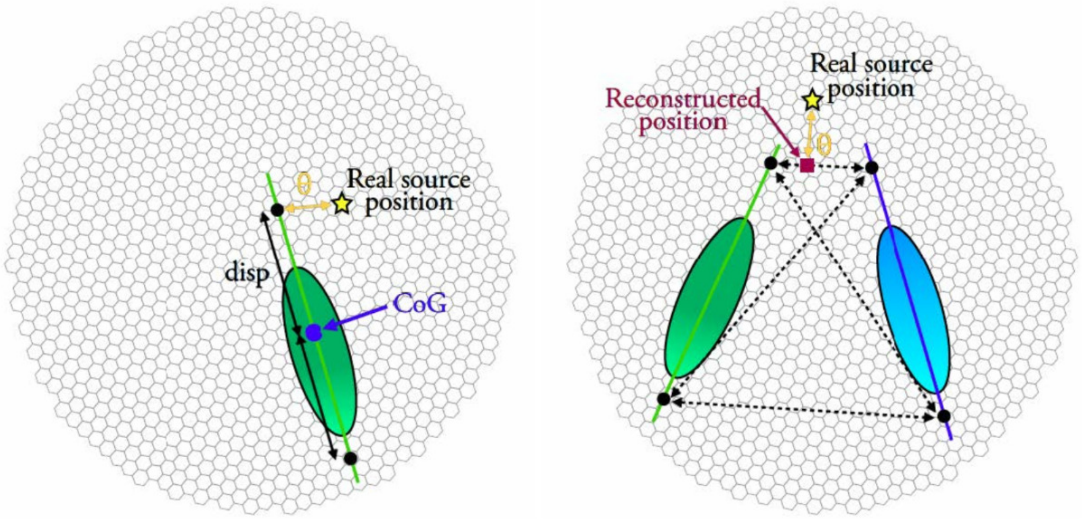

Figure 3.6: Sketch of the *Disp* method for the shower's direction reconstruction. The real source position is also displayed (yellow star). Left: single telescope reconstruction. Right: stereo reconstruction. The four possible pairs are shown (black dots) together with the reconstructed source position (red square). Credits: Fernández Barral (2017).

In the intermediate level of the analysis chain, individual data from M1 and M2 are joined together in a single file using the `superstar` program. `superstar` performs a 3D geometrical reconstruction of the shower starting from the Hillas parameters of the images. The result is a set of *stereo parameters*, the most important are:

- *Impact point*: impact position of the shower on the ground. It is given by the intersection of the two major axes of the ellipses in M1 and M2;
- *Impact parameter*: distance between the telescope pointing direction and the shower axis;
- *Shower axis*: direction of the shower. It is given by the intersection of the two major axes of the ellipses in M1 and M2 taking into account the telescopes' positions and pointings;
- *Height of shower maximum*: height at which the number of EAS's particles is maximum;
- *Cherenkov radius*: radius of the Cherenkov light pool on the ground from an 86 MeV electron at the height of the shower maximum.

The stereo reconstruction is usually performed by the OSA. The analyzers start the off-site analysis taking data from the `superstar` level, performing a first data-quality check (using `quate`, see Sec. 3.5) and then the reconstruction of the arrival direction, of energy of the primary particle and, finally, the γ/hadron separation. These three fundamental steps of the reconstruction involve machine learning algorithms, Random Forests (RFs) and Look-Up Tables (LUTs). The program *Compressed Osteria Alias Computation of the Hadronness* (`coach`)[10] creates the RFs and LUTs. The RFs are created through a multi-dimensional classification algorithm based on the construction of decision trees (Albert 2008) whereas the LUTs are multidimensional tables which store physical quantities (e.g. the energy of the primary particle) as a function of different parameters (e.g. the images' parameters). The RFs are trained with a sample of simulated MC γ-ray showers and a sample of hadronic showers (the OFF data used for the γ/hadron separation) which have to match as much as possible the observational conditions of the ON data, see Sec. 3.5. The *training* sample of MC γ-ray is only a subset of the whole MC data. The rest of the MC data, the *test* MC, is used in the following steps of the analysis[11]. The RF trees are generated considering the Hillas parameters computed on the single images and in stereo.

The **direction reconstruction** is performed through a RF method named *DispRF* (Fomin et al. 1994b, Aleksić, Ansoldi, et al. 2016b). *Disp* is the distance between the source position in the camera frame and the image CoG. Since the major axis of the image represents the direction of propagation of the shower, one side of the image (the image's "head") always points towards the source direction. Therefore the source direction should always lie on the image's axis at the distance Disp from the image's CoG. In particular, the Disp parameter can be estimated from the elongation of the ellipse itself. The DispRF is trained using γ-ray MC, for which the Disp parameter is known. During the `coach` training the RF learns the relation between the Disp parameter and all the other image parameters. For each image, two possible Disp values, one on each side of the ellipse major axis, can be estimated (i.e. the so-called head-tail ambiguity), see Fig. 3.6. In stereoscopic observations with M1 and M2, four possible source directions are found.

[10] `osteria` is the program used in the past for creating RF along with mono data. The *hadronness* parameter refers to γ/hadron separation (see later in the text).

[11] The separation between "training" and "test" MC data is applied in order to have two statistically independent samples.

Then, all the possible directions' pairs are considered, and the pair with the smallest angular distance is selected. The final source direction is estimated by averaging the direction of the selected pair weighted with the number of pixels in the individual image. Therefore, the stereo mode allows for a better reconstruction of the primary direction (see Fig. 3.6-right).

The **energy estimation** is performed either using a LUT (the standard method in MAGIC, see Aleksić, Alvarez, et al. 2012) or a RF (more efficient e.g. for sources emitting at the MAGIC energy threshold). As before, the LUTs are built using `coach` taking the MC γ-ray as input. For building the LUT, the energy of the primary γ-ray is supposed to be proportional to the total charge deposited in the camera, namely the image Size. Also the Impact parameter plays a crucial role because, given a certain primary energy, more distant showers will produce fainter images in the camera (i.e. with smaller Size). Therefore the energy LUTs are binned in Size and Impact parameter and each bin stores the corresponding true energy (E_{mc}) and RMS of the MC primary γ-rays. The estimated energy of a real shower (E_{reco}) is then computed by applying the LUTs to real ON data. E_{reco} is obtained by averaging the values of E_{mc} in the corresponding bins properly weighted with the RMS of each energy bin, for the individual telescope image.

The **γ/hadron separation** is performed with a RF classifier. The algorithm involves an iterative procedure. First, a parameter is randomly selected and the algorithm searches for the parameter's value (i.e. cut value) to best discriminate γ-ray and hadronic showers. Based on the cut value, the initial sample is split into two sub-samples, called *branches*. The cut value is obtained from the minimization of the *Gini index* (Gini 1921)

$$Q_g = \frac{4 N_\gamma N_h}{(N_\gamma + N_h)^2} \quad , \tag{3.1}$$

where N_γ and N_h are the number of γ-ray and hadron events respectively. Starting from the split samples, the algorithm randomly selects a new parameter, and the corresponding cut value is found. The process goes on until a branch contains a pure γ-ray or hadron population (or if the number of events in a sub-branch is below a defined threshold). These ending branches are called *leaves* of the tree. At each leaf a value called *hadronness* is assigned: it is 1 or 0 depending if the leaf contains (more) hadronic or γ-ray events. Usually, at least $N_t = 100$ trees are created to form a *forest* and to reduce the error associated with the γ/hadron discrimination. The data are processed through all the decision trees created in the RF training and, at the end, a hadronness value between 0 and 1 is assigned depending on the selected leaf of each tree. The final hadronness h of the event is given by the average of all the obtained values h_i over the N_t trees:

$$h = \frac{1}{N_t} \sum_{1}^{N_t} h_i \quad . \tag{3.2}$$

This parameter measures how hadron-like is the observed shower, thus, its probability to be a

γ-ray initiated shower is $1-h$. In later stages of the analysis, hadron-like events are rejected setting specific cuts on h.

The RF and LUT estimators resulting from `coach` training are applied to the ON data (observed source) and to the test MC sample using `melibea`. This allows to reconstruct all the three parameters described above for any shower event.

3.5.3 High-level analysis

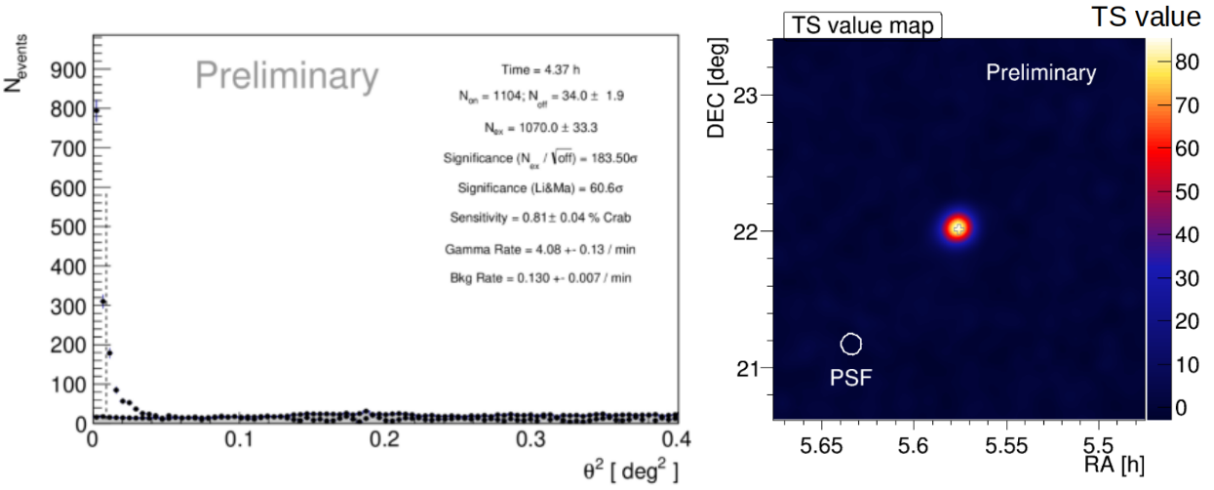

Figure 3.7: Examples of high-level analysis outputs for a Crab Nebula data analysis. Left: θ^2 plot. The grey shaded area at the bottom represents the background distribution, while the black points are signal events. The ON region cut is given by the vertical dashed line on the left. Right: skymap for the Crab Nebula. The x/y axes show the RA/Dec coordinates in the sky and the colorbar indicates the TS (Test-Statistic) value.

Once each event is associated with a hadronness, and a reconstructed direction and energy, the high-level analysis is performed. At this stage, the high-level scientific products for the source under investigation are produced, namely, the signal significance, the skymap, the energy spectrum and light curve. In the following, we will briefly describe how the signal significance and the skymaps are evaluated, keeping the energy spectrum and LC definitions for the next Subsec. 3.5.4.

The **signal significance** is evaluated through the program `odie` computing the θ^2 distribution of the reconstructed events. θ is the angular distance between the reconstructed and the expected source direction for each event. The γ-ray events from a source should accumulate at small θ values, resulting in a peak towards $\theta^2 = 0$ in the θ^2 distribution, see the θ^2 plot of the Crab Nebula in Fig. 3.7-left. The hadronic background events, instead, should be isotropically distributed and populate the θ^2 distribution also at larger θ^2 values. If the source is extended or there are additional γ-ray sources in the FoV, there could be some γ-ray events also for large θ^2 values. These cases require no standard analyses that are not considered here. In the standard

analysis, a cut on θ^2 defines the so-called ON region where the signal from the source is searched for. One or more OFF regions are defined for estimating the background level in the ON region. They are centred at a position where no γ-ray signal is expected and they are usually circles with the same angular radius θ of the ON region, see Fig. 3.3. The definition of more than one OFF regions leads to a better background evaluation. In the standard analysis, the significance is calculated by applying also other cuts on hadronness, image Size, and estimated energy. The cut values are chosen to obtain the best sensitivity for Crab Nebula observations (performed in the same observational period of the source under study) and they are optimized for three different energy ranges: *Low Energy* (LE, up to $\sim$ 100 GeV), *Full Range* (FR, centered at few hundreds of GeV), and *High Energy* (HE, up to the highest energies).

The significance estimation relies on a hypothesis test between the *null hypothesis* H_0, stating that the emission in the ON region is only due to the background, and the *alternative hypothesis* H_1, supporting the presence of the source's emission. The estimation consists of a statistical comparison between the number of ON events (N_{on}) and that of OFF events (N_{off}), both assumed to be Poissonian distributed. The emission excess can be written as

$$N_{ex} = N_{on} - \alpha N_{off} \quad , \tag{3.3}$$

where, for wobble observations, α is the ratio between the number of ON and OFF regions[12]. The signal significance (the so called *Li&Ma* significance) can be estimated following eq. 17 of Li and Ma (1983):

$$\sigma_{LM} = \sqrt{2\left\{N_{on}\ln\left[\frac{1+\alpha}{\alpha}\left(\frac{N_{on}}{N_{on}+N_{off}}\right)\right] + N_{off}\ln\left[(1+\alpha)\frac{N_{off}}{N_{on}+N_{off}}\right]\right\}} \quad . \tag{3.4}$$

If σ_{LM} is larger than 5σ, the VHE detection of the source can be claimed.

The **skymaps** are produced using `caspar`. They are 2D histograms in sky coordinates containing the arrival direction of the γ-rays surviving the LE, FR, or HE analysis cuts. Background estimation is the main challenge for the skymap creation. First, `caspar` generates a camera exposure model. Then, an OFF background map is created taking into account the camera exposure and an ON map using the γ-ray events. The *excess skymap* is obtained by subtracting the background map from the signal one. The *Test Statistic* (TS) *skymap* shows the significance of the signal in the skymap and is computed through a TS which in this case corresponds to the Li&Ma significance of eq. 3.4, see e.g. Fig. 3.7-right. All skymaps are smoothed by the MAGIC PSF and a Gaussian kernel (added in quadrature) to suppress the background fluctuations and highlight the source's emission.

[12]The underlying assumption is that the ON and OFF regions share the same circular shape (radius θ), and the detection efficiency is constant within all of them.

3.5.4 Spectra, lightcurves and flux upper limits calculation

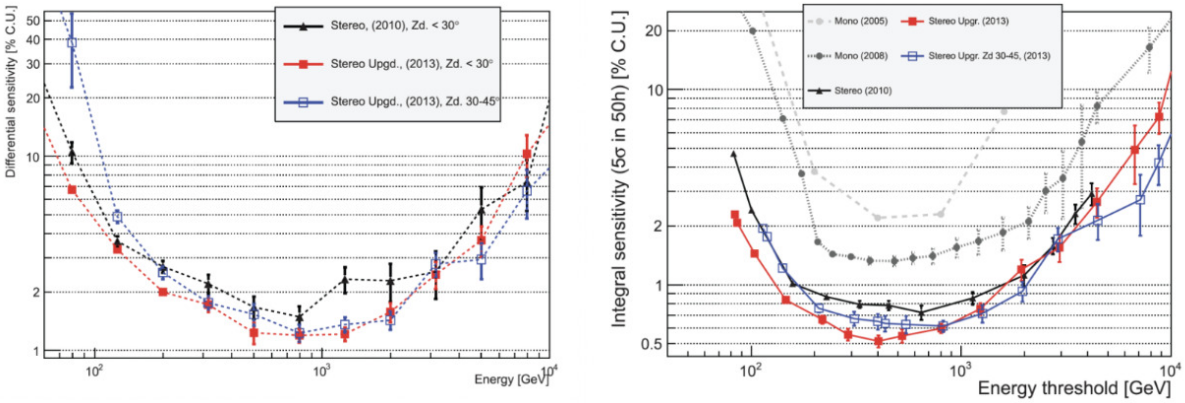

Figure 3.8: MAGIC differential (left) and integral (right) sensitivity after the 2012 upgrade. The curves refer to different years and zenith ranges for mono and stereo observation modes. Mono performance is shown for different readouts (grey and dark grey curves). Credits: Aleksić, Ansoldi, et al. 2016b.

Before proceeding with the spectra and LC computation, we will define the flux sensitivity, the effective area, and the effective observation time. For IACTs, the **flux sensitivity** is defined as the minimum γ-ray flux that can be detected with a significance of 5σ after 50 hours of observations. It is often expressed as a fraction of the Crab Nebula flux (in C.U.). Two types of flux sensitivities can be computed:

- the *differential sensitivity* which is computed optimizing the high-level cuts (θ^2, hadronness etc.) in single energy bins (usually 5 energy bins per decade);
- the *integral sensitivity* which is computed with global optimized cuts above an energy threshold E_{th}.

The differential and integral sensitivities of the MAGIC telescopes (before and after the 2012 major upgrade of the system) are shown in Fig. 3.8. Currently, the MAGIC differential sensitivity is 6.7% C.U. in the lowest energy bin (60-100 GeV) and its integral sensitivity is 0.55% C.U. at few hundred GeV for sources with a Crab-like spectrum[13].

The **effective area** (A_{eff}) is the area of an ideal instrument detecting the same amount of γ-rays as the real detector. It is computed by applying to MC simulations the same cuts used for real data. The definition of effective area is related to the capability of the instrument in collecting photons i.e. its *efficiency* $\varepsilon(E)$ which is the ratio of reconstructed photons to the total number of incoming photons at a given energy. In the energy bin $[E, E+dE]$, the effective area can be expressed as:

$$A_{eff}(E, E+dE) = \varepsilon(E, E+dE)\, A_{sim} = \frac{N_{reco}(E, E+dE)}{N_{sim}(E, E+dE)}\, A_{sim} \quad , \tag{3.5}$$

[13]Note that only the integral sensitivity depends on the source spectrum because the differential sensitivity is computed in small energy bins.

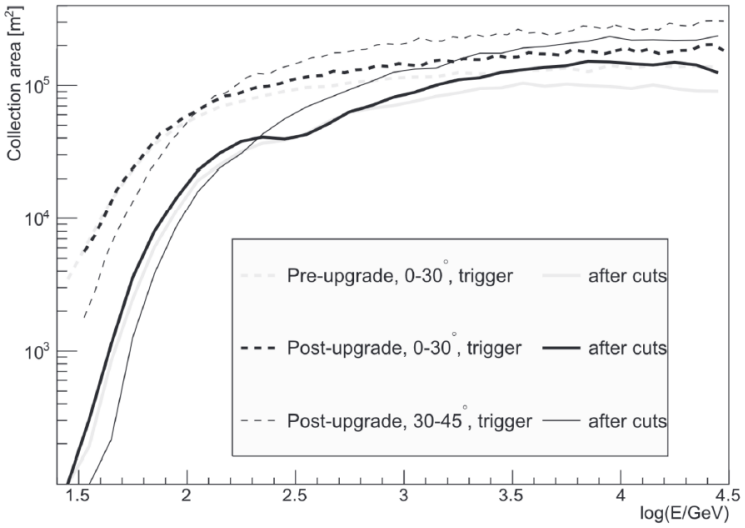

Figure 3.9: Effective areas of the MAGIC telescopes before and after the 2012 upgrade for different ZD (0°-30°). Credits: Aleksić, Ansoldi, et al. 2016b.

where A_{sim} is the geometric area on which the MC showers are simulated and N_{reco} is the number of photons passing the analysis cuts out to the total number of simulated γ-rays, N_{sim}. The effective area mainly depends on the shower's primary energy and on the observation's ZD. The MAGIC effective area before and after the 2012 upgrade is shown in Fig. 3.9.

The **effective observation time** (t_{eff}) is the amount of time during the observation when the telescope is taking data. t_{eff} is a fraction of the total time for which the source has been pointed i.e. the elapsed time t_{el}. In particular, t_{eff} accounts for the so-called *dead time* (t_d) of the telescope, in which MAGIC DRS4 readout is busy processing the event after each trigger. During this time the system does not accept further events and data-taking is stopped. For the MAGIC telescopes $t_d = 26\ \mu$s. Assuming the events' arrival time to follow a Poissonian distribution with event rate λ, t_{eff} can be computed as:

$$t_{eff} = \frac{t_{el}}{1 + \lambda\, t_d} \quad . \tag{3.6}$$

For the computation of the source spectrum and LC, the program *FLUx versus Time and Energy* (`flute`) is employed. `flute` takes as input the MC simulated γ-rays and the ON data. The former are used to estimate the effective collection area of the observation while the latter are used to compute the number of excess γ-ray events. The **differential energy spectrum** of a γ-ray source is defined as the number of γ-ray photons detected per unit surface, unit time, and unit energy[14]:

[14]Note that, hereafter, the reported units are the ones used in MAGIC.

$$\frac{d\Phi}{dE} = \frac{dN_\gamma(E)}{dA_{eff}\, dt_{eff}\, dE} \qquad [\mathrm{cm}^{-2}\ \mathrm{s}^{-1}\ \mathrm{TeV}^{-1}] \quad , \tag{3.7}$$

where $N_\gamma(E)$ is the number of γ-rays emitted from the source at energy E and is estimated as the number of excess events observed by the instrument. The **Spectral Energy Distribution** (SED) is often used instead of the differential energy spectrum. It is defined as

$$E^2 \frac{d\Phi}{dE} = E \frac{d\Phi}{d(\ln E)} \qquad [\mathrm{TeV\ cm}^{-2}\ \mathrm{s}^{-1}] \quad . \tag{3.8}$$

Note that if the differential energy spectrum is a power-law (PL) $d\Phi/dE \propto E^{-\alpha}$ (which is often the case for γ-ray sources), the multiplication by a term E^β has the advantage to enhance the deviations of the source's spectrum from the reference slope β. In particular, the $\beta = 2$ case allows identifying spectral deviations from a source spectrum with $\alpha = 2$ which is the typical slope expected for γ-ray emission from non-thermal processes[15].

The **integral flux** is defined as the integral of the differential energy spectrum above a given energy threshold E_{th}:

$$\Phi_{E>E_{th}} = \int_{E_{th}}^{+\infty} \frac{d\Phi}{dE}\, dE \qquad [\mathrm{cm}^{-2}\ \mathrm{s}^{-1}] \quad , \tag{3.9}$$

If the integral flux is computed on time bins, we have the **light curve** (LC), which shows the integral flux variations over time.

3.5.4.1 Flux upper limits

Whenever a source does not show a significant signal at some energy bins[16], **upper limits** (ULs) on the source flux are estimated. Usually, the calculation is done by assuming a 30% systematic uncertainty in the detection efficiency of γ-rays after analysis cuts and a 95% confidence level (CL). The UL calculation relies on the *Rolke* method (Rolke, Lopez, and Conrad 2005), which provides an estimation of the maximum number of the expected γ-rays by maximizing the following likelihood:

$$\mathscr{L}(\varepsilon, g, b; N_{on}, N_{off}) = \frac{(\varepsilon\, g + b)^{N_{on}}}{N_{on}!}\, e^{-(\varepsilon\, g + b)} \cdot \frac{(\tau\, b)^{N_{off}}}{N_{off}!}\, e^{-\tau b} \cdot \frac{1}{\sqrt{2\,\pi}\,\sigma_\varepsilon}\, e^{-\frac{(\varepsilon - \varepsilon_0)^2}{2\sigma_\varepsilon^2}} \quad , \tag{3.10}$$

[15] For further details about related acceleration mechanisms, see e.g. Chapter 6 of Spurio (2015).

[16] In particular, if the relative error on the estimated flux is larger than 50%.

where ε is the efficiency of the detector, g is the estimated number of γ-ray events in the ON region (which we need to derive), b is the estimated number of background events in the OFF region and τ is the ratio between the OFF and ON exposure. In particular, the first two terms of eq. 3.10 describe the signal and the background (which are assumed to have a Poissonian distribution) and the third one represents the detection efficiency (which is assumed to have a Gaussian distribution with mean $\varepsilon_0 = 1$ and standard deviation $\sigma_\varepsilon = 0.3$). τ, ε and b are considered nuisance parameters and the profile likelihood ratio $\lambda_p(g; N_{on}, N_{off})$ is considered. A likelihood ratio test is performed to estimate g, namely, the quantity $-2\ ln(\lambda_p)$ is minimized. Once g is computed through the Rolke method, an UL on the flux can be found. The source spectrum is assumed to be proportional to a certain spectral shape $S(E)$:

$$\frac{d\Phi}{dE} = k\, S(E), \tag{3.11}$$

where k is the normalization. The maximum number of expected events N_{UL} can be translated into an UL for the normalization k. From the definition of integral flux (see eq. 3.9) and equating eqs. 3.7 and 3.11, we have:

$$\Phi(E > E_0) = \int_{E_0}^{+\infty} \frac{d\Phi}{dE}\, dE = k \int_{E_0}^{+\infty} S(E)\, dE = \frac{N_{UL}}{t_{eff} \int_{E_0}^{+\infty} A_{eff}(E)\, dE} \quad , \tag{3.12}$$

thus

$$k_{UL} = \frac{N_{UL}}{t_{eff} \int_{E_0}^{+\infty} S(E) A_{eff}(E)\, dE} \quad . \tag{3.13}$$

The integral flux UL is then:

$$\Phi_{UL}(E > E_0) = k_{UL} \int_{E_0}^{+\infty} S(E)\, dE = \frac{N_{UL} \int_{E_0}^{+\infty} S(E)\, dE}{t_{eff} \int_{E_0}^{+\infty} S(E) A_{eff}(E)\, dE} \quad , \tag{3.14}$$

while the differential energy flux UL is

$$\frac{d\Phi_{UL}}{dE} = \frac{N_{UL}\, S(E)}{t_{eff} \int_{E_0}^{+\infty} S(E) A_{eff}(E)\, dE} \quad . \tag{3.15}$$

The energy bins should be narrow enough to avoid $S(E)$-dependent deviations, but sufficiently wide to include enough events and ensure the reliability of the ULs.

Chapter 4

Observational campaign of TON 116

This chapter is dedicated to the latest insights about the extragalactic source which we concentrated on for the present work, i.e., TON 116. Firstly, we provide the main motivations that led to the choice of TON 116 as an outstanding target to be studied. In particular, we stress the relevant role represented by TON 116 in the investigation of the *outliers* of the blazar sequence (Sub-subsec. 1.3.6.1). A "historical" overview is also given, starting from the very first time at which the source was discovered, and describing how the knowledge about its spectral and temporal properties evolved over time, up to now. Secondly, we provide an extensive description of the observations' analysis performed with major telescopes, spanning from optical to VHE γ-rays. We will present our VHE results related to the MAGIC telescopes, obtained by means of the standard analysis chain (Sec. 3.5). Then, we will put TON 116 in an MWL context by comparing the MAGIC outcomes with data from the other energy bands considered in this thesis work. All of these samples will allow us to study the broadband behaviour of our source of interest, and to model its SED by still including TON 116 within the discussion on the outliers of the blazar sequence.

4.1 The case of TON 116 as a sequence outlier

The blazar sequence represents one of the most intriguing but also most debated topics among the AGN scientific community. Indeed, as seen in Sub-subsec. 1.3.6.1 and 1.3.6.2, its appearance onto the scientific stage triggered an intense discussion going on over time. This basically led to an actual separation between groups supporting it (at least in a revised version, Ghisellini, Righi, et al. 2017), and groups somehow rejecting it (for selection or no-forbidden-zone reasons, e.g. Giommi et al. 2012, Keenan et al. 2021). One of the main aims of this thesis is to clarify the existence of the claimed trend in a MWL context, combining observations in the VHE regime with data at the lower energy bands. In order to study the so-called *blazar sequence outliers* for understanding if the blazar sequence is a feature of blazars or not, TON 116 has been selected as

a promising candidate since its location in the HE luminosity versus synchrotron peak frequency (Fig. 4.1).

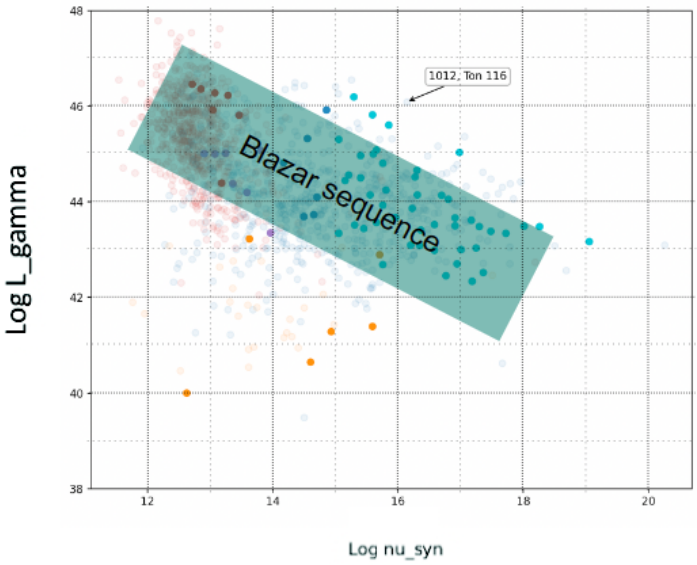

Figure 4.1: Log-scale scatter plot with estimated 0.1-100 GeV luminosity (y-axis) versus synchrotron peak frequency (x-axis) for the 4LAC catalogue sources (Ajello et al. 2020). Red and blue dots are FSRQs and BL Lacs respectively, orange dots are radiogalaxies, filled circles are TeV-detected sources. The highlighted strip represents the mean blazar sequence trend, while the arrow indicates the position of TON 116, our case study source (see text). Adapted from C. Righi (MAGIC proposal C16-18). Former figure in Keenan et al. (2021).

In order to somehow test the blazar sequence, our idea was to spot some "outliers", i.e., sources eventually showing an unexpected behaviour with respect to the one imposed by the sequence itself, but not only. Since the γ-ray band, especially the VHE part, has a key role for the comprehension of the blazar class, the opportunity to fully characterize the emission behaviour at the most extreme energies of the electromagnetic spectrum is given by the selection of targets which are well accessible by IACTs, in particular by MAGIC. We specifically concentrated on BL Lac objects since these sources seem to be the ones actually following a redder-when-brighter trend, yet assumed to be typically fainter (Sub-subsec. 1.3.6.1). In particular, we referred to the 4LAC *Fermi*-LAT Catalogue (Ajello et al. 2020), and we selected, among the BL Lacs listed therein, TeV-emitter candidates fulfilling $\nu_{p,s} > 10^{15}$ Hz and $L_{HE} > 10^{46}$ erg/s. Note that the former condition stands for HBLs (Subsec. 1.3.6), while the latter is a hint of the γ-ray (HE) trend as inferred by *Fermi* satellite. The combination of the two does indeed belong to a region not foreseen by the standard blazar sequence expectations (see Fig. 4.1). As a result, we selected 9 candidate sources. However, we noted that on average they are associated with high redshifts in the *Fermi* catalogue, reaching a value of around 1 in the most extreme cases, which turned out to be not reliable for many of them. Of course, these controversial distances have a serious impact for a certain source to be regarded as a real outlier of the blazar sequence. Indeed, there

could be fictitious cases of particularly luminous sources, but simply because they are closer (and viceversa). This very fact represents the fundamental blazar-related enigma that we wanted to investigate. Combining high state plus high redshift, with the additional constraint of being a good target for MAGIC, the number of candidates decreased to just two, namely, 1H 1515+660 and TON 116.

We decided to drive our attention to TON 116: this source has not only been assigned a high state at HE γ-ray band from the 4LAC catalogue, with supposed $z \approx 1$, but currently it is also associated with a smaller redshift limit ($z > 0.483$, see below). Our main purpose was to solve the uncertainty related to the distance of the source, applying the method developed by Prandini et al. 2010 (Sub-subsec. 1.3.6.3) provided a detection at VHE with MAGIC telescopes. This is expected to clarify a proximity-related, or an intrinsic-driven, enhanced emission, so that the outlier hypothesis can be rejected or confirmed respectively. As it will be clear further in the text, a preliminary inspection carried out in 2021 and 2022 with MAGIC led to a probable excess in the lower VHE bound, which we considered as an interesting clue to be better investigated (Subsec. 4.2.3). What made TON 116 an intriguing object to us is also the fact that, despite actually discovered in the late 1950's, it got somehow undeservedly shrouded in mystery since then (see next Subsec. 4.1.1). This is likely because its optical spectrum does not essentially show any apparent feature, so that in some way, deeper systematic studies as well as prompt cross-identifications were inhibited for a long time. In fact, the first real estimate, or rather lower limit, on its redshift was provided only quite recently, thanks to an optically-selected sample of BL Lac candidates from the 7th SDSS data release (Plotkin et al. 2010). In order to give a more complete picture of the selected source, wisely keeping in mind a MWL perspective, we review some of the most important observational achievements obtained so far, before moving to present and discuss current results.

4.1.1 Historical overview

The 116th object detected by means of the OANTON Schmidt telescope, namely TON 116, was firstly reported in one of the Observatory bulletins (Iriarte and Chavira 1957), basically the opening document of the whole TON catalogue (see Appendix A for further details). The source is located in the Canes Venatici constellation, at coordinates RA $= 12\,\mathrm{h}\,43\,\mathrm{m}\,12.7\,\mathrm{s}$ and Dec $= 36^\circ\,27'\,44.0''$ using the current J2000 absolute system[1] (the J1950 was originally used). The authors described TON 116 as a decidedly violet star having a photographic magnitude $m = (15.7 \pm 0.5)$ mag. The "decidedly" designation means that the object showed quite a strong UV-yellow intensity ratio, such that it was compatible with a star-type earlier than an absorption-dereddened A0. Like for all the other objects of the TON catalogue, a finding chart was also provided, which is visible in Fig. 4.2.

[1] In decimal units 190.803 and 36.462 respectively, from *NASA/IPAC Extragalactic Database* (NED, https://ned.ipac.caltech.edu/).

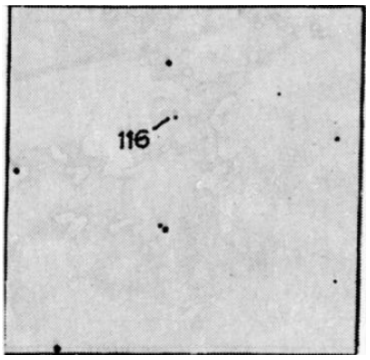

Figure 4.2: Identification sky chart of TON 116 included in the first detection document (Iriarte and Chavira 1957).

The second official detection was in the radio domain (third B2 radio survey, Colla et al. 1973), thanks to the Northern Cross Telescope located in Medicina, Bologna (Italy), which assigned TON 116 a 0.30 Jy peak flux[2] at a centred frequency of 408 MHz. However, both flux and coordinates were marked as particularly uncertain due to confusion effects between close radio sources. Fifteen years later, TON 116 was detected in the radio band again, during the compilation of the second part of the 6th Cambridge (6C) radio catalogue. Observations at 171 MHz with improved resolution, but still large positional error, allowed to obtain a peak density of 0.55 Jy (Hales, Baldwin, and Warner 1988). In 1990, the second MIT-Green Bank survey (MG) with the National Radio Astronomy Observatory (NRAO) confirmed TON 116 as having radio source properties (Langston et al. 1990). With a detection band centered at 4 830 MHz, a flux value of (91 ± 9) mJy was estimated (signal-to-noise ratio $S/N = 12$). Moreover, a first indication about the spectral index, assuming that the spectrum be described by a power-law in the range 1 400 MHz-4 830 MHz was included ($\alpha = -0.07$), albeit challenged by confusion effects again. The related paper also helped in the identification, providing both the J1950 coordinates and the new J2000 just one beside the other for convenience. Later on, Pesch, Sanduleak, and Stephenson (1991) reported about a UV-optical survey with the Burrell Schmidt Telescope at Kitt Peak, using low-dispersion objective-prism plates (spectral range 3 300-5 350 Å approximately) and detailed literature search. TON 116, referred to with this original name therein, showed an indicative magnitude of 16 mag, and likely due to low resolution, was included among the unresolved blue, rather flat, featureless sources. It was actually considered as a potential quasar, but no real proof about its nature was available.

A major step came in the X-ray band from ROSAT: its all-sky survey bright source catalogue (RASS-BSC) was obtained from data taken at the very starting of the satellite activity in 1990-1991 and revised later on, ending in the 1RXS version (Voges et al. 1999). In the spectral range 0.1-2.4 keV, a significant TON 116 rate was found of about 1.3 counts per second (roughly 130 erg cm^{-2} s^{-1}). Then, a radio-optical selection (combining VLA FIRST survey and APM catalogue of 1st Palomar Observatory Sky Survey respectively) of bright quasars, known as FBQS, was performed by White et al. (2000), in which our source was included. In particular,

[2] 1 *Jansky* := 10^{-26} W Hz^{-1} m^{-2}.

TON 116 was classified as a BL Lac object due to a featureless spectrum, with stellar-like visible appearance (both B and R emission between 16 and 17 mag). In the radio domain, quite a remarkable flux emerged: more than 100 mJy at 1 400 MHz, with a loudness $R_\ell \approx 160$.

In 2010 two redshift determinations were attempted for TON 116, $z \geq 0.485$ and $z = 0.50$. The first came from Plotkin et al. (2010), which presented a huge sample of BL Lac candidates, optically-selected by means of the Sloan Digital Sky Survey (SDSS, 7th data release) ensuring a high-quality spectrum for all of the entries (significantly matching either FIRST/NVSS radio or ROSAT X-ray targets). Our source was classified as a high-confidence blazar (i.e. showing a clear continuum against eventual features), thus a reliable EW classification as a BL Lac object (Subsec. 1.3.6) was pointed out. In figure 8 (bottom left panel) of the paper, the authors also showed TON 116 spectrum itself, in which an intervening MgII absorption doublet was found, allowing for a lower limit (see Subsec. 1.3.6 again) $z \geq 0.485$. Shortly after, Meisner and Romani (2010) worked with WIYN telescope on high-quality marginal detection of host galaxies related to a sample of BL Lac objects out of the radio CRATES catalogue (focus on *Fermi*-LAT sources or possible counterparts). A redshift of 0.50 came out for our source in such a study. In 2014, an emission in mid-IR bands was reported by D'Abrusco et al. 2014 for TON 116. The paper presented a catalogue of 7 855 radio-loud blazars, likely γ emitters too, which were detected in all the four spectral filters of WISE satellite. The wavelengths of the filters were 3.4, 4.6, 12, and 22 μm, and the targets presented a positive cross-match with the position of sources in either NVSS, FIRST, or SUMSS radio surveys.

4.1.2 Hot current topics

Nowadays, TON 116 firmly figures as a BL Lac object (BZB J1243+3627) in the Roma-BZCat catalogue (5th edition)[3]. This is a huge list of blazars with the primary goal to provide a complete, up-to-date, multi-frequency view for each single entry, in order to allow for nature-oriented studies about them, as well as facilitate the search for counterparts in the modern network of observational instruments (see e.g. Massaro et al. 2015 and references therein).

In order to properly characterize both the emission properties at the source, and the attenuation of the radiation along the path to us, an accurate distance determination would still be highly desirable. The most recent estimation yielded $z > 0.483$, from a spectroscopic campaign by Paiano et al. (2017) on a sample of TeV (or TeV candidate) BL Lac objects with the *Gran Telescopio Canarias* (GTC)[4]. This redshift derivation basically comes from the confirmation of the intervening MgII absorption feature previously noticed by Plotkin et al. 2010 (Fig. 4.3). On the other hand, the high HE state derived from the *Fermi* 4LAC catalogue (Ajello et al. 2020) assumed z to be around unity. As outlined above, here our goal is to clarify the nature of TON 116, and in particular, a detection at VHE would greatly shed light on whether it is a true

[3] https://www.ssdc.asi.it/bzcat5/ .

[4] https://www.gtc.iac.es/ .

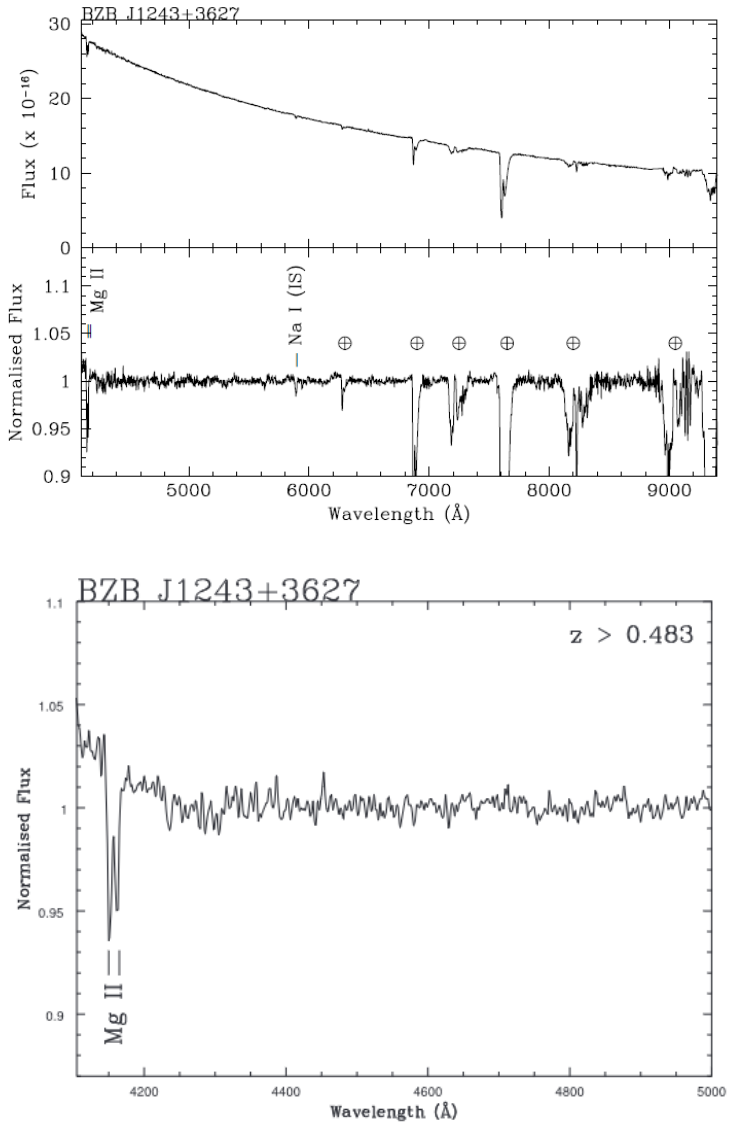

Figure 4.3: *On top*: flux-calibrated, dereddered (top panel) and normalized (bottom panel) spectrum of TON 116 recently obtained at GTC. "⊕" symbol indicates the main telluric bands, while "IS" indicates galactic absorption lines. A featureless trend is visible for our source, except for a MgII absorption doublet at the lower threshold. *At the bottom*: close-up of the TON 116 normalized spectrum, more clearly showing the MgII absorption doublet at around 4 160 Å (observed EW $\approx$ 0.90 Å), from which the latest redshift limit was derived ($z > 0.483$). Plots taken from Paiano et al. (2017).

outlier of the blazar sequence (Prandini et al. 2010 redshift estimation). If so, this source would not only be an unexpectedly luminous BL Lac object, but also one of the farthest ever observed at these extreme energies. Therefore, it could also be helpful in constraining EBL absorption (Sec. 1.2) occurring throughout cosmological distances. As an additional perspective, provided that our selected target is a HBL, a significant density of the X-ray photon field is expected, which could represent a valid target for the production of PeV neutrinos (Sub-subsec. 1.4.2.3).

On the other hand, we thought that a non-detection could be useful as well, because thanks to a deep enough exposure, one is given the possibility to effectively constrain the blue tail of the IC peak of TON 116, which was still unknown before this thesis. The only solid hint about the

latter spectral curve was provided by *Fermi*-LAT satellite, which revealed HE emission since the first years of operation; this also contributed for TON 116 to be regarded as a likely TeV-emitter.

In 2020, for the MAGIC observing campaign (Cycle 15), TON 116 was proposed as a potential candidate to shed light on the blazar sequence long-standing discussions, in particular related to its outliers (Sec. 4.1). In this context, a very preliminary *Fermi*-LAT analysis[5] was computed in order to extrapolate the VHE spectrum. In particular, since the *Fermi*-LAT sensitivity at hundreds of GeV is lower with respect to MAGIC one, the evidence of upper limits at those energies allowed us to fit the source with a simple power-law spectral shape (see Fig. 4.4). As a consequence, the estimated spectrum was considered to simulate 50 h of MAGIC data, with redshift equal to 0.6 and cut-off at 200 GeV as further conservative assumptions. Fig. 4.5 shows such expectations, where we also included LST-1, currently the only Large Size Telescope of the CTA array already in operation (Subsec. 2.3.3), as its addition could be beneficial due to an overall improved sensitivity.

In the next part of the chapter we present a detailed description of how did MAGIC and other telescopes recently explore the SED of the blazar TON 116.

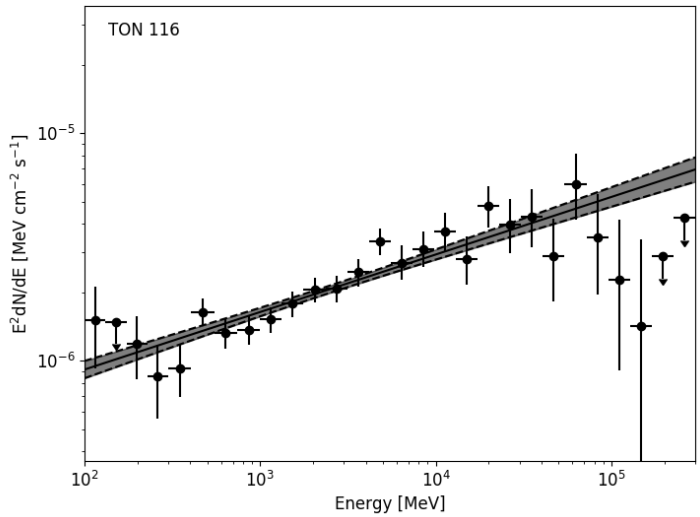

Figure 4.4: Very preliminary analysis of TON 116 (MAGIC proposal C18, 2022). The HE trend shows a spectral index $\Gamma \approx 1.75$ in the 100 MeV-300 GeV range, with a flux $F_{1\,\mathrm{GeV}} \approx 1.64\,\mathrm{MeV\,cm^{-2}\,s^{-1}}$. The overall behaviour suggests an IC bump peaking around 70 GeV, above which, despite larger instrumental uncertainties, the distribution seems to fade off.

4.2 MAGIC observations and data processing

From the MAGIC site, TON 116 is mostly visible between January and May every year (roughly 4 hours per night), with March-April as the best period. The source was observed for three years

[5]A detailed analysis of *Fermi*-LAT data is presented in Subsec. 2.3.1.

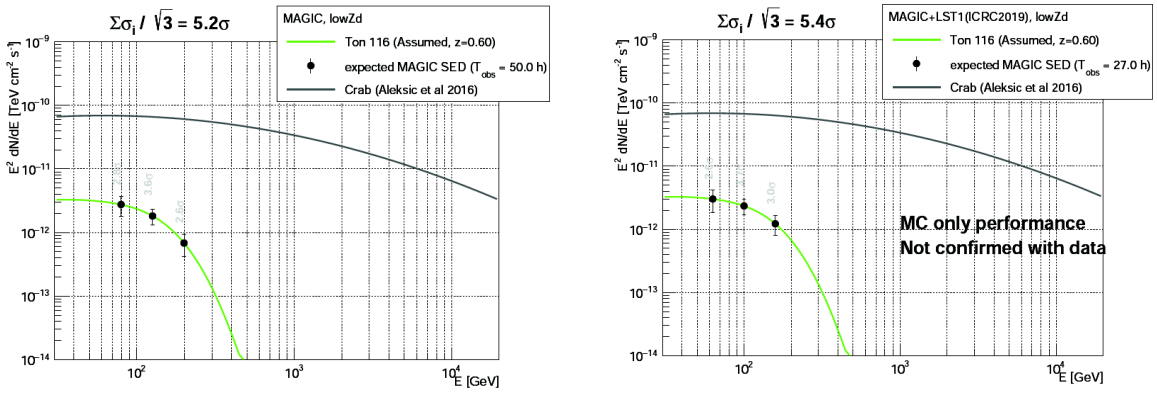

Figure 4.5: VHE flux of TON 116, extrapolated from the *Fermi*-LAT power-law spectrum, for MAGIC (left) and MAGIC + LST-1 (right). The plots are obtained assuming 50 h and 27 h of data respectively, $z = 0.6$, and a cut-off at 200 GeV.

accordingly, from 2021 to 2023. The adopted analysis procedure is divided in two main steps:

i) preliminary significance results on data taken in 2021 and 2022 (MARS V2.19.14, ROOT 5.34/38);

ii) preliminary significance results on data taken in 2023, and VHE upper limits on the flux of each single year of observation (2021, 2022, 2023) and on the flux of the total period of observation, with improved RF for 2022 (MARS V3.0.1, ROOT 6.26/10).

4.2.1 2021 dataset

The main characteristics of TON 116 data taken by MAGIC in 2021 (Cycle 16) are collected in table 4.1. In particular, the first column hosts the date of observation (year-month-day format), the second one the zenith distance range (in degrees), the third one contains some information about the observation status (such as eventual bad weather, main technical issues etc.), while the last one shows an estimate of both the selected ("Sel.") and the whole observation time ("Tot.") for that night (hour unit). If the conditions are simply labelled as "Ok", no serious anomaly (weather- or detector-related) arose during the correspondent night of observation. If this was the case instead, but still TON 116 data are to be considered not directly affected by it, then some indication does just appear in parentheses. On the contrary, if something heavily affected the source data-taking itself, the main issue is reported. Given the great importance of atmospheric transmission at 9 km, here indicated as "LIDAR", for the reconstruction of the primary γ-ray signal (Subsec. 3.3.2), we briefly include this information whenever it was not showing optimal values (namely, "low" means less than 0.7), was not properly working (giving some error, and eventually restarted or stopped), or was not used at all ("no LIDAR"). We stress that here all the

observations were done with both M1 and M2 (i.e. "Stereo" data), wobble mode (0.4° offset), Dark Extragalactic DTs, and standard L3 trigger. Regarding flux values reported by MOLA, in general no significant γ-ray emission was found for any of the nights, not in LE nor in HE. However, for the sake of completeness, just a few non-zero values occurred ("*" symbol beside the observation time). Namely, on 13rd February a HE flux of 0.05 C.U. with 3.1σ significance was reported in the runbook by shifters, and on 3rd June an identical flux value appeared, but most likely they are just background fluctuations. On 1st June no value was reported, but still no further hint of any signal was present.
In general, TON 116 observations were carried out under very good conditions in 2021. For a preliminary quality check we specified, besides the low zenith bounds (0°-35°), the PMT direct current (DC) maximum value to be 3 000 nA, and the minimum aerosol transmission at 9 km to be 0.7. The latter involved missing LIDAR data, which in case are replaced with a cloudiness value provided by the pyrometer, set to be 30 at maximum. We also use the same cloud cut as a standalone, in order to improve the quality of the source data. The selected time is 17.8 h out of about 18.7 h, which represents a confirmation of the goodness of data conditions, given that only some 5% (roughly 1 h) of the total observation time was discarded from further analysis.

For Monte Carlo data, we had to refer to ST.03.16 period, ranging from 20th October, 2020 to 30th December, 2021. The period started from the cleaning of the telescope mirrors by the October 2020 storm, and ended due to the last, big volcanic eruption in La Palma[6]. The ST.03.16 MC files are the same as the ST.03.12 ones, given the very similar performance of the MAGIC telescopes within the two periods. We used the MC superstar files for point-like sources at low zenith angle (0°-35°), according to the properties of our source. Moreover, we chose the LUT method (Subsec. 3.5.2) for the energy estimation. For the analysis validation of the RF and LUT associated with ST.03.16 MC period, we address the reader to Appendix B. The θ^2 plots, obtained with standard cuts according to the standard settings listed in table 4.2, are shown in Fig. 4.6. It is evident that TON 116 was not flaring in any of the three energy ranges (LE, FR, HE, Subsec. 3.5.3) during 2021 observations.

4.2.2 2022 dataset

The very preliminary analysis of TON 116 data involves also those taken in the first half of the year 2022. As previously done, we report the main characteristics of that set in tab. 4.3. The technical configuration employed by the MAGIC telescopes for the observation of the source is exactly the same as before, i.e., stereo wobble mode, with Dark Extragalactic DTs, and standard L3 trigger. Again, MOLA never reported a significant signal, except on 3rd March, when a HE γ-ray flux compatible with 0.1 C.U. was found. However, most likely it was just another random fluctuation.

[6]The erupting activity was located at *Cumbre Vieja* volcano, $\approx$ 15 km away from the Roque de Los Muchachos. The observation site was safe, but the local damages were many, and dust reached very high levels. MAGIC rails were covered to protect them against aerosol effects, and operations were stopped for about three months.

Table 4.1: Main characteristics of TON 116 data taken by MAGIC in 2021. Each column of the table reports details about every single night of observation: the first on the left contains the date, the second the zenith distance in degrees, the third some brief information about the overall condition, the fourth the observing time in hours. Condition can refer either to weather or detector, mainly: LIDAR = atmospheric transmission at 9 km ("low" if less than 0.7, "no" if not available), Hum. = high humidity (90% reached), cloud. = cloudiness parameter above 30 ("moderate"/"high" if less/larger than 45), high PSF = Point Spread Function value higher than expected (if about 11 mm or more in M1 or M2). Some further indication on bad weather (e.g. wind, dust, clouds, rain) or subsystem failure (DAQ, AMC, LIDAR etc.) is accounted for as well. In case condition at least "Ok", no serious issue during TON 116 observation. Regarding time, "Sel." means selected for analysis, "Tot." means total. For completeness, "*" indicates non-null flux by MOLA (likely background signals).

Date	*ZD* [deg]	*Condition*	*Sel./Tot. Time* [h]
2021-02-13	9.4 - 19.5	Ok (no LIDAR, DAQ restored)	0.8 / 0.8*
2021-02-14	7.6 - 10.0	Ok (no LIDAR)	0.7 / 0.7
2021-02-15	9.5 - 9.8	Wind	0.1 / 0.1
2021-02-16	7.2 - 19.1	Ok (no LIDAR)	1.6 / 1.6
2021-02-19	12.4 - 19.1	Ok (LIDAR error, DAQ and AMC restarted)	0.6 / 0.6
2021-02-22	16.1 - 21.4	Ok (hum.)	0.5 / 0.5
2021-03-11	26.3 - 35.7	Ok (wind)	0.7 / 0.7
2021-03-12	7.6 - 27.2	Ok (final clouds)	2.8 / 2.8
2021-03-18	7.6 - 10.3	Ok	0.8 / 0.8
2021-03-19	7.9 - 16.3	Ok	0.9 / 0.9
2021-04-10	7.6 - 8.1	Ok (clouds)	0.2 / 0.3
2021-04-16	8.8 - 11.1	Ok (hum., rain)	0.3 / 0.3
2021-05-04	9.0 - 19.3	Ok	1.0 / 1.0
2021-05-05	9.7 - 19.0	Ok (LIDAR restarted)	0.6 / 0.6
2021-05-07	7.6 - 18.5	Ok (LIDAR stopped)	1.6 / 1.6
2021-05-09	7.2 - 10.7	Ok (final hum.)	0.8 / 0.8
2021-05-10	7.6 - 19.0	Ok	1.5 / 1.6
2021-05-11	9.8 - 19.5	Ok	1.0 / 1.0
2021-05-13	9.7 - 18.3	Ok (low LIDAR)	0.4 / 0.9
2021-06-01	15.8 - 19.3	Ok	0.3 / 0.3
2021-06-03	17.3 - 20.9	Ok (hum.)	0.3 / 0.3*
2021-06-05	17.8 - 21.4	Ok	0.3 / 0.3

Table 4.2: Main odie values used for standard derivation of θ^2 plots (LE, FR, HE energy ranges) for MAGIC TON 116 observations. The first column is the zenith distance, the second column is the angle of wobble offset with respect to the camera center, the third column is the number of OFF regions, the fourth column is the σ value of PSF containment, the fifth column is the dead time. See Subsec. 3.5.3 for further details.

	ZD	Wobble offset	Wobble OFFs	psf40	t_d [μs]
LE	5°-35°	0.4°	3	0.056	26
FR	5°-35°	0.4°	3	0.046	26
HE	5°-35°	0.4°	3	0.037	26

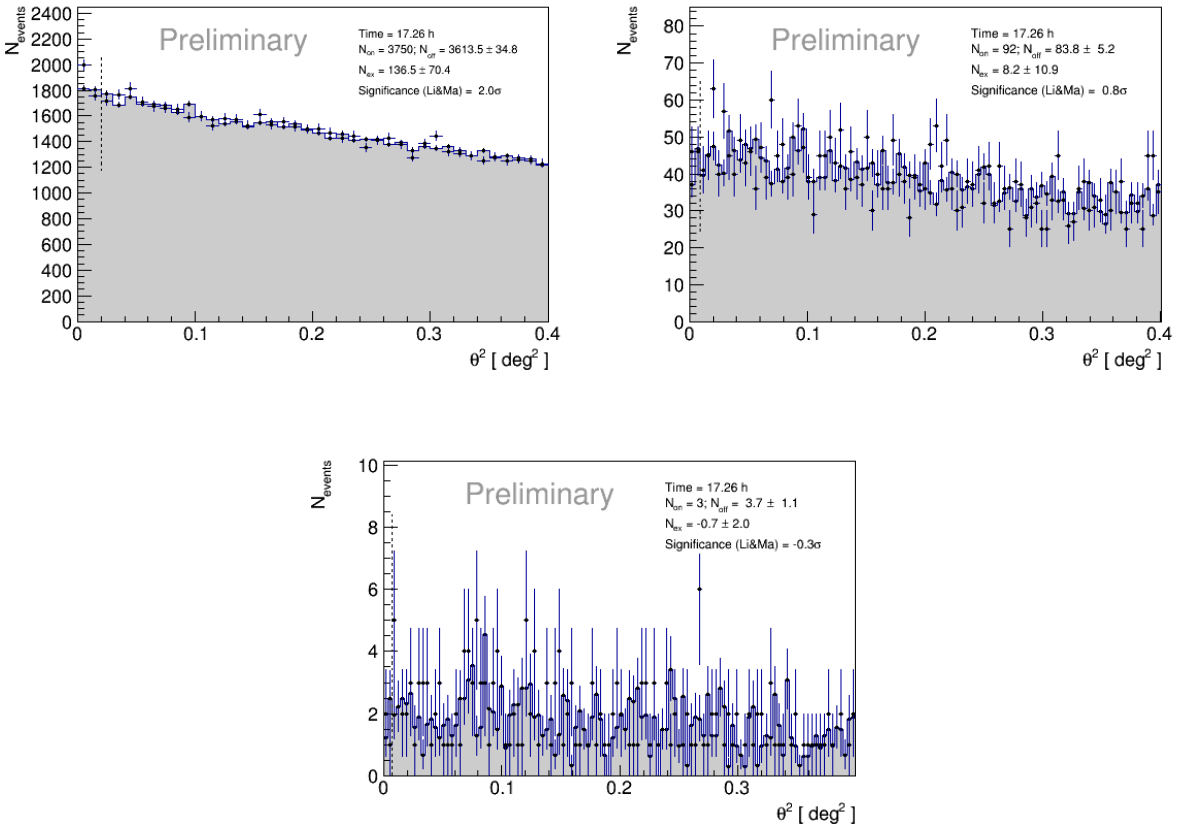

Figure 4.6: odie θ^2 plots related to the TON 116 data taken in 2021, for all the three energy ranges (LE top left, FR top right, HE bottom).

Table 4.3: Main characteristics of TON 116 observational data by MAGIC in 2022. The arrangement is the same as in table 4.1.

Date	*ZD* [deg]	*Condition*	*Sel./Tot. Time* [h]
2022-01-30	7.6 - 8.5	Ok (high PSF)	0.3 / 0.5
2022-03-03	26.1 - 35.4	Ok (high PSF)	0.7 / 0.7*
2022-03-05	18.6 - 27.0	Wind	0.4 / 0.4
2022-03-06	19.8 - 31.0	Ok	1.0 / 1.0
2022-03-09	11.7 - 18.2	Ok (low LIDAR)	0.2 / 0.6
2022-04-20	20.2 - 22.5	Wind	0.2 / 0.2
2022-04-28	10.1 - 20.6	Ok (no LIDAR)	1.0 / 1.0
2022-05-01	7.9 - 20.9	Ok (no LIDAR)	1.3 / 1.3
2022-05-02	7.6 - 26.9	Ok (no LIDAR)	1.9 / 1.9
2022-05-29	28.6 - 32.3	Ok	0.3 / 0.3

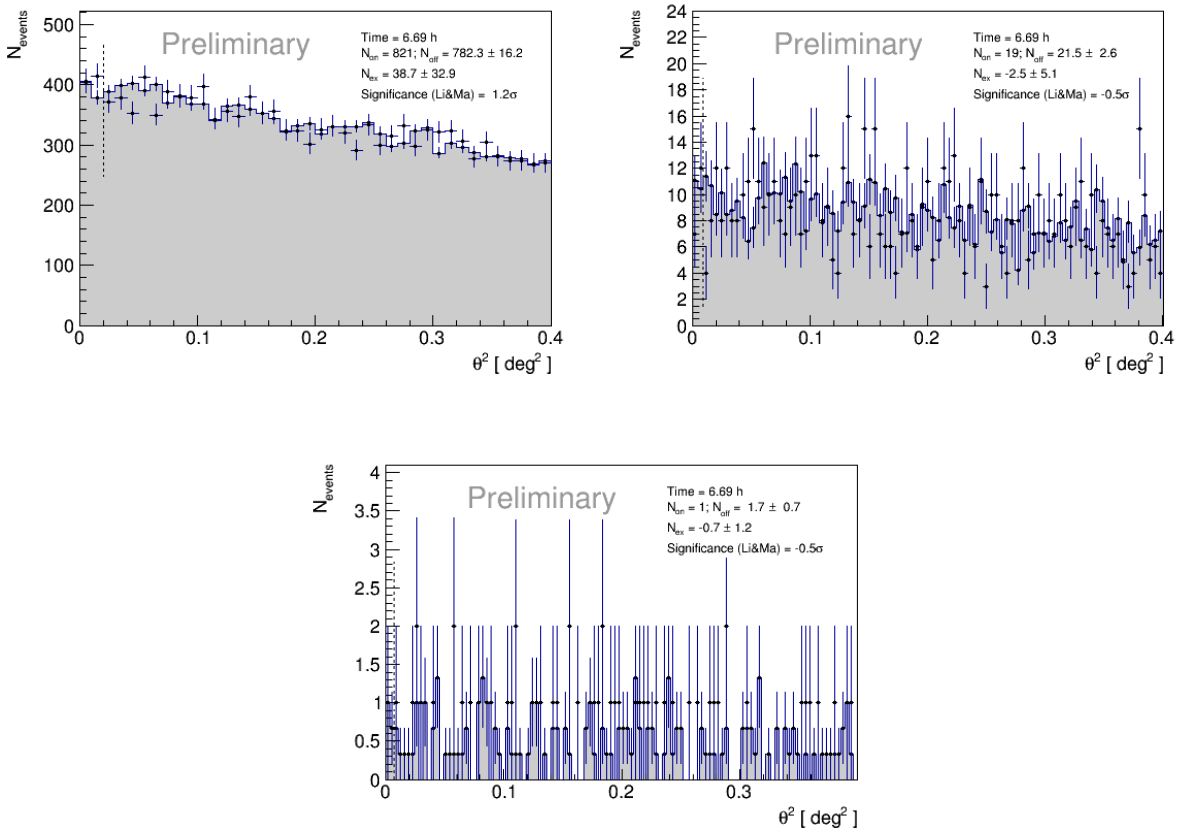

Figure 4.7: odie θ^2 plots of TON 116 data taken in 2022 (LE top left, FR top right, HE bottom).

The data selection, under the same high quality settings as before, led us to save about 7 h out of 8 h. Thus, the overall conditions for 2022 were quite good as well[7]. As a first simple check of this dataset, we used the RF results already obtained for the *Flare Advocate* (FA) activity performed during the P239 MAGIC period (18th April - 14th May, 2022). In that case, the ZD considered was 5°-62° (so-called "fat" range[8]), whereas the reference Monte Carlo set is ST.03.17. The latter is valid from 30th December, 2021 to 9th June, 2022, and takes into account the fact that the reflectivity of M1 got worse still due to the last volcanic eruption. Again, we address to Appendix B for the validation of the corresponding analysis tools. The results of this preliminary check are visible in Fig. 4.7: the `odie` plots clearly show, again, the absence of any hint of signal from TON 116.

For the sake of general cross-check, here we also show the main plots obtained by Dr. Paolo Da Vela. As the principal investigator (PI) of the TON 116 project for the last two years, he performed an analysis of the same datasets. The comparison focuses on LE, according to the VHE part in which we can expect a relevant γ-ray emission (Sec. 4.1 and Subsec. 4.1.2). In

[7]Only $\sim$ 1 h ($\approx$ 12%) of the total observation time was not considered for the data analysis.

[8]This is because the main task of a FA is to provide qualitative results from a fast analysis of any target of opportunity (ToO) that may be flaring, observed by MAGIC at any given zenith angle.

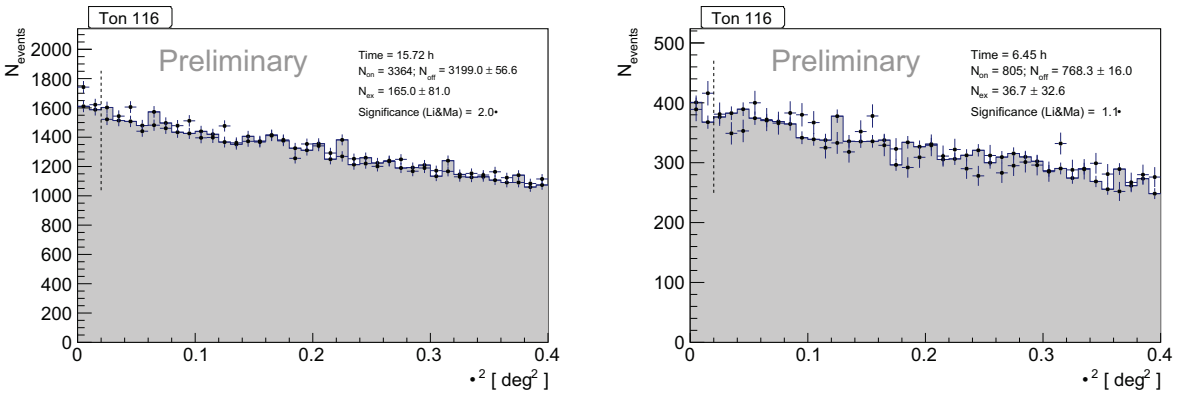

Figure 4.8: θ^2 plots (LE) of TON 116 data taken in 2021 (left) and 2022 (right), as obtained by Dr. Paolo Da Vela.

reality, due to slight differences concerning `MARS` version and selection criteria[9], the total amount of effective observation time, as well as the final results, are not strictly equal, yet they are perfectly compatible (see Fig. 4.8).

4.2.3 VHE excess hint

Once we analyzed 2021 and 2022 data separately, we proceeded by inspecting them all together, which accounts for more than 20 h of observation time for TON 116. This was the last part of our first insight, which gave us outstanding hints for the time being, as it is clear from the `odie` outputs shown in Fig. 4.9. There, a direct comparison with the ones obtained by Dr. Paolo Da Vela is also provided.

Looking at those plots, it is evident that both our results pointed to an eventual signal excess in LE. The associated significance was of more than 2σ, so it was worth to continue the investigation upon the energy at which we may have found it. More precisely, as for TON 116 we could expect an excess to be present in the low energy range, we considered two main possibilities. Namely, if some more signal had been going to come out around the MAGIC lower threshold, say, at approximately 100 GeV, it would have meant that likely it was real. Else, in case the excess had been found to be spread over the whole VHE band, it could have been seen just as an irrelevant fluctuation[10]. In order to solve this puzzling question, we firstly concentrated on the two excess-energy plots produced by `flute`. We could see, especially for the 2021 dataset (the bigger one), some additional counts just above 100 GeV, with a reported significance of 2.4σ (Fig. 4.10). At this point, as previously stated, a strong indication that this excess was not attributable to a background fluctuation would have been its presence for the joint dataset also. Thus, we relied on the use of `foam`, i.e., the `MARS` routine which aims at providing a

[9] LIDAR cut at 0.7 was also used, but further selection was based on data-taking rates instead of cloudiness. Moreover, the energy was estimated by means of the RF technique, instead of the look-up-table one (Subsec. 3.5.2).

[10] In practice, a well-defined excess in LE is a necessary but not sufficient condition for TON 116 to be considered as a VHE source.

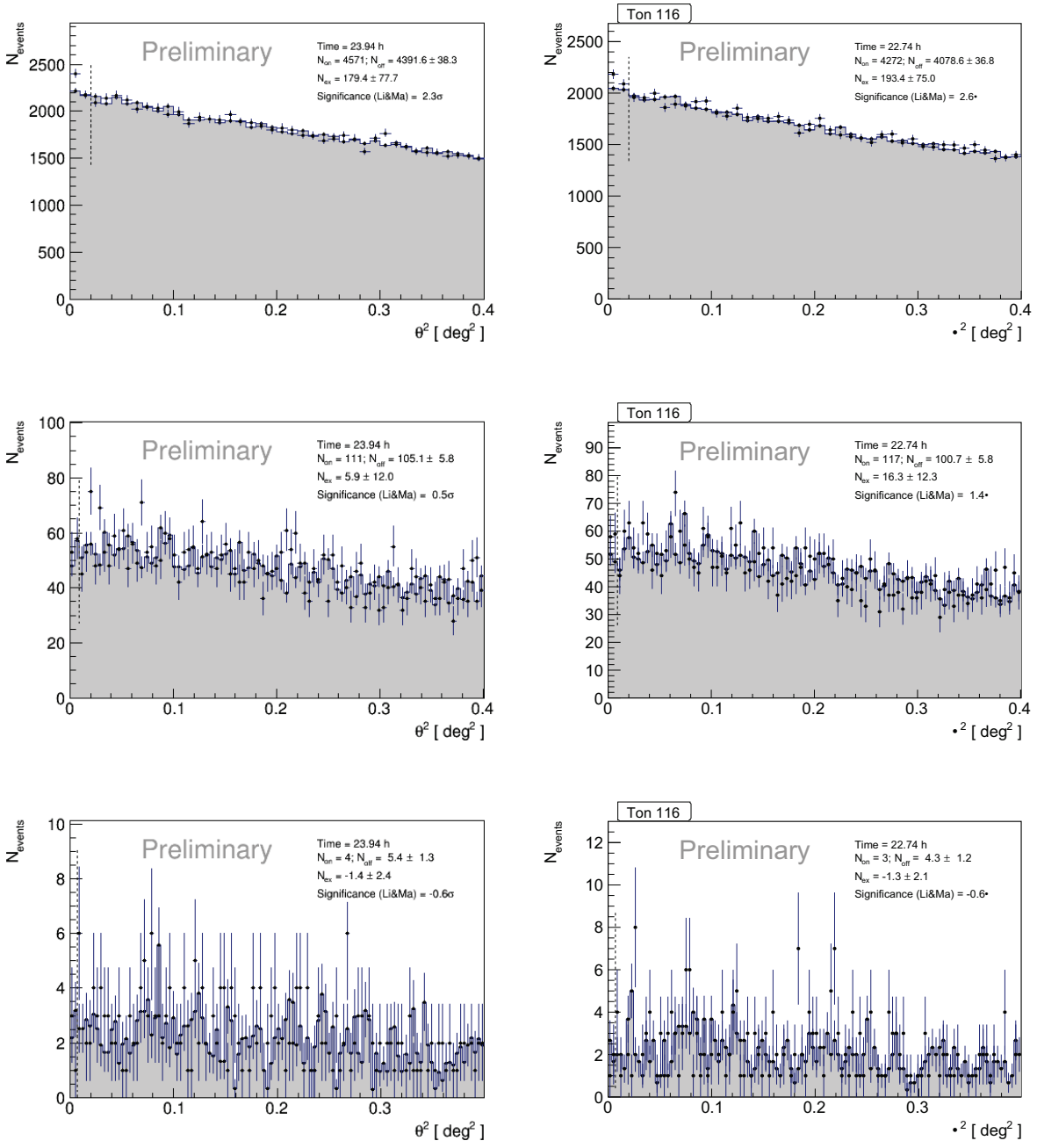

Figure 4.9: θ^2 plots of TON 116 for the joint 2021 and 2022 datasets. In particular, LE is on top, FR in the middle, HE at the bottom, with Dr. Paolo Da Vela's results on the right.

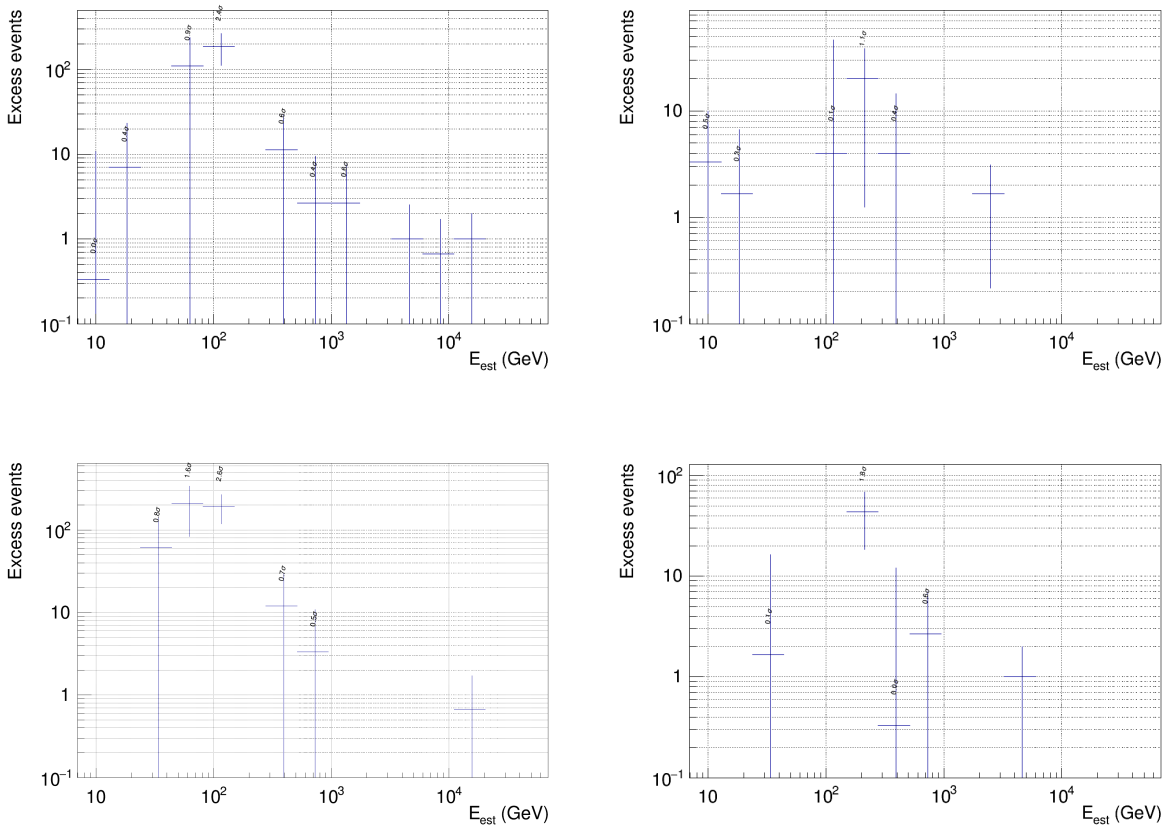

Figure 4.10: Excess counts versus energy plots from flute, for TON 116 2021 (left) and 2022 (right) dataset, with the ones by Dr. Paolo Da Vela at the bottom. Apparently, 2021 data showed quite a significant excess of events just above 100 GeV.

total flux trend from the merging of multiple `flute` outputs (see Subsec. 3.5.4). The related excess-energy plot in Fig. 4.11 clearly seemed to show a peak around 100 GeV as well, even if with no indication about the associated significance.

However, it was possible to infer the latter significance, and we could actually do it in two different ways. First, looking again at the `foam` plot of the number of excesses versus energy, we could see $N_{ex} \approx 190$ just above 100 GeV, while from the `foam` background-energy plot we inferred $N_{off} \approx 6\,000$ at the same energy location, so by means of the simple formula

$$s = \frac{N_{ex}}{\sqrt{N_{off}}} \quad , \tag{4.1}$$

a significance of 2.45σ was estimated. A more accurate number was obtained by getting the exact values for N_{ex} and N_{off} directly from the related energy bin, $s \approx 2.54\sigma$. The latter is still a rough result, because it does not take into account the wobble OFF regions, so it was convenient to find a better estimation with `odie`, which incorporates the proper Li&Ma formula for the significance. In particular, we restricted to the energy bin in which we noticed the previous excess, thanks to the bounds of the bin itself, the θ^2 cut, and the hadronness cut deduced from

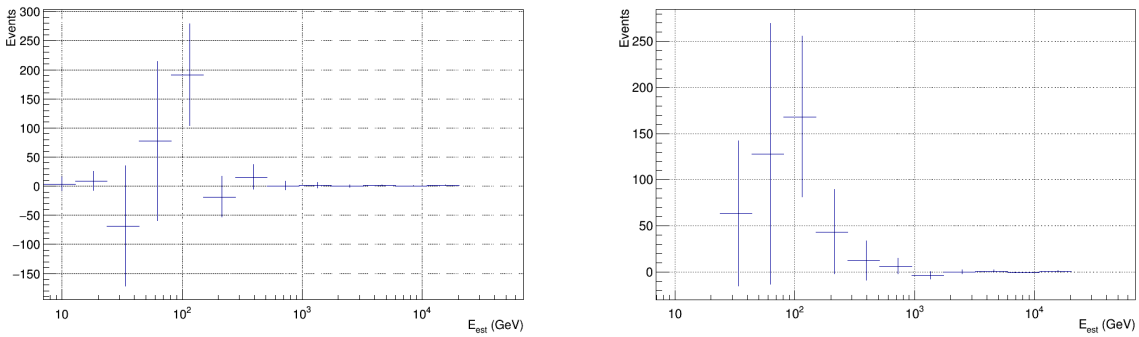

Figure 4.11: TON 116 events-energy plot for both 2021 and 2022 obtained with foam, still pointing to a presumed excess at about 100 GeV (Dr. Paolo Da Vela's plot on the right). The estimated significance for that excess is around 2.5σ (see text for details).

`flute` outputs[11]. As a result, we obtained a significance of $2.06\,\sigma$ and 2.61σ for the "standard" and "fitted" case of N_{on}-N_{off} distributions respectively[12]. Dr. Paolo Da Vela set a slightly larger hadronness cut, and found slightly lower significance values, yet pretty close to ours.

4.2.4 2023 dataset

The above-mentioned results pushed us towards a submission of a new proposal for Cycle 18. Indeed, it was worth to keep monitoring TON 116, so that some deeper conclusions could be drawn about the suspected LE excess, still together with the hope to catch the source during a γ-ray flare. Furthermore, we still aimed at obtaining good indications about the flux in the VHE band, either for every single year of observation, and most importantly, for the total joint dataset. For the latter, we were already confident that the increase of the observation time would have allowed us to put some heavier constraints to the ongoing VHE emission.

As usual, TON 116 has been observed with standard stereo, wobble, and dark extragalactic configurations in 2023; table 4.4 collects all the basic information. Note that here, in reality, the source was first observed on 30th December, 2022. However, we include that night among the 2023 slot, given its temporal proximity to the others, and also because it does still belong to the same observational cycle. The details obtained by MOLA did not include any value different from 0 C.U., apart from the 17th May, in which a HE flux compatible with 0.05 C.U., as well as a significance of $2.4\,\sigma$ in LE, were pointed out. Again, those values can be reasonably thought to be just spurious signals. In general, the weather condition has been quite worse than previous ones, mainly due to both low atmospheric transmission and high cloudiness, affecting roughly half of the nights in which the source was observed.

[11] We basically assumed the following custom settings: $81 \leq E \leq 150\,\text{GeV}$, $\theta^2 \leq 0.04$, $h \leq 0.4$. A minimum size content of 50 was also considered for both M1 and M2 (flute default in each energy bin).

[12] In the former, N_{on} and N_{off} events are found with the sum of the respective events up to a θ^2 cut, whereas in the latter, they are found from a fit on ON and OFF distributions with proper analytical functions.

Table 4.4: Main characteristics of TON 116 observational data by MAGIC in 2023. The arrangement is the same as in tab. 4.1.

Date	*ZD* [deg]	*Condition*	*Sel./Tot. Time* [h]
2022-12-30	27.6 - 34.4	Hum. (wind, dust, no LIDAR)	0.5 / 0.5
2023-01-27	7.6 - 19.0	Ok (initial clouds, no LIDAR)	1.5 / 1.5
2023-02-21	7.6 - 10.6	Ok (hum., high and difficult PSF)	1.0 / 1.0
2023-03-15	7.5 - 16.9	Ok	1.1 / 1.1
2023-03-16	7.4 - 13.8	Low LIDAR, moderate cloud.	0.0 / 1.2
2023-03-17	7.6 - 33.5	Low LIDAR, moderate cloud. (AMC error)	2.0 / 4.6
2023-03-19	7.4 - 35.0	Low LIDAR (inconsistent DAQ restored)	1.4 / 4.1
2023-03-21	11.0 - 34.9	Ok (untrustable LIDAR)	0.8 / 2.0
2023-03-25	10.4 - 28.3	Moderate cloud. (dust, initial LIDAR error)	0.0 / 1.6
2023-03-26	9.3 - 27.4	Moderate cloud. (dust, LIDAR error)	0.0 / 1.6
2023-04-16	8.4 - 33.2	Ok (no LIDAR)	2.2 / 2.2
2023-04-20	8.0 - 28.0	Ok (no LIDAR)	2.2 / 2.2
2023-05-16	7.6 - 13.7	High cloud. (final rain, no LIDAR)	0.0 / 1.0
2023-05-17	12.6 - 27.1	Ok	1.3 / 1.3*
2023-05-18	7.2 - 11.7	Ok (AMC powercycled, LIDAR restored)	1.3 / 1.3

We split this TON 116 dataset into two sub-samples. The first one, which we will refer to as "group I", includes the nights from 30th December, 2022 to 21st February, 2023, while the second, "group II", includes all the remaining ones, from 15th March to 18th May, 2023. This is because the latest data-taking period spans over at least two different MC configurations. Indeed, from 15th December, 2022 to 9th March, 2023 one is supposed to use a specific MC set, accounting for degraded reflectivity and bad PSF in M1 telescope due to AMC-related problems. However, at the time of the drafting process of this thesis, that set was still under development[13]. Thus, to be conservative, for the first three nights we considered the available MC set just prior to that, i.e., ST.03.18 (still accounting for worse M1 reflectivity after the eruption). From 10th March 2023 on, instead, the MC files belong to the currently valid ST.03.20 set, built after an important intervention to the AMC system, and the generation of new mirror look-up-tables as well. Details about the validation of the analysis related to both of these MC periods are in Appendix B.

The data selection yielded all of the 3 h of observation for group I, while 12.4 h out of 24.3 h for group II. This reflects some not optimal condition already outlined: one can notice from table 4.4 that group II observations were not only much longer in time, but also more affected by worse atmospheric transmission, with ≈ 0.4 as minimum value[14]. Cloudiness parameter provides a confirmation about the presence of more bad nights, reaching a maximum value of approximately 77. Thus, whereas for group I all the observation time has been considered, for

[13] Likely that, in turn, will be composed by two different MC sub-sets: the first ranging from 15th December, 2022 to 6th January, 2023, while the second ranging from 7th January to 9th March, 2023.

[14] Also, the instrument often showed an unexpected behaviour, or was not working at all.

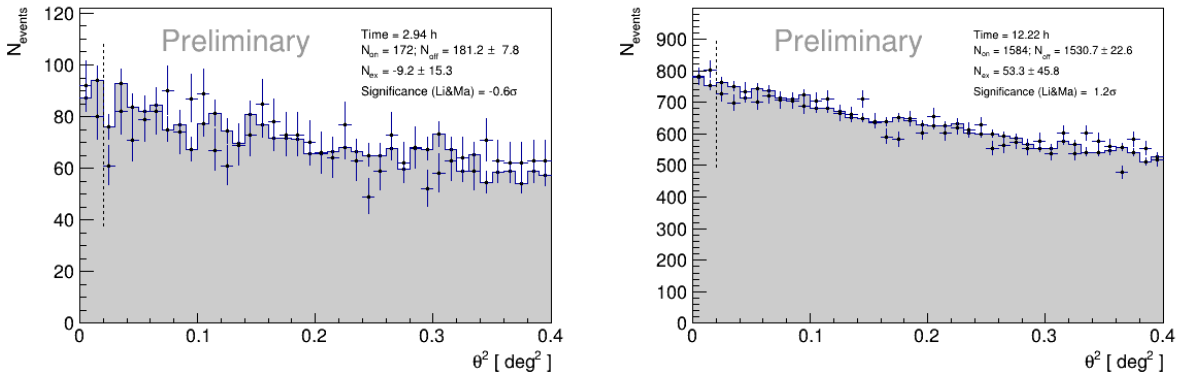

Figure 4.12: θ^2 plots (LE) of TON 116 data related to "group I", taken from December 2022 to February 2023 (left), and to "group II", taken from March to May 2023 (right).

group II only a bit more than a half of it passed quality cuts.

The most relevant results of the 2023 analysis are two. First of all, we will show the significance outputs for group I and group II separately, then we will give a joint insight. We will do the same also for higher level results.

The `odie` plots for the two single 2023 subsets are visible in Fig. 4.12, where as previously done, we only show the more meaningful part, that is LE. The signal found was still not supporting the hypothesis of an emitting source, especially for group I whose significance is negative, most likely because of a rather short observation time.

The `odie` results related to the combination of group I and group II datasets are shown in Fig. 4.13: the significance values turn out to be very similar to the one already found for group II, given the smaller contribution of group I. From them, especially looking at LE, we can safely state that TON 116 did not manifest any VHE emission for year 2023 too.
Next, we obtained the significance associated to all of the three years of observation. In order to do it in a more coherent way for our source, we created a new RF for the 2022 slot, such that only a ZD between 0° and 35° is considered. After a check whether the new plots for 2022 (Fig. 4.14) are compatible with the ones previously found (Fig. 4.7), we put all together to obtain the total results visible in Fig. 4.15. The joint observational dataset adds up to almost 40 h, but the detection response is still negative. In the next subsection we present the highest level outcomes of TON 116 analysis.

4.2.5 VHE results

The fact that no MAGIC detection was found in any of the periods in which it was observed, allowed us to only obtain upper limits for TON 116 flux at VHE. In Fig. 4.16 the SED for each of the three years is shown, obtained using the settings shown in table 4.5. We remind the reader that the last year includes two distinct datasets based on different MC periods (group I and group II, previous Subsec. 4.2.4), so we show the `foam` joint output for 2023. Note that there is just one flux point not reported as an upper limit, around 100 GeV for 2021. This is likely due to a larger

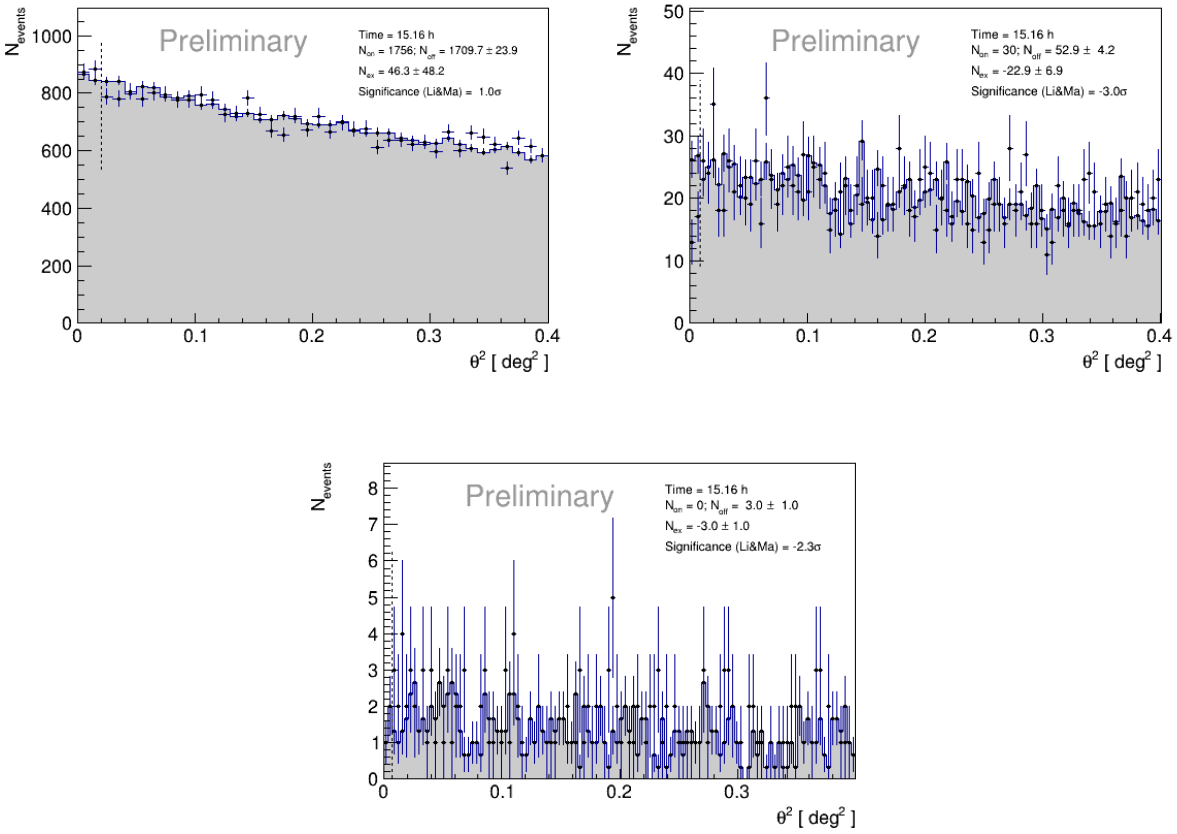

Figure 4.13: θ^2 plots of the whole TON 116 dataset taken in 2023, from a "group I" + "group II" joint analysis (LE top left, FR top right, HE bottom).

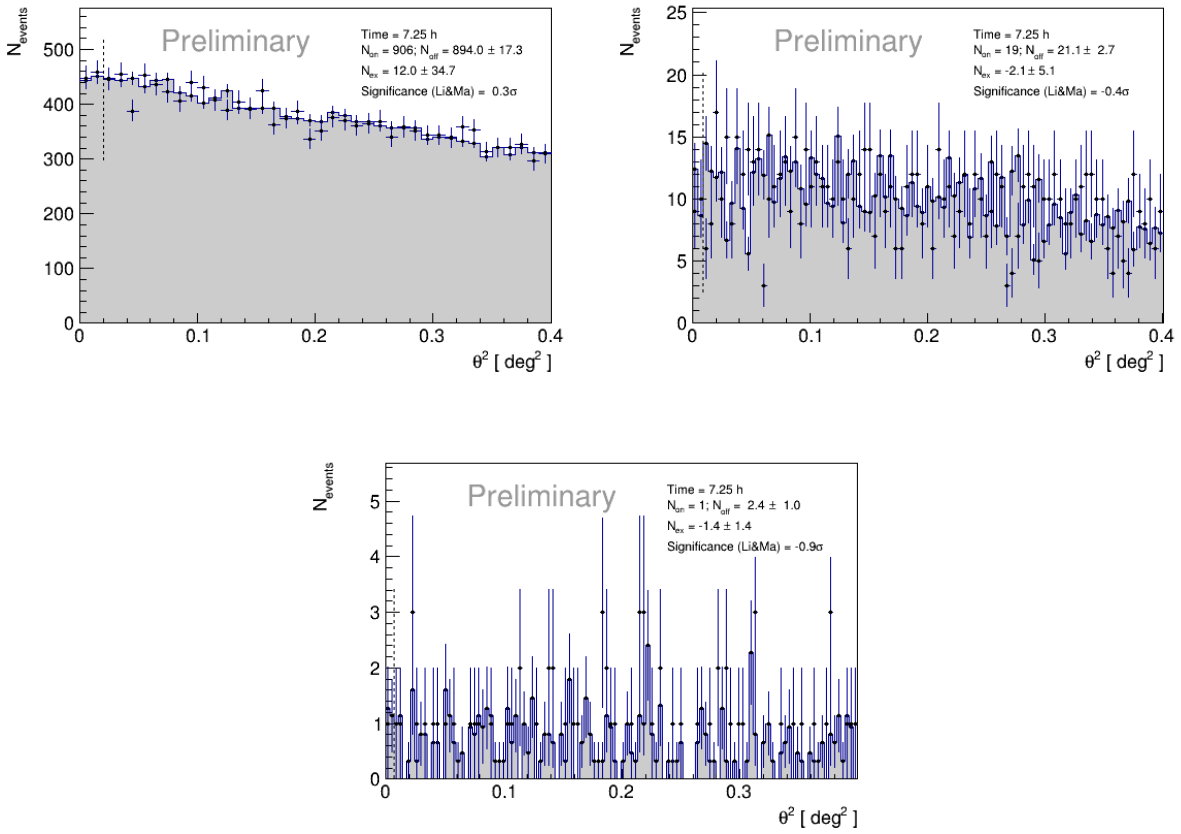

Figure 4.14: θ^2 plots of the TON 116 data of 2022, obtained with a new specific RF restricted to low zenith distances (LE top left, FR top right, HE bottom). Comparing them with the ones in Fig. 4.7, they do support the absence of any VHE signal for that slot.

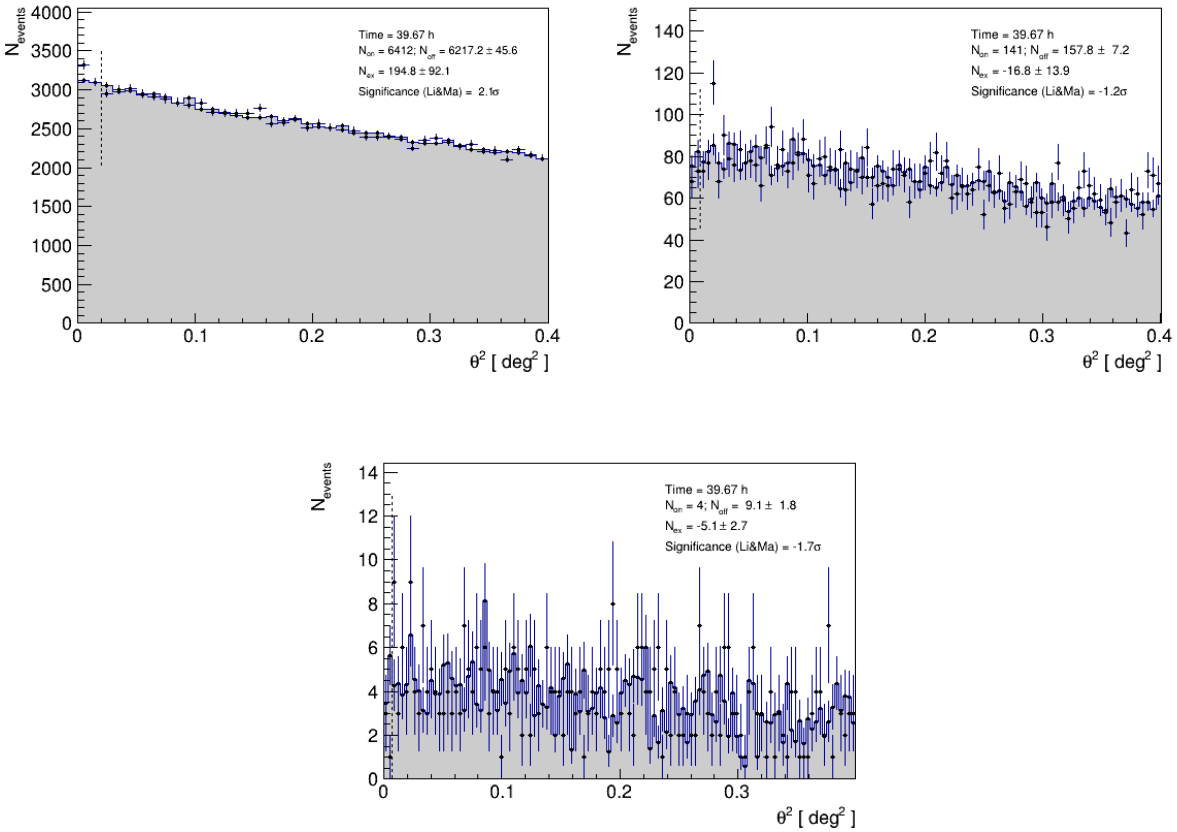

Figure 4.15: Integrated θ^2 plots of TON 116 for all the three years of observation, from 2021 to 2023. Top left is the LE range, top right is the FR range, bottom is the HE range. The first among them contains a significance larger than 2σ, but still not enough for a detection to be claimed.

Table 4.5: Main flute settings used for standard derivation of SED and LC plots for TON 116 observations with MAGIC. The first column is the zenith distance, the second column is the number of E_{est} bins, the third column is the number of Az bins, the fourth and the fifth columns are the minimum energy and the binning for LC computation, the sixth is the assumed source redshift, the seventh is the confidence level, and the eighth is the EBL model (D11 = Domínguez et al. 2011). See Subsec. 3.5.3 for further details about the entries.

ZD	N_{bin} (E_{est})	N_{bin} (Az)	LC E_{min}	LC binning	z	CL	EBL
5°-35°	20	1	100 GeV	Night-wise	0.5	95%	D11

observation time reached for that year (Subsec. 4.2.1), and also, it might reflect the eventual excess pointed out in 2022 (Subsec. 4.2.3).

In conclusion, the combined SED of the MAGIC observing campaign is displayed in Fig. 4.17. From this latter result, and looking also at the yearly fluxes above, we can presume to have put quite solid constraints to the most energetic side of the IC bump of the source. The related peak seems to be located below 100 GeV, in agreement with the outcomes of recent *Fermi*-LAT analysis (see figures of Subsec. 4.3.1, and also Fig. 4.4). Despite a difference of about 10 h with respect to the total observation time accounted for a priori, we can also notice a general agreement with the extrapolated VHE flux (Fig. 4.5). Our findings confirm that the blue tail of the IC bump is strongly suppressed well before 1 TeV.

4.3 Multi-wavelength data

4.3.1 *Fermi*-LAT observations

The *Fermi*-LAT analysis of TON 116, listed in the 4FGL catalogue (`4FGL J1243.2+3627`; Abdollahi et al. 2022) has been performed with `fermipy` version `1.2.0` and `ScienceTools` version `2.2.0` considering 15 years of data taking (247017601 ÷ 722995205 MET). The analysis has been computed in a RoI (Region of Interest) width of 10° binned in 0.1°. The reconstructed events are mapped in CEL coordinates and ARC projection in 10 energy bins per decade between 300 MeV and 500 GeV. The recommended quality cuts in zenith angle has been applied ($z_{\max} = 90$, `DATA_QUAL>0 && LAT_CONFIG==1 && ABS(ROCK_ANGLE)<5`), the applied event class is 128 relative to point source analysis, and event type 3 corresponding to `FRONT+BACK` data (Subsec. 2.3.1). The whole analysis has been performed with the *Instrument Response Function* (IRF) `P8R3_SOURCE_V3`, and the data has been reconstructed with `Pass8` algorithm. In the analysis the isotropic (`iso_P8R3_SOURCE_V3_v1`) and the galactic diffuse (`gll_iem_v07`) models have been implemented, including the 4FGL-DR3 source catalogue `gll_psc_v31` provided by the *Fermi* collaboration.

For performing the likelihood analysis, a region of 15° around the source has been considered,

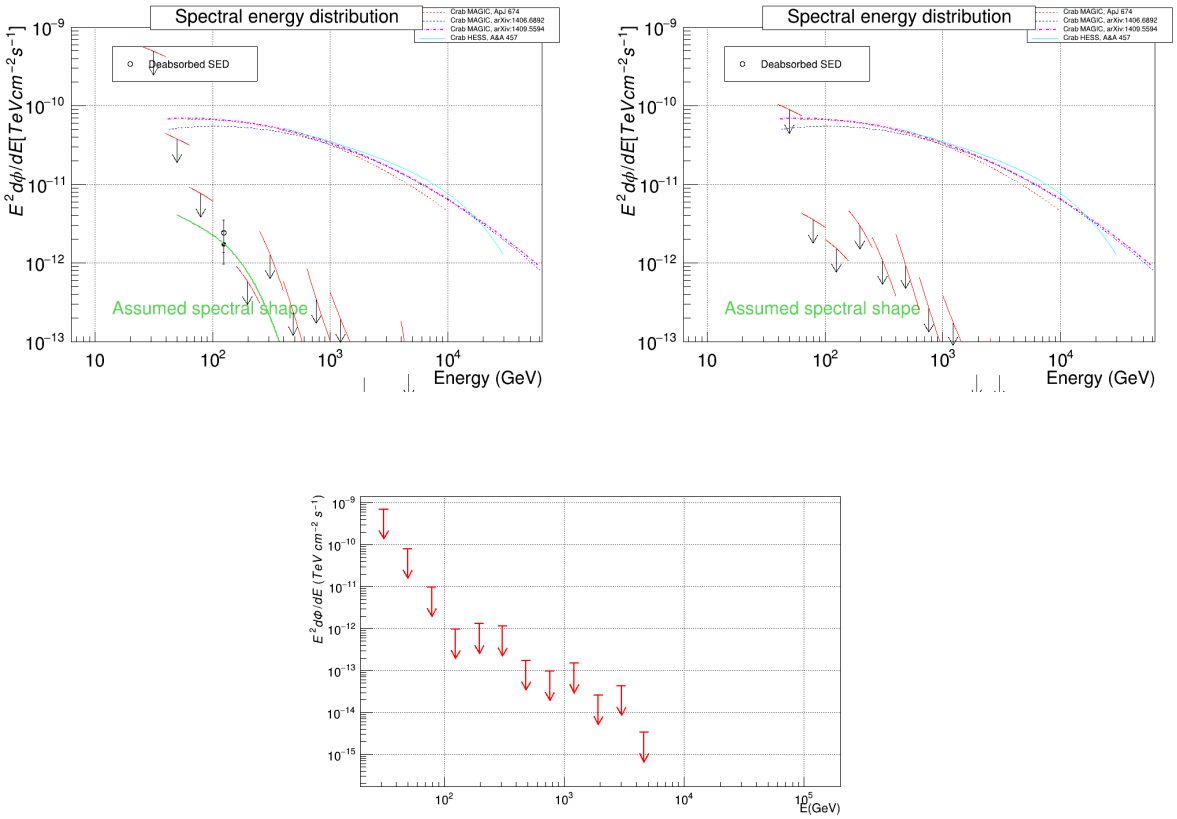

Figure 4.16: SED plots of TON 116 for 2021 (top left), 2022 (top right), and 2023 (bottom) datasets. The former two come from flute, whereas the latter from foam. Upper limits only are derived for the source, as no VHE emission was detected for none of the three years.

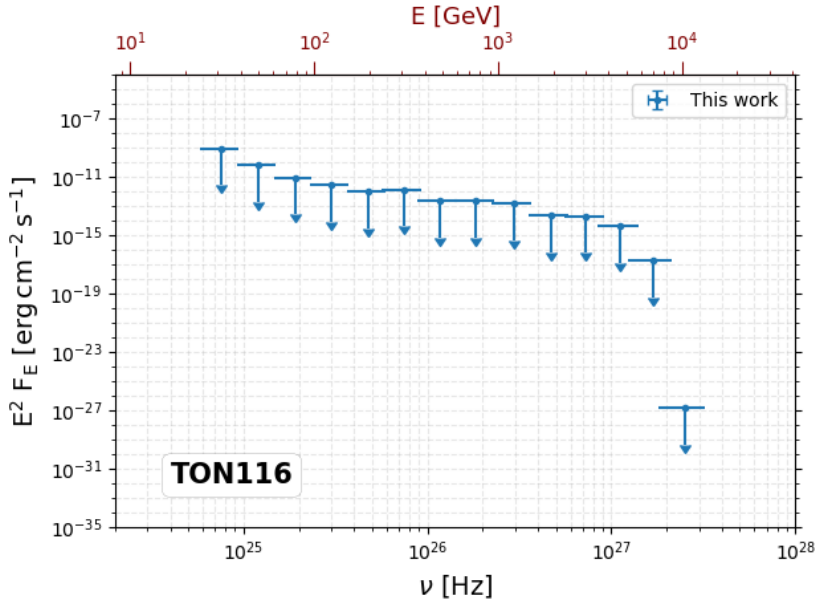

Figure 4.17: Upper limits on the VHE flux of TON 116, as seen by MAGIC for the total period 2021-2023. The plot indicates $\nu_{p,c} \lesssim 100$ GeV, which is also in agreement with the decreasing trend inferred by *Fermi*-LAT at its upper energy threshold (Subsec. 4.3.1). On top, a GeV scale is superimposed to make the conversion between SED frequency and VHE energy immediate by eye.

and the `Prefactor`, `norm` and `Index` parameters of sources within 3° from the TON 116 location have been set as free, while the sources with TS < 9 has been removed and the parameters of the objects with predicted counts in the range 10-100 have been fixed. In the 4FGL catalogue, TON 116 is parameterized as a `lognormal` distribution (LP) spectral function. Considering 15 years of observations, the best model fitting the data is represented by a power-law with exponential cut-off (PLEC, `expcutoff` model), that has been tested against the simple power-law (PL) shape and the LP function through the recommended $TS_{curvature}$ test[15]. Indeed, the $TS_{curvature}$ of LP model against PL is ~ 38, while the `expcutoff` model is ~ 52 [16]. As a result, the fit quality is 3, the estimated *logLikelihood* (logarithmic likelihood) is $\sim (-95278.26)$, and the total TS is ~ 6193. The TON 116 SED is fitted with the `expcutoff` function [MeV^{-1} cm^{-2} s^{-1}] as

$$\frac{dN}{dE} = N_0 \cdot \left(\frac{E}{10^3 \text{ MeV}} \right)^{-\gamma} \cdot \exp[-(E - E_b)/p_1] \quad . \tag{4.2}$$

In the period in coincidence with MAGIC observations, in particular the years 2021-2023 ($631152005 \div 712540805$ MET), the adopted parameterization for the source is represented as well by a power-law with exponential cut-off. Here, the $TS_{curvature}$ for the `expcutoff` model is ~ 10, but it is consistent with data and the best representation of the whole dataset (15 years). In this case, the resulting fit quality is still 3, the estimated logLikelihood is $\sim (-42985.74)$, and the total TS is ~ 1490. In both cases, the reconstructed position of TON 116 is $(\mathrm{RA},\ \mathrm{Dec}) = (132.98°,\ 80.51°)$.

The parameter values as results of the likelihood analysis for both periods are tabulated in tab. 4.6. In the fitting procedure, the E_b parameter has been fixed and assumed equal to the lower edge of the energy range, in particular 300 MeV.

Table 4.6: TON 116 spectral model parameters. The unit of N_0 is [MeV^{-1} cm^{-2} s^{-1}] and of both E_b and p_1 is [MeV].

Period	N_0 $[\cdot 10^{-13}]$	γ $[\cdot 10^{-2}]$	E_b	p_1 $[\cdot 10^4]$
15 years	16.70 ± 0.57	-1.61 ± 3.09	300	6.82 ± 1.27
2021-2023	4.15 ± 0.26	-1.70 ± 6.45	300	6.78 ± 3.08

In Fig. 4.18 and 4.19 the counts, TS and residuals maps, and the spectrum are displayed, relative to TON 116 analysis of 15 years of data taking and the period 2021-2023 in coincidence with MAGIC observations respectively.

[15] Curvature test webpage (https://fermipy.readthedocs.io/en/latest/advanced/curvature.html).

[16] As reference value to prefer the model against the simple PL is 25.

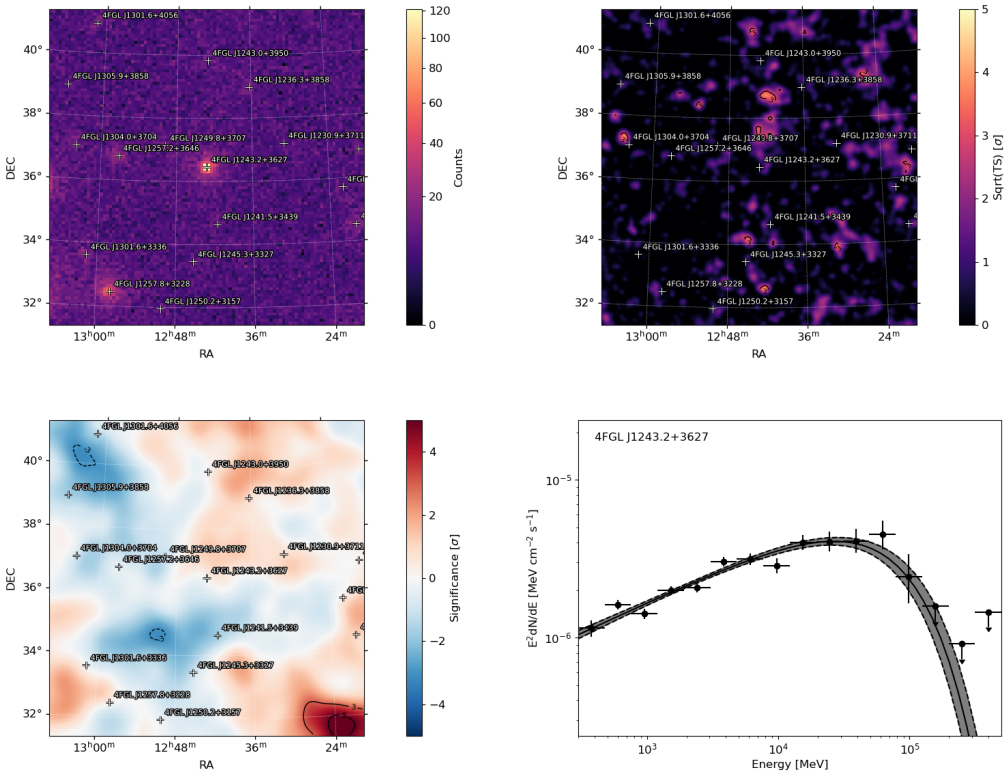

Figure 4.18: *Fermi*-LAT analysis of TON 116 of 15 years of data taking. *On the top left & right*: counts and TS maps. *On the bottom left & right*: residuals map and SED fitted with the expcutoff function (eq. 4.2). The parameters resulting from the likelihood analysis are listed in tab. 4.6.

The SEDs of both the analyses have been compared and in Fig. 4.20 they are displayed. As shown in the figure, in the years 2021-2023 the source has experienced a period of low activity and this evidence could have affected the non-detect ability of TON 116 at the VHEs covered by Cherenkov telescopes. Moreover, in order to check the non-variability of TON 116 in the MAGIC observation period, the light curves related to the whole dataset and the years 2021-2023 are displayed in Fig. 4.21. In particular, the aim of this analysis is to give us the opportunity to study the broadband spectrum of TON 116 in the years 2021-2023 (see Fig. 4.21-bottom). For the whole period (15 years) the adopted time binning is six months, while for the years 2021-2023 the time binning is three months. In both cases, the flux of TON 116 has been integrated in the whole energy range of the analysis, in particular between 300 MeV and 500 GeV.

4.3.2 Swift-XRT observations

Here, for TON 116 we just rely on the monitoring activity of Swift-XRT (Subsec. 2.2.2). With this respect, our source was observed eleven times in the period ranging from 2021 to 2023, out of which all but one were in 2021, and only the very last was in 2022. The basic information about those inspections are given in table 4.7. We removed one of the pointings (38445026) from the sample, as the associated duration was a factor of about 10 shorter than the others, and failed to provide adequate statistics. Each of the selected scans lasted about 1.6 ks on average, roughly

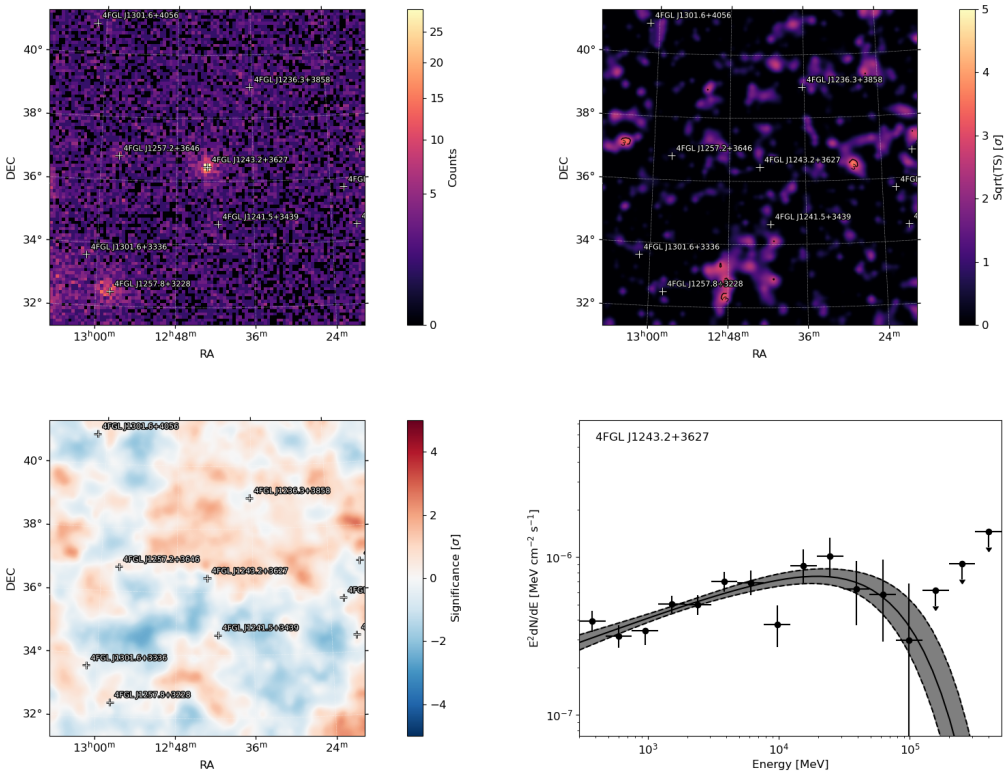

Figure 4.19: *Fermi*-LAT analysis of TON 116 in the period 2021-2023 in coincidence with MAGIC observations. *On the top left & right*: counts and TS maps. *On the bottom left & right*: residuals map and SED fitted with the expcutoff function (eq. 4.2). The parameters resulting from the likelihood analysis are listed in tab. 4.6.

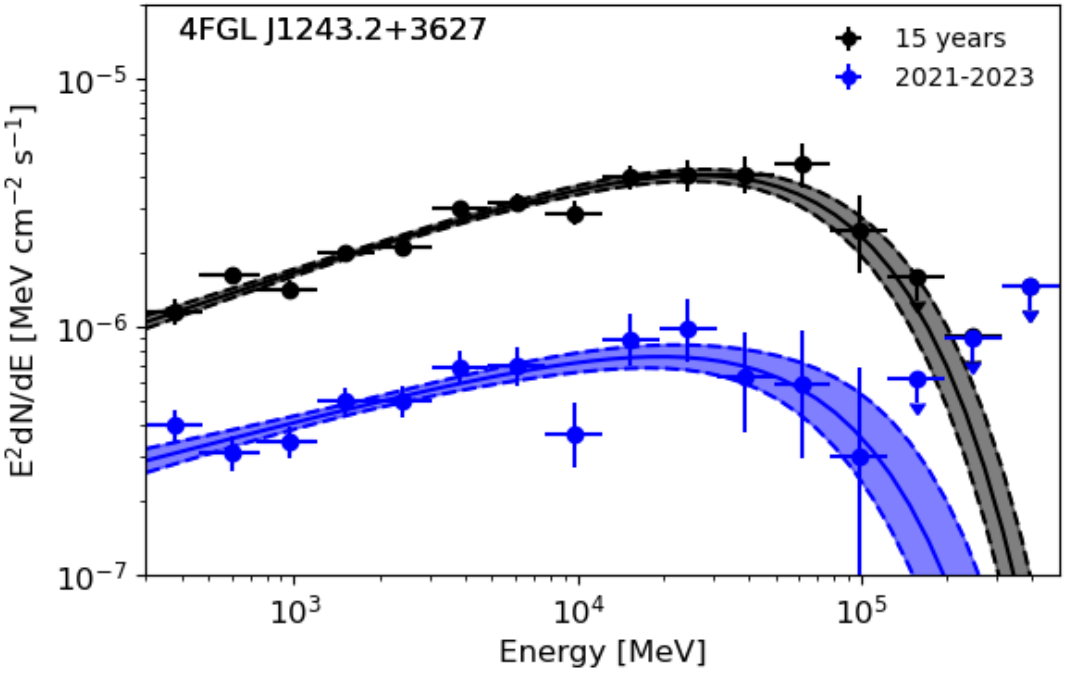

Figure 4.20: Comparison of the two SEDs showed in Figs. 4.18 and 4.19.

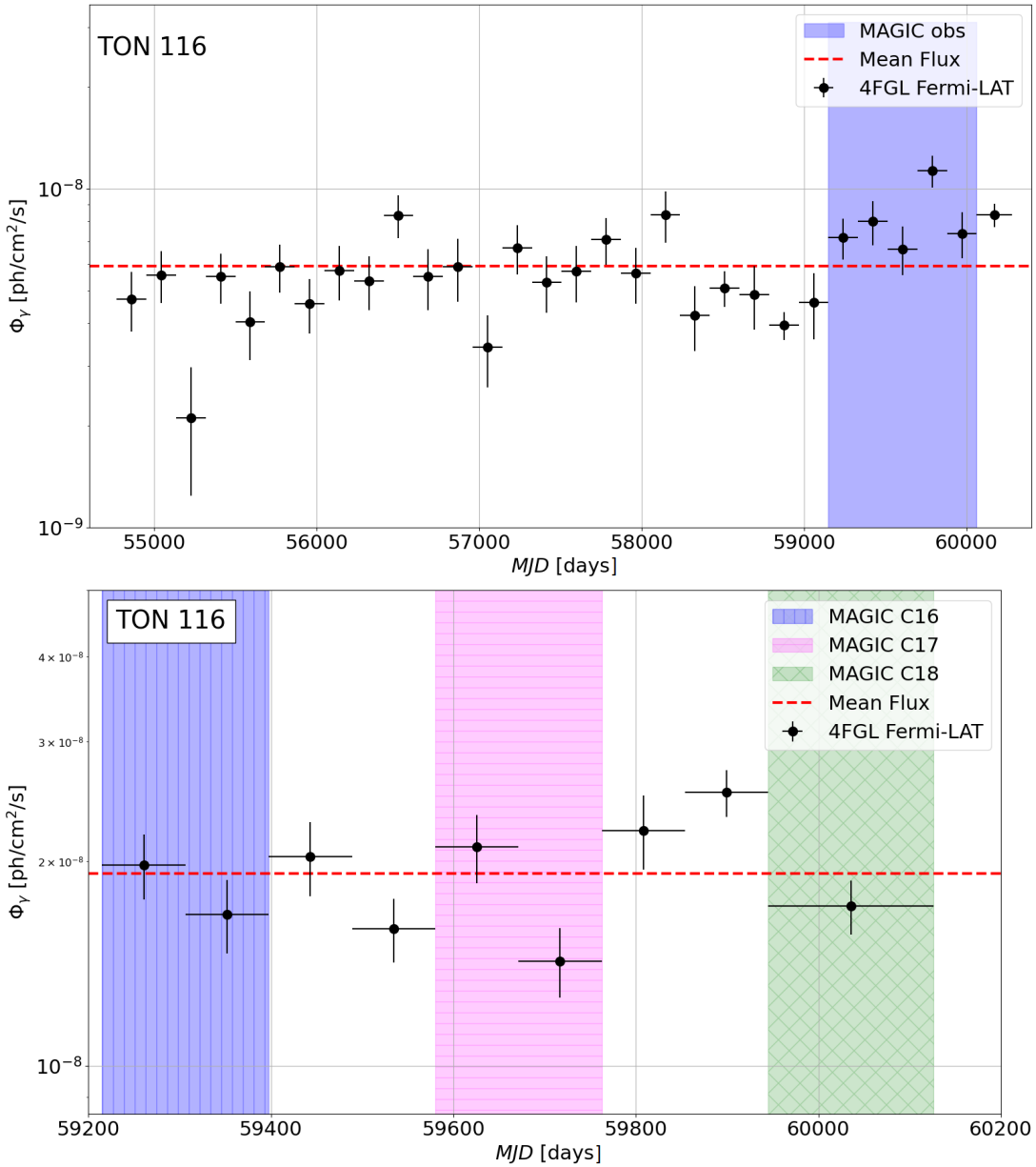

Figure 4.21: *On the top*: 15 years six months binned light curve of TON 116. The shaded blue region represents the period in coincidence with MAGIC observations (2021-2023). *At the bottom*: three months binned LC performed from January 2021 to July 2023. The shaded colored regions represent the observation time of MAGIC corresponding to observing cycles 16-17-18.

corresponding to 27 minutes. For what concerns the extraction of the X radiation, we refer to the photon counting (PC) readout mode, according to which the events within a maximum radius of 6 pixels from the center of the source are excluded. This is in order to avoid pile-up occurrence in the inner part of the PSF. The signal is taken up to an outer 30-pixel radius from the source position, and the flux is obtained by comparing it with the PSF shape of XRT detector. On the other hand, the background is estimated by the behaviour found in nearby circular regions, having a typical radius of 40 pixels. We processed the data by means of the tools included in the HEASoft software package (v.6.32.1) by NASA High Energy Astrophysics Archive Research

Table 4.7: TON 116 observational data by Swift-XRT for the period 2021-2023. The first column contains the identification number (ID) of the observation, the second column is the corresponding archiving date, the third column is the Swift-XRT exposure (unit 10^3 s), while the fourth and fifth columns show the normalization constant and the intrinsic spectral index of TON 116 (with related errors) resulting from a power-law fit of the data respectively.

Obs. ID	*Archive Date*	*Exposure* [ks]	k_x [10^{-12} erg cm^{-2} s^{-1}]	p_x
38445016	2021-03-01	2.0	2.9 ± 0.2	2.1 ± 0.2
38445017	2021-03-01	1.9	2.2 ± 0.3	2.4 ± 0.2
38445018	2021-03-02	1.7	3.2 ± 0.3	2.0 ± 0.2
38445019	2021-03-03	1.7	1.7 ± 0.2	2.6 ± 0.2
38445020	2021-03-04	1.6	2.1 ± 0.2	2.0 ± 0.2
38445021	2021-03-05	1.7	1.7 ± 0.2	2.4 ± 0.2
38445023	2021-03-23	1.4	3.2 ± 0.3	2.2 ± 0.2
38445024	2021-03-27	1.3	2.4 ± 0.4	2.6 ± 0.2
38445025	2021-03-30	1.4	2.1 ± 0.3	2.5 ± 0.3
38445027	2022-03-20	2.0	1.1 ± 0.2	2.3 ± 0.4

Center (HEASARC)[17]. The latter allows one to include ancillary response files for the derivation of the signal, and select a specific energy range of interest, as well as custom settings for count distribution. Specifically, we performed the extraction of the X-ray spectra with `xspec` in the 0.2-10 keV band, after binning with the `grppha` command in order to have at least 30 counts per channel bin. The modelization consists in a power-law trend, which results from a multiplication between a deabsorbed model and a data/model ratio accounting for the galactic absorption along the line of sight. The latter quantity is represented by a column density of $n_H \approx 1.29 \cdot 10^{22}$ cm^{-2}, still found within the HEASARC online archive[18]. Fig. 4.22 provides a joint view of the flux points as derived from each of the Swift-XRT visits to our source. The fit on the X-ray flux is done with a simple power-law, of the kind

$$F(E) = k_x \left(\frac{E}{E_x} \right)^{t_x} \tag{4.3}$$

with $E_x = 1.5$ keV, and k_x a normalization constant. However, taking into account the fact that we are dealing with a weighted distribution, the real TON 116 slope is to be found as $p_x = 2 - t_x$. Such intrinsic spectral index associated to each respective slot is listed in the last column of table 4.7. As it is also suggested by Fig. 4.23, which shows the source index seen by XRT on a daily basis[19], the values seem to be distributed around $p_x \approx 2.3$, with no significant change over time. In order to properly verify the latter assertion, we performed a χ^2 statistical test on the

[17] https://heasarc.gsfc.nasa.gov/ .

[18] https://heasarc.gsfc.nasa.gov/cgi-bin/Tools/w3nh/w3nh.pl .

[19] In case of multiple observations per day, the mean of p_x is considered.

slope values by assuming a linear trend. We considered both a generic line (1-deg polynomial) and a constant line (0-deg polynomial) to be good reproducers of our data, thus having the following simple equations respectively:

$$p_x = \begin{cases} \alpha_x D + p_{x,q} \\ p_{x,q} \end{cases} \quad , \tag{4.4}$$

with D the observation date, α_x the angular coefficient, and $p_{x,q}$ the intercept. To get more meaningful conclusions, we applied a re-definition of the date interval such that it starts from 0. This sort of normalization, obtained by subtracting the first MJD (Modified Julian Date)[20] of observation from all the dates, is visible in the upper part of the plots in Fig. 4.23. For the fit procedure, involving the normalized MJD set and the corresponding slopes, we relied on both `polyfit` and `curve_fit` class methods from `numpy` and `scipy` python packages respectively. Once we obtained the best-fit values (α_x, $p_{x,q}$) from both the methods and both the kinds of polynomial, we evaluated the goodness-of-fit by defining the Test-Statistic (TS) variable

$$\chi^2 = \sum_{i=1}^{N} \frac{(p_{xi,obs} - p_{xi,exp})^2}{p_{xi,exp}} \quad , \tag{4.5}$$

with N the size of the dataset, $p_{xi,obs}$ the observed values of the slope, and $p_{xi,exp}$ the expected values of the slope according to the fit function. The χ^2 values are found in two different ways. One, called χ^2_{np}, is by defining a custom `numpy` routine based on eq. 4.5. The other, χ^2_{sp}, exploits the method `stats.chisquare` incorporated in `scipy`. The latter also includes a calculation of the p-value ($p\text{-}val_{chi}$) and the critical value of the TS (χ^2_{crit}), under a significance set at 5% level[21]. An alternative p-value derivation ($p\text{-}val_{sf}$) is by the `chi2.sf` method, belonging to `scipy` package as well. Table 4.8 collects all the final results about the outlined procedures. One can notice an excellent agreement between the respective linear fits, which are associated $N-2$ and $N-1$ degrees of freedom for the generic and constant case respectively. At the end, the high (low) p-value (χ^2) results ensure that the linear behaviour is a very good representation. In particular, the generic linear fit turns out to be slightly better (Fig. 4.23 does explicitly include its results). Thus, the trend of TON 116 intrinsic spectral index in the 0.2-10 keV energy range is compatible with a mean value of 2.3 undergoing a tiny increase over time, equal to about $1.26 \cdot 10^{-4}$ per day (dy). This extremely small evolution can be unmistakably considered as negligible, at least for the whole period encompassing the single Swift observations of TON 116, spanning 384 days from March 2021 to March 2022. The mean slope that we derived is representative of the total Swift-XRT dataset of TON 116 for the period 2021-2023, which is

[20] Number of days since midnight on 17th November, 1858. The relation with the JD (Julian Date) is: MJD = JD − 2 400 000.5 .

[21] Essentially, the p-value is the probability of getting more "deviating" results than the one obtained, in case the model trend is assumed to be true. The critical value of the TS is the one up to which the model (commonly considered as *null hypothesis*) fails to be rejected.

Table 4.8: Fit results on TON 116 intrinsic slope (p_x) as inferred daily by Swift-XRT for the period 2021-2023 (see also tab. 4.7). The first column indicates the method used for the polynomial fit (polyfit from numpy package, curve_fit from scipy package) preceded by the polynomial degree (1 for generic line fit, 0 for constant line fit), the second column is the best-fit slope of p_x trend, the third column is the best-fit intercept (assuming a re-definition of the origin of the dates at 0), the fourth column is the χ^2 value obtained by a custom numpy function following equation 4.5 (dof = degrees of freedom), the fifth column is the associated p-value derived from stats.sf method from scipy, while the sixth, seventh, and eighth columns show the χ^2, the associated p-value, and the critical Test-Statistic value as provided by the chisquare method from scipy respectively. The generic linear trend seems to be slightly better than the constant, therefore is the one also reported in Fig. 4.23.

Method	α_x $[10^{-4}\ \mathrm{dy}^{-1}]$	$p_{x,q}$	χ^2_{np}/dof	$p\text{-}val_{sf}$	χ^2_{sp}/dof	$p\text{-}val_{chi}$	χ^2_{crit}
1-polyfit	1.26 ± 6.99	2.32 ± 0.09	0.184/7	1.000	0.184/7	1.000	14.07
1-curve_fit	1.26 ± 6.99	2.32 ± 0.09	0.184/7	1.000	0.184/7	1.000	14.07
0-polyfit	0	2.33 ± 0.08	0.185/8	1.000	0.185/8	1.000	15.51
0-curve_fit	0	2.33 ± 0.08	0.185/8	1.000	0.185/8	1.000	15.51

shown in Fig. 4.24. The associated normalization is $(2.2 \pm 0.1) \cdot 10^{-12}$ erg cm^{-2} s^{-1}, which is also in agreement with the mean value of k_x previously found from the global view of every single scan (see Fig. 4.22).

4.3.3 OSN observations

The optical side of TON 116 was covered by OSN in the period between 23rd February, 2022 to 12th February, 2023. Basically, the source was associated with few magnitude values per night, all of them in the 15-17 mag range, with empty periods of 5-15 days during which the source was not observed. To find the true magnitude $m_{R,t}$, galactic extinction in the TON 116 direction was accounted for by subtracting the correspondent absorption term A_R via

$$m_{R,t} = m_{R,o} - A_R \tag{4.6}$$

from the observed magnitude $m_{R,o}$. We used an extinction of $A_R = 0.026$ mag, i.e., the reference value of Landolt R bandpass (Schlafly and Finkbeiner 2011), which turns out to be the closest one to the effective wavelength of R filter (640.7 nm). For the latter observation range, we assumed the error to be consistent with an associated FWHM of $\Delta\lambda = 1580$ Å (Bessell 2005). The magnitudes $m_{R,t}$ were converted into the correspondent fluxes $f_{R,t}$ by means of the `magToFluxDensity_bessel98` method of `PyAstronomy.pyasl` python package, which is based on the transformations contained in Bessell, Castelli, and Plez (1998). We averaged the available values in order to have just one per day, and as a result we obtained 39 data points in

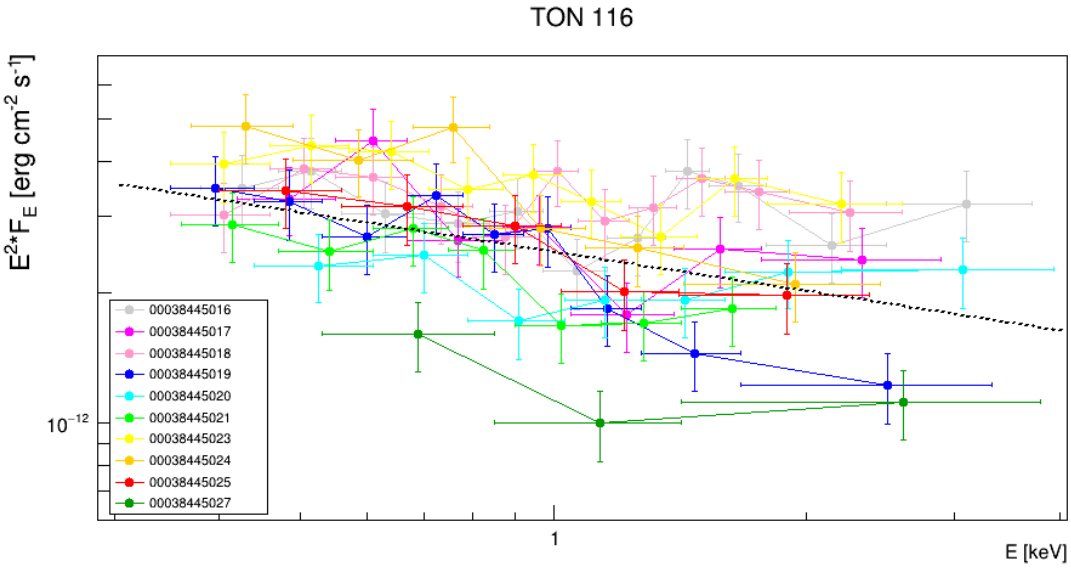

Figure 4.22: Composite plot of TON 116 SED points from each single observation ID taken by Swift-XRT. The source does generally show a low state, in particular in the very last inspection (dark green dataset at the bottom). The black dashed line represents the power-law function defined by the parameters $k_x = 2.2 \cdot 10^{-12}$ erg cm^{-2} s^{-1} and $t_x = -0.3$, which are the mean of the normalization constants and the mean of the weighted spectral indices from each of the IDs respectively (see tab. 4.7). TON 116 did not show any significant emission variation in the energy range considered.

total. The error associated to each averaged flux, both the lower and the upper one, was found with the propagation formula

$$\Delta f_R = \frac{1}{n}\sqrt{\sum_{i=1}^{n}(\Delta f_{R,i})^2} \quad , \tag{4.7}$$

where $\Delta f_{R,i}$ is the error associated to the i-th true flux taken in a given day, and n is the number of TON 116 observations performed in that same day. The final data points with related errors are plotted in Fig. 4.25. This light curve shows that the daily R flux of TON 116 is characterized by fluctuations within 22% with respect to a mean value of $F_R = (9.6 \pm 0.1) \cdot 10^{-13}$ erg cm^{-2} s^{-1}. The error on the latter flux is obtained by a mean of the associated lower and upper error found with eq. 4.7, as they are comparable enough (ratio ~ 1). The final flux is also confirmed by a constant fit procedure performed with both the same `polyfit` and `curvefit` methods used for the analysis of Swift data (previous Subsec. 4.3.2). Thus, the F_R value above is taken as representative of the total set of optical OSN observations of TON 116 in the period considered. Even in this case, the trend of optical LC of the period in coincidence with the MAGIC observations, is almost constant. Hence, as said earlier, in the years 2021-2023 TON 116 experienced a low state without evident flaring state.

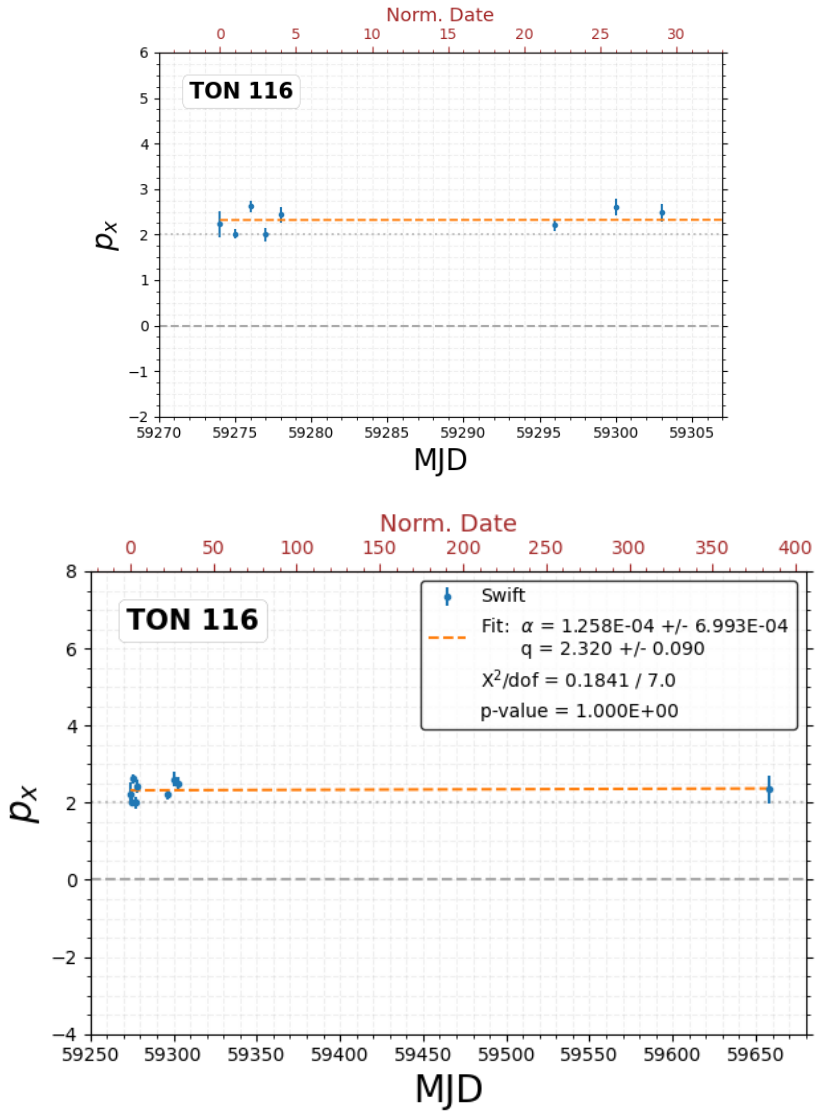

Figure 4.23: Intrinsic spectral index of TON 116 in the 0.2-10.0 keV range from Swift-XRT as a function of time (MJD). The spectral index values are the same as the ones in the last column of tab. 4.7, except for the first two entries, which are merged into an average because they were taken on the same day. The dashed fitting line, obtained after a 0-re-definition of the x-axis date origin (upper side of the plot), has a slope $\alpha_x \approx 1.26 \cdot 10^{-4}$/dy, so the trend is $p_x = 2.3 \pm 0.1$ with no significant changes if compared to the total period encompassing Swift observations (384 dy). The dotted line stands for $p_x = 2$ for reference. The figure on top is just an inset of the bottom one, for better displaying the first set of TON 116 observations performed by Swift (March-April 2021).

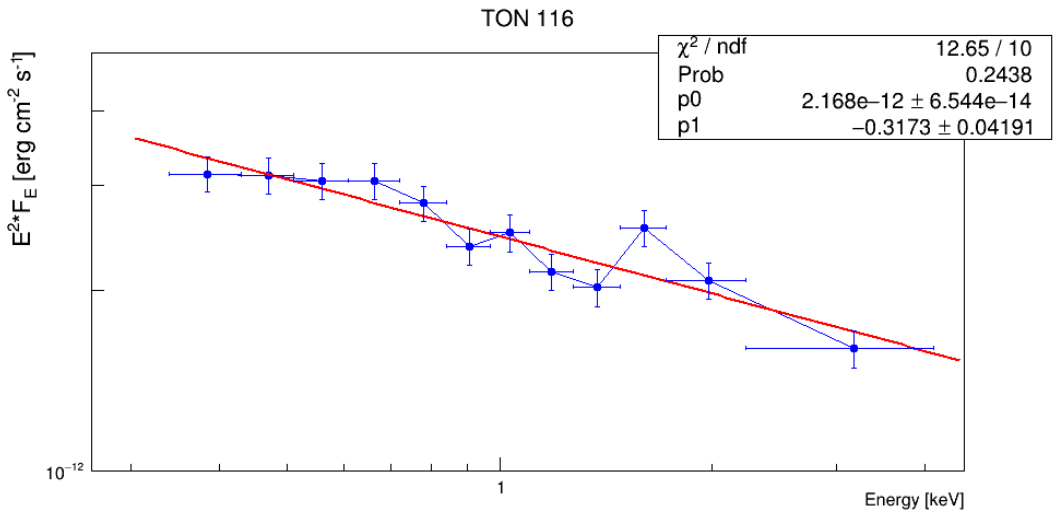

Figure 4.24: SED of TON 116 in the 0.2-10.0 keV range obtained by Swift-XRT for the total period 2021-2023. The data points are consistent with a power-law fit corresponding to an intrinsic spectral index $p_x = 2 - \mathrm{p}_1 = 2.3 \pm 0.1$ and a normalization constant $k_x = \mathrm{p}_0 = (2.2 \pm 0.1) \cdot 10^{-12}$ erg cm^{-2} s^{-1} (red solid line).

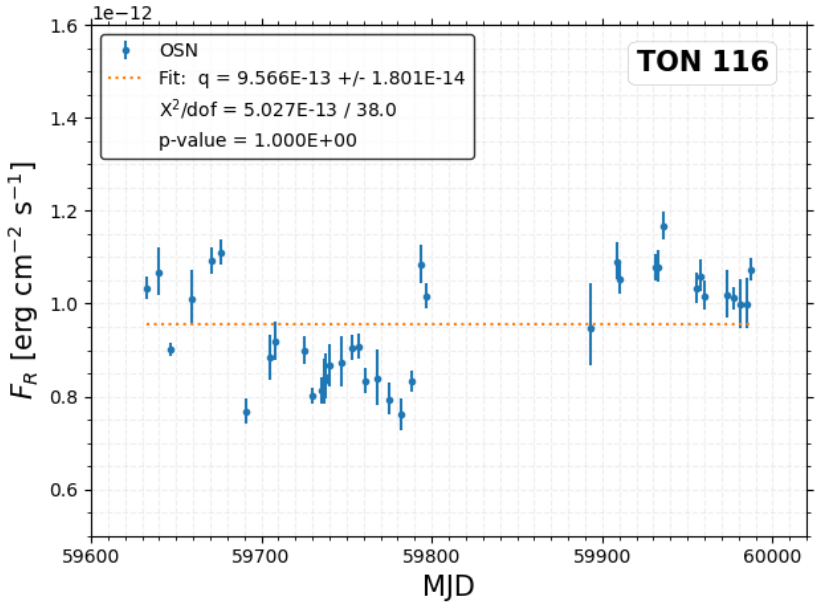

Figure 4.25: Light curve of TON 116 in the R optical band (Johnson-Cousins filter) made up of 39 observations averaged on a daily basis, which were taken by either T150 or T90 telescopes of OSN from 23rd February, 2022 to 12th February, 2023. The data points are fitted with a constant line representing a mean flux of $F_R = (9.6 \pm 0.2) \cdot 10^{-13}$ erg cm^{-2} s^{-1} (orange dotted trend).

4.3.4 Broadband Spectral Energy Distribution

In this subsection we put the TON 116 results obtained so far for the 2021-2023 time range, namely the SED data points as inferred by MAGIC (Subsec. 4.2.5), *Fermi*-LAT (Subsec. 4.3.1), Swift-XRT (Subsec. 4.3.2), and OSN (Subsec. 4.3.3) all together. The complete picture of such observational campaigns is given in Fig. 4.26, which shows the available datasets taken with different telescopes as markers having different shapes and colors. The spectral bands covered are the fundamental ones allowing for an approximate representation of the overall emission trend. In particular, the double-peak feature typical of blazars (Sub-subsec. 1.3.6.1) is roughly visible from the available data, and basically it seems to be at the same flux level. In other words, the source does not show any Compton-dominance. From the "revised blazar sequence" point of view, this is consistent for TON 116 to belong to the BL Lac class (see again Sub-subsec. 1.3.6.1). From the position of the OSN point and the X-ray slope depicted by Swift dataset, one can barely constrain the low-energy synchrotron peak to be located at a frequency $\nu_{p,s} \gtrsim 10^{16}$ Hz. This confirms the HBL nature of the source as has been already highlighted in the literature, in particular from the 4LAC *Fermi* catalogue (Sec. 4.1, Fig. 4.1). The Compton feature, although mostly through upper limits (especially for MAGIC, also showing some deviation in LE), is quite well represented thanks to the results provided by MAGIC. The latter also constitute the first information on the VHE behaviour ever for TON 116. More in detail, the combination of Fermi and MAGIC data, probing the hard and the steep part of the high energy bump respectively, sets the estimated high-energy peak to $\nu_{p,c} \lesssim 10^{25}$ Hz. Converting the latter frequency to energy, the Compton bump likely reaches its maximum at some tens of GeV, in agreement with the *Fermi* insights (Fig. 4.20). Beyond that value, the source emission at the most extreme energies seems to be highly suppressed. In order to get some plausible information about the SED behaviour of TON 116 in its entirety, in the next chapter the discussion will focus on how can the TON 116 broadband emission be best-modeled. For this purpose, we will refer to the main particle processes ongoing throughout BL Lac blazars (see Sub-subsec. 1.4.1.1).

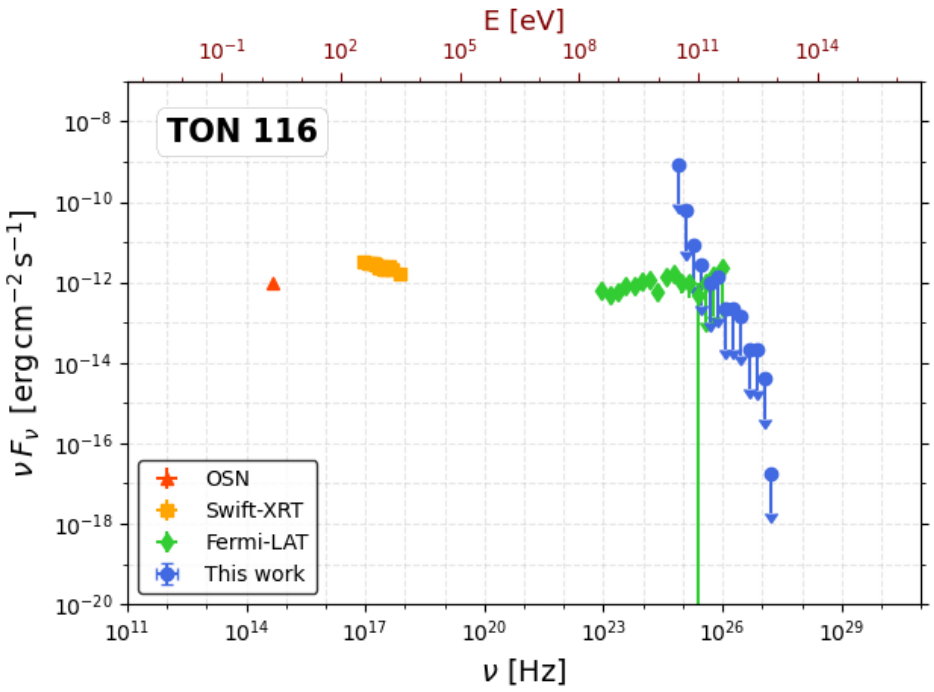

Figure 4.26: TON 116 total SED obtained by combining OSN (red triangles), Swift-XRT (orange squares), *Fermi*-LAT (green diamonds), and MAGIC (blue circles) observational datasets taken in the period 2021-2023. From the available X and γ slopes, a double-peak trend typical of BL Lacs (with no evidence of a Compton-dominance) can be guessed such that $\nu_{p,s} \gtrsim 10^{16}$ Hz (confirming source selection estimate, see Fig. 4.1), whereas $\nu_{p,c} \lesssim 10^{25}$ Hz, corresponding to an energy of some tens of GeV (as already suggested by *Fermi* satellite, Fig. 4.20). The MAGIC ULs are in good agreement with a fast decrease of the blue tail of the IC bump.

Chapter 5

SED modeling and interpretation

In this chapter we will discuss the results extensively described in the previous Ch. 4. In particular, we will focus on the modeling of the broadband SED already shown in Fig. 4.26 (Subsec. 4.3.4). In this framework, we will consider only the simple one-zone leptonic SSC model (Sub-subsec. 1.4.1.1). For implementing such a theoretical representation of the emission mechanisms powering the jetted AGNs, we considered two different approaches. In the first, we used the python package `agnpy` (Sec. 5.1). In this case, the fitting procedure has been implemented with the python-based statistical package for data handling called `sherpa`. On the other hand, as a second approach, we used the open-source MMDC (Sec. 5.2) online tool which accounts for the only implemented one-zone SSC model (further models are in developing phase). This tool also searches for archival MWL data in order to estimate the best parameterization for the source under investigation. In our framework, we decided to consider the MWL data that we have directly analyzed and extensively described in the previous Ch. 4.

We tested two different tools for model parameters estimation, in order to deeper understand what kind of procedure is more effective and returns increasingly realistic description of the phenomena operating in AGNs. In particular, the usage of the very recently released MMDC gives us the opportunity to test the convolutional neural network techniques implemented in this online tool against the standard statistical methods used by the `sherpa` package. Unfortunately, MMDC is still in a very initial phase and several methods have to be developed yet, such as the possibility to take into account upper limits. Indeed in this work, the ULs, especially at the VHE regime, assume a key role that it is worth to include. As a consequence, at the moment of this thesis writing, the most efficient method for dealing with MWL data and SSC models is `agnpy`, in combination with `sherpa` package.

5.1 agnpy-sherpa modeling

Among the currently-available open-source software, one of the latest and most promising code is `agnpy`[1]. It is a package built on `NumPy`, `SciPy`, and `astropy` python packages, specific for modeling radiative processes attributable to relativistic particles accelerated along the jets of AGNs (Nigro et al. 2022). The focus offered by the package is on leptonic scenarios, whose main radiative processes are implemented following notation and formulae by Dermer and Menon (2009b). Apart from being publicly available, its major advantage is that multiple host-galaxy structures other than just the jet are taken into account in the SED calculation, which are either associated thermal or line emission (Subsec. 1.3.2 and 1.3.3). Thermal radiation includes a geometrically thin accretion disk (modeled as in Dermer, Finke, et al. 2009 on the base of Shakura and Sunyaev 1973), the CMB, and a point-like source placed behind the jet[2]. On the other hand, line emission includes a BLR, assumed as an infinitesimally thin sphere re-processing some of the disk photons in a monochromatic final state (Finke 2016), and a dust torus represented as a ring re-emitting the absorbed radiation from the disk as a single-temperature black-body[3]. Some of the components can still be set as multi-temperature BBs. Furthermore, absorption phenomena due to EBL or γ-γ pair production on several photon fields are considered as well. For jetted point-like sources like blazars, radio frequencies below 10^{11} Hz are usually excluded from the calculation, as they are commonly associated with emission coming from nearby extended regions. The reliability of `agnpy` is ensured by comparison with outputs from both the literature and other open-source software, showing a general agreement within 30%. However, its main limitation is that no time evolution, e.g. the one describing the change of both blob and embedded electron properties, is accounted for. Nevertheless, self-consistency of the constraints on the model parameters is provided by the `constraints` module[4]. Another drawback is due to the fact that the package itself is meant for numerical modeling, therefore data handling and fitting are out of its primary scope. However, the latter functionalities can be achieved by combining `agnpy` with special wrappers specific of γ-ray `python`-oriented analysis tools, such as the ones implemented along with `gammapy` (Deil et al. 2017) or `sherpa` (Freeman, Doe, and Siemiginowska 2001) packages. These environments allow the user to easily define regriddable 1D models, which by means of a set of input parameters, can be used to fit broadband data accounting for different radiative processes.

5.1.1 Procedure implementation

Provided that TON 116 is a BL Lac source (Subsec. 1.3.6), in particular an HBL (see Sec. 4.1, broadband SED in Fig. 4.26), we considered its emission to be mainly due to a leptonic SSC

[1] https://agnpy.readthedocs.io/en/latest/.

[2] This is mainly useful for consistency checks in case very large distances from the SMBH are examined.

[3] A visual representation of the AGN structure is given in Fig. 1.2.

[4] For instance, γ_{br} and γ_{max} factors get assigned by simple evaluations involving acceleration, cooling, and ballistic time-scales associated with the blob.

model (Sub-subsec. 1.4.1.1). In this regard, the `SynchrotronSelfComptonModel` method is initialized by specifying a plausible initial electron distribution and a `sherpa` wrapper, for tuning the SSC scenario and loading the available dataset (`ecsv` format) respectively. Among all the parameters defining the model, we made sure that the redshift only is frozen at $z = 0.5$. The remaining ones were left free to vary, and reach their best values at the end of the procedure. The fit to the MWL points is done taking also into account systematics[5]. The Test-Statistic quantity is χ^2, and the procedure relies on the Levenberg-Marquardt method (Levenberg 1944, Marquardt 1963), acting as optimizer. Table 5.1 contains all the relevant quantities obtained from each of the `agnpy-sherpa` data fitting. Concerning the energy distribution of electrons streaming in the jet, here the SSC model is set by means of either a power-law (PL) and a broken power-law (BPL) functions. In particular, as the flux points represent the most certain spectral behaviour, while upper limits represent upper constraints on the high-energy bands, we wanted to find first a likely emission model including the former only. This is also because upper limits may generally show a more scattered displacement with respect to flux points, thus challenging the fit procedure (see e.g. the last *Fermi* HE points and the first MAGIC LE points in Fig. 4.26). Nevertheless, as observations by MAGIC somehow unveiled the most extreme emission from TON 116 for the first time, we also aimed at checking whether the new upper limits constitute a valid model discriminator. In other words, our goal was to see if the inclusion of the VHE flux constraints can effectively push towards some preferred emission model.

5.1.2 Fit results

An inset view of the broadband SED is displayed in Fig. 5.1. The SSC model based on a power-law for the description of the electron energies, which also comprehends the upper limits, is pretty coincident with the one not including them up to the low-energy side of the Compton bump, but beyond seems to be much more coherent with the constraints that we found at VHE. On the other hand, assuming the PL hypothesis implies that the synchrotron bump peaks at a frequency larger than 10^{17} Hz, which is equivalent to state that TON 116 belongs to the EHBL blazar class (Subsec. 1.3.6). This is something out of the state-of-the-art knowledge about the source (see e.g. Fig. 4.1). Beyond the low-energy peak, the computed SED is characterized by a steep decrease up to around 10 keV, followed by a hard rise of the Compton bump. The latter is foreseen to reach its peak at different frequencies depending on whether the upper limits are taken into account or not. If they are, the model locates $\nu_{p,c}$ at energies corresponding to some tens of GeV, as recent observations suggest (in particular by *Fermi* and MAGIC, Fig. 4.26). Otherwise, the Compton peak is expected to occur at least at 100 GeV, but as already outlined, MAGIC constraints turn out to not be respected. The third SSC model under study is set up with an energy distribution of accelerated electrons following a broken power-law like the one

[5]Systematic errors can be included through a python *dictionary* variable, and are summed in quadrature to the statistical ones. The following percentages are assumed: 5% for OSN, 10% for both Swift-XRT and *Fermi*-LAT, 30% for MAGIC.

in eq. 1.16. The output SED shows a decreased emission from radio to optical bands, but an increased one from optical up to $\sim$ MeV range, above which the high energy bump starts to dominate. The most remarkable aspect of the latter is that it is well reproduced in its entirety, also for what concerns the ULs coming from MAGIC, even if they are not included in the fit procedure. Indeed, we decided to exclude them, and the associated broadband behaviour too, as they somehow introduced some disturbance during the fit operation, ending in a not reliable result for the general SED. The BPL model predicts the synchrotron peak to be located at $E \approx 100$ eV, whose corresponding frequency is certainly closer to $\nu_{p,s} \gtrsim 10^{16}$ Hz (Fig. 4.1), and more compatible with HBL objects.

Among the whole set of parameters returned by this `sherpa`-based `agnpy` fit, a particularly interesting one is the time variability t_{var}. As already described in Sub-subsec. 1.4.1.1, it represents the minimum amount of time after which a significant change of incoming flux from a certain source is detected. In the SSC framework of blazar radiation, this time quantity can be related to the size of the emitting blob relativistically moving outward along the jet (see causality relation eq. 1.13). In the case of TON 116, basically no firm information about t_{var} is available. The presented fit predicts it to be of the order of 10^3-10^4 s, roughly corresponding to 0.5-10 h. Hopefully, in the near future deeper observational campaigns can help not only in investigating more spectral windows for the best model to be selected, but also in shedding light on the variability time, which is one of the most fascinating parameters characteristic of the blazar class.

5.2 MMDC fit

In this section we present the fit results on the total energy distribution of TON116 (Fig. 4.26) using the *Markarian Multi-wavelength Data Center* (MMDC) online tool[6]. This is a newly-developed platform owned by ICRANet Armenia Center, which is publicly available to allow for either searching for archival data and building fitted SEDs for a huge set of known blazars. The tool offers the possibility to visualize flux points in a highly interactive manner, by means of several band/time filters. For what concerns data interpretation, the fitting procedure relies on convolutional neural networks (CNNs) algorithms, trained on a huge set of blazar spectra created with SOPRANO (Simulator Of Processes in Relativistic AstroNomical Objects) kinetic code. The main strong point is a computationally intensive structure which, despite a time-demanding training phase, can rapidly create a plausible modelization according to the selected emission scenario. The procedure also takes into account secondary radiation processes in a self-consistent way. The conjunction with the bayesian inference algorithm *MultiNest* (Feroz, Hobson, and Bridges 2009) ensures high-accuracy results for the posterior distribution of model parameters, efficiently found starting from broadband SED data. The latter can be directly uploaded in a specific format by the user, with the only caveat that frequencies $\nu < 10^{11}$ Hz are excluded due

[6] http://www.mmdc.am.

Table 5.1: Fit results for TON 116 broadband SED data (by OSN, Swift-XRT, *Fermi*-LAT, and MAGIC, see also fig. 5.1). The procedure is based on a sherpa wrapper throughout the agnpy python package, specific for modeling of AGN radiative processes. Given the BL Lac nature of TON 116, leptonic SSC emission models have been considered: the first column contains the best-fit parameters assuming a simple power-law (PL) for the electron energy distribution, with no upper limits (ULs) included for simplicity (neither by *Fermi* nor by MAGIC), the second column contains the best-fit parameters assuming again a power-law for the electron energies but including the total dataset (both flux points and upper limits), while the third column lists the best parameters assuming instead a broken power-law (BPL) for the electrons but excluding upper limits, as apparently, inclusion of the latter introduces too much noise for a reliable convergence. Other than the parameters specific for SSC models (Sec. 1.4) and the ones describing the goodness of fit (χ^2/dof, where χ^2 is the TS and dof are the degrees of freedom), the modelization does also allow for a rough estimate of the time variability t_{var}, which is derived from eq. 1.13.

	PL (no ULs)	PL (ULs included)	BPL (no ULs)
χ^2/dof	26.35/19	40.74/36	17.28/17
Q-val	0.121	0.270	0.435
$\mathrm{Log}\,(k\,[\mathrm{cm}^{-3}])$	5.74 ± 0.84	5.14 ± 0.15	-6.1 ± 1.1
p_1	2.54 ± 0.04	2.54 ± 0.03	2.16 ± 0.23
p_2	–	–	3.68 ± 0.16
γ_{min}	1.00	1.00	100
$\mathrm{Log}\,(\gamma_{br})$	–	–	4.59 ± 0.31
$\gamma_{max}\,[10^5]$	2.10	2.10	10.0
δ_D	100 ± 189	23.1 ± 1.5	19.4 ± 7.5
$\mathrm{Log}\,(B\,[\mathrm{G}])$	-1.32 ± 0.81	-0.683 ± 0.077	-0.329 ± 0.556
t_{var} [ks]	1.93 ± 7.26	35.0	29.3

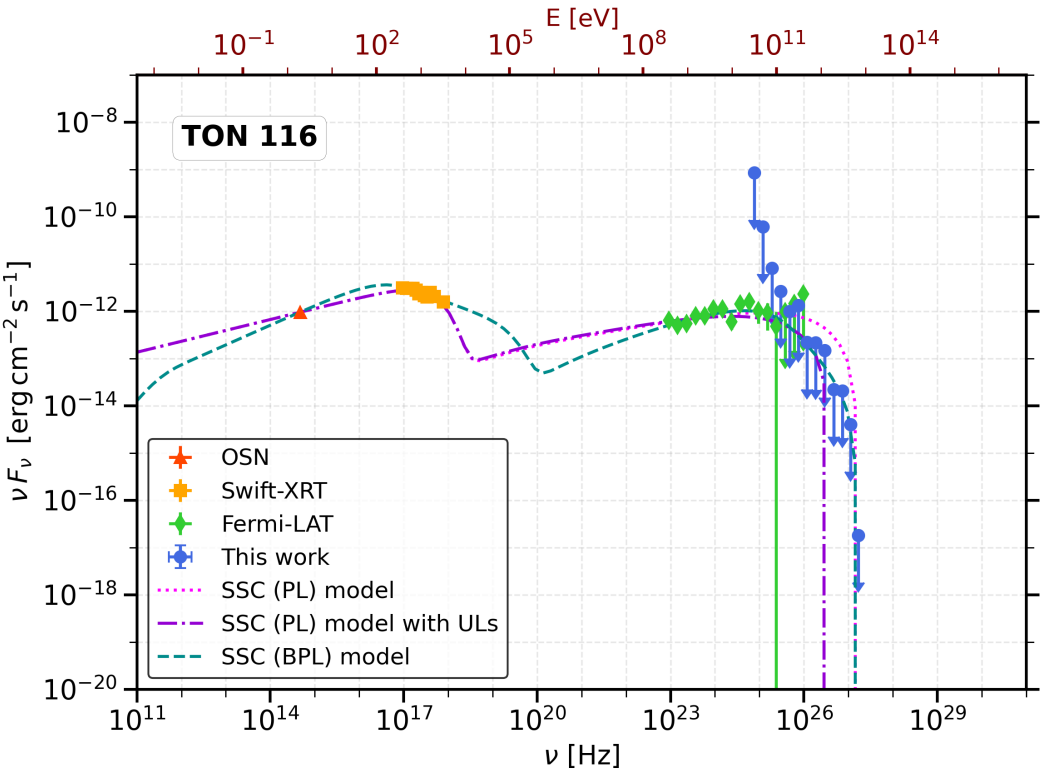

Figure 5.1: Fit on TON 116 broadband dataset (already shown in Fig. 4.26) as obtained by a sherpa wrapper throughout the agnpy python environment. Three likely trends of the overall SED behaviour, all of them in a leptonic SSC context with a fixed redshift $z = 0.5$, are represented: the magenta dotted line represents an SSC (PL) model, computed assuming a simple power-law (PL) for the energy distribution $n(\gamma)$ of electrons, with the exclusion of both *Fermi*-LAT and MAGIC upper limits. The violet dash-dotted line also stands for an SSC (PL) model but includes the *Fermi* and MAGIC upper limits (ULs). The dashed cyan line is an SSC (BPL) model, which incorporates a broken power-law (BPL) as electron energy distribution, with upper limits excluded. For the associated list of the best-fit parameters, see table 5.1. The SSC (PL) model including both *Fermi* and MAGIC upper limits (basically coincident with the one excluding the latter up to a frequency $\nu \lesssim 10^{25}$ Hz) significantly improves the assumed behaviour of the source, as it effectively takes into account the constraints to the flux at the most extreme energies. The BPL scenario, computed without upper limits for a reliable output, apparently constitutes a good representative of the VHE constraints too despite not including them.

Table 5.2: Fit results for TON 116 broadband SED data (by OSN, Swift-XRT, *Fermi*-LAT, and MAGIC, see also Fig. 5.1) obtained through the MMDC online tool, based on a CNN procedure. A leptonic SSC emission model has been considered again, with a power-law for the electron energies (the only available therein). The fundamental parameters are basically the same as before, apart from the electron luminosity L_e, which represents a different normalization quantity.

p	δ_D	γ_{min}	γ_{max}	B [G]	R_b [cm]	L_e [erg s^{-1}]
2.11	22.0	256	$2.57 \cdot 10^5$	0.0929	$1.25 \cdot 10^{16}$	$2.61 \cdot 10^{43}$

to hard convergence associated with self-absorption processes. The method has been successfully tested on both the well-known Mrk 421 and 1ES 1959+650 blazars, as shown by Bégué et al. (2023). The paper also contains further details about how such an advanced fit works.

Given the HBL nature of TON 116, once again we concentrated on a leptonic scenario, i.e., an SSC model (Sub-subsec. 1.4.1.1). Beside the basic synchrotron and IC emission mechanisms, this model incorporates both a self-consistent cooling for electrons, and pair creation/annihilation phenomena. Absorption from EBL is also considered in our fit attempt, according to the model provided by Domínguez et al. (2011). As a data-related input, we included all the inferred TON 116 datasets (frequency, flux, flux error) for the years 2021-2023, but we decided to not use MAGIC information. Indeed, at the writing time of this thesis, the MMDC online tool cannot handle ULs, since, if implemented, they are considered as flux points and not as ULs. Hence, the fitting procedure tries to fit these ULs returning an unplausible Compton-dominated SED.

5.3 SSC model parameters

The best-fit parameters resulting from both the `agnpy` (table 5.1) and MMDC (table 5.2) fitting procedures show some similarities, but also some major differences. First of all, it is worth to recall that in the MMDC procedure, only a simple power-law can be considered for the energy distribution of electrons $n(\gamma)$ in the SSC scenario (at present at least). The `agnpy` package, instead, offers the possibility to implement one out of a set of different functions for $n(\gamma)$. The slope of the assumed energy distribution of electrons (p), if a simple power-law (PL) function (eq. 1.15) is assumed for the electron distribution, is between 2.11 and 2.54, as reported by MMDC and `agnpy` respectively. The discrepancy is only 0.43, so they are in good agreement between each other. The latter `agnpy` case is valid for either the inclusion and exclusion of the *Fermi* and MAGIC upper limits. For what concerns the alternative BPL model, assuming a broken power-law (eq. 1.16) for the electron distribution, the first slope is intermediate of the two above-mentioned values, yet very close to the unique MMDC slope ($p_1 = 2.16$ and $p = 2.11$ in the respective case). The second slope (beyond γ_{br}) is quite steep, as it approaches a value $p_2 = 4$. Note, however, that the reported energy interval of the electron distribution is different in the two cases. Indeed, although the minimum Lorentz factor is basically of the same

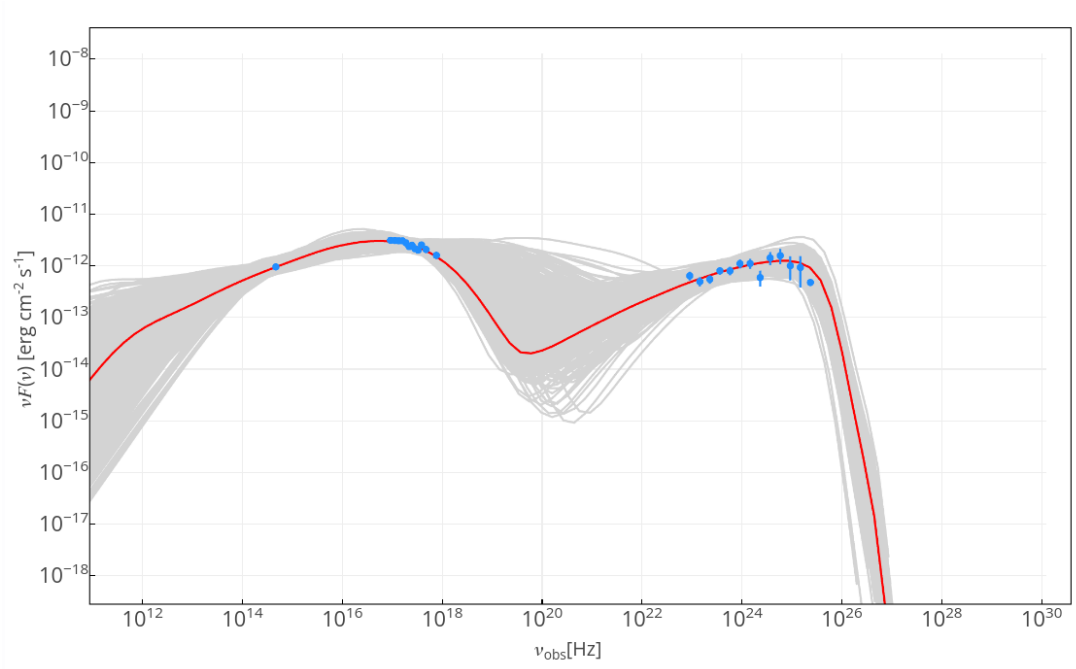

Figure 5.2: Fit on TON 116 broadband dataset as obtained by the CNN procedure integrated in the MMDC online tool. The most plausible SED of the source (red line) is computed including the observed flux values from OSN, Swift-XRT, and *Fermi*-LAT (from left to right, blue points). MAGIC outcome, as well as the last three high-energy points by *Fermi*, were excluded, as upper limits are prone to too noisy effects with respect to the overall behaviour. The double-peaked trend is compatible with an SSC one-zone model, assuming a simple power-law for the energy distribution of the electrons. The list of all the best-fit parameters is shown in table 5.2. A redshift $z = 0.5$ and EBL absorption are also considered. The software efforts in finding the best emission model for TON 116 are appreciable by means of the grey lines densely displaced in the background. The selected spectral behaviour is similar to the one resulting from an SSC model with a broken power-law for the electron energy distribution, as given in Fig. 5.1. The predicted SED does still appear to be highly suppressed at the highest energies. Plot credits MMDC.

order of magnitude (100 for agnpy, 256 for MMDC), the maximum one is increased by a factor ~ 10. For the PL model instead, the opposite is true. Namely, agnpy and MMDC do agree with each other for the same order of magnitude of the maximum Lorentz factor ($\sim 2 \cdot 10^5$), but the returned minimum one is 1 and 256 respectively. Again, this is true if either ULs are included or not. In the case of BPL, the γ_{br} value is located at quite a high energy value with respect to the total energy range ($\approx 10^{4.59}$). This is consistent with the HBL nature of TON 116.

The blob, assumed to be relativistically moving outward of the TON 116 blazar system (Sub-subsec. 1.4.1.1), shows different properties in the context of the two fits considered. The best-fit blob radius from MMDC is $R_b \approx 1.25 \cdot 10^{16}$ cm, corresponding to ≈ 4.05 mpc. The one from agnpy is not directly returned by the procedure, but can be inferred through the variability time according to eq. 1.13. Namely, for the SSC PL models, $R_b \approx 3.86 \cdot 10^{15}$ cm (≈ 1.25 mpc) and $R_b \approx 1.62 \cdot 10^{16}$ cm (≈ 5.25 mpc) with ULs excluded and included respectively. For the BPL model instead, $R_b \approx 1.14 \cdot 10^{16}$ cm (≈ 3.69 mpc). Another quantity linked to the blob radius via the variability time is the Doppler factor δ_D (same eq. 1.13), standing for the relativistic boost of incoming radiation (see eq. 1.14). The one returned by MMDC agrees with both the one of BPL and PL with ULs models by agnpy, all basically being around 20. A remarkable exception is represented by the PL model with no ULs, giving a much larger $\delta_D = 100$, which is associated a much larger error as well.

The magnetic field, a fundamental ingredient for giving rise to the exceptional emission from blazars (see Sub-subsec. 1.3.6.1 and 1.4), turns out to be of the order of 10^{-2}-10^{-1} G for MMDC and PL with no ULs agnpy model, while it is larger for PL model including ULs and BPL model (≈ 0.21 G, 0.47 G respectively).

In the MMDC and the agnpy fit procedures there is an additional difference, which is the normalization constant. In general, this is used to initialize the particle energy distribution to a fixed value (eq. 1.15 and footnote below). MMDC uses the electron total luminosity L_e, whose best-fit value is $2.61 \cdot 10^{43}$ erg/s, while agnpy uses the total particle density. The latter parameter is very high in the case of both the SSC PL models ($\approx 10^{5.1}$ and $10^{5.7}$ cm^{-3} with and without ULs respectively), while very low for the BPL model ($\sim 10^{-6}$ cm^{-3}). From the χ^2 value, the best agnpy model turns out to be the SSC BPL model. As already outlined in Sec. 5.1.2, the model can effectively reproduce the synchrotron peak of an HBL object and the available IC-bump dataset. In particular, MAGIC ULs represent a good constraint even if they are not included in the fit procedure.

5.4 Discussion

The chance to catch overluminous BL Lacs is an intriguing opportunity for finding the outliers of the blazar sequence (Sub-subsec. 1.3.6.1). In this context, we proposed an observing campaign of selected sources with the MAGIC telescopes (Subsec. 4.1.2). In particular, we focused on TON 116 that represents the source of interest of this thesis work, and it has been for the first time

observed at VHE and analyzed. TON 116 has been selected as a potential outlier of the sequence because of its enhanced luminosity listed in the 4LAC catalogue (Ajello et al. 2020). The *Fermi* collaboration assumed a redshift $z \approx 1$, but the distance of the source is still uncertain. The latest estimation gave a less lower limit $z > 0.483$ (Paiano et al. 2017). In this framework, the estimation of the source distance – if it is detected – exploiting an alternative method, accounting for the combination of high and very-high energies (Prandini et al. 2010, see Sub-subsec. 1.3.6.3), represents a significant opportunity in order to shed light on the potential sequence outlier.

Although TON 116 has not been detected by the MAGIC telescopes (see Fig. 4.15) during three observing cycles (2021, 2022, 2023), the estimation of the spectral ULs (see Fig. 4.17) allowed us to shed light on the blue tail of its SED. Indeed, as you can see from the *Fermi*-LAT spectra (see Fig. 4.20), the curvature of the spectrum above some tens of GeV constitutes an evidence of the EBL absorption suppressing the spectrum at VHE, and leads to the estimation of the IC peak position (see Subsec. 5.1.2, Sec. 5.2). Moreover, TON 116 has experienced a low activity in the period 2021-2023 in coincidence with MAGIC observations (see Fig. 4.20). The non-detection of TON 116 has not allowed us to set an alternative estimation of the redshift of the source through γ-ray observations, as done by Prandini et al. (2010).

Nevertheless, the constraints on the blue tail of the broadband SED allowed us to discuss on the theoretical models fitting the MWL behaviour of TON 116. Indeed, as you can see in Figs. 4.21, 4.23, and 4.25, in the period under investigation with MAGIC (2021-2023), TON 116 did not show a significant variability pattern. Hence, the collected and analyzed data (see Ch. 4) have been used to build the MWL SED displayed in Fig. 4.26.

In order to understand the emission mechanisms powering the jetted AGNs and to shed light on the relativistic phenomena within the jets, we modeled the broadband SED with one-zone leptonic SSC model (Sub-subsec. 1.4.1.1). In this sense, we used two different approaches based on two different tools: `agnpy` and MMDC (Sec. 5.1 and 5.2 respectively).

Here we recall the main parameters used for the modelization of the blazar phenomenon. In particular, we focus on HBL objects (Subsec. 1.3.6), in accordance with the TON 116 type (Sec. 4.1). Being BL Lac objects, this kind of sources likely host a scarce radiation environment (Subsec. 1.3.6), thus the preferred scenario is the SSC model (Sub-subsec. 1.4.1.1). According to this model, the emitting region is a spherical blob with radius R_b, moving farther from the SMBH in the jet at relativistic velocity v. The blob is associated with a bulk Lorentz factor Γ_b, which together with $\beta = v/c$ and the direction of propagation with respect to the line of sight θ, defines the Doppler factor δ_D (eq. 1.14). The latter links the comoving frame (with the blob) to the galactic frame, thus represents the relativistic boosting of the radiation emitted[7]. We remind that, at fixed redshift, the time variability can be used as a link between δ_D and the blob radius through eq. 1.13. The blob radiation is due to a population of embedded relativistic electrons emitting by synchrotron, as the blob moves in a tangled magnetic field $\overline{B}$ assumed to be uniform. In the SSC

[7]To calculate the contribution to an inertial frame observer, a further factor $(1+z)$ has to be accounted for, and the perceived flux is δ_D^4 times the one in the comoving frame.

scenario, synchrotron photons are up-scattered by IC process with the same parent electrons, giving rise to the high-energy bump. The electrons are assumed to have a uniform and isotropic energy distribution that can be expressed solely in terms of their Lorentz factor γ (Dermer and Menon 2009b) through the numerical density $n(\gamma)$. As the radiation processes are non-thermal, usually a power-law (PL, eq. 1.15) or a broken power-law (BPL, eq. 1.16) are assumed for the numerical density[8]. The function is only considered in an energy range $[\gamma_{min}, \gamma_{max}]$. The PL case assumes a unique slope p_1, while the BPL case assumes two different slopes p_1 and p_2. In particular, the break value γ_{br} represents the energy at which the power-law slope changes from p_1 to p_2, which gives the maximum synchrotron contribution. The normalization constant k of $n(\gamma)$ depends on the different approach used to define a global fixed quantity, obtained by a proper integration of $n(\gamma)$. In our `agnpy` fit case, for instance, it refers to the total volume density of electrons (still comoving frame) via

$$n_{tot} = \int_1^{+\infty} n(\gamma)\, d\gamma \quad . \tag{5.1}$$

The total electron luminosity L_e used in MMDC, instead, can be seen as related to the total energy in electrons

$$W_{tot} = m_e c^2 \int_1^{+\infty} \gamma N(\gamma)\, d\gamma \quad , \tag{5.2}$$

where m_e is the electron mass, c is the speed of light in vacuum, and $N(\gamma)$ is the differential number of electrons. At a fixed energy, the latter quantity is given by the electron density times the volume of the blob, namely $n(\gamma) \cdot \frac{4}{3}\pi R_b^3$. The parameters listed so far are used to compute the energy densities of photon fields coming from different AGN components, at different distances from the central SMBH (see e.g. Appendix A of Nigro et al. 2022). In case of FSRQs, given their rich environment (Subsec. 1.3.6), contributions from the disk, dusty torus, BLR (thermal/line emitters, Subsec. 1.3.2 and 1.3.3), and γ-γ absorption ($\tau_{\gamma\gamma}$, Sub-subsec. 1.4.1.3) are taken into account. Thus, the modeling of FSRQs is analytically more complicated, as it requires a larger number of model parameters. Indeed, the location of the blob and the properties of the single AGN components must be defined for properly setting the respective contribution to the total radiation field. For such objects, it is worth to follow the work of Ghisellini and Tavecchio (2009), as it contains prescriptions and scaling laws that are very useful to solve the puzzle. For instance, the size of the BLR region and that of the torus can be estimated through $10^{17} L_{d,45}^{1/2}$ and $2.5 \cdot 10^{18} L_{d,45}^{1/2}$ respectively, where $L_{d,45}^{1/2}$ basically is $L_{disk}/[10^{45}$ erg/s$]$. Further assumptions can be made on the inner and outer radii of the accretion disk, as well as on the SMBH mass M_{BH}, the efficiency η, and the accretion $\dot{m}$ (see Subsec. 1.3.2). One is also supposed to consider the fraction of the disk radiation reprocessed by the BLR or the torus, and the temperature of

[8]Further functions can be considered, e.g. a power-law with an exponential cut-off, or a *log-parabola* (slope changing logarithmically with γ).

the latter. In the case of BL Lac objects, as already mentioned, these contributions are usually neglected due to the poorly-populated environment at the sources.

In order to check for compatibility of the inferred parameters with the literature, we firstly looked at the fit results contained in Nigro et al. (2022) itself. The work applied the `agnpy` software tools to two sources, namely, Mrk 421 and PKS 1510-089. We considered the former, provided that it is an HBL like TON 116. Comparing the best-fit parameters in Table 1 of the paper (Fig. 5.3-left) with the parameters that we derived for TON 116 (tab. 5.1 and 5.2), especially the ones for the BPL model, they are in overall agreement between each other. The main differences are the density normalization, almost two orders of magnitude smaller than ours, and the magnetic field, which is larger in our case. In addition, the blob radius of Mrk 421 is at least a factor of 5 larger than the one obtained for TON 116 in the `agnpy` (and MMDC) case. This is consistent with a higher state of Mrk 421, despite the much lower density and magnetic field. However, the latter parameters agree with the lack of Compton dominance for both of the sources. The larger γ_{min} can explain the larger luminosity and the more peaked appearance of the SED bumps in the Mrk 421 case. Instead, the compatibility of γ_{br} and γ_{max} is consistent with basically the same $\nu_{p,s}$ and the high-energy limit of the bumps. The reader can have a direct look at the Mrk 421 spectral features in Fig. 5.3-right, where we show the fit on the Mrk 421 broadband SED by Nigro et al. (2022) for convenience.

	Mrk 421		PKS 1510-089	
Parameter	`Gammapy`	`sherpa`	`Gammapy`	`sherpa`
(a) Best-fit parameters				
$\log_{10}(\frac{k_e}{\mathrm{cm}^{-3}})$	−7.89	−7.89	−2.06	−2.05
p_1	2.06	2.06	2.00	2.00
p_2	3.54	3.54	3.16	3.16
$\log_{10}(\gamma'_b)$	4.99	4.99	3.01	3.01
$\log_{10}(B/\mathrm{G})$	−1.33	−1.33	−0.42	−0.42
δ_D	19.74	19.76	–	–
χ^2/d.o.f.	271.2/80	271.2/80	230.5/36	230.5/36
(b) Fixed parameters				
Parameter	Mrk421	PKS 1510-089		
δ_D	–	25		
γ'_{min}	500	1		
γ'_{max}	10^6	3×10^4		
R_b / cm	5.3×10^{16}	2.4×10^{16}		
θ_s	2.90°	2.22°		
r/cm	–	6×10^{17}		
$L_{disc}/(\mathrm{erg\,s}^{-1})$	–	6.7×10^{45}		
η	–	1/12		
$M_{BH}/M_\odot$	–	5.71×10^7		
R_{in}/R_g	–	6		
R_{out}/R_g	–	10^4		
ξ_{DT}	–	0.6		
R_{DT} / cm	–	6.5×10^{18}		
T_{DT} / K	–	10^3		
z	0.0308	0.361		

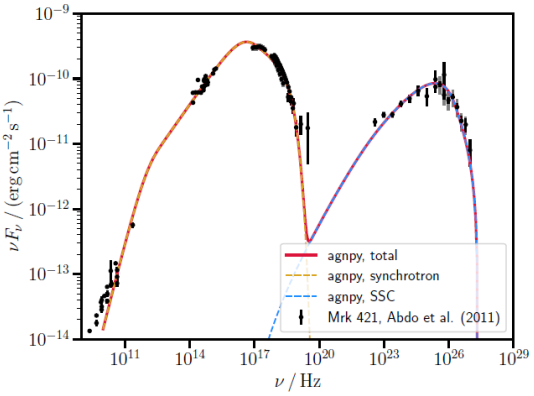

Figure 5.3: *Left*: Best-fit parameters obtained for the modelization (SSC one-zone scenario) of Mrk 421 and PKS 1510-089 SED with `agnpy` (`gammapy` and `sherpa` wrappers) by Nigro et al. (2022). *Right*: Plot of the resulting fit on Mrk 421 broadband data with `gammapy` wrapper. Table and plot taken from the same paper.

The compatibility of TON 116 parameters with those ones of Mrk 421 is good, but the latter source is much closer, having an estimated redshift of 0.031 (Ulrich et al. 1975). In order to avoid distance-related effects, we selected an additional target, PKS 1424+240. The latter source is also an HBL, whose γ-ray emission was discovered by *Fermi* (Abdo et al. 2009), and later on was detected at VHE first by VERITAS (Ong and VERITAS Collaboration 2009) and then by MAGIC (Teshima and MAGIC Collaboration 2009). PKS 1424+240 is among the farthest VHE emitters known, having an estimated redshift $z > 0.604$ (Furniss et al. 2013) similar to the one of TON 116 (Subsec. 4.1.2). Acciari et al. (2010) performed a fit on its broadband SED using an improved one-zone SSC model (Böttcher and Chiang 2002, with time evolution included), and found the best-fit parameters in Table 1 of the paper (Fig. 5.4). We refrain from showing the plot of the fit on the broadband PKS 1424+240 data, as the procedure and parameters are quite different from the ones used here. Still, from the table we can note that the blob radii are compatible with the ones of all our models for TON 116 ($R_b \sim 10^{16}$ cm), except for the PL with no ULs `agnpy` case which is an order of magnitude less. However, R_b of PKS 1424+240 is some factor larger at the estimated redshift of the source (last two columns on the right). The magnetic field is also quite compatible, as it ranges from ≈ 0.05 (PL with no ULs model) to ≈ 0.5 G (BPL model). The reported Doppler factor is also in general agreement, being comprised between ≈ 20 and 100 (PL model with no ULs). L_e is 1-2 orders of magnitude higher than the one inferred by MMDC, but maybe it depends on the different analytic method; see caption of Fig. 5.4 for some further detail.

Parameter	$z = 0.05$	$z = 0.10$	$z = 0.2$	$z = 0.3$	$z = 0.4$	$z = 0.5$	$z = 0.7$
L_e (10^{43} erg s^{-1})	1.60	4.12	10.7	18.9	29.2	47.1	88.8
L_B (10^{43} erg s^{-1})	1.66	5.47	16.9	31.1	45.9	49.8	66.2
γ_1 (10^4)	3.7	3.7	3.6	3.4	3.2	3.6	3.7
γ_2 (10^5)	4.0	4.0	4.0	4.0	4.5	4.0	4.0
D	15	18	25	30	35	45	60
B (G)	0.37	0.31	0.25	0.24	0.25	0.18	0.14
ϵ_B	1.04	1.33	1.59	1.65	1.57	1.06	0.75
R_B (10^{16} cm)	1.2	2.2	3.4	4.0	4.0	4.5	5.0

Figure 5.4: Best-fit parameters obtained for the modelization (improved SSC model) of PKS 1424+240 broadband SED as a function of redshift by Acciari et al. (2010). Some different notation and parameters were used, in particular, from top to bottom: L_B is the Poynting luminosity from magnetic energy density, γ_1 and γ_2 are the low- and high-energy cut-off of the *particle injection* function (resulting in a slowly varying broken power-law energy distribution of electrons), D is the Doppler factor, $\varepsilon_B := L_B/L_e$ is the magnetic field equipartition. Table taken from the same paper.

Few years later, MAGIC Collaboration, Aleksić, et al. (2014) reported on a MWL long-term study about PKS 1424+240. The authors performed a new fit on the broadband SED of the source, using a fully automatized χ^2-minimization procedure developed by Mankuzhiyil et al. (2011). The resulting best-fit parameters are shown in Fig. 5.5. Focusing on the one-zone SSC model, we can note that our TON 116 parameters are in overall agreement with the ones reported by that paper. In particular, the lower bounds of the electron distribution and γ_{br} (BPL model) are very compatible, while the upper ones are up to ~ 3 orders of magnitude larger, which results

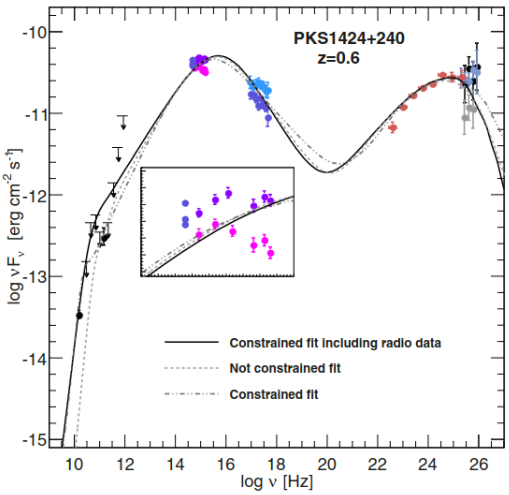

Model	$\gamma_{\rm min}$ [10^3]	$\gamma_{\rm b}$ [10^4]	$\gamma_{\rm max}$ [10^5]	n_1	n_2	B [G]	K [cm^{-3}]	R [10^{16} cm]	δ	$L_{\rm kin(p)}$ [10^{45} erg s^{-1}]	$L_{\rm kin(e)}$ [10^{45} erg s^{-1}]	L_B [10^{43} erg s^{-1}]
One-zone (No radio)	0.260	3.2	8.9×10^3	1.9	3.9	0.018	2×10^2	6.5	70	5	7.0	3
One-zone	0.016	2.6	3.9×10^2	1.7	3.7	0.006	50	5	131	64	21	0.8
One-zone (Constrained)	0.004	5.3	3.2×10^4	2.0	4.0	0.017	1.7×10^2	19	40	371	11	8.8
2 zones (in)	8.0	3.9	7.0	2.0	3.1	0.033	3.1×10^3	4.8	30	0.07	1.2	1.1
2 zones (out)	0.6	3.0	0.5	2.0	3.0	0.033	23	190	9	1.3	2.3	159

Figure 5.5: *On top*: Plot of the fit on the PKS 1424+240 broadband SED by MAGIC Collaboration, Aleksić, et al. (2014) using the automatized χ^2-minimization procedure of Mankuzhiyil et al. (2011), assuming SSC scenarios with $z = 0.6$. The inset is a zoom on the optical-UV range. *At the bottom*: Best-fit parameters obtained for the modelization of PKS 1424+240 broadband SED by MAGIC Collaboration, Aleksić, et al. (2014). Four SSC models were considered, from top to bottom: one-zone with no radio data, one-zone with radio data, one-zone with VLBA data constraints, and two-zone model with VLBA constraints in the outer emission region. The following quantities have different notation from ours: n_1 and n_2 are the spectral indices of the assumed broken power-law of the electron distribution, R is the blob radius, δ is the Doppler factor. The kinetic energy of electrons ($L_{kin,(e)}$) and protons ($L_{kin,(p)}$), as well as the contribution related to the magnetic field energy (L_B), were also considered. Plot and table taken from the same paper.

in a more extended blue tail of both of the bumps for PKS 1424+240. The slopes of the electron distribution are compatible as well, despite the fact that our BPL model predicts a slightly softer value for p_1. Concerning the magnetic field, our values are significantly higher (at least by a factor 4), which does not explain the smaller luminosity of the bumps of TON 116, but agrees with the peak shift towards slightly higher frequencies (especially the synchrotron one). The density normalization for both our PL `agnpy` models is larger (~ 3 orders of magnitude or more), whereas our BPL model predicts a much lower density normalization ($\sim 10^{-6}$ cm^{-3} against $\sim 10^2$ cm^{-3}). This is consistent with the larger luminosity of PKS 1424+240 bumps. The same holds for the resulting blob radius for TON 116, which apparently seems to be, again, smaller by a factor of at least ~ 5. Finally, the Doppler factor is rather compatible with the one inferred here, although generally higher. This supports a higher state of the overall trend of the PKS 1424+240 bumps too.

In summary, we can state that the best-fit parameters found for the modeling of the TON 116 broadband SED, by means of both `agnpy` and MMDC, are basically compatible with the ones that we can expect from the modeling of other HBL sources. The differences likely rely on the different properties of the objects considered, as well as different calculation procedures. In any case, the parameters' differences are overall consistent with the analytic construction of the SSC model.

We conclude this discussion by resuming the main scientific case that motivated us to undertake a detailed study of TON 116 like a potential outlier of the blazar sequence. This question basically arose from both a high luminosity in HE γ-ray band observed by *Fermi*-LAT – reported in the 4LAC catalogue (Ajello et al. 2020) assuming a redshift $z \approx 1$ – and an uncertain redshift estimation ($z > 0.483$, Paiano et al. 2017), which stimulated us to deeper investigate its behaviour at the extreme energies (VHE) with the MAGIC telescopes (Sec. 4.1, Subsec. 4.1.2). Unfortunately, the VHE detection of the source has not been achieved during the MAGIC observing campaign, preventing, as already mentioned, an alternative distance estimation. Indeed, the knowledge of the redshift allows to clarify whether the source is an exceptionally luminous BL Lac object simply because it is relatively close to us (like Mrk 421, see above) or, instead, it is an intrinsically luminous object located at farther distances. Under the latter condition, the source should effectively deviate from the standard framework of the blazar sequence. The lack of a new redshift estimation essentially keeps the question open.

In summary, the broadband emission of TON 116 (Subsec. 4.2.5 and Sec. 4.3, Fig. 4.26) is compatible with an SSC one-zone model (Subsec. 5.1.2 and Sec. 5.2), as expected for BL Lac objects (Sub-subsec. 1.4.1.1). In particular, `agnpy-sherpa` and MMDC results suggest that TON 116 SED can be best defined by a density-normalized SSC model assuming a broken power-law for the electron energy distribution (table 5.1) or by an L_e-normalized SSC model assuming a simple power-law with slightly hardened spectral index with respect to the first index of the BPL model. The latter PL case returns an electron energy range slightly restricted in its bounds, and a magnetic field decreased by a factor ~ 5. In the same PL case, the `agnpy-sherpa` model accounting for TON 116 upper limits is effectively consistent with the VHE ULs, but both of these models indicate TON 116 to behave like an extreme HBL. Additional observations can surely help in the choice of the best emission model. However, we could not rely on further *X*-ray observations provided e.g. by *NuSTAR* satellite, which would have allowed us to probe the spectral band (hard X) where the two broad bumps connect to each other. Further spectral bands were not available to us as well, like the radio domain. Indeed, the lower side of the synchrotron peak could be constrained by radio observations, allowing to discriminate among the suggested models.

Conclusions

This PhD thesis explored the intricate panorama of the long-standing discussion around the existence of the blazar sequence as an actual trend featuring the broadband spectrum of these objects or an observing bias affecting the measurements from the Earth position.

In this context, we presented an extensive multi-wavelength study of the extragalactic emitter TON 116. The source was discovered in 1957 in the optical band (Iriarte and Chavira 1957), and it is officially known as a jetted Active Galactic Nucleus (AGN) since 2000 (combining optical with radio and X-ray observations, White et al. 2000). TON 116 is a blazar, a subclass of AGNs,characterized by a radio jet nearly pointing towards the Earth. The reason that motivated us to study this source is the high state in the HE γ-ray band inferred by *Fermi*-LAT measurements and listed in the 4LAC catalogue (Ajello et al. 2020). Indeed, this feature apparently made the source go against the *blazar sequence* expectations (Ghisellini, Righi, et al. 2017) in consideration of an assumed redshift of $z \approx 1$. Precisely, the sequence – recently considered as ended by Keenan et al. 2021 – predicts the double-peaked trend of the blazar SED – thought to be due to synchrotron and inverse-Compton emission from particles streaming in the jet, in the low- and high-energy part of the spectrum respectively – becomes fainter and shifted towards higher frequencies for BL Lac sources. Therefore, if a BL Lac is found to be an overluminous object, it likely is an outlier of the sequence itself. Moreover by definition, BL Lacs basically show a featureless optical spectrum,as it implies an extremely challenging redshift determination. Indeed, our source is only assigned a lower limit on the redshift, namely $z > 0.483$ from a doublet MgII absorption feature recently confirmed by GTC observations (Paiano et al. 2017). The redshift information is crucial in order to define the actual luminosity of the source and its relation with the distance itself (larger/smaller when closer/farther and vice versa).

In order to deeper investigate the unexpectedly luminous TON 116, potentially belonging to the farthest known BL Lac objects, as reported in the 4LAC catalogue (Ajello et al. 2020) where at some extent the distance has been overestimated – we proposed to observe it for three observing cycles (Feb 2021 - May 2023) with the MAGIC telescopes. Unfortunately, our source has not been detected by MAGIC, whose observations allowed us to derive upper limits only for its VHE flux. As a consequence, no new redshift estimation was possible, exploiting the EBL-absorption-corrected method which provides the hardening of the VHE spectrum until the limit set by the HE slope measured by *Fermi* (Prandini et al. 2010). In turn, this prevented us

from clarifying the nature of TON 116 as an actual outlier of the blazar sequence.

Nevertheless, MAGIC observations allowed us to have the first inspection ever into the VHE side of the source, and to effectively constrain the blue tail of its IC bump, as it indicates an IC peak at $\lesssim 100$ GeV and a strong cut-off well before 1 TeV.

In this framework, we also combined MAGIC measurements with further instruments' data for reaching a general view of the TON 116 MWL SED. In particular, we exploited *Fermi*-LAT satellite to get new information about the hard tail of the IC bump. In the period 2021-2023, *Fermi* observations, in comparison with the whole dataset of the last 15 years, confirmed an exceptional low-state for TON 116. Despite that, *Fermi* measurements provided a confirmation about the expected location of the high-energy peak at some tens of GeV. The combination of this information with MAGIC results returns a good picture of the overall IC bump.

On the other hand, for probing the high-energy tail of the synchrotron bump, we made use of observations from Swift-XRT satellite in the X-ray regime. The analysis of these data showed a decreasing, quite hard trend of the flux with increasing energy, with no significant changes for all the spanned period (Mar 2021 - Mar 2022). Then, in order to investigate the low-energy side of the synchrotron bump, we exploited the R-band optical observations from the Sierra Nevada Observatory (OSN). These observations, apart from small fluctuations of the order of 22% at maximum, did not show any significant variation of the observed flux in the period under investigation (Feb 2022 - Feb 2023).

Finally combining all the results, we obtained the broadband SED for TON 116 which it has been modeled by means of two recently-developed software platforms, i.e., the python-based `agnpy` and the convolutional-neural-network-based MMDC tool. According to the `agnpy` fit, relying on the `sherpa` package, the TON 116 broadband emission is consistent with a simple one-zone Synchrotron-Self-Compton (SSC) model, as expected for the blazar type of our source. We essentially applied three different parameterizations of this leptonic model, considering a power-law (PL) or a broken power-law (BPL) for the electron energy distribution in the jet, with VHE upper limits (ULs) excluded or included in the procedure. The inclusion of the VHE upper limits in the PL model significantly improves the fit quality, as the ULs represent a good constraint at VHE on the expected trend at such high energies. However, both of these PL models push towards an extreme HBL behaviour for TON 116, which is in disagreement with the current classification of the source as a simple HBL.

In summary, the `agnpy-sherpa` modeling suggests the best representation for the TON 116 broadband emission is the SSC BPL model. This result is not only consistent with the HBL nature of the source, but it naturally takes into account for the VHE upper limits even if they are not included in the fitting procedure. On the other hand, the MMDC results predict a SED trend very similar to the one of the `agnpy` BPL model. In this case, the main differences with the `agnpy` model are a simple power-law for the electron distribution (with a slope very close to the first one of the BPL model), and a normalization to the electron luminosity instead of the particle density.

These results were finally compared with best-fit parameters associated with other HBLs

reported in the literature, namely Mrk 421 (Nigro et al. 2022) and PKS 1424+240 (Acciari et al. 2010, MAGIC Collaboration, Aleksić, et al. 2014). Particularly, PKS 1424+240 represents the most similar target to TON 116 based on its estimated distance ($z > 0.604$, Furniss et al. 2013). We found that the TON 116 best-fit parameters are in overall agreement with the ones of the compared HBLs, hence supporting the obtained results of the source under investigation in this PhD thesis.

In conclusion, the lack of a VHE detection by MAGIC has not allowed us to find a new redshift constraint. In turn, this prevented us from drawing a final statement about the nature of TON 116 as an actual outlier of the blazar sequence, that is, assessing whether its luminosity is due to a smaller distance or to an intrinsic enhanced emission. In any case, the fact that the source did not show any significant emission at VHE, combined with no apparent changes in the other spectral bands considered, leads us to doubt about TON 116 being a good candidate among the outliers of the blazar sequence.

Future perspectives could involve further multi-wavelength observations of the fascinating blazar TON 116. Two aims can be traced, both related to the well-known variability of this kind of objects. On one side, it could be worth to keep monitoring the VHE behaviour of the source. Particularly, in case of an enhanced emission at VHE associated to the detection of the source, a new redshift estimation can shed more light on its nature. If not, the source can still be interesting in the context of the upcoming observing facilities like CTAO, potentially reaching the weak VHE flux of the target more efficiently, thanks to a much improved sensitivity and effective area. On the other hand, observations in spectral bands different from the ones investigated in this work can help in confirming which emission model is the most suitable for describing the broadband SED of TON 116, like radio measurements.

Acknowledgements

For the completion of this work, the supervisors, cross-checkers, referees, and in general all the helpful colleagues found along with the PhD path are sincerely thanked. The MAGIC Collaboration is acknowledged for allowing the use of proprietary observational VHE data. Yet, MAGIC results presented in this thesis have not undergone the internal review procedure of MAGIC publications. For Swift data and analysis, the reference paper Evans et al. (2009) is acknowledged. This work made use of X-ray data supplied by the UK Swift Science Data Centre at the University of Leicester. *Fermi* Collaboration is acknowledged for its publicly available HE data used here. Also, this thesis was based on observations made with 150 cm and 90 cm optical telescopes at the Sierra Nevada Observatory, operated by the Instituto de Astrofísica de Andalucía (IAA-CSIC). Finally, some of the SED data used in this work were obtained from `agnpy` (Nigro et al. 2022) and from the MMDC, which both are acknowledged as public, innovative tools for current and future interpretation of astrophysical results.

Appendix A

TON Catalogue

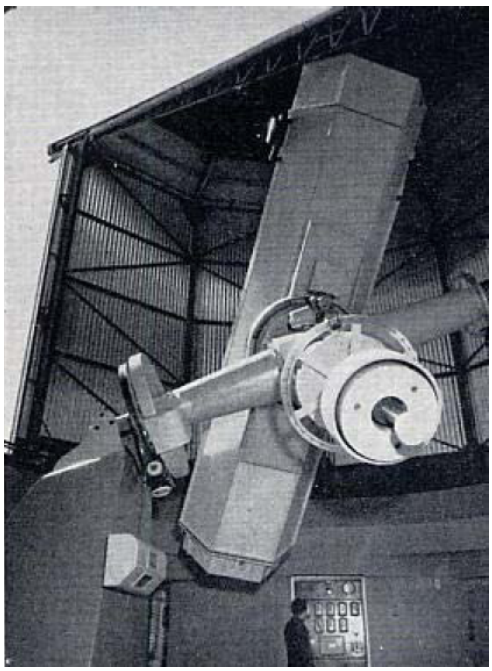

Figure A.1: Picture of the Schmidt camera of the OANTON telescope at nearly the time of inauguration. Taken from the INAOE website (https://astro.inaoep.mx/observatorios/oanton/camara-schmidt).

The National Astrophysical Observatory of Tonantzintla (OANTON) is located in the municipality of San Andrés Cholula, Puebla, Mexico. Its major instrument is a 0.77-m Schmidt telescope inaugurated in 1942 (see Fig. A.1), mainly thanks to both the founder prof. Luis Enrique Erro and the president of Mexico Manuel Ávila Camacho, exploiting a favourable geographical position[1]. The expectations of the facility were very high, mainly due to high quality instrumentation, which represented a real breakthrough for the development of modern astrophysics in Mexico. Furthermore, the relatively low latitude of the place ($\approx 19^\circ$ N) made it possible to explore both of the celestial hemispheres, in order to carry out studies on many different galactic as well as extragalactic objects. Nowadays, the facility is under the management of the National Institute

[1] https://www.inaoep.mx/.

of Astrophysics, Optics and Electronics (INAOE), founded in 1971 to carry on research projects in a multidisciplinary perspective.

One of the most important observational campaigns aimed at discovering new population-II stars with dominant blue or ultraviolet emission in the halo of our galaxy, following some previous works including also white dwarfs (e.g. Humason and Zwicky 1947, Luyten 1953). At the time, that was one of the hottest topics because blue stars were considered to be very rare, and none of them was expected to be located far from the galactic disk. Therefore, the detection and mapping of faint blue star-like objects in the direction of the Milky Way poles for further investigation was highly desirable (see Peimbert 2011). The second director of Tonantzintla observatory, Dr. Guillermo Haro, developed a new visualization method specific for UV-emitting stellar sources to be exploited in the dark Schmidt camera of the telescope. Namely, special 103 a-D photographic plates into which it was possible to gather images from three different filters all in one. The selected bands approximately corresponded to the yellow, blue, and ultraviolet, which therefore resulted on the same plate just one beside the other, ready for a direct inspection. This way, it was easier not only to state which was the color tendency of any given target, but also to spot changes between different observations of it, eventually leading to the detection of a variable source[2].

All the newly detected objects, with photographic magnitude $m < 17$ mag, were listed in a series of three Observatory Bulletins, making up the *TON* catalogue. In particular, the first one resulted from a preliminary insight into the northern hemisphere of the sky, with 817 entries (including TON 116, Iriarte and Chavira 1957), the second was related to the southern hemisphere, with 419 entries (Chavira 1958), while the third was basically a continuation of the research carried out for the first one, with 772 new entries (Chavira 1959).

In reality, the authors were open to the possibility to be dealing with at least some galaxies, rather than stars only, inside the sample created (see e.g. the second of the three above-mentioned articles). Indeed, as it became clear from later papers about the identified objects, the TON catalogue includes a wide range of completely different sources, e.g., nuclei of planetary nebulae, blue galaxies, and AGNs, which are seen as faint, point-like objects due to their large distances. For instance, at nearly the time of QSO outbreak, a general revision by Sandage and Luyten 1967 (see also Sandage and Luyten 1969) already led to the conclusion that a large part of all the blue star-like objects fainter than 14.5 mag discovered between the ’20s and the ’60s are actually quasars. In general, from modern multi-wavelength comparisons, a fraction up to at least 15% of the TON sources are most likely extragalactic (Andernach et al. 2016).

[2]As the main focus was on blue objects, the exposure time was such that an A5-type star would have given about the same amount of brightness in each of the three filters.

Appendix B

Crab Nebula as a VHE standard candle

For IACT instruments like MAGIC, it is useful to select some VHE source whose known spectrum can represent a reference behaviour. The strongest TeV γ-ray source is *Crab Nebula*, located at RA $= 05\,\mathrm{h}\,34'\,32.0''$ and Dec $= +22^\circ\,00'\,52.1''$, at (2.0 ± 0.2) kpc from the Earth (Spurio 2015). It was firstly reported by Chinese astronomers in 1054, when it became well visible by naked-eye, as it reached an apparent magnitude much less than the Venus planet one. In the second half of XVIII century, the French astronomer Charles Messier (1730-1817) included the source in his catalogue of comet-like objects as very first entry (M1). Crab is a *Supernova Remnant* (SNR), i.e., what is left from a huge explosion through which stars with mass above $\gtrsim 8\ \mathrm{M}_\odot$ conclude their existence. This is due to a collapse of the core, not anymore sustained by thermo-nuclear reactions, which causes the outer gaseous layers to fall towards the nucleus and bounce back in the space. At the center, the remnant is a very compact object with a typical radius of 20-30 km mainly formed by degenerated neutrons, known as *neutron star*[1]. For Crab, the neutron star is named PSR J0534 + 2200, and is rapidly spinning at a rate of around 30 rotations per second. Crab Nebula is a strong emitter at all wavelengths, and currently is well-sampled from radio ($\sim 10^{-5}$ eV) up to γ-ray bands (hundreds of TeV). Its non-thermal, broadband emission can be well explained by an SSC magneto-hydrodynamical model (Subsubsec. 1.4.1.1) consisting of a wind of energetic e^--e^+ pairs interacting with the *Interstellar Medium* (ISM). This allows to estimate the magnetic field to be approximately 100 μG, with basically no need for any hadronic component (see Fig. B.1).

Crab Nebula was discovered to be a γ-ray source by the IACT Whipple in 1989 (Subsec. 2.3.3). The integral flux (Subsec. 3.5.4) above 1 TeV is $\Phi(E > 1\ \mathrm{TeV}) = (2.1 \pm 0.1) \cdot 10^{-11}\ \mathrm{cm}^{-2}\ \mathrm{s}^{-1}$ (Spurio 2015). The strong, steady γ emission of Crab can be considered as a standard candle for cross-calibrations of ground-based instruments. In particular, IACTs like MAGIC usually exploit a fundamental flux unit, defined as 1 *Crab Unit* (C.U.) = $(3.39 \pm 0.09) \cdot 10^{-11}\ \mathrm{cm}^{-2}\ \mathrm{s}^{-1}\ \mathrm{TeV}^{-1}$ (at 1 TeV, Aleksić, Ansoldi, et al. 2016b). Given the well-established state, the source spectrum is also referred to for MAGIC analysis validation. Namely, Crab Nebula data have to be analyzed through the standard `MARS` chain, and the `odie` and `flute`

[1]This occurs if the progenitor star has a mass less than $\sim 25\ \mathrm{M}_\odot$, else the remnant object is a black hole.

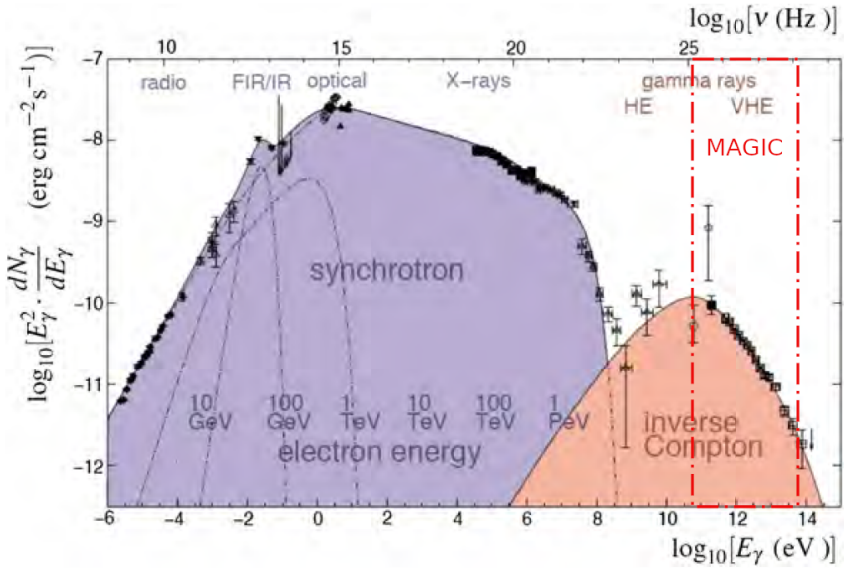

Figure B.1: Multi-wavelength SED of Crab Nebula, generally well described by an SSC model giving rise to a synchrotron bump (on the left) and to an inverse-Compton one (on the right). On top, the frequencies corresponding to the x axis energies, with band denominations, are displayed. At the bottom left, decades of electron energies producing the synchrotron trend are reported. The dash-dotted red contour on the right marks the VHE spectral band investigated by MAGIC ($\sim$ 50 GeV-50 TeV). Plot adapted from Spurio (2015).

results have to be carefully inspected. In particular, the θ^2 plots have to show the usual peak of an emitting source towards $\theta^2 = 0$, with high significance for all the three energy ranges (LE, FR, HE). Also, the sensitivities should be compatible with reference values (1.2, 0.8, 1.0 for LE, FR, HE respectively). On the other hand, the SED and LC found for Crab Nebula should be consistent with the source standard state. The most important check is on the SED, whose spectral behaviour has to be as similar as possible to the one known from the literature (explicitly reported in the `flute` SED plots for a direct comparison). If this "sanity" check passes, then the RF-based `coach` tools used by `MARS` analysis chain can be trusted for the reconstruction of VHE γ-rays starting from the detected Cherenkov radiation.

The plots below show the Crab Nebula θ^2 (FR) plots and SEDs that we obtained with `flute` for all the four MC periods during which the source TON 116 has been observed by MAGIC. The positive results of each Crab test validate our whole analysis of TON 116 at VHE band.

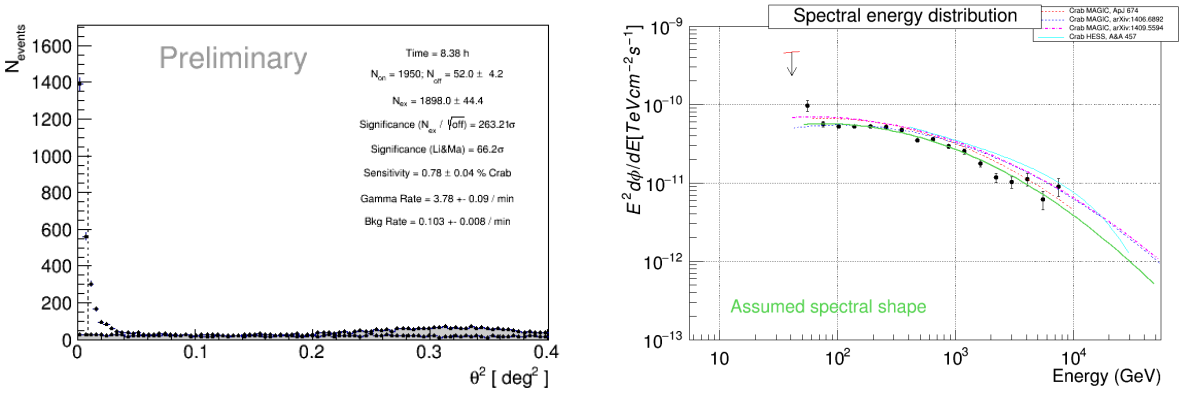

Figure B.2: Crab Nebula θ^2 plot (FR, left) and SED (right) obtained by flute for ST.03.16 MC period, for the validation of the MARS analysis chain used for the 2021 dataset (Subsec. 4.2.1) of TON 116 by MAGIC.

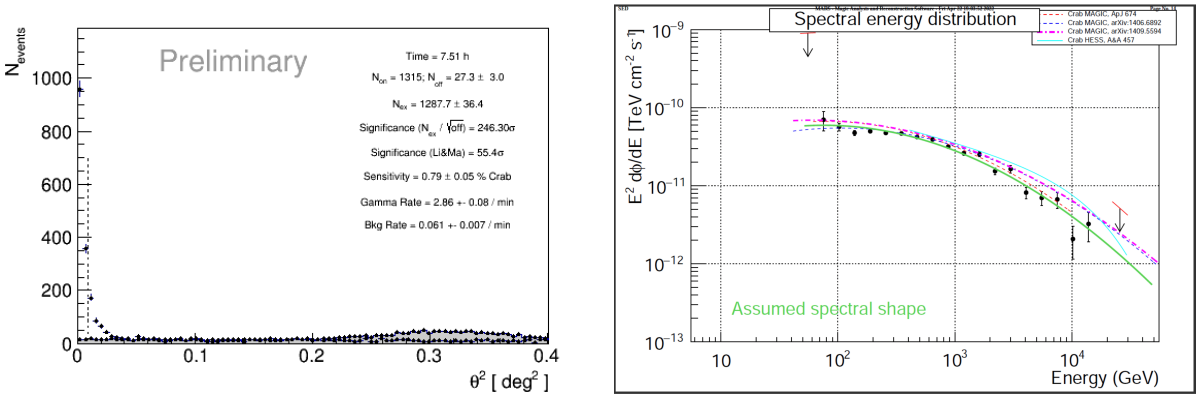

Figure B.3: Crab Nebula θ^2 plot (FR, left) and SED (right) obtained by flute for ST.03.17 MC period, for the validation of the MARS analysis chain used for the 2022 dataset (Subsec. 4.2.2) of TON 116 by MAGIC.

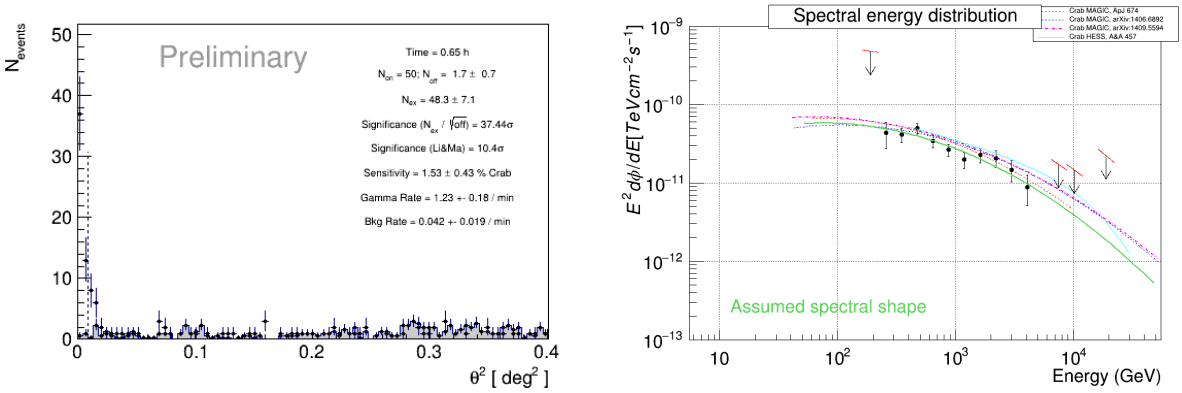

Figure B.4: Crab Nebula θ^2 plot (FR, left) and SED (right) obtained by flute for ST.03.18 MC period, for the validation of the MARS analysis chain used for the 2023 "group I" dataset (Subsec. 4.2.4) of TON 116 by MAGIC. For this period, no specific MC file was generated yet, thus we used the files of the MC period just prior to that (ST.03.18). Moreover, no Crab data with the same zenith range as TON 116 (0°-35°) was available, thus the test has been performed on the one at which Crab has been observed (50°-62°).

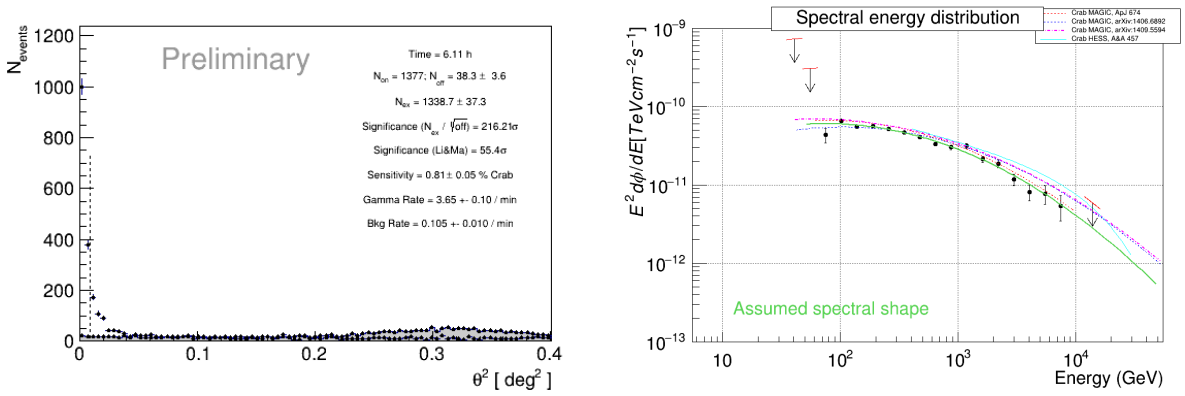

Figure B.5: Crab Nebula θ^2 plot (FR, left) and SED (right) obtained by flute for ST.03.20 MC period, for the validation of the MARS analysis chain used for the 2023 "group II" dataset (Subsec. 4.2.4) of TON 116 by MAGIC.

List of Figures

List of Tables

Acronyms

1ES = First Einstein (HEAO-2) Slew Survey Catalogue of X-ray Sources
1H = HEAO-1 Survey Catalogue of X-ray Sources

1RXS = First ROSAT X-ray Survey Catalogue

4FGL-DR3 = Fourth Fermi-LAT Catalogue of Gamma-ray Sources - Data Release 3

4LAC = Fourth Fermi-LAT Catalogue of AGN Sources

6C = Sixth Cambridge Catalogue of Radio Sources

AAS = Automatic Alert System

ADAF = Advection-Dominated Accretion Flow

ADC = Analog-to-Digital Converter

AGN = Active Galactic Nuclei

AMC = Active Mirror Control

APM = Automated Plate Measuring Facility

ASI = Agenzia Spaziale Italiana

B = Blue optical filter

B2 = Bologna Second Survey of Radio Sources

BAL = Broad Absorption Line Quasar

BAT = Burst Alert Telescope (Swift-BAT)

BB = Black-Body

BLR = Broad Line Region

BLRG = Broad-Line Radio Galaxy

BPL = Broken Power-Law

BZB = Blazar BL Lac Object (Roma-BZCAT Catalogue)

CaCo = Camera Control

Caltech = California Institute of Technology

CC = Central Control

CCD = Charge Coupled Device

CDQ = Core-Dominated Quasar

CERN = Conseil Européen pour la Recherche Nucléaire

CGRO = Compton Gamma-Ray Observatory

CH = Counting House

CL = Confidence Level

CMB = Cosmic Microwave Background

CNN = Convolutional Neural Network

coach = Compressed Osteria Alias Computation of the Hadronness

CoG = Center of Gravity

CORSIKA = Cosmic Ray Simulations for Kascade

CR = Cosmic Ray

CRATES = Combined Radio All-sky Targeted Eight GHz Survey

CSIC = Consejo Superior de Investigaciones Científicas

CTAC = Cherenkov Telescope Array Consortium

CTAO = Cherenkov Telescope Array Observatory

C.U. = Crab Unit

DAQ = Data Acquisition

DC = Direct Current

DE = Dark Energy

DM = Dark Matter

dof = Degrees of Freedom

DRS4 = Domino Ring Sampler 4

DT = Discriminator Threshold

EAS = Extensive Air Shower

EBL = Extragalactic Background Light

EC = External Compton

ecsv = Enhanced Character Separated Value

EGRET = Energetic Gamma Ray Experiment Telescope

EHBL = Extremely High-frequency-peaked BL Lac

EHE = Extremely High Energy

EM = Electromagnetic

ESO = European Southern Observatory

EW = Equivalent Width

FA = Flare Advocate

FBQS = FIRST Bright Quasar Survey

FIRST = Faint Images of the Radio Sky at Twenty-cm

FITS = Flexible Image Transport System

flute = Flux versus Time and Energy

foam = Flute Output Averaging Merger

FoV = Field of View

FR = Full Range

FR I/II = Fanaroff-Riley I/II type Radio Galaxy

FSRQ = Flat Spectrum Radio Quasar

FWHM = Full Width at Half Maximum

GCN = General Coordinates Network

GRB = Gamma-Ray Burst

GSFC = Goddard Space Flight Center

GTC (GranTeCan) = Gran Telescopio Canarias

GUI = Graphical User Interface

GW = Gravitational Wave

GZK = Greisen-Zatsepin-Kuzmin

HAWC = High Altitude Water Cherenkov

HBL = High-frequency-peaked BL Lac Object

HE = High Energy

HEAO = High Energy Astronomy Observatory

HEASARC = NASA High Energy Astrophysics Archive Research Center

HEASoft = NASA HEASARC Software

HEGRA = High Energy Gamma-Ray Astronomy

HESS = High Energy Stereoscopic System

HPQ = Highly Polarized Quasar

HV = High Voltage

IAA = Instituto de Astrofísica de Andalucía

IAC = Instituto de Astrofísica de Canarias

IACT = Imaging Atmospheric Cherenkov Telescope

IBL = Intermediate-frequency-peaked BL Lac Object

IC = Inverse-Compton

ICRANet = International Center for Relativistic Astrophysics Network

ID = Identification number

INAOE = Instituto Nacional de Astrofísica, Óptica y Electrónica

IPAC = Infrared Processing and Analysis Center

IR = Infrared

IRF = Instrument Response Function

ISM = Interstellar Medium

JD = Julian Date

L0, L1, L3 = Level 0, Level 1, Level 3 MAGIC trigger

ΛCDM = Λ Cold Dark Matter

LAT = Large Area Telescope (Fermi-LAT)

LBL = Low-frequency-peaked BL Lac Object

LC = Light Curve

LE = Low Energy

LED = Light Emitting Diode

LHAASO = Large High Altitude Air Shower Observatory

LHC = Large Hadron Collider

LIDAR = Light Detection And Ranging

LoS = Line of Sight

LP = Log Parabola

LST = Large Size Telescope

LUT = Look-Up-Table

M = Messier Catalogue of Comet-like Objects (**M**1 = Crab Nebula)

M1, M2 = MAGIC Telescope 1, MAGIC Telescope 2

MAGIC = Major Atmospheric Gamma Imaging Cherenkov

MARS = MAGIC Analysis and Reconstruction Software

MC = Monte Carlo

ME = Medium Energy

MET = Mission Elapsed Time

merpp = Merging and Preprocessing Program

MG = MIT - Green Bank Catalogue of Radio Sources

MIR = MAGIC Integrated Readout

MIT = Massachusetts Institute of Technology

MJD = Modified Julian Date

MM = Multi-Messenger

mmcs = MAGIC Monte Carlo Simulations

MMDC = Markarian Multi-wavelength Data Center

MOLA = MAGIC Online Analysis

Mrk = Markarian Object (Byurakan Catalogue of UV-excess galaxies)

MST = Medium Size Telescope

MultiNest = Multimodal Nested Sampling Algorithm

MWL = Multi-Wavelength

NASA = National Aeronautics and Space Administration

NED = NASA/IPAC Extragalactic Database

NLR = Narrow Line Region

NLRG = Narrow-Line Radio Galaxy

NN = Next Neighbour

NOAO = National Optical Astronomy Observatory

NOIRLab = National Optical-Infrared Astronomy Research Laboratory

NRAO = National Radio Astronomy Observatory

NSB = Night Sky Background

NSF = National Science Foundation

NuSTAR = Nuclear Spectroscopic Telescope Array

NVSS = NRAO VLA Sky Survey

OANTON = Observatorio Astrofísico Nacional de Tonantzintla

ORM = Observatorio de Roque de los Muchachos

OSA = On-Site Analysis

OSN = Observatorio de Sierra Nevada

OVV = Optically Violently Variable Quasar

PC = Personal Computer

PC = Photon Counting Readout Mode

p.e. = Photoelectrons

PHA = Pulse Height Amplitude

PhD = Philosophiae Doctor

PI = Principal Investigator

PIC = Port d'Informació Científica

PKS = Parkes Catalogue of Radio Sources

PL = Power-Law

PLEC = Power-Law with Exponential Cut-off

PMT = Photo-Multiplier Tube

POSS = Palomar Observatory Sky Survey

PSF = Point Spread Function

PSR = Pulsar (Pulsating Radio Source)

QE = Quantum Efficiency

QSO = Quasi-Stellar Object

quate = Quality Tester

R = Red optical filter

RA = Right Ascension

RASS-BSC = ROSAT All-Sky Survey - Bright Source Catalogue

RF = Random Forest

RMS = Root Mean Square

RoI = Region of Interest

Roma-BZCAT = Roma Multi-frequency Catalogue of Blazars

ROSAT = Röntgensatellit

SA = SuperArehucas

SBIG = Santa Barbara Instrument Group

SDSS = Sloan Digital Sky Survey

SED = Spectral Energy Distribution

SM = Standard Model

SMBH = Super Massive Black Hole

S/N = Signal-to-Noise Ratio

SNR = Supernova Remnant

SOPRANO = Simulator Of Processes in Relativistic Astronomical Objects

sorcerer = Simple Outright Raw Calibration Easy and Reliable Extraction Routines

SSC = Synchrotron Self Compton

SSD = Shakura-Sunyaev Disk

SSDC = Space Science Data Center

SSRQ = Steep Spectrum Radio Quasar

SST = Small Size Telescope

(super)star = (Super) Standard Analysis and Image Reconstruction

SUMSS = Sydney University Molonglo Sky Survey

T150, T90 = 150-cm-aperture OSN Telescope, 90-cm-aperture OSN Telescope

TeVCat = TeV Gamma-ray Sources Catalogue

TON = Tonantzintla Catalogue of Faint Blue Star-like Objects

ToO = Target of Opportunity

TS = Test-Statistic

TXS = Texas Catalogue of Radio Sources

UHBL = Ultra-High-frequency-peaked BL Lac Object

UHE = Ultra High Energy

UHECR = Ultra High Energy Cosmic Ray

UK = United Kingdom

UL = Upper Limit

USA = United States of America

UV = Ultraviolet

UVOT = Ultraviolet-Optical Telescope (Swift-UVOT)

VCSEL = Vertical Cavity Surface Emitting Laser

VERITAS = Very Energetic Radiation Imaging Telescope Array System

VHE = Very High Energy

VLA = Very Large Array

VLBA = Very Long Baseline Array

WISE = Wide-field Infrared Survey Explorer

WIYN = Wisconsin-Madison Indiana Yale Universities and NSF NOIRLab (formerly NOAO)

XRT = X-ray Telescope (Swift-XRT)

ZD = Zenith Distance

Bibliography

Abdo, A. A. et al. (Dec. 1, 2009). "Fermi Observations of TeV-Selected Active Galactic Nuclei". In: *The Astrophysical Journal* 707. ADS Bibcode: 2009ApJ...707.1310A, pp. 1310–1333. ISSN: 0004-637X. DOI: 10.1088/0004-637X/707/2/1310. URL: https://ui.adsabs.harvard.edu/abs/2009ApJ...707.1310A.

Abdollahi, S. et al. (June 1, 2022). "Incremental Fermi Large Area Telescope Fourth Source Catalog". In: *The Astrophysical Journal Supplement Series* 260. Publisher: IOP ADS Bibcode: 2022ApJS..260...53A, p. 53. ISSN: 0067-0049. DOI: 10.3847/1538-4365/ac6751. URL: https://ui.adsabs.harvard.edu/abs/2022ApJS..260...53A.

Abe, H. et al. (Dec. 1, 2023). "Performance of the joint LST-1 and MAGIC observations evaluated with Crab Nebula data". In: *Astronomy & Astrophysics* 680. Publisher: EDP Sciences, A66. ISSN: 0004-6361, 1432-0746. DOI: 10.1051/0004-6361/202346927. URL: https://www.aanda.org/articles/aa/abs/2023/12/aa46927-23/aa46927-23.html.

Abeysekara, A. U. et al. (July 1, 2017). "Observation of the Crab Nebula with the HAWC Gamma-Ray Observatory". In: *The Astrophysical Journal* 843. ADS Bibcode: 2017ApJ...843...39A, p. 39. ISSN: 0004-637X. DOI: 10.3847/1538-4357/aa7555. URL: https://ui.adsabs.harvard.edu/abs/2017ApJ...843...39A.

Acciari, V. A. et al. (Jan. 1, 2010). "Discovery of Very High Energy Gamma Rays from PKS 1424+240 and Multiwavelength Constraints on Its Redshift". In: *The Astrophysical Journal* 708. ADS Bibcode: 2010ApJ...708L.100A, pp. L100–L106. ISSN: 0004-637X. DOI: 10.1088/2041-8205/708/2/L100. URL: https://ui.adsabs.harvard.edu/abs/2010ApJ...708L.100A.

Aharonian, F. A. et al. (Oct. 1, 2006). "Observations of the Crab nebula with HESS". In: *Astronomy & Astrophysics* 457.3. Number: 3, Publisher: EDP Sciences, pp. 899–915. ISSN: 0004-6361, 1432-0746. DOI: 10.1051/0004-6361:20065351. URL: https://www.aanda.org/articles/aa/abs/2006/39/aa5351-06/aa5351-06.html.

Ahnen, M. L. et al. (Sept. 1, 2017). "Performance of the MAGIC telescopes under moonlight". In: *Astroparticle Physics* 94, pp. 29–41. ISSN: 0927-6505. DOI: 10.1016/j.astropartphys.2017.08.001. URL: https://www.sciencedirect.com/science/article/pii/S092765051730110X.

Ajello, M. et al. (Apr. 1, 2020). "The Fourth Catalog of Active Galactic Nuclei Detected by the Fermi Large Area Telescope". In: *The Astrophysical Journal* 892. Publisher: IOP

ADS Bibcode: 2020ApJ...892..105A, p. 105. ISSN: 0004-637X. DOI: 10.3847/1538-4357/ab791e. URL: https://ui.adsabs.harvard.edu/abs/2020ApJ...892..105A.

Albert, J. (Apr. 2008). "Implementation of the Random Forest Method for the Imaging Atmospheric Cherenkov Telescope MAGIC". In: *Nuclear Instruments and Methods in Physics Research Section A: Accelerators, Spectrometers, Detectors and Associated Equipment* 588.3, pp. 424–432. ISSN: 01689002. DOI: 10.1016/j.nima.2007.11.068. arXiv: 0709.3719[astro-ph]. URL: http://arxiv.org/abs/0709.3719.

Aleksić, J., E. A. Alvarez, et al. (Feb. 2012). "Performance of the MAGIC stereo system obtained with Crab Nebula data". In: *Astroparticle Physics* 35.7, pp. 435–448. ISSN: 09276505. DOI: 10.1016/j.astropartphys.2011.11.007. arXiv: 1108.1477[astro-ph]. URL: http://arxiv.org/abs/1108.1477.

Aleksić, J., S. Ansoldi, et al. (Jan. 1, 2016a). "The major upgrade of the MAGIC telescopes, Part I: The hardware improvements and the commissioning of the system". In: *Astroparticle Physics* 72, pp. 61–75. ISSN: 0927-6505. DOI: 10.1016/j.astropartphys.2015.04.004. URL: https://www.sciencedirect.com/science/article/pii/S0927650515000663.

— (Jan. 2016b). "The major upgrade of the MAGIC telescopes, Part II: A performance study using observations of the Crab Nebula". In: *Astroparticle Physics* 72, pp. 76–94. ISSN: 09276505. DOI: 10.1016/j.astropartphys.2015.02.005. arXiv: 1409.5594[astro-ph]. URL: http://arxiv.org/abs/1409.5594.

Andernach, H. et al. (2016). "The Nature of Faint Blue Stars in the PHL and Ton Catalogues based on Digital Sky Surveys". In: vol. 42, pp. 97–100. DOI: 10.1007/978-3-319-19330-4_14. arXiv: 1504.07471[astro-ph]. URL: http://arxiv.org/abs/1504.07471.

Angel, J. R. P. and H. S. Stockman (1980). *Optical and infrared polarization of active extragalactic objects*. URL: https://adsabs.harvard.edu/full/1980ARA%26A..18..321A.

Atoyan, Armen M. and C. D. Dermer (Mar. 20, 2003). "Neutral Beams from Blazar Jets". In: *The Astrophysical Journal* 586.1, pp. 79–96. ISSN: 0004-637X, 1538-4357. DOI: 10.1086/346261. arXiv: astro-ph/0209231. URL: http://arxiv.org/abs/astro-ph/0209231.

Atwood, W. B. et al. (June 1, 2009). "THE LARGE AREA TELESCOPE ON THE *FERMI GAMMA-RAY SPACE TELESCOPE* MISSION". In: *The Astrophysical Journal* 697.2, pp. 1071–1102. ISSN: 0004-637X, 1538-4357. DOI: 10.1088/0004-637X/697/2/1071. URL: https://iopscience.iop.org/article/10.1088/0004-637X/697/2/1071.

Barthelmy, S. D. et al. (Oct. 1, 2005). "The Burst Alert Telescope (BAT) on the SWIFT Midex Mission". In: *Space Science Reviews* 120. ADS Bibcode: 2005SSRv..120..143B, pp. 143–164. ISSN: 0038-6308. DOI: 10.1007/s11214-005-5096-3. URL: https://ui.adsabs.harvard.edu/abs/2005SSRv..120..143B.

Beckmann, Volker and Chris R. Shrader (Aug. 1, 2012). *Active Galactic Nuclei*. Publication Title: Active Galactic Nuclei ADS Bibcode: 2012agn..book.....B. URL: https://ui.adsabs.harvard.edu/abs/2012agn..book.....B.

Bednarek, W. and R. J. Protheroe (Jan. 11, 1999). "Gamma-ray and neutrino flares produced by protons accelerated on an accretion disk surface in AGN". In: *Monthly Notices of the Royal*

Astronomical Society 302.2, pp. 373–380. ISSN: 0035-8711, 1365-2966. DOI: 10.1046/j.1365-8711.1999.02132.x. arXiv: astro-ph/9802288. URL: http://arxiv.org/abs/astro-ph/9802288.

Bégué, D. et al. (Nov. 6, 2023). *Modeling blazar broadband emission with convolutional neural networks – I. Synchrotron self-Compton model*. arXiv.org. URL: https://arxiv.org/abs/2311.02979v1.

Berti, A. (2018). "Study of astrophysical transients with the MAGIC telescopes". PhD thesis. Trieste U.

Bessell, M. S. (Aug. 11, 2005). "Standard Photometric Systems". In: *Annual Review of Astronomy and Astrophysics* 43 (Volume 43, 2005). Publisher: Annual Reviews, pp. 293–336. ISSN: 0066-4146, 1545-4282. DOI: 10.1146/annurev.astro.41.082801.100251. URL: https://www.annualreviews.org/content/journals/10.1146/annurev.astro.41.082801.100251.

Bessell, M. S., F. Castelli, and B. Plez (May 1, 1998). "Model atmospheres broad-band colors, bolometric corrections and temperature calibrations for O - M stars". In: *Astronomy and Astrophysics* 333. ADS Bibcode: 1998A&A...333..231B, pp. 231–250. ISSN: 0004-6361. URL: https://ui.adsabs.harvard.edu/abs/1998A&A...333..231B.

Biland, A. et al. (2007). *The Active Mirror Control of the MAGIC Telescope*. arXiv: 0709.1574 [astro-ph].

Blandford, R. D., D. Meier, and A. C. S. Readhead (2019). "Relativistic Jets from Active Galactic Nuclei". In.

Blandford, R. D. and D. G. Payne (Aug. 1, 1982). "Hydromagnetic flows from accretion discs and the production of radio jets". In: *Monthly Notices of the Royal Astronomical Society* 199.4, pp. 883–903. ISSN: 0035-8711, 1365-2966. DOI: 10.1093/mnras/199.4.883. URL: https://academic.oup.com/mnras/article-lookup/doi/10.1093/mnras/199.4.883.

Blandford, R. D. and M. J. Rees (Mar. 1978). "Extended and Compact Extragalactic Radio Sources: Interpretation and Theory". In: *Physica Scripta* 17.3, p. 265. ISSN: 1402-4896. DOI: 10.1088/0031-8949/17/3/020. URL: https://dx.doi.org/10.1088/0031-8949/17/3/020.

Blandford, R. D. and R. L. Znajek (1977). "Electromagnetic extraction of energy from Kerr black holes". In: *Monthly Notices of the Royal Astronomical Society* 179, pp. 433–456. URL: http://arxiv.org/abs/astro-ph/9802288.

Böttcher, M. and J. Chiang (Dec. 2002). "X-Ray Spectral Variability Signatures of Flares in BL Lacertae Objects". In: *The Astrophysical Journal* 581.1, p. 127. ISSN: 0004-637X. DOI: 10.1086/344155. URL: https://dx.doi.org/10.1086/344155.

Braibant, Sylvie, Giorgio Giacomelli, and Maurizio Spurio (2012). *Particelle e interazioni fondamentali*. Milano: Springer Milan. ISBN: 978-88-470-2753-4 978-88-470-2754-1. DOI: 10.1007/978-88-470-2754-1. URL: http://link.springer.com/10.1007/978-88-470-2754-1.

Bretz, T. et al. (Mar. 1, 2009). "The drive system of the major atmospheric gamma-ray imaging Cherenkov telescope". In: *Astroparticle Physics* 31.2, pp. 92–101. ISSN: 0927-6505. DOI: 10.1016/j.astropartphys.2008.12.001. URL: https://www.sciencedirect.com/science/article/pii/S0927650508001898.

Brun, Rene and Fons Rademakers (Apr. 11, 1997). "ROOT — An object oriented data analysis framework". In: *Nuclear Instruments and Methods in Physics Research Section A: Accelerators, Spectrometers, Detectors and Associated Equipment*. New Computing Techniques in Physics Research V 389.1, pp. 81–86. ISSN: 0168-9002. DOI: 10.1016/S0168-9002(97)00048-X. URL: https://www.sciencedirect.com/science/article/pii/S016890029700048X.

Burrows, D. N. et al. (Oct. 1, 2005). "The Swift X-Ray Telescope". In: *Space Science Reviews* 120. ADS Bibcode: 2005SSRv..120..165B, pp. 165–195. ISSN: 0038-6308. DOI: 10.1007/s11214-005-5097-2. URL: https://ui.adsabs.harvard.edu/abs/2005SSRv..120..165B.

Cao, Z. et al. (Feb. 18, 2022). *The Large High Altitude Air Shower Observatory (LHAASO) Science Book (2021 Edition)*. DOI: 10.48550/arXiv.1905.02773. arXiv: 1905.02773[astro-ph]. URL: http://arxiv.org/abs/1905.02773.

Cerruti, M. et al. (Mar. 1, 2015). "A hadronic origin for ultra-high-frequency-peaked BL Lac objects". In: *Monthly Notices of the Royal Astronomical Society* 448. ADS Bibcode: 2015MNRAS.448..910C, pp. 910–927. ISSN: 0035-8711. DOI: 10.1093/mnras/stu2691. URL: https://ui.adsabs.harvard.edu/abs/2015MNRAS.448..910C.

Chavira, E. (1958). "Estrellas Azules en el Casquete Galactico Sur". In: *Boletín de los Observatorios de Tonantzintla y Tacubaya* 2.17. URL: http://www.astroscu.unam.mx/bott/BOTT..2-17/PDF/BOTT..2-17_echavira.pdf.

— (1959). "Estrellas Azules en el Casquete Galactico Norte - II". In: *Boletín de los Observatorios de Tonantzintla y Tacubaya* 2.18. URL: http://www.astroscu.unam.mx/bott/BOTT..2-17/PDF/BOTT..2-17_echavira.pdf.

Colla, G. et al. (Sept. 1, 1973). "The B2 catalogue of radio sources - third part". In: *Astronomy and Astrophysics Supplement Series* 11. ADS Bibcode: 1973A&AS...11..291C, p. 291. ISSN: 0365-0138. URL: https://ui.adsabs.harvard.edu/abs/1973A&AS...11..291C.

Costamante, L. et al. (May 1, 2001). "Extreme synchrotron BL Lac objects. Stretching the blazar sequence". In: *Astronomy and Astrophysics* 371. ADS Bibcode: 2001A&A...371..512C, pp. 512–526. ISSN: 0004-6361. DOI: 10.1051/0004-6361:20010412. URL: https://ui.adsabs.harvard.edu/abs/2001A&A...371..512C.

CTA Consortium, The Cherenkov Telescope Array et al. (Mar. 2019). *Science with the Cherenkov Telescope Array*. DOI: 10.1142/10986. arXiv: 1709.07997[astro-ph,physics:hep-ex]. URL: http://arxiv.org/abs/1709.07997.

D'Abrusco, R. et al. (Oct. 31, 2014). "THE *WISE* BLAZAR-LIKE RADIO-LOUD SOURCES: AN ALL-SKY CATALOG OF CANDIDATE γ-RAY BLAZARS". In: *The Astrophysical*

Journal Supplement Series 215.1, p. 14. ISSN: 1538-4365. DOI: 10.1088/0067-0049/215/1/14. URL: https://iopscience.iop.org/article/10.1088/0067-0049/215/1/14.

Daum, A. et al. (Apr. 11, 1997). *First Results on the Performance of the HEGRA IACT Array*. DOI: 10.48550/arXiv.astro-ph/9704098. arXiv: astro-ph/9704098. URL: http://arxiv.org/abs/astro-ph/9704098.

Dazzi, F. (2012). "A new stereoscopic 'Sum-Trigger-II' for the MAGIC Telescopes". PhD thesis. Udine U.

— (Apr. 28, 2016). "A new stereoscopic 'Sum-Trigger-II' for the MAGIC Telescopes". In: URL: https://www.semanticscholar.org/paper/A-new-stereoscopic-'Sum-Trigger-II'-for-the-MAGIC-Dazzi/c906787bf852e68bd8bc4df55668613f2aa3b4da.

De Naurois, M. and D. Mazin (Aug. 1, 2015). "Ground-based detectors in very-high-energy gamma-ray astronomy". In: *Comptes Rendus. Physique* 16.6, pp. 610–627. ISSN: 1878-1535. DOI: 10.1016/j.crhy.2015.08.011. arXiv: 1511.00463[astro-ph]. URL: http://arxiv.org/abs/1511.00463.

Deil, Christoph et al. (Aug. 16, 2017). "Gammapy - A prototype for the CTA science tools". In: *Proceedings of 35th International Cosmic Ray Conference — PoS(ICRC2017)*. 35th International Cosmic Ray Conference. Bexco, Busan, Korea: Sissa Medialab, p. 766. DOI: 10.22323/1.301.0766. URL: https://pos.sissa.it/301/766.

Dermer, C. D., J. D. Finke, et al. (Feb. 1, 2009). "Gamma-Ray Studies of Blazars: Synchro-Compton Analysis of Flat Spectrum Radio Quasars". In: *The Astrophysical Journal* 692. ADS Bibcode: 2009ApJ...692...32D, pp. 32–46. ISSN: 0004-637X. DOI: 10.1088/0004-637X/692/1/32. URL: https://ui.adsabs.harvard.edu/abs/2009ApJ...692...32D.

Dermer, C. D. and G. Menon (Nov. 10, 2009a). *High Energy Radiation from Black Holes | Princeton University Press*. ISBN: 9780691144085. URL: https://press.princeton.edu/books/paperback/9780691144085/high-energy-radiation-from-black-holes.

— (Jan. 1, 2009b). *High Energy Radiation from Black Holes: Gamma Rays, Cosmic Rays, and Neutrinos*. Publication Title: High Energy Radiation from Black Holes: Gamma Rays ADS Bibcode: 2009herb.book.....D. URL: https://ui.adsabs.harvard.edu/abs/2009herb.book.....D.

Domínguez, A. et al. (Feb. 1, 2011). "Extragalactic background light inferred from AEGIS galaxy-SED-type fractions: EBL from AEGIS galaxy-SED-type fractions". In: *Monthly Notices of the Royal Astronomical Society* 410.4, pp. 2556–2578. ISSN: 00358711. DOI: 10.1111/j.1365-2966.2010.17631.x. URL: https://academic.oup.com/mnras/article-lookup/doi/10.1111/j.1365-2966.2010.17631.x.

Dondi, L. and G. Ghisellini (Apr. 1, 1995). "Gamma-ray-loud blazars and beaming". In: *Monthly Notices of the Royal Astronomical Society* 273. ADS Bibcode: 1995MNRAS.273..583D, pp. 583–595. ISSN: 0035-8711. DOI: 10.1093/mnras/273.3.583. URL: https://ui.adsabs.harvard.edu/abs/1995MNRAS.273..583D.

Escudero, J., D. Morcuende, and J. Otero-Santos (Mar. 2024). *IOP4*. Version v1.0.0. DOI: 10.5281/zenodo.10222722. URL: https://zenodo.org/doi/10.5281/zenodo.10222722.

Evans, P. A. et al. (Aug. 1, 2009). "Methods and results of an automatic analysis of a complete sample of Swift-XRT observations of GRBs". In: *Monthly Notices of the Royal Astronomical Society* 397. Publisher: OUP ADS Bibcode: 2009MNRAS.397.1177E, pp. 1177–1201. ISSN: 0035-8711. DOI: 10.1111/j.1365-2966.2009.14913.x. URL: https://ui.adsabs.harvard.edu/abs/2009MNRAS.397.1177E.

Fanaroff, B. L. and J. M. Riley (1974). "The Morphology of Extragalactic Radio Sources of High and Low Luminosity". In: *Monthly Notices of the Royal Astronomical Society* 167, 31P–35P. URL: https://articles.adsabs.harvard.edu/pdf/1974MNRAS.167P..31F.

Fermi-LAT Collaboration, The (June 9, 2015). *Fermi Large Area Telescope Third Source Catalog*. arXiv: 1501.02003[astro-ph]. URL: http://arxiv.org/abs/1501.02003.

Fernández Barral, A. (2017). "Extreme particle acceleration in microquasar jets and pulsar wind nebulae with the magic telescopes". http://purl.org/dc/dcmitype/Text. Universitat Autònoma de Barcelona. URL: https://dialnet.unirioja.es/servlet/tesis?codigo=181891.

— (2018). *Extreme Particle Acceleration in Microquasar Jets and Pulsar Wind Nebulae with the MAGIC Telescopes*. Springer Theses. Cham: Springer International Publishing. ISBN: 978-3-319-97537-5 978-3-319-97538-2. DOI: 10.1007/978-3-319-97538-2. URL: http://link.springer.com/10.1007/978-3-319-97538-2.

Feroz, F., M. P. Hobson, and M. Bridges (Oct. 1, 2009). "MultiNest: an efficient and robust Bayesian inference tool for cosmology and particle physics". In: *Monthly Notices of the Royal Astronomical Society* 398.4, pp. 1601–1614. ISSN: 0035-8711. DOI: 10.1111/j.1365-2966.2009.14548.x. URL: https://doi.org/10.1111/j.1365-2966.2009.14548.x.

Finke, J. D. (Oct. 1, 2016). "External Compton Scattering in Blazar Jets and the Location of the Gamma-Ray Emitting Region". In: *The Astrophysical Journal* 830. ADS Bibcode: 2016ApJ...830...94F, p. 94. ISSN: 0004-637X. DOI: 10.3847/0004-637X/830/2/94. URL: https://ui.adsabs.harvard.edu/abs/2016ApJ...830...94F.

— (June 20, 2018). "External Compton Scattering in Blazar Jets and the Location of the Gamma-Ray Emitting Region". In: *The Astrophysical Journal* 860.2, p. 178. ISSN: 0004-637X, 1538-4357. DOI: 10.3847/1538-4357/aac9c6. arXiv: 1607.03907[astro-ph]. URL: http://arxiv.org/abs/1607.03907.

Finke, J. D., C. D. Dermer, and M. Böttcher (Oct. 1, 2008). "Synchrotron Self-Compton Analysis of TeV X-Ray-Selected BL Lacertae Objects". In: *The Astrophysical Journal* 686. ADS Bibcode: 2008ApJ...686..181F, pp. 181–194. ISSN: 0004-637X. DOI: 10.1086/590900. URL: https://ui.adsabs.harvard.edu/abs/2008ApJ...686..181F.

Foffano, L. et al. (June 21, 2019). "A new hard X-ray-selected sample of extreme high-energy peaked BL Lac objects and their TeV gamma-ray properties". In: *Monthly Notices of the Royal Astronomical Society* 486.2, pp. 1741–1762. ISSN: 0035-8711. DOI: 10.1093/mnras/stz812. URL: https://doi.org/10.1093/mnras/stz812.

Fomin, V. P. et al. (May 1, 1994a). "New methods of atmospheric Cherenkov imaging for gamma-ray astronomy. I. The false source method". In: *Astroparticle Physics* 2.2, pp. 137–150. ISSN: 0927-6505. DOI: 10.1016/0927-6505(94)90036-1. URL: https://www.sciencedirect.com/science/article/pii/0927650594900361.

— (May 1, 1994b). "New methods of atmospheric Cherenkov imaging for gamma-ray astronomy. I. The false source method". In: *Astroparticle Physics* 2.2, pp. 137–150. ISSN: 0927-6505. DOI: 10.1016/0927-6505(94)90036-1. URL: https://www.sciencedirect.com/science/article/pii/0927650594900361.

Fossati, G. et al. (Sept. 1, 1998). "A Unifying View of the Spectral Energy Distributions of Blazars". In: *Monthly Notices of the Royal Astronomical Society* 299.2, pp. 433–448. ISSN: 0035-8711, 1365-2966. DOI: 10.1046/j.1365-8711.1998.01828.x. arXiv: astro-ph/9804103. URL: http://arxiv.org/abs/astro-ph/9804103.

Franceschini, A., G. Rodighiero, and M. Vaccari (Sept. 2008). "The extragalactic optical-infrared background radiations, their time evolution and the cosmic photon-photon opacity". In: *Astronomy & Astrophysics* 487.3, pp. 837–852. ISSN: 0004-6361, 1432-0746. DOI: 10.1051/0004-6361:200809691. arXiv: 0805.1841[astro-ph]. URL: http://arxiv.org/abs/0805.1841.

Frank, Juhan, Andrew King, and Derek Raine (2002). *Accretion Power in Astrophysics*. 3rd ed. Cambridge: Cambridge University Press. ISBN: 978-0-521-62957-7. DOI: 10.1017/CBO9781139164245. URL: https://www.cambridge.org/core/books/accretion-power-in-astrophysics/947D22ABED5F539344E230AD5D02A7F5.

Freeman, Peter, Stephen Doe, and Aneta Siemiginowska (Nov. 1, 2001). "Sherpa: a mission-independent data analysis application". In: *Astronomical Data Analysis*. Astronomical Data Analysis. Vol. 4477. SPIE, pp. 76–87. DOI: 10.1117/12.447161. URL: https://www.spiedigitallibrary.org/conference-proceedings-of-spie/4477/0000/Sherpa-a-mission-independent-data-analysis-application/10.1117/12.447161.full.

Furniss, A. et al. (Apr. 2013). "THE FIRM REDSHIFT LOWER LIMIT OF THE MOST DISTANT TeV-DETECTED BLAZAR PKS 1424+240". In: *The Astrophysical Journal Letters* 768.2. Publisher: The American Astronomical Society, p. L31. ISSN: 2041-8205. DOI: 10.1088/2041-8205/768/2/L31. URL: https://dx.doi.org/10.1088/2041-8205/768/2/L31.

Gaidos, J. A. et al. (Sept. 1996). "Extremely rapid bursts of TeV photons from the active galaxy Markarian 421". In: *Nature* 383.6598. Publisher: Nature Publishing Group, pp. 319–320. ISSN: 1476-4687. DOI: 10.1038/383319a0. URL: https://www.nature.com/articles/383319a0.

Gaug, Markus (2006). "Calibration of the MAGIC Telescope and Observation of Gamma Ray Bursts". In: *PhD Thesis*. URL: https://s3.cern.ch/inspire-prod-files-4/40aaaa58c4e6be2f04b4fc8483419927.

Ghisellini, G. (June 1, 1999). "Extreme blazars". In: *Astroparticle Physics* 11. ADS Bibcode: 1999APh....11...11G, pp. 11–18. ISSN: 0927-6505. DOI: 10.1016/S0927-6505(99)00018-3. URL: https://ui.adsabs.harvard.edu/abs/1999APh....11...11G.

Ghisellini, G., A. Celotti, et al. (Dec. 1, 1998). "A theoretical unifying scheme for gamma-ray bright blazars". In: *Monthly Notices of the Royal Astronomical Society* 301. ADS Bibcode: 1998MNRAS.301..451G, pp. 451–468. ISSN: 0035-8711. DOI: 10.1046/j.1365-8711.1998.02032.x. URL: https://ui.adsabs.harvard.edu/abs/1998MNRAS.301..451G.

Ghisellini, G., P. Padovani, et al. (Apr. 1, 1993). "Relativistic Bulk Motion in Active Galactic Nuclei". In: *The Astrophysical Journal* 407. ADS Bibcode: 1993ApJ...407...65G, p. 65. ISSN: 0004-637X. DOI: 10.1086/172493. URL: https://ui.adsabs.harvard.edu/abs/1993ApJ...407...65G.

Ghisellini, G., C. Righi, et al. (July 2017). "The Fermi blazar sequence". In: *Monthly Notices of the Royal Astronomical Society* 469.1, pp. 255–266. ISSN: 0035-8711, 1365-2966. DOI: 10.1093/mnras/stx806. arXiv: 1702.02571[astro-ph]. URL: http://arxiv.org/abs/1702.02571.

Ghisellini, G. and F. Tavecchio (Aug. 1, 2009). "Canonical high-power blazars". In: *Monthly Notices of the Royal Astronomical Society* 397.2, pp. 985–1002. ISSN: 0035-8711. DOI: 10.1111/j.1365-2966.2009.15007.x. URL: https://doi.org/10.1111/j.1365-2966.2009.15007.x.

Ghisellini, G., F. Tavecchio, et al. (July 1, 2011). "The transition between BL Lac objects and Flat Spectrum Radio Quasars". In: *Monthly Notices of the Royal Astronomical Society* 414.3, pp. 2674–2689. ISSN: 00358711. DOI: 10.1111/j.1365-2966.2011.18578.x. arXiv: 1012.0308[astro-ph]. URL: http://arxiv.org/abs/1012.0308.

Gilmore, R. C. et al. (June 1, 2012). "Semi-analytic modeling of the EBL and consequences for extragalactic gamma-ray spectra". In: *Monthly Notices of the Royal Astronomical Society* 422.4, pp. 3189–3207. ISSN: 00358711. DOI: 10.1111/j.1365-2966.2012.20841.x. arXiv: 1104.0671[astro-ph]. URL: http://arxiv.org/abs/1104.0671.

Gini, Corrado (1921). "Measurement of Inequality of Incomes". In: *The Economic Journal* 31.121. Publisher: [Royal Economic Society, Wiley], pp. 124–126. ISSN: 0013-0133. DOI: 10.2307/2223319. URL: https://www.jstor.org/stable/2223319.

Giommi, P. et al. (Mar. 11, 2012). "A simplified view of blazars: clearing the fog around long-standing selection effects: A simplified view of blazars". In: *Monthly Notices of the Royal Astronomical Society* 420.4, pp. 2899–2911. ISSN: 00358711. DOI: 10.1111/j.1365-2966.2011.20044.x. URL: https://academic.oup.com/mnras/article-lookup/doi/10.1111/j.1365-2966.2011.20044.x.

Greisen, K. (Apr. 25, 1966). "End to the Cosmic-Ray Spectrum?" In: *Physical Review Letters* 16.17. Publisher: American Physical Society, pp. 748–750. DOI: 10.1103/PhysRevLett.16.748. URL: https://link.aps.org/doi/10.1103/PhysRevLett.16.748.

Hales, S. E. G., J. E. Baldwin, and P. J. Warner (Oct. 1, 1988). "The 6C survey of radio sources - II. The zone 30". In: *Monthly Notices of the Royal Astronomical Society* 234. ADS Bibcode:

1988MNRAS.234..919H, pp. 919–936. ISSN: 0035-8711. DOI: 10.1093/mnras/234.4.919. URL: https://ui.adsabs.harvard.edu/abs/1988MNRAS.234..919H.

Hauser, M. G. and E. Dwek (Sept. 1, 2001). "The Cosmic Infrared Background: Measurements and Implications1". In: *Annual Review of Astronomy and Astrophysics* 39 (Volume 39, 2001). Publisher: Annual Reviews, pp. 249–307. ISSN: 0066-4146, 1545-4282. DOI: 10.1146/annurev.astro.39.1.249. URL: https://www.annualreviews.org/content/journals/10.1146/annurev.astro.39.1.249.

Heck, D. et al. (1998). "CORSIKA: A Monte Carlo code to simulate extensive air showers". In: Medium: PDF. [object Object]. DOI: 10.5445/IR/270043064. URL: https://publikationen.bibliothek.kit.edu/270043064.

Hillas, A. M. (Aug. 1, 1985). "Cerenkov Light Images of EAS Produced by Primary Gamma Rays and by Nuclei". In: 3. Conference Name: 19th International Cosmic Ray Conference (ICRC19), Volume 3 ADS Bibcode: 1985ICRC....3..445H, p. 445. URL: https://ui.adsabs.harvard.edu/abs/1985ICRC....3..445H.

Humason, M. L. and F. Zwicky (Jan. 1, 1947). "A Search for Faint Blue Stars." In: *The Astrophysical Journal* 105. ADS Bibcode: 1947ApJ...105...85H, p. 85. ISSN: 0004-637X. DOI: 10.1086/144884. URL: https://ui.adsabs.harvard.edu/abs/1947ApJ...105...85H.

IceCube, The et al. (July 13, 2018). "Multi-messenger observations of a flaring blazar coincident with high-energy neutrino IceCube-170922A". In: *Science* 361.6398, eaat1378. ISSN: 0036-8075, 1095-9203. DOI: 10.1126/science.aat1378. arXiv: 1807.08816[astro-ph, physics:hep-ex]. URL: http://arxiv.org/abs/1807.08816.

Inoue, Y. et al. (Apr. 26, 2013). "EXTRAGALACTIC BACKGROUND LIGHT FROM HIERARCHICAL GALAXY FORMATION: GAMMA-RAY ATTENUATION UP TO THE EPOCH OF COSMIC REIONIZATION AND THE FIRST STARS". In: *The Astrophysical Journal* 768.2, p. 197. ISSN: 0004-637X, 1538-4357. DOI: 10.1088/0004-637X/768/2/197. URL: https://iopscience.iop.org/article/10.1088/0004-637X/768/2/197.

Iriarte, B. and E. Chavira (1957). "Estrellas Azules en el Casquete Galactico Norte". In: *Boletín de los Observatorios de Tonantzintla y Tacubaya* 2.16. URL: http://www.astroscu.unam.mx/bott/BOTT..2-16/PDF/BOTT..2-16_biriarte.pdf.

Jansky, Karl G. (July 1933). "Radio Waves from Outside the Solar System". In: *Nature* 132.3323. Publisher: Nature Publishing Group, pp. 66–66. ISSN: 1476-4687. DOI: 10.1038/132066a0. URL: https://www.nature.com/articles/132066a0.

Keenan, Mary et al. (June 26, 2021). "The Relativistic Jet Dichotomy and the End of the Blazar Sequence". In: *Monthly Notices of the Royal Astronomical Society* 505.4, pp. 4726–4745. ISSN: 0035-8711, 1365-2966. DOI: 10.1093/mnras/stab1182. arXiv: 2007.12661[astro-ph]. URL: http://arxiv.org/abs/2007.12661.

Kelner, S. R. and F. A. Aharonian (Aug. 14, 2008). "Energy spectra of gamma-rays, electrons and neutrinos produced at interactions of relativistic protons with low energy radiation". In: *Physical Review D* 78.3, p. 034013. ISSN: 1550-7998, 1550-2368. DOI: 10.1103/PhysRevD.78.034013. arXiv: 0803.0688[astro-ph]. URL: http://arxiv.org/abs/0803.0688.

Kneiske, T. M. and H. Dole (June 2010). "A Lower-Limit Flux for the Extragalactic Background Light". In: *Astronomy and Astrophysics* 515, A19. ISSN: 0004-6361, 1432-0746. DOI: 10.1051/0004-6361/200912000. arXiv: 1001.2132[astro-ph]. URL: http://arxiv.org/abs/1001.2132.

Langston, G. I. et al. (Mar. 1, 1990). "The Second MIT–Green Bank 5 GHz Survey". In: *The Astrophysical Journal Supplement Series* 72. ADS Bibcode: 1990ApJS...72..621L, p. 621. ISSN: 0067-0049. DOI: 10.1086/191427. URL: https://ui.adsabs.harvard.edu/abs/1990ApJS...72..621L.

Levenberg, Kenneth (1944). "A method for the solution of certain non-linear problems in least squares". In: *Quarterly of Applied Mathematics* 2.2, pp. 164–168. ISSN: 0033-569X, 1552-4485. DOI: 10.1090/qam/10666. URL: https://www.ams.org/qam/1944-02-02/S0033-569X-1944-10666-0/.

Li, Ti-pei and Yu-qian Ma (1983). "ANALYSIS METHODS FOR RESULTS IN GAMMA-RAY ASTRONOMY". In: *ApJ*. . . 272.1.

López Coto, R. (2015). "Very-high-energy γ-ray observations of pulsar wind nebulae and cataclysmic variable stars with MAGIC and development of trigger systems for IACTs". In.

— (2017). *Very-high-energy Gamma-ray Observations of Pulsar Wind Nebulae and Cataclysmic Variable Stars with MAGIC and Development of Trigger Systems for IACTs*. en. Springer Theses. Cham: Springer International Publishing. ISBN: 978-3-319-44750-6 978-3-319-44751-3. DOI: 10.1007/978-3-319-44751-3. URL: http://link.springer.com/10.1007/978-3-319-44751-3.

Luyten, W. J. (Apr. 1, 1953). "A further search for faint blue stars". In: *The Astronomical Journal* 58. ADS Bibcode: 1953AJ.....58...75L, p. 75. ISSN: 0004-6256. DOI: 10.1086/106823. URL: https://ui.adsabs.harvard.edu/abs/1953AJ.....58...75L.

MAGIC Collaboration, The, V. A. Acciari, et al. (June 2020). "Broadband characterisation of the very intense TeV flares of the blazar 1ES 1959+650 in 2016". In: *Astronomy & Astrophysics* 638, A14. ISSN: 0004-6361, 1432-0746. DOI: 10.1051/0004-6361/201935450. arXiv: 2002.00129[astro-ph]. URL: http://arxiv.org/abs/2002.00129.

MAGIC Collaboration, The, M. L. Ahnen, et al. (Dec. 2018). "The extreme HBL behaviour of Markarian 501 during 2012". In: *Astronomy & Astrophysics* 620, A181. ISSN: 0004-6361, 1432-0746. DOI: 10.1051/0004-6361/201833704. arXiv: 1808.04300[astro-ph]. URL: http://arxiv.org/abs/1808.04300.

MAGIC Collaboration, The, J. Aleksić, et al. (July 2014). "MAGIC long-term study of the distant TeV blazar PKS 1424+240 in a multiwavelength context". In: *Astronomy & Astrophysics* 567, A135. ISSN: 0004-6361, 1432-0746. DOI: 10.1051/0004-6361/201423364. URL: http://www.aanda.org/10.1051/0004-6361/201423364.

Majumdar, P (2005). "Monte Carlo simulation for the MAGIC telescope". In: URL: https://cds.cern.ch/record/963471.

Mankuzhiyil, N. et al. (May 1, 2011). "The Environment and Distribution of Emitting Electrons as a Function of Source Activity in Markarian 421". In: *The Astrophysical Journal* 733. ADS

Bibcode: 2011ApJ...733...14M, p. 14. ISSN: 0004-637X. DOI: 10.1088/0004-637X/733/1/14. URL: https://ui.adsabs.harvard.edu/abs/2011ApJ...733...14M.

Mannheim, K. and P. L. Biermann (Jan. 1992). "Gamma-ray flaring of 3C 279: a proton-initiated cascade in the jet?" In: *Astronomy and Astrophysics* 253, pp. L21–L24. URL: https://articles.adsabs.harvard.edu/pdf/1992A%26A...253L..21M.

Maraschi, L. et al. (Apr. 1995). "ROSAT Observations of Blazars from a Polarized Radio Selected Sample". In: *The Astrophysical Journal* 443, p. 578. ISSN: 0004-637X, 1538-4357. DOI: 10.1086/175550. arXiv: astro-ph/9412002. URL: http://arxiv.org/abs/astro-ph/9412002.

Marquardt, Donald W. (June 1963). "An Algorithm for Least-Squares Estimation of Nonlinear Parameters". In: *Journal of the Society for Industrial and Applied Mathematics* 11.2. Publisher: Society for Industrial and Applied Mathematics, pp. 431–441. ISSN: 0368-4245. DOI: 10.1137/0111030. URL: https://epubs.siam.org/doi/abs/10.1137/0111030.

Massaro, E. et al. (May 2015). "The 5th edition of the Roma-BZCAT. A short presentation". In: *Astrophysics and Space Science* 357.1, p. 75. ISSN: 0004-640X, 1572-946X. DOI: 10.1007/s10509-015-2254-2. arXiv: 1502.07755[astro-ph]. URL: http://arxiv.org/abs/1502.07755.

Matthews, J. (Jan. 1, 2005). "A Heitler model of extensive air showers". In: *Astroparticle Physics* 22.5, pp. 387–397. ISSN: 0927-6505. DOI: 10.1016/j.astropartphys.2004.09.003. URL: https://www.sciencedirect.com/science/article/pii/S0927650504001598.

Meisner, A. M. and R. W. Romani (Mar. 1, 2010). "Imaging Redshift Estimates for BL Lacertae Objects". In: *The Astrophysical Journal* 712. ADS Bibcode: 2010ApJ...712...14M, pp. 14–25. ISSN: 0004-637X. DOI: 10.1088/0004-637X/712/1/14. URL: https://ui.adsabs.harvard.edu/abs/2010ApJ...712...14M.

Mirzoyan, R. (Jan. 1, 1997). "On the Calibration Accuracy of Light Sensors in Atmospheric Cherenkov Fluorescence and Neutrino Experiments". In: 7. Conference Name: International Cosmic Ray Conference ADS Bibcode: 1997ICRC....7..265M, p. 265. URL: https://ui.adsabs.harvard.edu/abs/1997ICRC....7..265M.

Montigny, C. von et al. (Feb. 1, 1995). "High-Energy Gamma-Ray Emission from Active Galaxies: EGRET Observations and Their Implications". In: *The Astrophysical Journal* 440. ADS Bibcode: 1995ApJ...440..525V, p. 525. ISSN: 0004-637X. DOI: 10.1086/175294. URL: https://ui.adsabs.harvard.edu/abs/1995ApJ...440..525V.

Mücke, A. and R. J. Protheroe (Mar. 2001). "A Proton Synchrotron Blazar Model for Flaring in Markarian~501". In: *Astroparticle Physics* 15.1, pp. 121–136. ISSN: 09276505. DOI: 10.1016/S0927-6505(00)00141-9. arXiv: astro-ph/0004052. URL: http://arxiv.org/abs/astro-ph/0004052.

Müller, Cornelia et al. (June 2011). "Dual-frequency VLBI study of Centaurus A on sub-parsec scales". In: *Astronomy & Astrophysics* 530, p. L11. ISSN: 0004-6361, 1432-0746. DOI: 10.1051/0004-6361/201116605. arXiv: 1104.0804[astro-ph]. URL: http://arxiv.org/abs/1104.0804.

Narayan, Ramesh and Insu Yi (June 1994). "Advection-Dominated Accretion: A Self-Similar Solution". In: *The Astrophysical Journal* 428, p. L13. ISSN: 0004-637X, 1538-4357. DOI: 10.1086/187381. arXiv: astro-ph/9403052. URL: http://arxiv.org/abs/astro-ph/9403052.

Netzer, H. (2013). *The Physics and Evolution of Active Galactic Nuclei*. Cambridge: Cambridge University Press. ISBN: 978-1-107-02151-8. DOI: 10.1017/CBO9781139109291. URL: https://www.cambridge.org/core/books/physics-and-evolution-of-active-galactic-nuclei/2A36453A413D67311D59A8A5CEA7117C.

Nigro, C. et al. (Apr. 1, 2022). "agnpy: An open-source python package modelling the radiative processes of jetted active galactic nuclei". In: *Astronomy & Astrophysics* 660. Publisher: EDP Sciences, A18. ISSN: 0004-6361, 1432-0746. DOI: 10.1051/0004-6361/202142000. URL: https://www.aanda.org/articles/aa/abs/2022/04/aa42000-21/aa42000-21.html.

Oke, J. B. and J. E. Gunn (Apr. 1974). "The Distance of BL Lacertae". In: *The Astrophysical Journal* 189, p. L5. ISSN: 0004-637X, 1538-4357. DOI: 10.1086/181450. URL: http://adsabs.harvard.edu/doi/10.1086/181450.

Ong, R. A. and The VERITAS Collaboration (June 15, 2009). *ATel #2084: Discovery of VHE Gamma-Ray Emission from the Fermi-LAT Source PKS 1424+240*. The Astronomer's Telegram. URL: https://www.astronomerstelegram.org/?read=2084.

Orr, M. J. L. and I. W. A. Browne (1982). *Relativistic beaming and quasar statistics*. URL: https://adsabs.harvard.edu/full/1982MNRAS.200.1067O.

Otero-Santos, J. et al. (Mar. 1, 2024). "Characterization of High-polarization Stars and Blazars with DIPOL-1 at Sierra Nevada Observatory". In: *The Astronomical Journal* 167.3, p. 137. ISSN: 0004-6256, 1538-3881. DOI: 10.3847/1538-3881/ad250d. URL: https://iopscience.iop.org/article/10.3847/1538-3881/ad250d.

Oya, I. et al. (2010). "Data Quality Check and On-Site Analysis of the MAGIC Telescope". In: *Highlights of Spanish Astrophysics V*. Ed. by Jose M. Diego et al. Berlin, Heidelberg: Springer, pp. 519–519. ISBN: 978-3-642-11250-8. DOI: 10.1007/978-3-642-11250-8_156.

Padovani, P. (June 25, 2007). "The Blazar Sequence: Validity and Predictions". In: *Astrophysics and Space Science* 309.1, pp. 63–71. ISSN: 0004-640X, 1572-946X. DOI: 10.1007/s10509-007-9455-2. arXiv: astro-ph/0610545. URL: http://arxiv.org/abs/astro-ph/0610545.

— (Aug. 1, 2017). "On the two main classes of active galactic nuclei". In: *Nature Astronomy* 1. ADS Bibcode: 2017NatAs...1E.194P, p. 0194. ISSN: 2397-3366. DOI: 10.1038/s41550-017-0194. URL: https://ui.adsabs.harvard.edu/abs/2017NatAs...1E.194P.

Padovani, P., B. Boccardi, et al. (Feb. 26, 2022). "PKS 1424+240: yet another masquerading BL Lac object as a possible IceCube neutrino source". In: *Monthly Notices of the Royal Astronomical Society* 511.4, pp. 4697–4701. ISSN: 0035-8711, 1365-2966. DOI: 10.1093/mnras/stac376. arXiv: 2202.04363[astro-ph,physics:hep-ex,physics:hep-ph]. URL: http://arxiv.org/abs/2202.04363.

Padovani, P. and P. Giommi (May 1, 1995). "The Connection between X-Ray– and Radio-selected BL Lacertae Objects". In: *The Astrophysical Journal* 444. ADS Bibcode: 1995ApJ...444..567P, p. 567. ISSN: 0004-637X. DOI: 10.1086/175631. URL: https://ui.adsabs.harvard.edu/abs/1995ApJ...444..567P.

Padovani, P., F. Oikonomou, et al. (Mar. 1, 2019). "TXS 0506+056, the first cosmic neutrino source, is not a BL Lac". In: *Monthly Notices of the Royal Astronomical Society* 484. ADS Bibcode: 2019MNRAS.484L.104P, pp. L104–L108. ISSN: 0035-8711. DOI: 10.1093/mnrasl/slz011. URL: https://ui.adsabs.harvard.edu/abs/2019MNRAS.484L.104P.

Padovani, P. and C. M. Urry (Mar. 1, 1992). "Luminosity Functions, Relativistic Beaming, and Unified Theories of High-Luminosity Radio Sources". In: *The Astrophysical Journal* 387. ADS Bibcode: 1992ApJ...387..449P, p. 449. ISSN: 0004-637X. DOI: 10.1086/171098. URL: https://ui.adsabs.harvard.edu/abs/1992ApJ...387..449P.

Paiano, S. et al. (Mar. 1, 2017). "On the Redshift of TeV BL Lac Objects". In: *The Astrophysical Journal* 837. ADS Bibcode: 2017ApJ...837..144P, p. 144. ISSN: 0004-637X. DOI: 10.3847/1538-4357/837/2/144. URL: https://ui.adsabs.harvard.edu/abs/2017ApJ...837..144P.

Paoletti, R. et al. (Apr. 2007). "The Trigger System of the MAGIC Telescope". In: *IEEE Transactions on Nuclear Science* 54.2. Conference Name: IEEE Transactions on Nuclear Science, pp. 404–409. ISSN: 1558-1578. DOI: 10.1109/TNS.2007.892649. URL: https://ieeexplore.ieee.org/document/4155102.

Peimbert, M. (Apr. 1, 2011). "Retrospective on "The Search for Blue Starlike Objects in the direction of the Poles of the Galaxy", by Haro & Luyten (1962)". In: 39. Conference Name: Revista Mexicana de Astronomia y Astrofisica Conference Series ADS Bibcode: 2011RMxAC..39...59P, pp. 59–64. URL: https://ui.adsabs.harvard.edu/abs/2011RMxAC..39...59P.

Perlman, Eric S. et al. (June 1, 1996). "The Einstein Slew Survey Sample of BL Lacertae Objects". In: *The Astrophysical Journal Supplement Series* 104. ADS Bibcode: 1996ApJS..104..251P, p. 251. ISSN: 0067-0049. DOI: 10.1086/192300. URL: https://ui.adsabs.harvard.edu/abs/1996ApJS..104..251P.

Pesch, P., N. Sanduleak, and C. B. Stephenson (Aug. 1, 1991). "The Case Low-Dispersion Northern Sky Survey. XII. A Region in Southern Canes Venatici". In: *The Astrophysical Journal Supplement Series* 76. ADS Bibcode: 1991ApJS...76.1043P, p. 1043. ISSN: 0067-0049. DOI: 10.1086/191589. URL: https://ui.adsabs.harvard.edu/abs/1991ApJS..76.1043P.

Pier, Edward A. and Julian H. Krolik (1993). "Infrared Spectra of Obscuring Dust Tori around Active Galactic Nuclei. II. Comparison with Observations." In: *The Astrophysical Journal* 418, pp. 673–686. URL: https://articles.adsabs.harvard.edu/pdf/1993ApJ...418..673P.

Plotkin, Richard M. et al. (Feb. 1, 2010). "Optically Selected BL Lacertae Candidates from the Sloan Digital Sky Survey Data Release Seven". In: *The Astronomical Journal* 139. ADS Bibcode: 2010AJ....139..390P, pp. 390–414. ISSN: 0004-6256. DOI: 10.1088/0004-6256/139/2/390. URL: https://ui.adsabs.harvard.edu/abs/2010AJ....139..390P.

Prandini, E. et al. (June 1, 2010). "Constraining blazar distances with combined *Fermi* and TeV data: an empirical approach". In: *Monthly Notices of the Royal Astronomical Society: Letters* 405.1, pp. L76–L80. ISSN: 1745-3933, 1745-3925. DOI: 10.1111/j.1745-3933.2010.00862.x. URL: https://academic.oup.com/mnrasl/article/405/1/L76/1069642.

Punch, M. et al. (Aug. 1, 1992). "Detection of TeV photons from the active galaxy Markarian 421". In: *Nature* 358. ADS Bibcode: 1992Natur.358..477P, pp. 477–478. ISSN: 0028-0836. DOI: 10.1038/358477a0. URL: https://ui.adsabs.harvard.edu/abs/1992Natur.358..477P.

Rees, M. J. (July 1966). "Appearance of Relativistically Expanding Radio Sources". In: *Nature* 211.5048. Publisher: Nature Publishing Group, pp. 468–470. ISSN: 1476-4687. DOI: 10.1038/211468a0. URL: https://www.nature.com/articles/211468a0.

Rolke, Wolfgang A., Angel M. Lopez, and Jan Conrad (Oct. 2005). "Limits and Confidence Intervals in the Presence of Nuisance Parameters". In: *Nuclear Instruments and Methods in Physics Research Section A: Accelerators, Spectrometers, Detectors and Associated Equipment* 551.2, pp. 493–503. ISSN: 01689002. DOI: 10.1016/j.nima.2005.05.068. arXiv: physics/0403059. URL: http://arxiv.org/abs/physics/0403059.

Roming, P. W. A. et al. (Oct. 1, 2005). "The Swift Ultra-Violet/Optical Telescope". In: *Space Science Reviews* 120. ADS Bibcode: 2005SSRv..120...95R, pp. 95–142. ISSN: 0038-6308. DOI: 10.1007/s11214-005-5095-4. URL: https://ui.adsabs.harvard.edu/abs/2005SSRv..120...95R.

Sambruna, R. M., L. Maraschi, and C. M. Urry (June 1, 1996). "On the Spectral Energy Distributions of Blazars". In: *The Astrophysical Journal* 463. ADS Bibcode: 1996ApJ...463..444S, p. 444. ISSN: 0004-637X. DOI: 10.1086/177260. URL: https://ui.adsabs.harvard.edu/abs/1996ApJ...463..444S.

Sandage, A. and W. J. Luyten (June 1967). "On the Nature of Faint Blue Objects in High Galactic Latitudes. I. Photometry, Proper Motions, and Spectra in PHL Field 1:36+6° and Richter Field M3, II". In: *The Astrophysical Journal* 148, p. 767. ISSN: 0004-637X, 1538-4357. DOI: 10.1086/149200. URL: http://adsabs.harvard.edu/doi/10.1086/149200.

— (Mar. 1, 1969). "On the Nature of Faint Blue Objects in High Galactic Latitudes. II. Summary of Photometric Results for 301 Objects in Seven Survey Fields". In: *The Astrophysical Journal* 155. ADS Bibcode: 1969ApJ...155..913S, p. 913. ISSN: 0004-637X. DOI: 10.1086/149921. URL: https://ui.adsabs.harvard.edu/abs/1969ApJ...155..913S.

Sbarufatti, B., A. Treves, and R. Falomo (Dec. 10, 2005). "Imaging Redshifts of BL Lacertae Objects". In: *The Astrophysical Journal* 635.1. Publisher: IOP Publishing, p. 173. ISSN: 0004-637X. DOI: 10.1086/497022. URL: https://iopscience.iop.org/article/10.1086/497022/meta.

Scarpa, R. et al. (Apr. 1, 2000). "The Hubble Space Telescope Survey of BL Lacertae Objects. I. Surface Brightness Profiles, Magnitudes, and Radii of Host Galaxies". In: *The Astrophysical Journal* 532.2. Publisher: IOP Publishing, p. 740. ISSN: 0004-637X. DOI: 10.1086/308618. URL: https://iopscience.iop.org/article/10.1086/308618/meta.

Scheuer, P. a. G. and A. C. S. Readhead (Jan. 1979). "Superluminally expanding radio sources and the radio-quiet QSOs". In: *Nature* 277.5693. Publisher: Nature Publishing Group, pp. 182–185. ISSN: 1476-4687. DOI: 10.1038/277182a0. URL: https://www.nature.com/articles/277182a0.

Schlafly, E. F. and D. P. Finkbeiner (Aug. 1, 2011). "Measuring Reddening with Sloan Digital Sky Survey Stellar Spectra and Recalibrating SFD". In: *The Astrophysical Journal* 737. ADS Bibcode: 2011ApJ...737..103S, p. 103. ISSN: 0004-637X. DOI: 10.1088/0004-637X/737/2/103. URL: https://ui.adsabs.harvard.edu/abs/2011ApJ...737..103S.

Schmidt, M. (Mar. 1963). "3C 273 : A Star-Like Object with Large Red-Shift". In: *Nature* 197.4872. Publisher: Nature Publishing Group, pp. 1040–1040. ISSN: 1476-4687. DOI: 10.1038/1971040a0. URL: https://www.nature.com/articles/1971040a0.

Schmuckermaier, Felix et al. (Dec. 1, 2022). "Correcting MAGIC Telescope data taken under non-optimal atmospheric conditions with an elastic LIDAR". In: *Journal of Physics: Conference Series* 2398.1, p. 012011. ISSN: 1742-6588, 1742-6596. DOI: 10.1088/1742-6596/2398/1/012011. URL: https://iopscience.iop.org/article/10.1088/1742-6596/2398/1/012011.

Schneider, P. (2006). *Extragalactic Astronomy and Cosmology: An Introduction | SpringerLink*. URL: https://link.springer.com/book/10.1007/978-3-642-54083-7.

Shakura, N. I. and R. A. Sunyaev (1973). "Black Holes in Binary Sistems. Observational Appearance." In: *Astronomy and Astrophysics* 24, pp. 337–355. URL: https://articles.adsabs.harvard.edu/pdf/1973A%26A....24..337S.

Spurio, Maurizio (2015). *Particles and Astrophysics: A Multi-Messenger Approach*. en. Astronomy and Astrophysics Library. Cham: Springer International Publishing. ISBN: 978-3-319-08050-5 978-3-319-08051-2. DOI: 10.1007/978-3-319-08051-2. URL: http://link.springer.com/10.1007/978-3-319-08051-2.

Stalevski, Marko et al. (Mar. 11, 2012). "Three-dimensional radiative transfer modeling of AGN dusty tori as a clumpy two-phase medium". In: *Monthly Notices of the Royal Astronomical Society* 420.4, pp. 2756–2772. ISSN: 00358711. DOI: 10.1111/j.1365-2966.2011.19775.x. arXiv: 1109.1286[astro-ph]. URL: http://arxiv.org/abs/1109.1286.

Stecker, F. W., O. C. De Jager, and M. H. Salamon (May 1992). "TeV gamma rays from 3C 279 - A possible probe of origin and intergalactic infrared radiation fields". In: *The Astrophysical Journal* 390, p. L49. ISSN: 0004-637X, 1538-4357. DOI: 10.1086/186369. URL: http://adsabs.harvard.edu/doi/10.1086/186369.

Stecker, F. W., M. A. Malkan, and S. T. Scully (Sept. 10, 2006). "Intergalactic Photon Spectra from the Far-IR to the UV Lyman Limit for $0 < z < 6$ and the Optical Depth of the Universe to High-Energy Gamma Rays". In: *The Astrophysical Journal* 648.2, pp. 774–783. ISSN:

0004-637X, 1538-4357. DOI: 10.1086/506188. URL: https://iopscience.iop.org/article/10.1086/506188.

Stickel, M., K. Meisenheimer, and H. Kuehr (June 1, 1994). "The optical identification status of the 1 Jy radio source catalogue". In: *Astronomy and Astrophysics Supplement Series* 105. ADS Bibcode: 1994A&AS..105..211S, pp. 211–234. ISSN: 0365-0138. URL: https://ui.adsabs.harvard.edu/abs/1994A&AS..105..211S.

Stocke, John T., Simon L. Morris, I. M. Gioia, et al. (July 1, 1991). "The Einstein Observatory Extended Medium-Sensitivity Survey. II. The Optical Identifications". In: *The Astrophysical Journal Supplement Series* 76. ADS Bibcode: 1991ApJS...76..813S, p. 813. ISSN: 0067-0049. DOI: 10.1086/191582. URL: https://ui.adsabs.harvard.edu/abs/1991ApJS...76..813S.

Stocke, John T., Simon L. Morris, Ray J. Weymann, et al. (1992). *1992ApJ...396..487S Page 487*. URL: https://adsabs.harvard.edu/full/1992ApJ...396..487S.

Tavecchio, F., J. Becerra González, et al. (Oct. 2011). "On the origin of the gamma-ray emission from the flaring blazar PKS 1222+216". In: *Astronomy & Astrophysics* 534, A86. ISSN: 0004-6361, 1432-0746. DOI: 10.1051/0004-6361/201117204. arXiv: 1104.0048[astro-ph]. URL: http://arxiv.org/abs/1104.0048.

Tavecchio, F. and G. Ghisellini (Sept. 11, 2014). "On the spine-layer scenario for the very high-energy emission of NGC 1275". In: *Monthly Notices of the Royal Astronomical Society* 443.2, pp. 1224–1230. ISSN: 1365-2966, 0035-8711. DOI: 10.1093/mnras/stu1196. arXiv: 1404.6894[astro-ph]. URL: http://arxiv.org/abs/1404.6894.

Tavecchio, F., L. Maraschi, and G. Ghisellini (Dec. 20, 1998). "Constraints on the Physical Parameters of TeV Blazars". In: *The Astrophysical Journal* 509.2. Publisher: IOP Publishing, p. 608. ISSN: 0004-637X. DOI: 10.1086/306526. URL: https://iopscience.iop.org/article/10.1086/306526/meta.

Tescaro, Diego et al. (2013). *The MAGIC telescopes DAQ software and the on-the-fly online analysis client*. arXiv: 1310.1565 [astro-ph.IM].

Teshima, M. and The MAGIC Collaboration (June 24, 2009). *ATel #2098: MAGIC observes very high energy gamma ray emission from PKS 1424 +240*. The Astronomer's Telegram. URL: https://www.astronomerstelegram.org/?read=2098.

Ulrich, M. -H. et al. (June 1, 1975). "Nonthermal continuum radiation in three elliptical galaxies." In: *The Astrophysical Journal* 198. ADS Bibcode: 1975ApJ...198..261U, pp. 261–266. ISSN: 0004-637X. DOI: 10.1086/153603. URL: https://ui.adsabs.harvard.edu/abs/1975ApJ...198..261U.

Urry, C. M. and P. Padovani (June 9, 1995). *Unified Schemes for Radio-Loud Active Galactic Nuclei*. DOI: 10.1086/133630. arXiv: astro-ph/9506063. URL: http://arxiv.org/abs/astro-ph/9506063.

Urry, C. M., R. Scarpa, et al. (Apr. 1, 2000). "The Hubble Space Telescope Survey of BL Lacertae Objects. II. Host Galaxies". In: *The Astrophysical Journal* 532.2. Publisher: IOP Publishing,

p. 816. ISSN: 0004-637X. DOI: 10.1086/308616. URL: https://iopscience.iop.org/article/10.1086/308616/meta.

Ventura, S. (2023). "Non-Thermal Features in TeV-Blazars and the Galactic Center Region with MAGIC and Prospects for CTA". PhD thesis. Siena U. DOI: https://dx.doi.org/10.25434/ventura-sofia_phd2023. URL: https://hdl.handle.net/11365/1245254.

Verna, G. (Nov. 9, 2022). "Study of the PeVatron candidate SNR G106.3+2.7 and optimization of the CTA-North sensitivity at high energies". These de doctorat. Aix-Marseille. URL: https://theses.fr/2022AIXM0388.

Voges, W. et al. (Sept. 1, 1999). "The ROSAT all-sky survey bright source catalogue". In: *Astronomy and Astrophysics* 349. ADS Bibcode: 1999A&A...349..389V, pp. 389–405. ISSN: 0004-6361. DOI: 10.48550/arXiv.astro-ph/9909315. URL: https://ui.adsabs.harvard.edu/abs/1999A&A...349..389V.

Wagner, Robert Marcus (Oct. 2007). "Measurement of Very High Energy Gamma-Ray Emission from Four Blazars Using the MAGIC Telescope and a Comparative Blazar Study". In: *Publications of the Astronomical Society of the Pacific* 119.860, pp. 1201–1203. ISSN: 0004-6280, 1538-3873. DOI: 10.1086/522380. URL: http://iopscience.iop.org/article/10.1086/522380.

Wakely, S. P. and D. Horan (2008). "TeVCat: An online catalog for Very High Energy Gamma-Ray Astronomy". In: *International Cosmic Ray Conference* 3, pp. 1341–1344.

Weekes, T. C. (May 2002). "VERITAS: the Very Energetic Radiation Imaging Telescope Array System". In: *Astroparticle Physics* 17.2, pp. 221–243. ISSN: 09276505. DOI: 10.1016/S0927-6505(01)00152-9. arXiv: astro-ph/0108478. URL: http://arxiv.org/abs/astro-ph/0108478.

Weekes, T. C. et al. (July 1, 1989). "Observation of TeV Gamma Rays from the Crab Nebula Using the Atmospheric Cerenkov Imaging Technique". In: *The Astrophysical Journal* 342. ADS Bibcode: 1989ApJ...342..379W, p. 379. ISSN: 0004-637X. DOI: 10.1086/167599. URL: https://ui.adsabs.harvard.edu/abs/1989ApJ...342..379W.

White, R. L. et al. (Feb. 1, 2000). "The FIRST Bright Quasar Survey. II. 60 Nights and 1200 Spectra Later". In: *The Astrophysical Journal Supplement Series* 126.2. Publisher: IOP Publishing, p. 133. ISSN: 0067-0049. DOI: 10.1086/313300. URL: https://iopscience.iop.org/article/10.1086/313300/meta.

Wiebel-Sooth, B., P. L. Biermann, and H. Meyer (1998). "VII. Individual element spectra: prediction and data". In.

Zanin, Roberta (2013). "MARS, the MAGIC analysis and reconstruction software". In: *33rd International Cosmic Ray Conference*, p. 0773.

Zatsepin, G. T. and V. A. Kuzmin (Aug. 1, 1966). "Upper Limit of the Spectrum of Cosmic Rays". In: *Soviet Journal of Experimental and Theoretical Physics Letters* 4. ADS Bibcode: 1966JETPL...4...78Z, p. 78. ISSN: 0021-3640. URL: https://ui.adsabs.harvard.edu/abs/1966JETPL...4...78Z.